

NONLINEAR DYNAMIC AND STATIC ANALYSIS OF I-5
RAVENNA BRIDGE

By

REZA SHAFIEI-TEHRANY

A thesis submitted in partial fulfillment of
the requirements of the degree of

MASTER OF SCIENCE IN CIVIL ENGINEERING

WASHINGTON STATE UNIVERSITY
Department of Civil and Environmental Engineering

DECEMBER 2008

To the faculty of Washington State University:

The members of the Committee appointed to examine the thesis of REZA SHAFIEI-TEHRANY
find it satisfactory and recommend that it be accepted.

Chair

ACKNOWLEDGEMENTS

This research was performed in the Department of Civil and Environmental Engineering at Washington State University, Pullman, Washington. Funding was provided by the Washington State Department of Transportation. Their support is greatly appreciated.

I am grateful to Dr. Mohamed A. ElGawady, the chairman of my committee, for his patience and guidance through this project. I would also like to thank Dr. William Cofer and Dr. Balasingam Muhunthan for their participation and assistance on my committee. A special thanks for Steve Greenwood who partnered with me on this project. I like to thank my family for supporting me throughout, specially my mom who always pushes me to be the best I can be.

NONLINEAR DYNAMIC AND STATIC ANALYSIS OF I-5 RAVENNA BRIDGE

Abstract

By Reza Shafiei-Tehrany, M.S.
Washington State University
December 2008

Chair: Dr. Mohamed A. ElGawady

The Washington State Department of Transportation (WSDOT) developed a bridge seismic retrofit program in 1990 in order to address seismic risk associated with state owned bridges. Of particular interest are bridges with multiple column bents and those founded on precast/prestressed hollow core concrete piles. A number of deficiencies in the seismic behavior of these piles were observed. They have minimal energy-absorbing hysteretic behavior, and failure in such piles is sudden and violent.

Knowing the behavioral properties of prestressed hollow core piles, a typical bridge built on them was evaluated for seismic loading. The outcome for this task is knowledge of the failure mechanisms for this type of bridge, the forces required for various levels of failure, and a definition of the earthquake magnitude that will cause failure. Two types of analysis were performed: pushover analysis and nonlinear dynamic analysis. The same type of structural model was used for both.

A three-dimensional “spine” model of the bridge was developed using SAP2000 (2007), including modeling of the bridge bearings, expansions joints, and soil-structure interaction. The dynamic nonlinear response of the bridge was investigated by using three ground motions with different return periods. The nonlinear static response of the bridge was investigated using different variants of capacity spectrum methods. Nonlinear static analysis provided poor results

compared to nonlinear dynamic analysis, due to higher mode effects. Results of both nonlinear static and dynamic analysis showed that the piles fail in a brittle fashion under seismic loading.

Using results from 3D finite element analysis of the piles and pile-crossbeam connection, a more advanced spine model was created. The pile-crossbeam connection improved the strength of the bridge. The effect of foundation soil flexibility was examined by running analysis on three different soil types and comparing the results. Dense sand proved to be the most conservative soil model. Also, the effects on the seismic demand due to period lengthening and damping increase produced by structural deterioration were evaluated.

TABLE OF CONTENTS

	Page
ACKNOWLEDGMENTS.....	III
ABSTRACT.....	IV
TABLE OF CONTENTS	VI
TABLE OF FIGURES.....	X
TABLE OF TABLES.....	XIV
CHAPTER 1: INTRODUCTION.....	1
1.1. INTRODUCTION AND BACKGROUND	1
1.2. RESEARCH OBJECTIVES	2
1.3. SEISMICITY IN WESTERN WASHINGTON STATE	3
CHAPTER 2: LITERATURE REVIEW	4
CHAPTER 3: SEISMIC ASSESSMENT METHODOLOGY	9
3.1. PUSHOVER CURVES AND CAPACITY DIAGRAMS	11
3.2. REVIEW OF THE AVAILABLE VARIANTS OF THE CAPACITY SPECTRUM METHOD	15
3.2.1. CSM in ATC-40.....	15
3.2.2. CSM with Inelastic Design Spectra.....	20
3.2.2.1. <i>Demand Reduction Factors from Newmark and Hall (1982).....</i>	<i>22</i>
3.2.2.2. <i>Demand Reduction Factors from Krawinkler and Nassar (1992).....</i>	<i>23</i>
3.2.2.3. <i>Demand Reduction Factors from Vidic et al. (1994).....</i>	<i>23</i>
3.2.2.4. <i>Demand Reduction Factors from Miranda and Bertero (1994).....</i>	<i>24</i>
3.2.2.5. <i>Comparison of Different Demand Reduction Factors</i>	<i>24</i>
3.2.3. CSM with Equivalent Elastic Spectra from Damping Models.....	26
3.2.3.1. <i>Iwan and Gates (1979) – According to Average Stiffness and Energy (ASE) Method</i>	<i>27</i>
3.2.3.2. <i>Priestley et al. (1996).....</i>	<i>28</i>
3.2.3.3. <i>WJE (1996)</i>	<i>28</i>

3.2.3.4. Kowalsky et al. (1994b)	29
3.2.4. Improved Capacity Spectrum Method	29
3.2.5. An Advanced Capacity Spectrum Method	30
3.3. COEFFICIENT METHOD (CM)	32
3.3.1. Improved Coefficient Method	34
3.4. TIME-HISTORY ANALYSIS	34
3.4.1. Damping	35
CHAPTER 4: I-5 RAVENNA BRIDGE	36
4.1. LAYOUT AND GEOMETRY	36
4.2. STRUCTURAL MODEL	44
4.2.1. Boundary and connectivity conditions	46
4.2.1.1. Bearings	46
4.2.1.2. Expansion Joints	47
4.2.1.3. Abutments	49
4.2.1.4. Soil-pile interaction	52
4.2.2. Plastic hinge definition for piles	55
4.2.2.1. Moment curvature relationship	56
4.2.2.2. Plastic hinge length	57
4.2.2.3. Plastic hinge location	58
4.2.2.4. Plastic Hinge input in SAP2000	60
4.3. PLASTIC HINGE LENGTH USING DETAILED FINITE ELEMENT OF THE PILE	64
4.4. FE MODEL OF PILE TOP BOUNDARY CONDITION	66
4.5. SEISMIC EXCITATIONS	68
CHAPTER 5: NONLINEAR DYNAMIC ANALYSIS RESULTS	73
5.1. LOOSE SAND	73
5.2. DENSE SAND	79
5.3. STIFF CLAY	85
CHAPTER 6: NONLINEAR STATIC ANALYSIS RESULTS	90

6.1. SECOND-ORDER EFFECTS OF GEOMETRIC NONLINEARITY (P-DELTA)	96
6.2. TARGET DISPLACEMENT FROM NONLINEAR STATIC ANALYSIS	98
6.2.1. Capacity Spectrum Method in ATC-40	99
6.2.2. Improved Capacity Spectrum Method (FEMA 440).....	101
6.2.3. Capacity Spectrum Method with Inelastic Design Spectra	102
6.2.4. CSM with Equivalent Elastic Spectra from Damping Models.....	105
6.2.5. Advanced CSM.....	107
6.2.6. Displacement Coefficient Method (DCM)	109
6.2.7. Conclusions on the Methodology for Structural Assessment	111
6.3. DIFFERENT SOILS	112
CHAPTER 7: EFFECTS OF PILE-CROSSBEAM CONNECTION	118
7.1. NLS ANALYSIS	119
7.2. NDL ANALYSIS	122
CHAPTER 8: CONCLUSIONS	125
REFERENCE	127
APPENDIX	134
APPENDIX A	135
A.1. DEMAND DIAGRAM ACCORDING TO NEWMARK AND HALL (1982)	135
A.2. DAMPING MODIFICATION FACTOR, K, IN ACT-40(1996)	137
A.3. MODIFICATION FACTORS IN CM (FEMA356, 2000)	138
A.3.1. Improved modification factors (FEMA440, 2005)	140
APPENDIX B	141
B.1. SUPERSTRUCTURE GEOMETRY.....	141
B.2. ABOVE-GROUND HEIGHT OF PILES	143
B.3. BEARINGS	144
B.4. MATERIALS.....	146
B.5. EXPANSION JOINTS	148
B.6. FOUNDATION STIFFNESS – FEMA 356 (2000).....	148

B.7. LONGITUDINAL BACK WALL RESPONSE – CALTRANS (2008).....	150
B.8. SOIL-PILE INTERACTION	152
B.9. SOIL PROPERTIES	158
B.10. PLASTIC HINGES	158
APPENDIX C	160
C.1. SHEAR CAPACITY DEGRADATION MODEL	160
C.2. NLD ANALYSIS RESULTS	164

TABLE OF FIGURES

Figure 1.1. Cascadia Subduction Zone.....	3
Figure 2.1. (a) Pile test setup; (b) Moment-curvature diagram for a prestressed hollow core pile (Budek, et al., 1997b)	8
Figure 3.1. Pushover Curves	11
Figure 3.2. Demand diagram in (Left): Standard format; (Right): Acceleration-Displacement format.....	12
Figure 3.3. Conversion of pushover curves to capacity diagrams	14
Figure 3.4. Bilinear representations based on equal energy principle	16
Figure 3.5. Plot demand and capacity diagrams to determine the displacement demand	17
Figure 3.6. (Left): Equivalent SDOF system based on secant stiffness; (Right): Equivalent viscous damping due to hysteretic energy dissipation	18
Figure 3.7. Relation between the equivalent viscous damping and damping modification factor ...	19
Figure 3.8. Elasto-plastic representation of the capacity diagram required in using CSM with inelastic design spectra	21
Figure 3.9. Comparison of reduction factors from different studies; Newmark and Hall (1982), Kranwinkler and Nassar (1992); Vidic et al. (1994); Miranda and Bertero (1994).....	25
Figure 3.10. Inelastic design spectra calculated using different demand reduction factors; NH: Newmark and Hall (1982), KN: Krawinkler and Nassar (1992); VFF: Vidic et al. (1994); MB: Miranda and Bertero (1994); ATC-40 (1996).....	26
Figure 3.11. Ductility damping relationships from different studies	27
Figure 3.12. Force-deformation relationship for kinematic hardening behavior	30
Figure 3.13. Mass-spring-damper system used for Advanced CSM	31
Figure 3.14. Determine of the elastic period, reproduced from FEMA 356 (2000).....	33
Figure 4.1. Aerial view of the I-5 Ravenna Bridge.....	36
Figure 4.2. Elevation and plan view of I-5 Ravenna Bridge.....	37
Figure 4.3. Superstructure cross-sections	38
Figure 4.4. Plan (for typical six column bent) and section view of crossbeam	39
Figure 4.5. Typical pile (section and elevation view)	40
Figure 4.6. Crossbeam-pile connection	41
Figure 4.7. Bearing pad	41
Figure 4.8. Girder restrainer	41
Figure 4.9. Expansion joint at intermediate piers.....	42
Figure 4.10. Abutment sub-ground column and footing	43
Figure 4.11. Test holes classifying soil layers.....	43
Figure 4.12. Column/pile cross-section model: (a) top 4 feet; and (b) rest of pile.....	45
Figure 4.13. Crossbeam cross-section model	45
Figure 4.14. Model for elastomeric bearings	47
Figure 4.15. Pounding of bridge decks	48
Figure 4.16. Characterization of contact element	49
Figure 4.17. Spill-through abutment type.....	50
Figure 4.18. Definition of longitudinal abutment behavior	51

Figure 4.19. Model for abutment back wall.....	52
Figure 4.20. Schematic model of laterally loaded pile (Lymon, et al., 2006)	53
Figure 4.21. Definition of p and y as related to response of a pile to lateral loading (Lymon, et al., 2006)	53
Figure 4.22. The relation between the lateral force and displacement used for characterization of the springs along the pile in the loose sand	54
Figure 4.23. SAP model of column/pile	55
Figure 4.24 Moment-curvature curves of the columns/piles	56
Figure 4.25. Transverse seismic response of extended pile-shafts (Chai, et al., 2002)	59
Figure 4.26. Generalized force-deformation relations for concrete elements	60
Figure 4.27. Moment-rotation relationship of the columns.....	61
Figure 4.28. Axial load-moment interaction diagram of the columns.....	62
Figure 4.29. Final spine model of the Ravenna Bridge.....	63
Figure 4.30. FE model of pile	64
Figure 4.31. Failure of pile at plastic hinge location	65
Figure 4.34. FE model of pile-crossbeam connection.....	66
Figure 4.35. Failure of pile-crossbeam connection.....	67
Figure 4.36. Moment-rotation relationship for pile-crossbeam connection	68
Figure 4.37. DRS corresponding to 475, 975, and 2475-year return period	69
Figure 4.38. Moquegua, Peru Ground Motion (E-W) Spectral Acceleration.....	70
Figure 4.39. Modified and Original Moquegua, Peru Ground Motion (E-W) Time History	70
Figure 4.40. Time Histories for Olympia 475	71
Figure 4.41. Time Histories for Olympia 975	71
Figure 4.42. Time Histories for Peru 2475.....	72
Figure 5.1. Hinge development for EQs in the longitudinal direction with loose sand.....	74
Figure 5.2. Hinge development for EQs in the transverse direction with loose sand	75
Figure 5.3. Target column displacement-time history for longitudinal EQs with loose sand	76
Figure 5.4. Target column displacement-time history for transverse EQs with loose sand	77
Figure 5.5. Force-Displacement hysteresis curves of the target column in the longitudinal (left) and transverse (right) direction with loose sand	78
Figure 5.6. Hinge development for EQs in the longitudinal direction with dense sand	80
Figure 5.7. Hinge development for EQs in the transverse direction with dense sand	81
Figure 5.8. Target column displacement-time history for longitudinal EQs with dense sand	82
Figure 5.9. Target column displacement-time history for transverse EQs with dense sand	83
Figure 5.10. Force-Displacement hysteresis curves of the target column in the longitudinal (left) and transverse (right) direction with dense sand	84
Figure 5.11. Hinge development for earthquakes in the longitudinal direction with stiff clay.....	85
Figure 5.12. Hinge development for earthquakes in the transverse direction with stiff clay.....	86
Figure 5.13. Target column displacement-time history for longitudinal EQs with stiff clay	87
Figure 5.14. Target column displacement-time history for transverse EQs with stiff clay	88
Figure 5.15. Force-Displacement hysteresis curves of the target column in the longitudinal (left) and transverse (right) direction with stiff clay	89
Figure 6.1. Four highest MPMRs in longitudinal and transverse direction of the bridge	91

Figure 6.2. Hinging sequence up to transverse ultimate limit state condition.....	92
Figure 6.3. Hinging sequence up to longitudinal ultimate limit state condition.....	93
Figure 6.4. Capacity curves for longitudinal and transverse directions	94
Figure 6.5. Yielding increase in effective viscous damping	95
Figure 6.6. Influence of yielding on the natural period	95
Figure 6.7. Longitudinal capacity curve with (continuous line) and without P-delta effects.....	97
Figure 6.8. Transverse capacity curve with (continuous line) and without P-delta effects	98
Figure 6.9. Capacity diagrams for both fundamental directions.....	99
Figure 6.10. Results from CSM in ATC-40 in the longitudinal direction	100
Figure 6.11. Results from CSM in ATC-40 in the transverse direction	101
Figure 6.12. Improved CSM results for both fundamental directions.....	102
Figure 6.13. Elasto-plastic representations (solid lines) for capacity diagrams (dashed lines) in both fundamental directions	103
Figure 6.14. Results from CSM with inelastic design spectra for the longitudinal direction.....	104
Figure 6.15. Results from CSM with inelastic design spectra for the transverse direction	105
Figure 6.16. Graphical solution from CSM with equivalent elastic spectra from damping models for the longitudinal direction	106
Figure 6.17. Graphical solution from CSM with equivalent elastic spectra from damping models for the transverse direction	107
Figure 6.18. Results for advanced CSM using SDOF considering longitudinal direction	108
Figure 6.19. Results for advanced CSM using SDOF considering transverse direction	109
Figure 6.20. Effects of soil type on the pushover curve in longitudinal direction	113
Figure 6.21. Effects of soil type on the pushover curve in transverse direction	114
Figure 6.22. Pushover hinge development in longitudinal direction with stiff clay	115
Figure 6.23. Pushover hinge development in transverse direction with stiff clay	115
Figure 6.24. Pushover hinge development in longitudinal direction with dense sand	116
Figure 6.25. Pushover hinge development in transverse direction with dense sand	116
Figure 7.1. Capacity curve comparison between different models.....	118
Figure 7.2. Capacity curves for different soil models in the longitudinal direction.....	119
Figure 7.3. Capacity curves for different soil models in the transverse direction.....	120
Figure 7.4. Hinge development for EQ3 in the longitudinal direction of dense sand model.....	121
Figure 7.5. Hinge development for EQ3 in the transverse direction of dense sand model.....	121
Figure 7.6. Hinge development of dense sand model with FE pile-crossbeam connections under EQ3 ground motion and given direction.	123
Figure 7.7. Force-Displacement hysteresis curves of the target column in dense sand model with FE pile-crossbeam connections for EQ3 and given directions.	123
Figure 7.8. Target column displacement-time history in dense sand model with FE pile-crossbeam connections for EQ3 and given directions.	124
Figure A.1. Newmark and Hall (1982) elastic spectrum, reproduced from Chopra (2000).....	136
Figure B.1. WSDOT girder	141
Figure B.3. Girder numbering along the width of spans.....	142
Figure A.2. Model of all girders used in the Ravenna Bridge (with series numbers)	142
Figure B.4. Orientation of piers.....	144

Figure B.5. Bearing dimensions	145
Figure B.6. Stress-strain curve for 7800 psi concrete	146
Figure B.7. Stress-strain curve for 4000 psi concrete (Class A).....	146
Figure B.8. Compressive stress-strain curve for grade 40 steel	147
Figure B.9. Compressive stress-strain curve for grade 270 steel (Prestress).....	147
Figure B.10. Elastic solutions for rigid footing spring constraints (FEMA356, 2000).....	149
Figure B.11. Effective abutment stiffness	151
Figure B.12. Effective abutment area.....	152
Figure B.13. Effective abutment width for skewed bridges	152
Figure B.14. The relation between the lateral force and displacement used for characterization of the springs along the pile in the dense sand.....	156
Figure B.15. The relation between the lateral force and displacement used for characterization of the springs along the pile in the stiff clay.....	157
Figure C.1. Neutral Axis Positions for Hollow Circular Columns	161
Figure C.2. Reduction of Concrete Shear Component (γ) with Curvature Ductility	161
Figure C.3. Effects of concrete compression zone on truss mechanism	163
Figure C.4. Axial load component of shear	163

TABLE OF TABLES

Table 3.1. Constants for reduction factors from Krawinkler and Nassar (1992)	23
Table 3.2. Φ as function of period, ductility and soil conditions	24
Table 3.3. Effective damping ratio based on WJE damping model (WJE, 1996)	28
Table 6.1 Summary of results in nonlinear static analysis	110
Table 6.2. Displacement summary and assessment of NLS with different soil models	117
Table 7.1. Displacement summary and assessment of NLS with different soil models	122
Table A.1. Amplification factors: elastic design spectra, Newmark and Hall (1982)	136
Table A.2. Equations used for calculation the damping modification factor, κ (ATC-40, 1996).....	137
Table A.3. Structural behavior types (ATC-40, 1996)	137
Table A.4. Values for the modification factor C_0	138
Table A.5. Values for the modification factor C_2	139
Table B.1. Girder dimension (in inches)	141
Table B.2. Assigned girder to individual spans	142
Table B.3. Span properties	143
Table B.4. Cross-beam length and above ground height of columns	144
Table B.5. Bearing properties and calculated model	145
Table B.6. Gap element calculations	148
Table B.7. Footing spring stiffness for loose sand (kip/in)	148
Table B.8. Footing spring stiffness for dense sand (kip/in)	148
Table B.9. Footing spring stiffness for stiff clay (kip/in)	149
Table B.10. Results of p-y curves for dense sand	153
Table B.11. Results of p-y curves for loose sand	154
Table B.12. Results of p-y curves for stiff clay	155
Table B.13. Soil parameters	158
Table B.14. Bilinearized moment-curvature data	159
Table B.15. Average below ground depth of plastic hinges for bents	159
Table C.1. NLD results for loose sand model in the longitudinal direction.....	165
Table C.2. NLD results for loose sand model in the transverse direction.....	166
Table C.3. NLD results for dense sand model in the longitudinal direction.....	167
Table C.4. NLD results for dense sand model in the transverse direction.....	168
Table C.5. NLD results for stiff clay model in the longitudinal direction.....	169
Table C.6. NLD results for stiff clay model in the transverse direction.....	170
Table C.7. SRSS combined NDL results for the loose sand model.....	171
Table C.8. SRSS combined NDL results for the dense sand model.....	172
Table C.9. SRSS combined NDL results for the stiff clay model.....	173

CHAPTER 1: INTRODUCTION

1.1. INTRODUCTION AND BACKGROUND

Washington State Department of Transportation (WSDOT) has the responsibility for maintaining approximately 3,000 bridges in Washington State. Many of these bridges were constructed in the 1950's and 1960's prior to developing modern seismic design standards and may be seismically vulnerable. WSDOT developed a retrofitting program to address the State's bridges that do not meet current seismic standards. Of particular interest for WSDOT are bridges with multiple column bents founded on precast/prestressed hollow core concrete piles, since in the Puget Sound region of Washington State, there are 22 major bridges that are founded on precast/prestressed hollow core concrete piles. These piles possess a low to moderate displacement ductility (Budek, et al., 1997b).

Traditional retrofit techniques, such as supplying additional confinement and longitudinal reinforcement through the plastic hinge region, have been shown to be effective in increasing the shear capacity of hollow piles. However, stiffening the region adjacent to the pile-to-pile-cap connection causes the plastic hinge to form near mid-height of the above ground portion of the pile, reducing displacement ductility in the process (Abebaw, 2008). Currently, no effective retrofitting techniques exist to improve the ductility capacity of prestressed hollow-core piles.

The general objective of this research is to determine the seismic vulnerability of the I-5 Ravenna Bridge due to different ground motions. Determining the seismic vulnerability of the I-5 Ravenna Bridge may help the WSDOT determine the seismic vulnerability of similar bridges. Quantifying the seismic vulnerability of bridges founded on precast/prestressed hollow core piles

will provide a rational basis for decision making with regard to replacement or retrofit of those bridges.

The work presented in this thesis is part of a larger research project. In phase one of the project (Greenwood, 2008) finite element analyses of the actual I-5 Ravenna piles and pile-to-cross-beam connections have been developed to better understand the performance of hollow core piles. In phase two, the results from phase one were implemented in other finite element models to study the seismic vulnerability of the I-5 Ravenna Bridge. This thesis presents phase two of this research where SAP 2000 was used to carry out a nonlinear time history analysis and nonlinear static analyses of the I-5 Ravenna Bridge.

1.2. RESEARCH OBJECTIVES

The specific objectives of this research include:

- Evaluate the performance of the bridge under different seismic loads using nonlinear dynamic (NLD) analysis and nonlinear static (NLS) analysis. To do so, a 3-D “spine” detailed model of the Ravenna Bridge has been developed. The model includes nonlinear frame hinges, modeling of the bridge bearings, expansion-joints, and soil-structure interaction. The NLS analysis was carried out using the capacity spectrum method.
- Investigate the accuracy of available variants of the Capacity Spectrum Method (CSM) by comparing results to NLD analysis.
- Investigate the effects of soil type on the seismic bridge performance. The soils considered are loose sand, dense sand, and stiff clay.

1.3. SEISMICITY IN WESTERN WASHINGTON STATE

Large magnitude earthquakes in the Pacific Northwest have occurred along the Cascadia Subduction Zone (CSZ) where the Juan de Fuca Plate, made of oceanic crust, subducts under the North American Plate, made of continental crust (see Figure 1.1). Recent geological evidence indicates that the potential exists for additional large earthquakes in the Pacific Northwest as a result of rupturing of the locked interface between the Juan de Fuca and the North American Plate. This rupture scenario would cause the longest earthquakes experienced in the Pacific Northwest in modern times (Gregor, et al., 2002). Deep subduction zone earthquakes are a function of the size of the fault. Since the CSZ fault area is large, an earthquake larger than a moment magnitude of 9 could take place if the rupture occurs along the entire fault (PNSN, 2008). Another type of earthquake that could occur in the Puget Lowland results from crustal faults. Earthquakes of this mode can reach moment magnitudes of greater than 7 (PNSN, 2008). Active crustal faults exist under key cities including: Seattle, Tacoma, and Olympia, WA (PNSN, 2008). Currently, geologic mapping and surveying is being performed to determine how many additional crustal faults may be active in the Puget Lowlands.

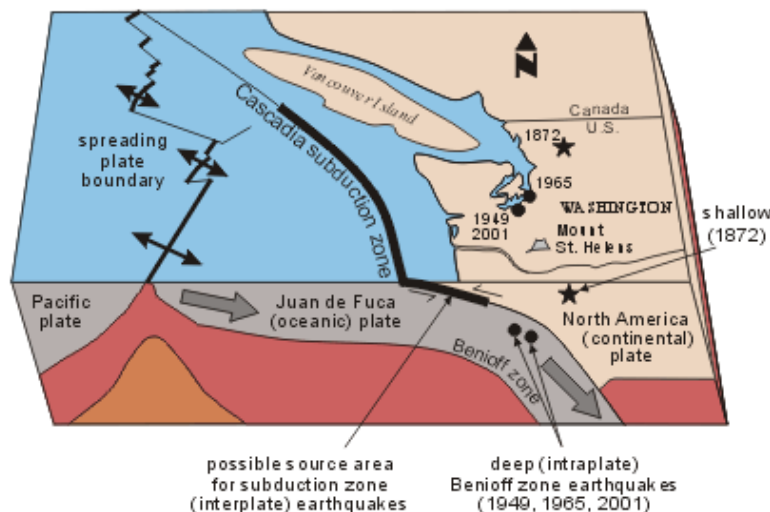


Figure 1.1. Cascadia Subduction Zone

CHAPTER 2: LITERATURE REVIEW

The need for seismic retrofitting of highway bridges and the current process for accomplishing it are described succinctly in the FHWA retrofitting manual (Buckle, et al., 2006). The evolution of retrofitting philosophy and techniques began after the 1971 San Fernando earthquake, through which a number of deficiencies in structural bridge design practices were exposed. The initial retrofit strategy was to add restrainers to bridge superstructures to limit movement at expansion joints and tie individual spans to piers. Column damage during the 1987 Whittier Narrows earthquake prompted researchers to also develop methods that would be effective in increasing their ductility, which usually consisted of the addition of jacketing to enhance confinement.

Since 1990, the WSDOT has pursued a bridge seismic retrofit program, for which bridges were prioritized through groupings based on the nature and extent of structural deficiencies. The first two groups dealt with superstructure issues, and that portion of the retrofit program is complete. The second group contained bridges with single-column piers, and those with multiple-column piers and substructure deficiencies. A final group included large and untypical bridges. Retrofit procedures for major bridges and those with single-column piers are in progress. The last major group of bridges to be considered contains those with multiple-column piers.

Several studies have been performed to evaluate the performance of bridges with multiple-column piers. Cofer, et al (1997), and Zhang, et al (1999), performed nonlinear dynamic analyses on two two-dimensional bent models: one for a two-column bent and one for a five-column bent. A version of the software, NEABS, was used for the analyses, modified to

consider the effect of damage from lack of confinement in unretrofitted columns. Structural behavior, including levels of column plasticity/damage up to collapse, was monitored for combinations of retrofitted/unretrofitted columns. The authors concluded that, even though collapse was avoided for some partial retrofit cases, significant damage to unretrofitted columns may occur. Only one earthquake record was considered, however, which limited general application of the conclusions. Regardless, it was recommended that separate analysis be performed for individual bridges.

Symans, et al. (2003), performed a study to evaluate methods of displacement-based seismic analysis. They used three different computer programs, SC-Push3D, SAP2000, and GTSTRUDL, to analyze the seismic response of a simple two-span highway bridge with three-column bents. The basic approach was to perform a pseudo-static multi-degree-of-freedom pushover analysis of the bridge to establish the capacity curve. The authors concluded from a survey of bridge engineers that SAP2000 was the software most frequently used for inelastic static analysis, while ADINA was the software most frequently used for inelastic dynamic analysis. They also noted that the Capacity Spectrum Analysis technique was, at that time, being used to a limited degree in practice while the Inelastic Demand Spectrum Analysis technique was primarily being used in research studies.

Itani and Liao (2003) used the Capacity Spectrum Method and SAP2000 to evaluate the effect of different retrofit applications for a short-span, three-column-bent bridge. They concluded that partial retrofit schemes can be effective and that middle columns and those with relatively short effective height are most critical to retrofit to improve bridge ductility.

McDaniel (2006) evaluated the seismic performance of three bridges having three-column bents using the Ruaumoko3D software for nonlinear dynamic analysis. Spine models

were used with nonlinear column elements as well as expansion joints and soil-structure interaction, and eight earthquake ground motions were applied. The bridge deck design and column aspect ratios were shown to greatly influence bridge response, and it was recommended that individual bridge assessment should be performed. For the bridges with non-monolithic decks, the column shear force/displacement demands approached capacity for large Cascadia Subduction Zone ground motions. However, although moderate column damage was shown to be likely, actual column failure was not predicted for any of the cases considered.

Cofer, et al. (2002), studied the ability of current software to accurately simulate the cyclic behavior of reinforced concrete columns. An effective model was constructed of beam elements within the ABAQUS software. Bonvalot (2006) used a similar type of model to consider the effect of the pulse-type ground motions that result from forward directivity earthquakes on short span bridges. Nonlinear dynamic analysis was conducted for three bridges when subjected to a suite of ground motions specifically derived for them by Gillie (2005). Ground motions with and without forward directivity were considered. Two of the bridges were supported by two-column piers and spread footing foundations, while the third had single-column piers and pile foundations. Effects of inelastic/hysteretic column behavior, soil-structure interaction, and gap/contact at abutments and expansion joints were all included. Comparison was made with other methods, and spectral methods of analysis were shown to be somewhat inaccurate for this type of earthquake due to the presence of a strong acceleration pulse in the ground motion.

Methods for evaluating seismic structural vulnerability of bridges are discussed and recommended in the FHWA retrofitting manual (Buckle, et al., 2006). Three methods are described for computing structure capacity/demand. The first, labeled Method D1, is the

Capacity Spectrum Method. The second method, labeled Method D2 and considered to be more advanced, is similar, but with a few differences. While a pushover analysis is also required to determine displacement at which limit states are reached, it is performed here for individual piers rather than for the complete bridge. Then, a response spectrum analysis is performed for the entire bridge to compute displacement demands for each pier, which are used to develop capacity/demand ratios. The authors note that the response spectrum analysis method is only valid for elastic systems and must be modified to reflect the actual conditions of the structure. Presumably, this is accomplished by modifying the design response spectrum with ductility-dependent reduction factors. The third method is the Nonlinear Dynamic Procedure. Here, a detailed model of the complete bridge is analyzed for a minimum of three earthquake ground motions, based upon expected site response. Significant nonlinearities and component interaction are included. Displacements and member actions are obtained as a function of time, and seismic demands can be compared directly with member capacities and system performance.

Budek, et al (1997a; 1997b), investigated the behavior of solid and hollow prestressed concrete piles. Nonlinear finite element analyses were first conducted for single piles with a bilinear, Winkler-type soil model and various end connections and axial force values. The hollow piles were shown to display only limited ductility, which was also degraded at high levels of axial force. They also found that, in developing the full inelastic potential of the pile-cap connection, a plastic hinge is expected to form in the pile shaft. Consequently, an experimental program was conducted to investigate the bending behavior of these types of piles. The tests were set up with saddles to simulate the soil confinement. Figure 2.1a shows the test apparatus.

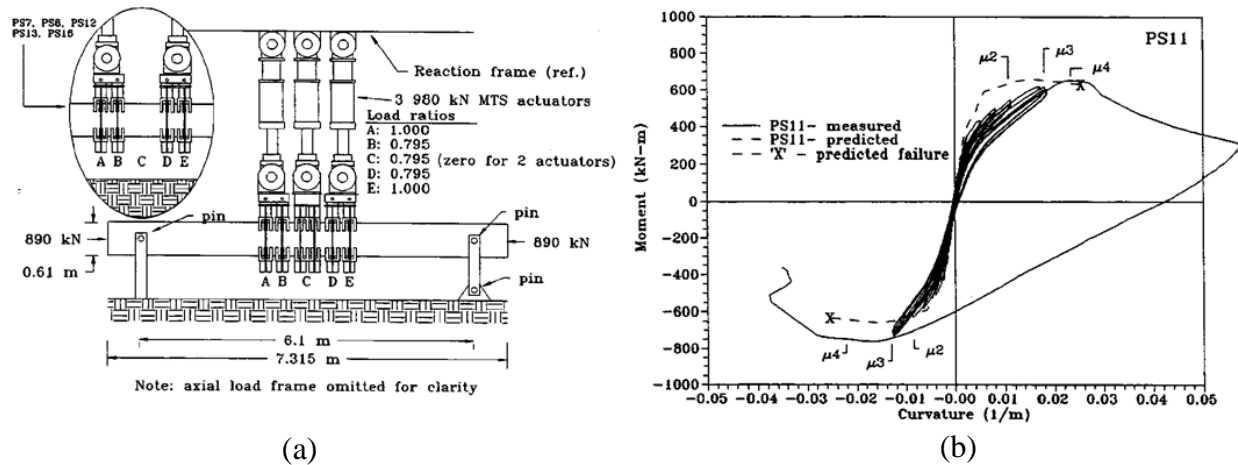


Figure 2.1. (a) Pile test setup; (b) Moment-curvature diagram for a prestressed hollow core pile (Budek, et al., 1997b)

For hollow piles, the results showed the following:

- With cyclic loading, the behavior was essentially nonlinear-elastic, having little hysteretic energy dissipation. This suggests the formation of tensile cracks in the pile wall that open and close with little or no plastic deformation in the steel. Figure 2.1b shows a typical moment-curvature diagram.
- Failure was abrupt and catastrophic, with gross concrete failure on the compression side of the pile. This type of behavior suggests the occurrence concrete cracking and crushing.
- The level of transverse reinforcement and external confinement had no influence on ductility capacity.

CHAPTER 3: SEISMIC ASSESSMENT METHODOLOGY

In this chapter, the methodology for structural assessment is investigated. The capacity of buildings and earthquake demand are used together by the methodology for structural assessment proposed below to obtain the response data. The methodology for structural assessment is of considerable importance inasmuch as it should yield an accurate prediction of displacement response of a structure under the given ground motion.

Structural analysis methods are classified into two generic groups – linear and nonlinear – which can each then be subdivided into static and dynamic. Equivalent static analysis is a typical example of linear static procedures; most of the current seismic design codes employ it, and horizontal force distribution is the required input for this method. On the other hand, modal and spectral analysis uses superposition and fall under linear dynamic procedures. In both methods, a multi-degree-of-freedom (MDOF) system is decomposed into a series of single-degree-of-freedom (SDOF) systems and elastic response history analysis performed.

Nonlinear dynamic analysis (i.e. Time-History Analysis, THA), using the combination of ground motion records with a detailed structural model, theoretically is capable of producing results with relatively high accuracy. In nonlinear dynamic analyses, the detailed structural model subjected to a ground-motion record produces estimates of component deformations for each degree of freedom in the model. There is still uncertainty with the detailed models, associated primarily with the lack of data on actual component behavior, particularly at high ductilities. In addition, the variability of ground motion results in significant dispersion in engineering demand parameters. THA is very time consuming and the extensive output can be difficult to interpret while masking important aspects of the seismic response.

Nonlinear Static (NLS) analysis is a popular method for existing and new structures. One procedure for carrying NLS analysis is the Displacement Coefficient Method (DCM) (FEMA356, 2000). The DCM is fundamentally a displacement modification procedure that estimates the maximum displacement of the oscillator by multiplying the elastic response, assuming initial linear properties and damping, by one or more coefficients. The coefficients are typically derived empirically from series of nonlinear response history analyses of oscillators with varying periods and strengths (FEMA356, 2000). Another procedure for NLS analysis is the Capacity-Spectrum Method (CSM) (ATC-40, 1996). In both procedures the global deformation (elastic and inelastic) demand on the structure is computed from the response of an equivalent single-degree-of-freedom system having the load-deformation properties determined from the pushover analysis. They differ, however, in the technique used to estimate the maximum deformation demand (elastic and inelastic).

Various researchers have found that the DCM and CSM may provide substantially different estimates of target displacement for the same ground motion and the same structure (Miranda, et al., 1994; Chopra, et al., 2000) and have proposed improved procedures for estimating the target displacement. FEMA-440 (2005) revised the DCM and CSM methods and proposed improvements to both methods. Since CSM is more extensively used in practice, this chapter provides a critical review of the available variants of the CSM and then illustrates their applicability and accuracy for the requirements of the structural response assessment considered in the present study.

As mentioned previously, one of the targets of this study is to compare the accuracy of NLS to NLD. Using different methods to calculate target displacement will give insight on which method is best fit for this kind of bridge when using NLS.

3.1. PUSHOVER CURVES AND CAPACITY DIAGRAMS

In this study, structure capacity is represented using pushover curves (capacity diagrams). A pushover curve can be thought of as an envelope for the cyclic response of a structure. The pushover curve can be obtained by applying a monotonically increasing pattern of lateral forces, representing the inertial forces that the structure would experience when subjected to ground motion. The characteristic nonlinear force-displacement relationship of the multi-degree of freedom system is presented in terms of base shear V_b , and roof displacement (or target node displacement). Figure 3.1 represents the pushover curve.

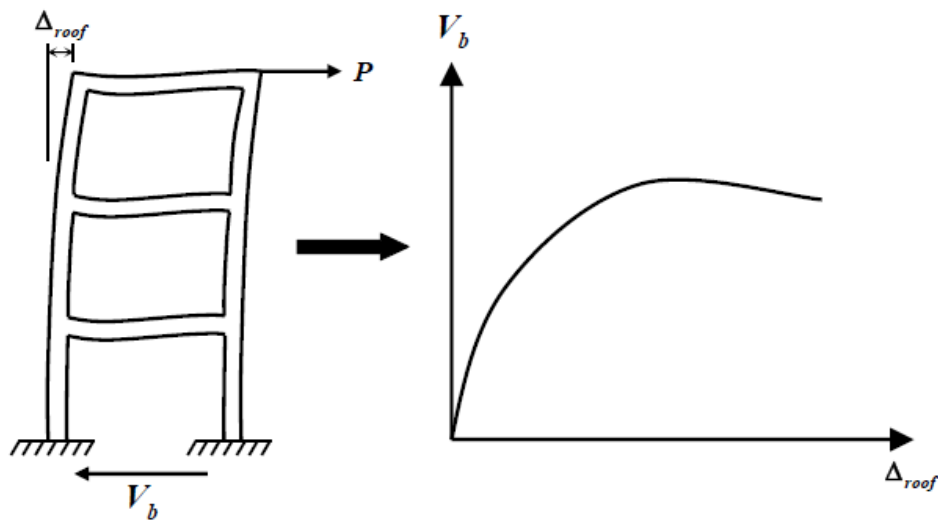


Figure 3.1. Pushover Curves

CSM requires bridge capacity to be represented in the Acceleration-Displacement (AD) format, named by Mahaney et al. (1993). The AD format is obtained by plotting spectral acceleration against spectral displacement, as opposed to period vs. spectral acceleration or period vs. spectral displacement as in the case of commonly used spectra. This type of representation does not explicitly include period (or frequency); however, radial lines drawn

from the origin to a point on the curve in the AD format define a specific period or frequency, as seen in Figure 3.2. Representation of the capacity curve (or pushover curve for this study) in AD format is referred to as a capacity diagram.

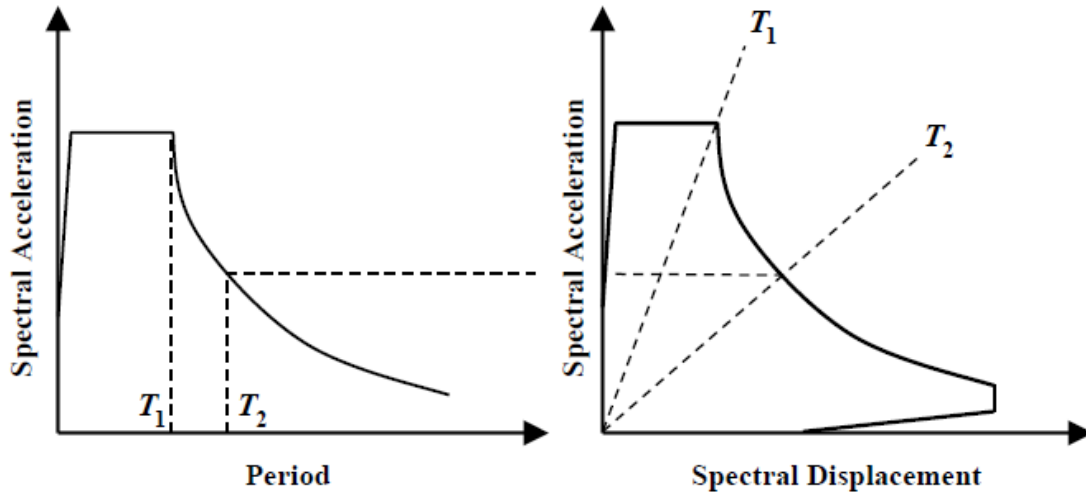


Figure 3.2. Demand diagram in (Left): Standard format; (Right): Acceleration-Displacement format

A brief description of how to obtain pushover curves as well as the derivation of the equations used for converting them into capacity diagrams is provided below using the description and notation of Fajfar (2000).

For the following description, a monotonically increasing pattern of lateral forces is applied, representing the inertial forces that the structure would experience when subjected to ground motion, obtaining the characteristic nonlinear force-displacement relationship of the multi-degree of freedom system in terms of base shear and roof displacement, as shown Figure 3.1.

The vector of lateral loads, \mathbf{P} , used in the pushover analysis is given by:

$$\mathbf{P} = p\mathbf{\Psi} = p\mathbf{M}\mathbf{\Phi} \quad (3.1)$$

where \mathbf{M} is the diagonal mass matrix and the magnitude of lateral loads is controlled by p . Ψ denotes the distribution of lateral loads and it is related to the assumed displacement shape Φ .

In the conversion from pushover curves to capacity diagrams, the multi-degree-of-freedom (MDOF) system is represented as an equivalent single-degree-of-freedom (SDOF) system. The equation of motion for the MDOF system is given by:

$$\mathbf{M}\ddot{\mathbf{U}} + \mathbf{C}\dot{\mathbf{U}} + \mathbf{R} = -\mathbf{M}\mathbf{I}\ddot{x}_g \quad (3.2)$$

where \mathbf{U} is the displacement vector, \mathbf{C} is the damping matrix, \mathbf{R} is the vector of internal forces, \ddot{x}_g is the ground acceleration, and (\cdot) denotes the time derivative.

Assuming that the displacement shape, Φ , does not change during the structural response to ground motion and knowing that the internal forces, \mathbf{R} , are equal to externally applied loads, \mathbf{P} , by defining the displacement vector as in Equation 3.3; Equation 3.2 is transformed into Equation 3.4.

$$\mathbf{U} = \Phi\eta \quad (3.3)$$

$$\Phi^T \mathbf{M} \Phi \ddot{\eta} + \Phi^T \mathbf{C} \Phi \dot{\eta} + \Phi^T \mathbf{M} \Phi p = -\Phi^T \mathbf{M} \mathbf{I} \ddot{x}_g \quad (3.4)$$

Multiplying and dividing the left hand side of Eq. (3.4) by $\Phi^T \mathbf{M} \mathbf{I}$ yields:

$$M^* \ddot{\eta}^* + c^* \dot{\eta}^* + F^* = -\ddot{x}_g^* \quad (3.5)$$

where m^* and c^* is the equivalent mass and equivalent viscous damping constant of the SDOF system respectively and the latter quantities are given by:

$$m^* = \Phi^T \mathbf{M} \mathbf{I} = \sum m_i \Phi_i \quad (3.6)$$

$$c^* = \Gamma \Phi^T \mathbf{C} \Phi \quad (3.7)$$

Also, η^* and F^* are the displacement and force of the SDOF system:

$$\eta^* = \frac{\eta}{\Gamma} \quad (3.8)$$

$$F^* = \frac{V_b}{\Gamma} \quad (3.9)$$

Γ is the modal participation factor and it is used to convert from the MDOF system to SDOF system and vice-versa. It is given by the equation below where m_i is the story mass.

$$\Gamma = \frac{\Phi^T M \mathbf{1}}{\Phi^T M \Phi} = \frac{\sum m_i \Phi_i}{\sum m_i \Phi_i^2} \quad (3.10)$$

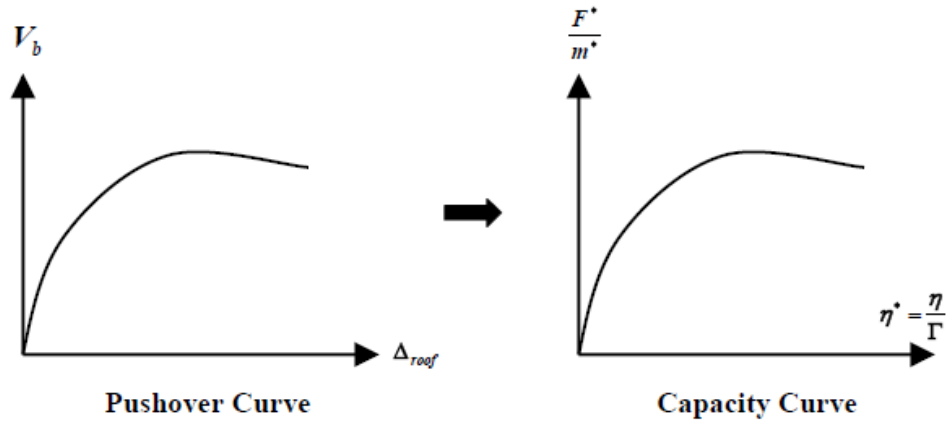


Figure 3.3. Conversion of pushover curves to capacity diagrams

It is important to note that the assumed displacement shape is normalized such that it is equal to unity at the top (roof) of the building.

The spectral acceleration values of the capacity diagram in AD format are obtained by dividing the force, F^* , by the mass of the SDOF system, that is:

$$S_a = \frac{F^*}{m^*} \quad (3.11)$$

For the conversion of pushover to capacity diagrams, this study utilizes the same displacement shape, Φ , as the one used in obtaining the pushover curve.

The capacity of buildings and earthquake demand are used together by the methodology for structural assessment proposed below to obtain the response data. The methodology for

structural assessment is of considerable importance inasmuch as it should yield an accurate prediction of displacement response of a structure under the given ground motion.

3.2. REVIEW OF THE AVAILABLE VARIANTS OF THE CAPACITY SPECTRUM METHOD

CSM was first proposed by Freeman et al. (1975) and Freeman (1978), and after it had appeared in ATC-40 (1996) it became the subject of several studies and various revisions for improvement. This section summarizes previously developed versions of the CSM under four headings: CSM in ATC-40, CSM with Inelastic Design Spectra, CSM with Equivalent Elastic Spectra from Damping Models, Improved CSM and Advanced CSM.

3.2.1. CSM IN ATC-40

The original CSM (ATC-40, 1996) proposes three analogous but different procedures, namely, Procedures A, B, and C. Procedure C being purely graphical and not lending itself to programming and is not considered here. Procedure A provides the most direct application of CSM, and it updates the bilinear representation of the capacity diagram depending on the performance point chosen. Procedure B does not include this feature. Procedures A and B not only differ in updating the bilinear representation but they also utilize different procedures to determine structural performance. Procedure A reduces the demand diagram depending on the equivalent damping obtained from the trial performance point until convergence is satisfied. Procedure B obtains the performance point from the intersection of the capacity diagram and the “constant period curve” which is constructed by joining points obtained for different values of ductility for a given SDOF system with prefixed period and hardening values (or bilinear representation).

Since Procedure A is reported to fail satisfying in convergence in certain cases (Chopra, et al., 1999; Chopra, et al., 2000; Lin, et al., 2004b) and Procedure B lacks updating of the bilinear representation of the capacity diagram, the forthcoming test case will use a combined procedure for assessment using this version of CSM. In other words, different bilinear representations will be developed depending on the trial performance point and the displacement demand will be determined using the technique of Procedure B.

Bilinearization of the pushover curve is done based on the equal energy principle. Figure 3.4 shows how the equal energy method is applied, by matching the area under the pushover curve to the area under the bilinearization.

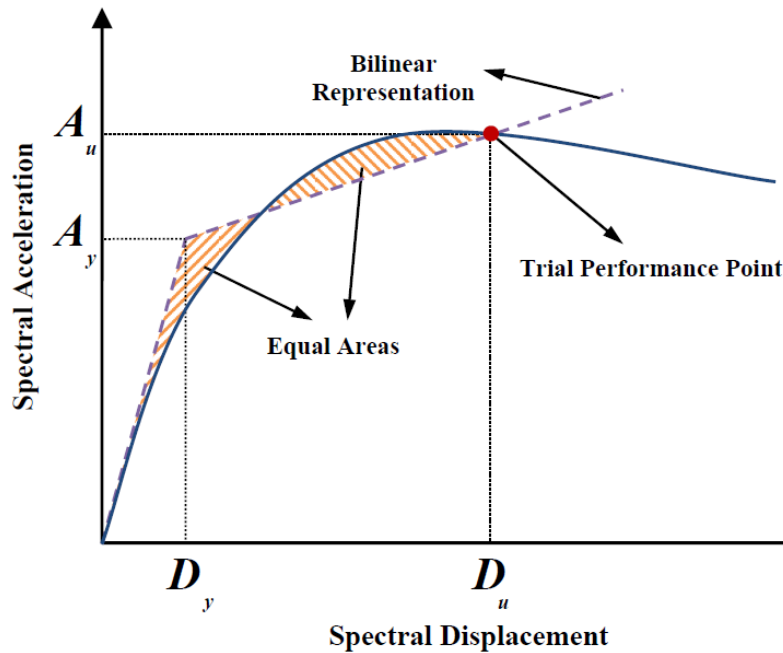


Figure 3.4. Bilinear representations based on equal energy principle

The criteria giving the actual performance point is the agreement between the viscous damping of the demand diagram and the equivalent viscous damping of the structure obtained from the intersection point (Figure 3.5). Iterations start with the 5 percent damped elastic spectrum. If the structure acts within the elastic range, the demand diagram should intersect the

capacity diagram at a deformation level less than the yield deformation. If this is not true, it indicates that the structure will deform beyond its elastic limits. Hence, the elastic demand diagram should be reduced so as to incorporate the inelastic energy dissipation of the structure.

Effective viscous damping associated with the capacity diagram is obtained from an equivalent linear system described by the bilinear representation of the capacity diagram at the trial performance point. The inherent assumption is that the hysteretic energy dissipated due to the inelastic deformation of the structure can be represented as equivalent viscous damping. Hence, the intersection point of capacity and demand diagrams is used to develop the equivalent linear system based on secant stiffness.

When the force deformation relationship of the SDOF system is represented as a bilinear system with elastic stiffness k_e and yielding branch stiffness of αk_e (Figure 3.6) the natural vibration period of the equivalent linear system, T_{eq} , with secant stiffness k_{sec} , is given by:

$$T_{eq} = T_n \sqrt{\frac{\mu}{1 + \alpha\mu - \alpha}} \quad (3.12)$$

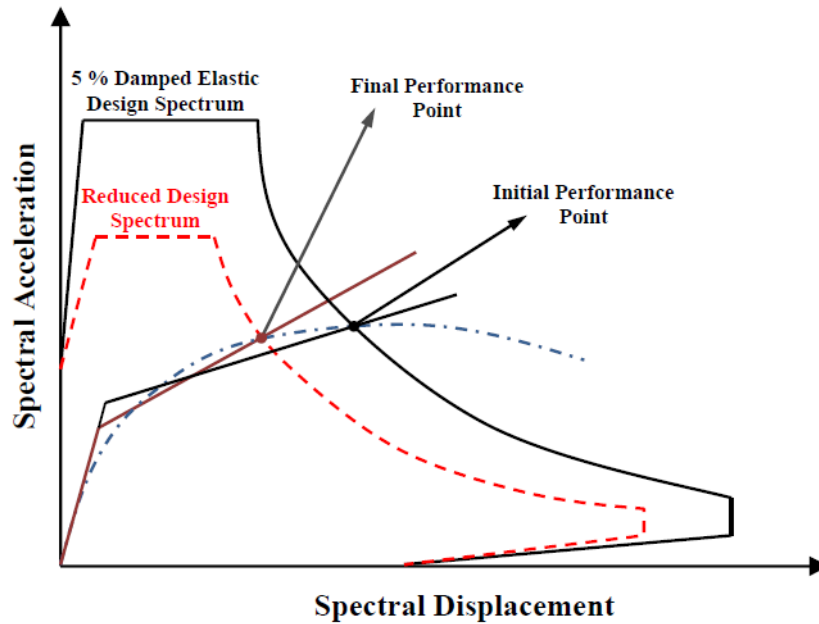


Figure 3.5. Plot demand and capacity diagrams to determine the displacement demand

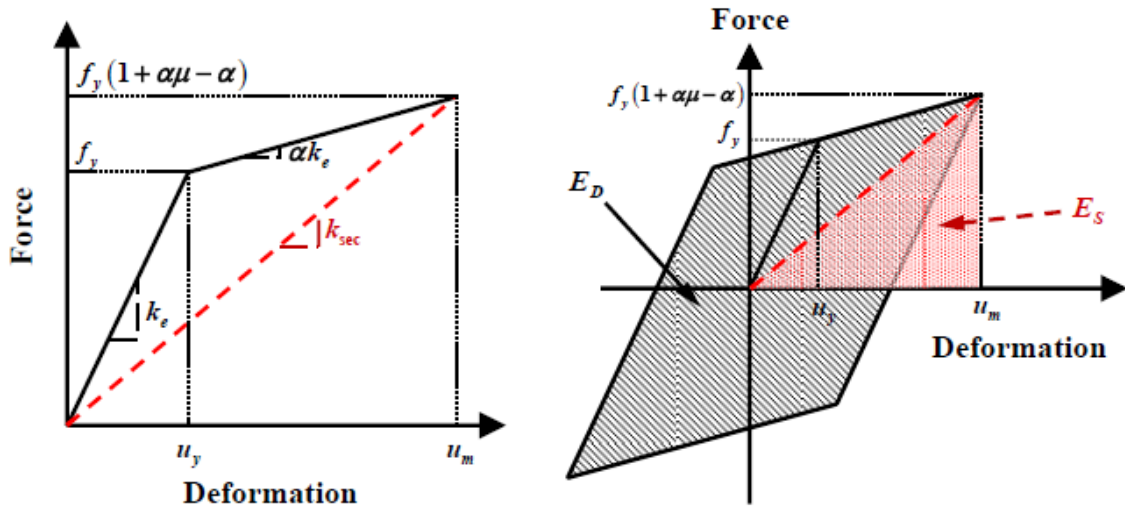


Figure 3.6. (Left): Equivalent SDOF system based on secant stiffness; (Right): Equivalent viscous damping due to hysteretic energy dissipation

The displacement ductility factor μ is determined by the performance point, indicated by deformation u_m , and the yield point of the structure, shown as (u_y, f_y) in Figure 3.6, as:

$$\mu = \frac{u_m}{u_y} \quad (3.13)$$

Equivalent viscous damping here is calculated by equating the energy dissipated in a vibration cycle of the inelastic system and of the equivalent linear system.

$$\zeta_{eq} = \frac{1}{4\pi} \frac{E_D}{E_S} \quad (3.14)$$

The energy dissipated in the inelastic system, shown as E_D in above figure, is equal to the area enclosed by the hysteresis loop. The strain energy of the elastic system is given by Equation 3.15.

$$E_S = k_{sec} \frac{u_m^2}{2} \quad (3.15)$$

Thus equivalent viscous damping ratio takes the form:

$$\zeta_{eq} = \frac{2}{\pi} \frac{(\mu-1)(1-\alpha)}{(1+\alpha\mu-\alpha)} \quad (3.16)$$

The total (or effective) viscous damping of the equivalent linear system is obtained by adding the viscous damping ratio of the bilinear system acting within its elastic range, ζ , to the equivalent viscous damping ratio obtained through Equation 3.17.

$$\zeta_{eff} = \zeta + \zeta_{eq} \quad (3.17)$$

ATC-40 (1996) introduces the damping modification factor, in order to account for the effect of imperfect hysteresis loops, which are reduced in area when compared with the ones shown in Figure 3.6 due to duration effects and poor structural ductility detailing. The relation between the equivalent viscous damping and the damping modification factor is shown in Figure 3.7. Steps for calculating the damping modification factor based on ACT-40(1996) provision are described in Appendix A. With this term included, the effective viscous damping ratio is given by:

$$\zeta_{eff} = \zeta + \kappa \zeta_{eq} \quad (3.18)$$

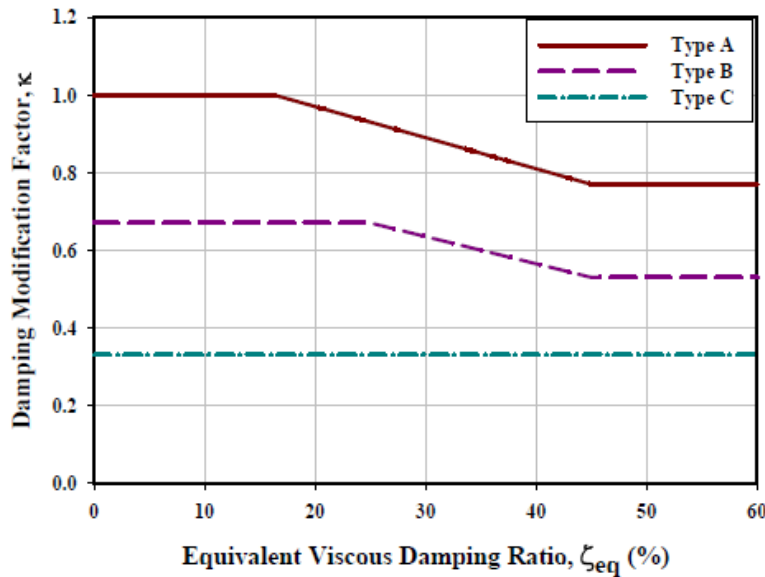


Figure 3.7. Relation between the equivalent viscous damping and damping modification factor

Once the effective damping, ζ_{eff} , is known, the necessary reduction factors for the demand diagram are calculated using the Newmark and Hall relations (Appendix A, Table A.1). Iterations are continued until the difference between the effective damping calculated at the trial performance point from the capacity diagram and the damping associated with demand diagram are within a predefined tolerance.

Because CSM in ATC-40 utilizes spectral reduction factors, and because they are not applicable to spectra from specific records, this method is only suitable for evaluating structures under code-conforming demand diagrams; that is, those having distinct regions of constant acceleration, velocity, and displacement.

3.2.2. CSM WITH INELASTIC DESIGN SPECTRA

First Bertero (1995) and Reinhorn (1997), and later Fajfar (1999) and Chopra and Goel (1999; 2000) proposed the direct use of inelastic design spectra instead of utilizing equivalent linear systems. They suggested obtaining inelastic design spectra from their elastic counterparts by using the force reduction factors. Chopra and Goel (1999; 2000) used reduction factors from different studies (Newmark, et al., 1982; Krawinkler, et al., 1992; Vidic, et al., 1994) and showed that up to a 50 percent difference, on the nonconservative side, can be obtained between the results of CSM in ATC-40 and those of CSM with inelastic design spectra. Since force reduction factors can only be used for reducing design (or code conforming) spectra, similar to CSM in ATC-40, this version of CSM is not suitable for assessment of structures under specific earthquake records.

The most important limitation that comes with employing force reduction factors is that they are derived for systems with elasto-plastic (EP) force-deformation relationships (or for

systems with small strain hardening values). However, during the process of updating the bilinear representation of the capacity diagram, strain hardening values of up to 25% or more are observed. Rahnema and Krawinkler (1993) showed that if the strain hardening is increased from 0 to 10%, a difference of about 20% is observed in force reduction factors. The structures in this study have strain hardening values of 25% or more, which would result in 20% error or more if updating the bilinear representation was used in this version of CSM. Such a level of error is not acceptable. Therefore, in the light of above discussion, it can be concluded that certain types of capacity diagrams, i.e. those that cannot be idealized with bilinear representations having small strain hardening values, are not amenable for evaluation with this version of CSM. To overcome this incompatibility occurring between the capacity and the demand diagrams, a single EP representation, again making use of the equal energy principle, needs to be developed (Figure 3.8).

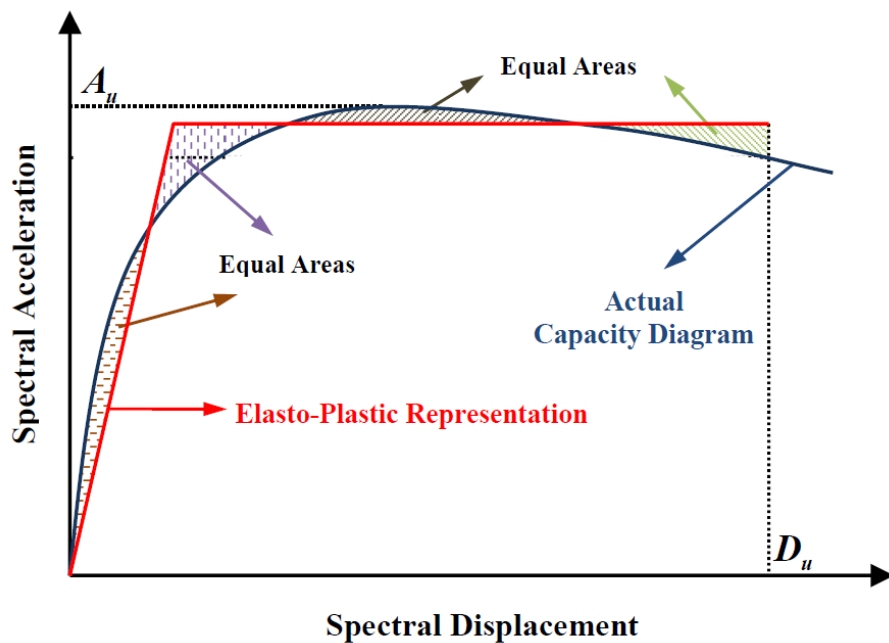


Figure 3.8. Elasto-plastic representation of the capacity diagram required in using CSM with inelastic design spectra

For the assessment of the bridge with this version of CSM, this study uses force reduction factors from Newmark and Hall (1982), Krawinkler and Nassar (1992), Vidic et al. (1994) and Miranda and Bertero (1994). The criterion to obtain the performance point is akin to the one in CSM in ATC-40, though here the ductility ratio replaces effective damping. Agreement of the effective damping from the capacity diagram and the same quantity associated with inelastic design spectra yields the structural response.

3.2.2.1. DEMAND REDUCTION FACTORS FROM NEWMARK AND HALL (1982)

The demand reduction factor derived by Newmark and Hall (1982) is in the following form:

$$R_\mu = \begin{cases} 1 & T_n < T_a \\ (2\mu - 1)^{\beta/2} & T_a \leq T_n < T_b \\ \sqrt{2\mu - 1} & T_b \leq T_n < T_{c'} \\ \frac{T_n}{T_c} \mu & T_{c'} \leq T_n < T_c \\ \mu & T_n \geq T_c \end{cases} \quad (3.19)$$

where:

$$\beta = \frac{\ln\left(T_n/T_a\right)}{\ln\left(T_b/T_a\right)} \quad (3.20)$$

The periods, T_a and T_b are equal to 1/33 sec, 1/8 sec, respectively. T_c is the period where the constant velocity branch of the inelastic spectrum begins. $T_{c'}$ is the period where the constant acceleration and constant velocity branches of the inelastic spectrum intersect (see Appendix B).

3.2.2.2. DEMAND REDUCTION FACTORS FROM KRAWINKLER AND NASSAR (1992)

The demand reduction factor as proposed by Krawinkler and Nassar (1992) is in the following form:

$$R_\mu = [c(\mu - 1) + 1]^{1/c} \quad (3.21)$$

where:

$$c(T_n, \alpha) = \frac{T_n^a}{1 + T_n^a} + \frac{b}{T_n} \quad (3.22)$$

The constants a and b can be obtained using Table 3.1, depending on α , which defines the slope of the yielding branch.

Table 3.1. Constants for reduction factors from Krawinkler and Nassar (1992)

α	a	b
0.00	1.00	0.42
0.02	1.00	0.37
0.10	0.80	0.29

3.2.2.3. DEMAND REDUCTION FACTORS FROM VIDIC ET AL. (1994)

Vidic et al. (1994), propose the use of following reduction factor:

$$R_\mu = \begin{cases} 1.35(\mu - 1)^{0.95} \frac{T_n}{T_0} + 1 & T_n \leq T_0 \\ 1.35(\mu - 1)^{0.95} + 1 & T_n > T_0 \end{cases} \quad (3.23)$$

where:

$$T_0 = 0.75\mu^{0.2}T_c, \quad T_0 \leq T_c \quad (3.24)$$

3.2.2.4. DEMAND REDUCTION FACTORS FROM MIRANDA AND BERTERO (1994)

The reduction factors developed by Miranda and Bertero (1994) are in the following form:

$$R_\mu = \frac{\mu - 1}{\Phi} + 1 \geq 1 \quad (3.25)$$

Where Φ is a function of μ , T_n and the soil conditions at the site, and is given by the equations provided in Table 3.2:

Table 3.2. Φ as function of period, ductility and soil conditions

Rock Sites	$\Phi = 1 + \frac{1}{10(T_n - \mu)} - \frac{1}{2T} \exp \left[-1.5 (\ln T_n - 0.6)^2 \right]$
Alluvium Sites	$\Phi = 1 + \frac{1}{12(T_n - \mu)} - \frac{2}{5T} \exp \left[-2 (\ln T_n - 0.2)^2 \right]$
Soft Soil Sites*	$\Phi = 1 + \frac{T_g}{3T_n} - \frac{3T_g}{4T_n} \exp \left[-3 \left(\ln \frac{T_n}{T_g} - 0.25 \right)^2 \right]$

* T_g is the predominant period of the ground motion, defined as the period at which maximum relative velocity of the 5% damped linear elastic system is maximum throughout the whole period range

3.2.2.5. COMPARISON OF DIFFERENT DEMAND REDUCTION FACTORS

In order to illustrate the differences between these three studies, reduction factors are plotted for different values of ductility (Figure 3.9). In addition, as an example, an elastic design spectrum of a ground motion with the parameters $PGA = 1g$, $PGV = 48 \text{ in/sec}$, and $PGD = 36 \text{ in}$, for a mean earthquake is reduced using the four different reduction factors described above for a ductility ratio of $\mu = 4$. The results are shown in Figure 3.10 together with the spectrum predicted by ATC-40 according to the effective damping ratio obtained from the ductility factor.

As can be observed from Figure 3.10, there is a significant discrepancy between the inelastic design spectra obtained using the ATC-40 procedure with effective damping and from other studies. The other studies proved to be more accurate (Newmark, et al., 1982; Krawinkler, et al., 1992; Vidic, et al., 1994; Miranda, et al., 1994).

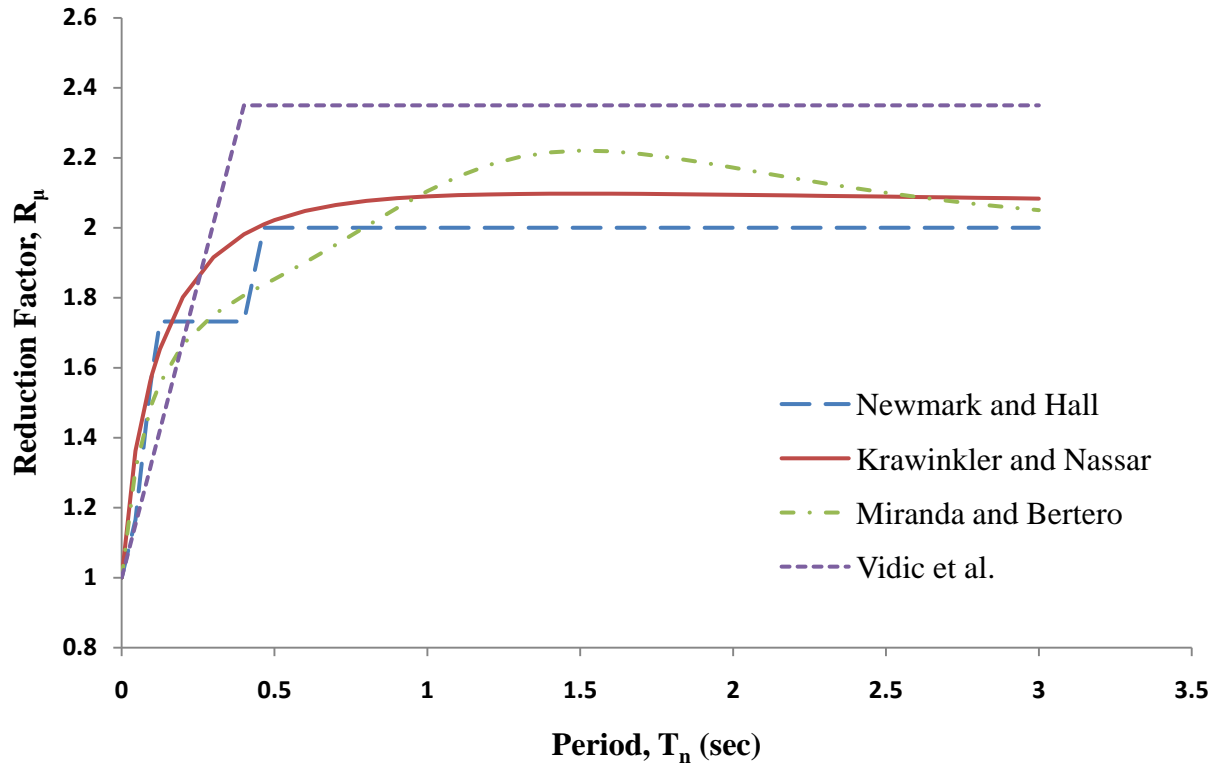


Figure 3.9. Comparison of reduction factors from different studies; Newmark and Hall (1982), Krawinkler and Nassar (1992); Vidic et al. (1994); Miranda and Bertero (1994)

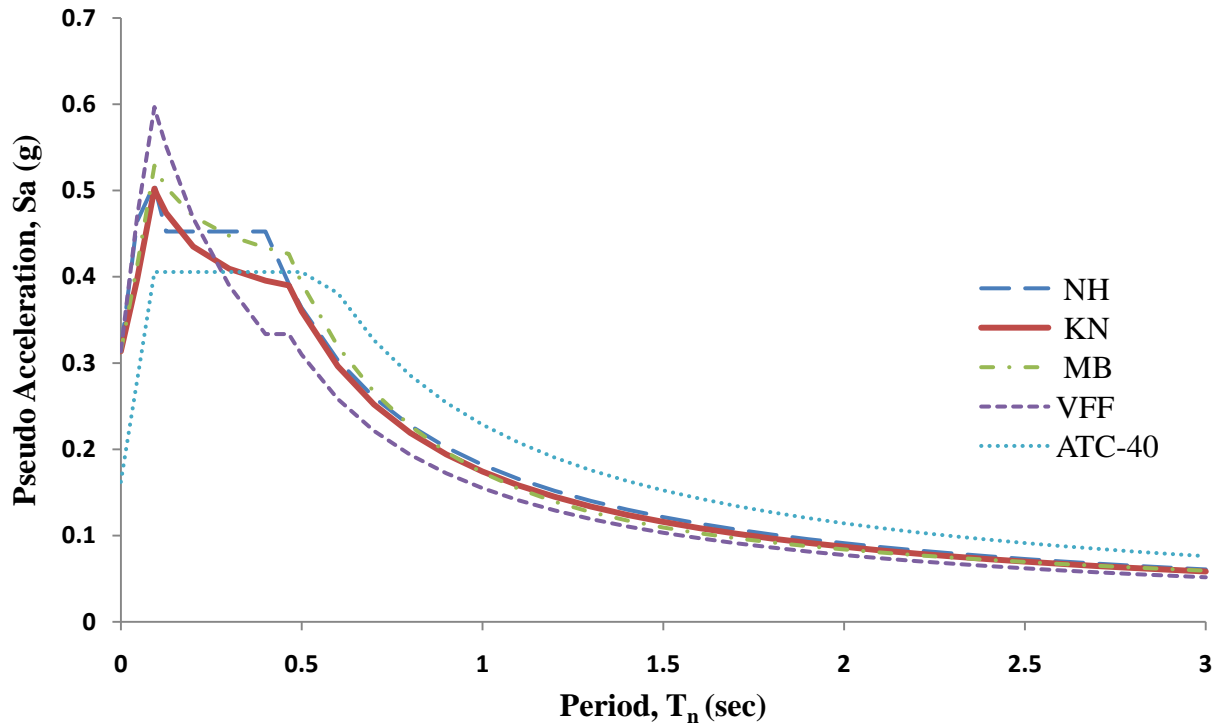


Figure 3.10. Inelastic design spectra calculated using different demand reduction factors; NH: Newmark and Hall (1982), KN: Krawinkler and Nassar (1992); VFF: Vidic et al. (1994); MB: Miranda and Bertero (1994); ATC-40 (1996).

3.2.3. CSM WITH EQUIVALENT ELASTIC SPECTRA FROM DAMPING MODELS

As an alternative improvement to CSM in ATC-40 (1996), using equivalent viscous damping models from different studies is proposed (Reinhorn, 1997; Lin, et al., 2003; Lin, et al., 2004a; Kim, et al., 2005). Lin and Chang (2003) used damping models from Iwan and Gates (1979), WJE (1996), and Kowalsky et al. (1994b) to show that the deviation in the results of Chopra and Goel (1999; 2000) from the exact solution can be further reduced.

In contrast to the versions of CSM described up to this point, CSM with equivalent elastic spectra is proper for predicting displacement demands under specific earthquake records. Damping and the period of the equivalent linear system are calculated from the properties of the inelastic system. These two parameters are used to derive the over-damped elastic demand diagram; and the performance point is obtained, through iterations, as the intersection point of

demand and capacity diagrams. Similar to the ATC-40 methodology and unlike the CSM with inelastic design spectra, the bilinear representation of the capacity diagram is updated depending on the trial performance point in this version of CSM.

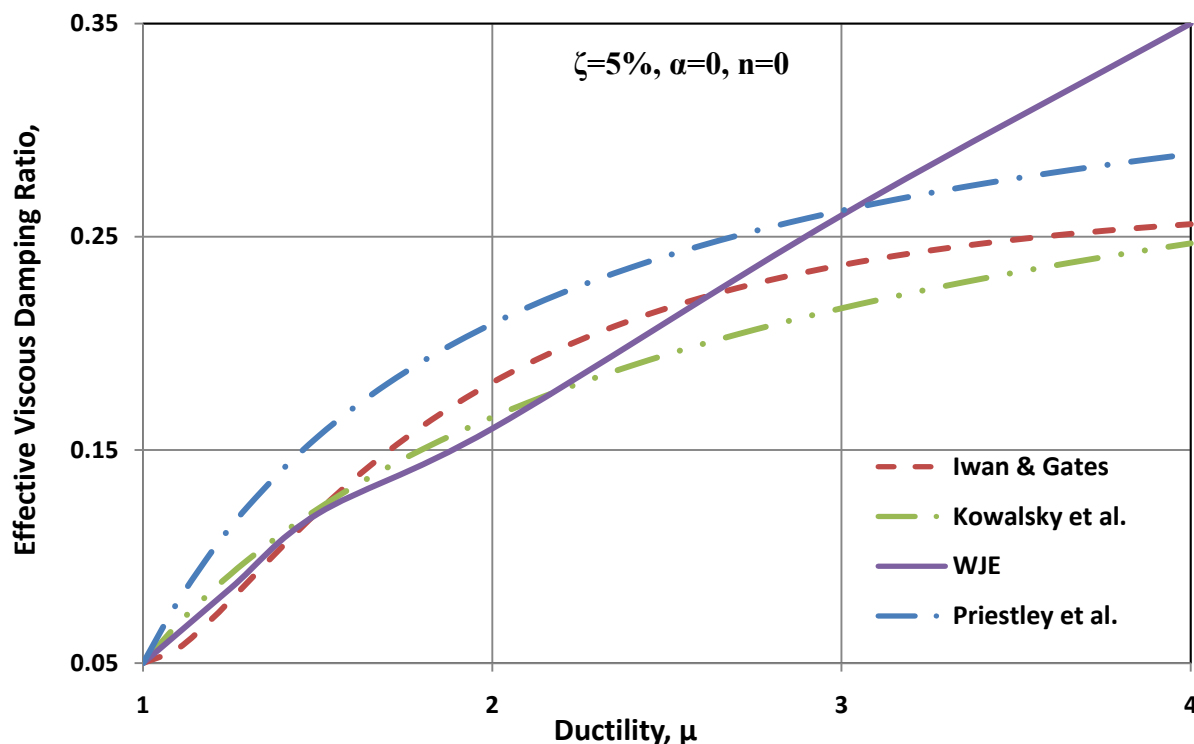


Figure 3.11. Ductility damping relationships from different studies

Damping models from Iwan and Gates (1979), Priestley et al. (1996a), WJE (1996) and Kowalsky et al. (1994b) are included in this study. A Comparison of different ductility damping relationships used in the test case is shown in Figure 3.11.

3.2.3.1. IWAN AND GATES (1979) – ACCORDING TO AVERAGE STIFFNESS AND ENERGY (ASE) METHOD

Among many other methods considered by Iwan and Gates (1979), average stiffness and energy is found to give the least overall error. Therefore, the ductility damping relationship from this method is presented here.

The effective damping ratio is given by:

$$\zeta_{\text{eff}} = \frac{3}{2\pi\mu^2} \frac{2(1-\alpha)(\mu-1)^2 + \pi\zeta \left[(1-\alpha) \left(\mu^2 - \frac{1}{3} \right) + \frac{2}{3} \alpha \mu^3 \right]}{(1-\alpha)(1+\ln\mu) + \alpha\mu} \quad (3.26)$$

3.2.3.2. *PRIESTLEY ET AL. (1996)*

This damping model is based on the Takeda hysteresis model (Takeda, et al., 1970). The effective damping ratio is given by:

$$\zeta_{\text{eff}} = \zeta + \frac{1}{\pi} \left[1 - \mu^n \left(\frac{1-\alpha}{\mu} + \alpha \right) \right] \quad (3.27)$$

Where the stiffness degradation factor, n , is suggested as zero for steel structures and 0.5 for reinforced concrete structures.

3.2.3.3. *WJE (1996)*

The WJE (1996) damping model is based on the maximum displacement determined from the elastic response spectrum being equal to that obtained from inelastic response spectrum. Table 3.3 gives the effective damping ratio depending on the ductility ratio. The study covers ductility ratios up to 4.

Table 3.3. Effective damping ratio based on WJE damping model (WJE, 1996)

μ	1.0	1.25	1.5	2.0	3.0	4.0
ζ_{eff} (%)						
(Based on Median + 1 Standard-Deviation Spectrum)	5	7.5	10	14	21	26
ζ_{eff} (%)						
(Based on Median Spectrum)	5	8.5	12	16	26	35

3.2.3.4. KOWALSKY ET AL. (1994B)

The damping model used by Kowalsky et al. (1994b) is based on laboratory test results and curve fitting.

The effective damping ratio is given by:

$$\zeta_{\text{eff}} = \zeta + 0.39372 \left[1 - \frac{1}{\sqrt{\mu}} \right] \quad (3.28)$$

3.2.4. IMPROVED CAPACITY SPECTRUM METHOD

The improved Capacity Spectrum Method presented in the FEMA-440(2002) document includes new expressions to determine the effective period and effective damping. Consistent with the original ATC-40 (1996) procedure, three iterative procedures for estimating the target displacement are also outlined. Finally, a limitation on the strength is imposed to avoid dynamic instability.

The improved formulas for effective period and damping ratio in the FEMA-440 document are:

$$T_{\text{eff}} = \begin{cases} [0.2(\mu - 1)^2 - 0.038(\mu - 1)^3 + 1]T_0 & \mu < 4.0 \\ [0.28 + 0.13(\mu - 1) + 1]T_0 & 4.0 \leq \mu \leq 6.5 \\ \left[0.89 \left(\sqrt{\frac{(\mu - 1)}{1 + 0.05(\mu - 2)}} - 1 \right) + 1 \right] T_0 & \mu > 6.5 \end{cases} \quad (3.29)$$

$$\zeta_{\text{eff}} = \begin{cases} 4.9(\mu - 1)^2 - 1.1(\mu - 1)^3 + \zeta_0 & \mu < 4.0 \\ 14 + 0.32(\mu - 1) + \zeta_0 & 4.0 \leq \mu \leq 6.5 \\ 19 \left[\frac{0.64(\mu - 1) - 1}{0.64(\mu - 1)^2} \right] \left(\frac{T_{eq}}{T_0} \right)^2 + \zeta_0 & \mu > 6.5 \end{cases} \quad (3.30)$$

These formulas apply for periods in the range of 0.2 to 2.0s. The FEMA-440 document also provides formulas with constants A to L that are specified depending on the force deformation relationships (bilinear, stiffness-degrading, strength-degrading) and the post yield stiffness ratio, α ; these formulas are not included here for brevity.

3.2.5. AN ADVANCED CAPACITY SPECTRUM METHOD

The advanced CSM proposed in this section aims to overcome the difficulties encountered in nonlinear static analysis and provide better estimates of structural response. The underlying idea is to utilize inelastic dynamic analysis of SDOF systems represented by bilinear force deformation relationships. Even though it might seem contradictory with the original CSM, where only static procedures and equivalent linear systems are used, with today's computing technology, nonlinear time history analysis of SDOF systems is a matter of minutes on an average personal computer. In addition, this method eliminates approximations and hence errors introduced into the solution with the use of equivalent linear systems, design spectra (in lieu of actual spectra), and force reduction factors.

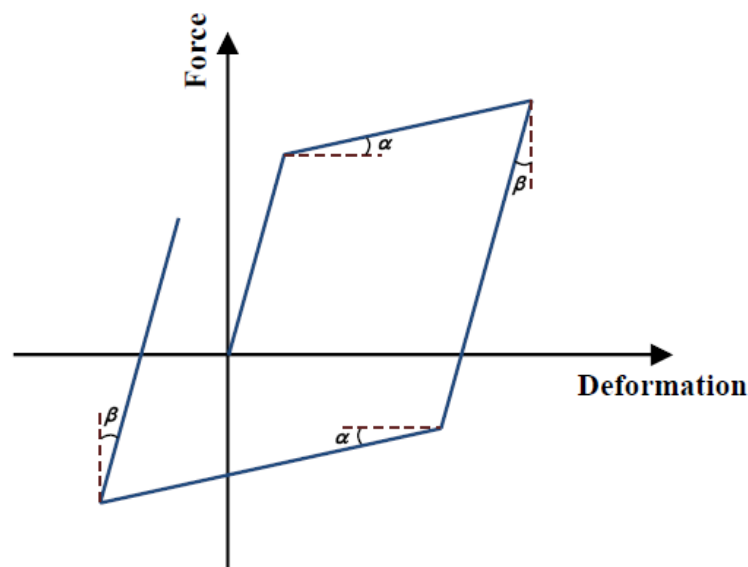


Figure 3.12. Force-deformation relationship for kinematic hardening behavior

The step by step procedure to determine the displacement demand with the advanced method is given below:

- i. Develop a bilinear representation of the pushover curve.
- ii. Obtain the mass participation for the modal pushover analysis, and use this for the SDOF.
- iii. Obtain peak responses of the SDOF system, whose force deformation relations are defined by the bilinear representations, using nonlinear time history analysis.

Kinematic hardening behavior is assumed for hysteretic response (Figure 3.12).

A somewhat similar approach was proposed for vulnerability analysis of RC structures by Rossetto and Elnashai (2005) using adaptive pushover analysis that is sensitive to the specific input motion record. The current method is, however, distinct in its direct use of the inelastic response history analysis of a bilinear system. A depiction of the SDOF structural model is given in Figure 3.13.

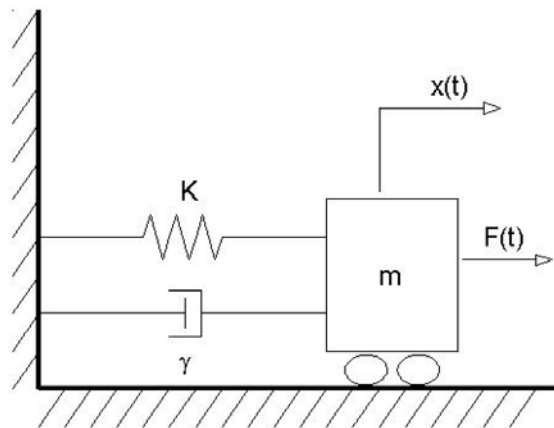


Figure 3.13. Mass-spring-damper system used for Advanced CSM

3.3. COEFFICIENT METHOD (CM)

The Displacement Coefficient method (FEMA356, 2000) is similar to CSM, and the aim is to calculate the performance point (referred to as the target displacement in FEMA 356) using a procedure that takes into account the effects of nonlinear response on displacement amplitude. Similar to the use of inelastic design spectra in CSM, the displacement demand is determined from inelastic displacement spectra which are obtained from the elastic displacement spectra by using a number of correction factors based on statistical analysis. The application of CM is described below.

i. Obtain the pushover curve:

Guidelines to obtain the pushover curve of the structure are provided in FEMA 356, but results of any convenient pushover analysis can be used.

ii. Determine the elastic period of the structure:

The notation of FEMA 356 (2000) is followed here. First construct a bilinear representation of the pushover curve (with reference to Figure 3.14):

- a) Draw the post-elastic stiffness, $K_s = \alpha K_e$, by judgment to represent an average stiffness in the range in which the structure strength has leveled off.
- b) Draw the effective stiffness, K_e , by constructing a secant line passing through the point on the capacity curve corresponding to a base shear of $0.6V_y$, where V_y is defined by the intersection of the K_e and K_s lines.

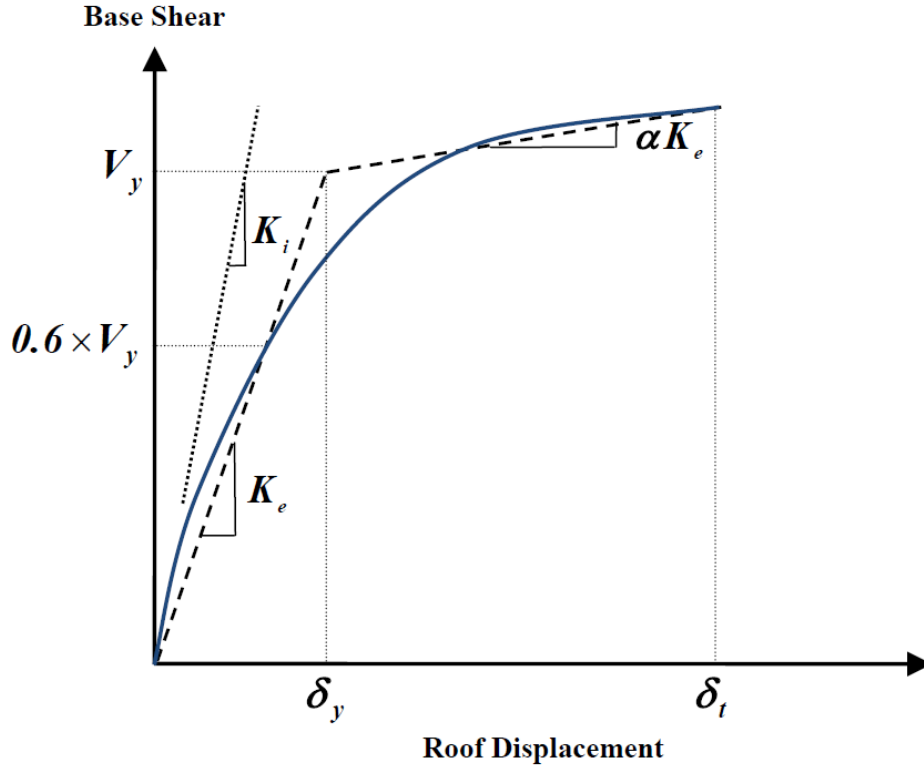


Figure 3.14. Determine of the elastic period, reproduced from FEMA 356 (2000)

Note that this procedure requires some trial and error since the value V_y is not known until the K_e line is drawn. Calculate the effective fundamental period, T_{eff} , using the following equation:

$$T_{eff} = T_i \sqrt{\frac{K_i}{K_e}} \quad (3.31)$$

Where, T_i is the elastic fundamental period (in seconds), K_i is the elastic lateral stiffness of the building, and K_e is the effective lateral stiffness of the building.

iii. Calculate the Target Displacement:

The target displacement of the structure, δ_t , can be calculated using Equation 3.32:

$$\delta_t = C_0 C_1 C_2 C_3 S_a \frac{T_{eff}^2}{4\pi^2} g \quad (3.32)$$

The constant in Equation 3.32 (C 's) are modification factors which are used in CM to calculate target displacement. The definitions for these constants can be found in Appendix B.

3.3.1. IMPROVED COEFFICIENT METHOD

The FEMA-440 (2002) document proposes several improvements to the FEMA-356 Coefficient Method for estimating the target displacement. Improvements are made on definitions of modification factors which are defined in Appendix B.

3.4. TIME-HISTORY ANALYSIS

Time-history analysis is used to determine the dynamic response of a structure to arbitrary loading. The dynamic equilibrium equations to be solved are given by Equation 3.12.

$$\mathbf{K} \mathbf{u}(t) + \mathbf{C} \dot{\mathbf{u}}(t) + \mathbf{M} \ddot{\mathbf{u}}(t) = \mathbf{r}(t) \quad (3.33)$$

Where \mathbf{K} is the stiffness matrix; \mathbf{C} is the damping matrix; \mathbf{M} is the diagonal mass matrix; $\mathbf{u}, \dot{\mathbf{u}},$ and $\ddot{\mathbf{u}}$ are the displacements, velocities, and accelerations of the structure; and \mathbf{r} is the applied load. If the load includes ground acceleration, the displacements, velocities, and accelerations are relative to this ground motion. In a nonlinear analysis, the stiffness, damping, and load may all depend upon the displacements, velocities, and time. This requires an iterative solution to the equations of motion.

Direct integration of the full equations of motion without the use of modal superposition is available in SAP2000 (2007). A variety of common methods are available for performing direct-integration time history analysis. The “Hilber-Hughes-Taylor alpha” (HHT) method was used, which was recommended in the SAP2000 (2007) manual. The HHT method uses a single parameter called alpha. This parameter may take values between 0 and -1/3. In this study the value was set to -1/3 which encourages convergence.

3.4.1. DAMPING

In direct-integration time-history analysis, the damping in the structure is modeled using a full damping matrix. This allows coupling between the modes to be considered.

For each direct-integration time-history Analysis Case, proportional damping coefficients that apply to the structure as a whole were specified. The damping matrix was calculated as a linear combination of the stiffness matrix scaled by a coefficient that was specified, and the mass matrix was scaled by a second coefficient. These two coefficients were computed by specifying equivalent fractions of critical modal damping at two different periods.

Stiffness proportional damping is linearly proportional to frequency. It is related to the deformations within the structure. Stiffness proportional damping may excessively damp out high frequency components. Mass proportional damping is linearly proportional to period. It is related to the motion of the structure, as if the structure is moving through a viscous fluid. Mass proportional damping may excessively damp out long period components. For all NDL analysis, the damping ratio was specified as 5%.

CHAPTER 4: I-5 RAVENNA BRIDGE

In this chapter, the I-5 Ravenna Bridge will be described in detail. The first part focuses on the actual bridge geometry and plan details. The second part describes the computer model created based on the actual bridge components.

4.1. LAYOUT AND GEOMETRY

The I-5 Ravenna Bridge is located on I-5, which is the main interstate highway in Washington State. The bridge is approximately 5 miles north of downtown Seattle. It overpasses the NE Ravenna Blvd., NE 65th St., and Weedon Place NE. An aerial view of the bridge is shown in Figure 4.1.



Figure 4.1. Aerial view of the I-5 Ravenna Bridge

The bridge extends 1310 ft and has 19 spans. The bridge supports two lanes of traffic in each direction and it is shaped in a curve with a radius of 5787 ft. Each of the first five bents in the North direction (Bents 15 to 19 in Figure 4.2) has six columns while each of the last three bents (Bents 1 to 3 in Figure 2) has seven columns. Each of the remaining bents has four columns.

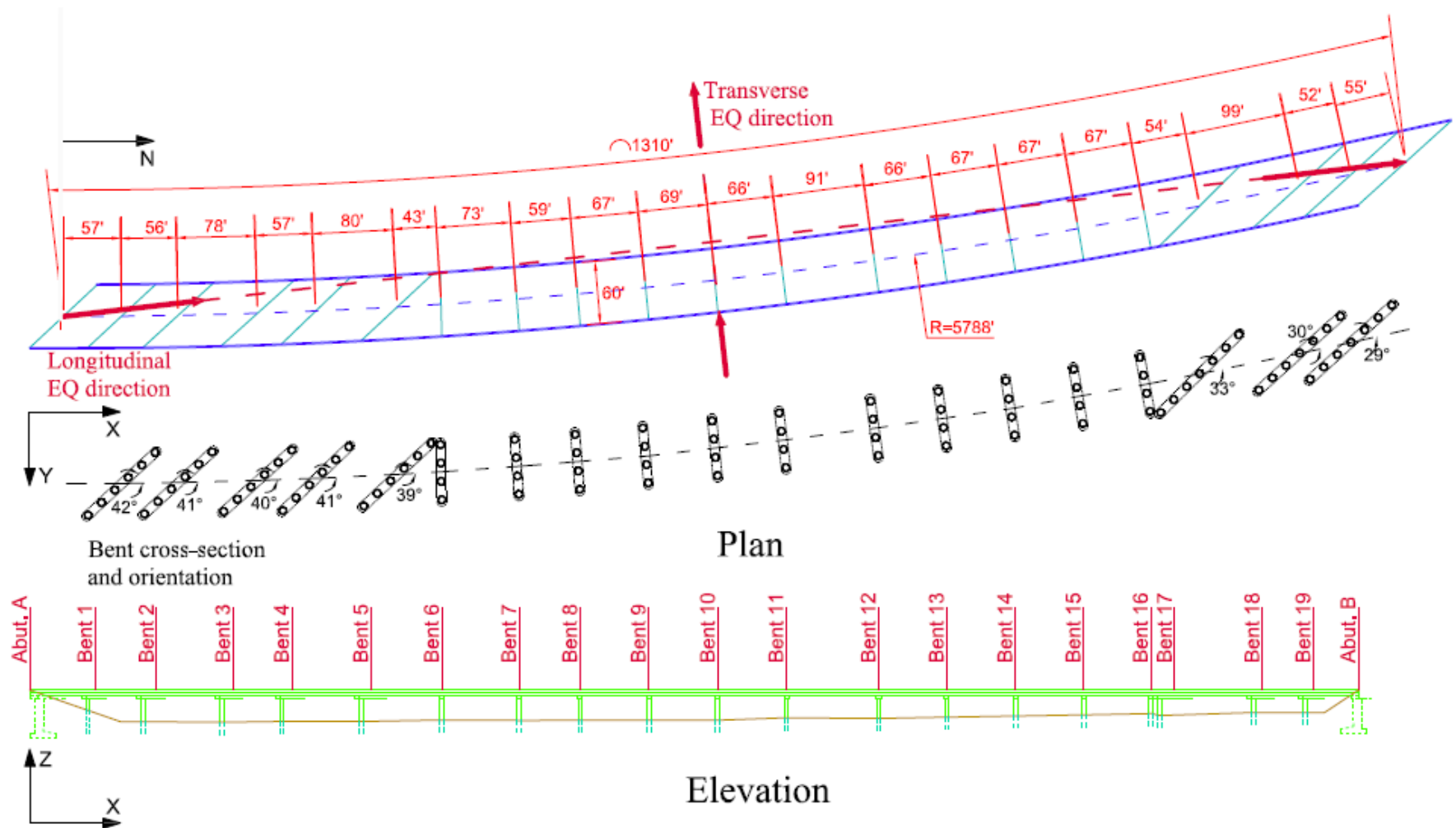


Figure 4.2. Elevation and plan view of I-5 Ravenna Bridge

All columns are extended into the ground to act as pile shafts. The above ground height of the columns varies from 15 to 27 ft. The column spacing is 18 ft on center for every bent. Bents have different skew angles ranging from 29° to 42°. The plan and elevation view of the bridge are shown in Figure 4.2.

The superstructure is composed of twelve simply supported I-shaped prestressed concrete girders with a composite 5.5 in thick cast in-place reinforced concrete deck. Spans are configured using combinations of different girders. The different assembled sections can be found in Figure 4.3, linking them to their assigned span number. Appendix A.1 offers more details on the girders and span properties.

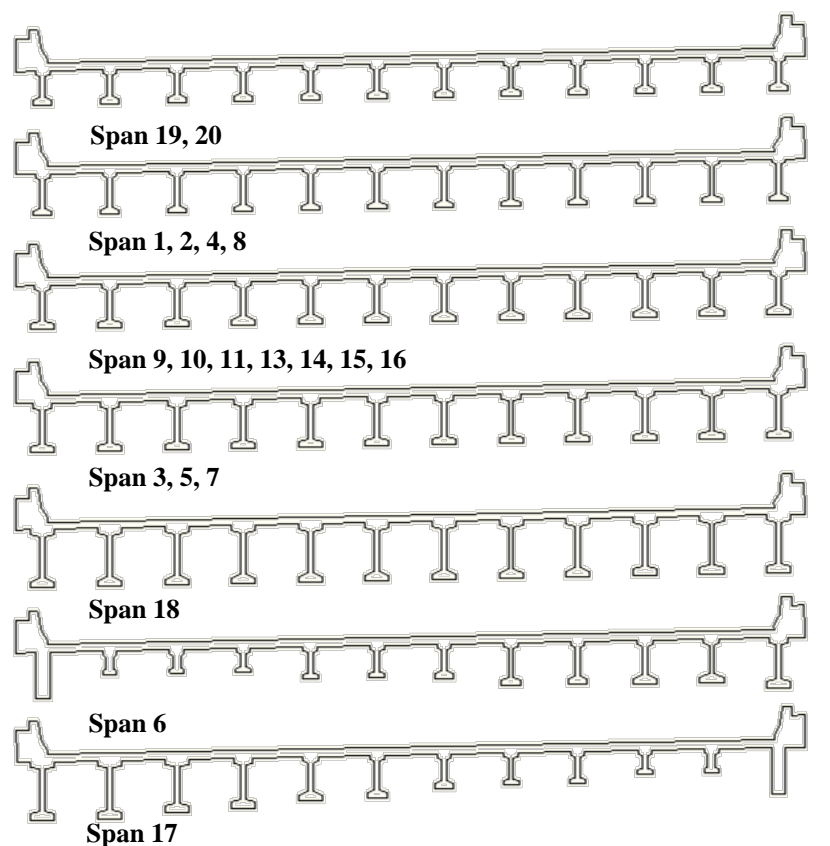


Figure 4.3. Superstructure cross-sections

At each bent, a 3x4.6 ft crossbeam transversely connects the columns. Figure 4.4 shows the geometry and steel reinforcement of a typical crossbeam. The length of the beams varies for each bent (Appendix A.2). The steel reinforcement consists of nine No. 10 bars located at the top and at the bottom of each crossbeam. Two No. 5 bars are located at the side edges and run longitudinally along the crossbeam. For shear reinforcement, No. 5 stirrups are spaced evenly along each member.

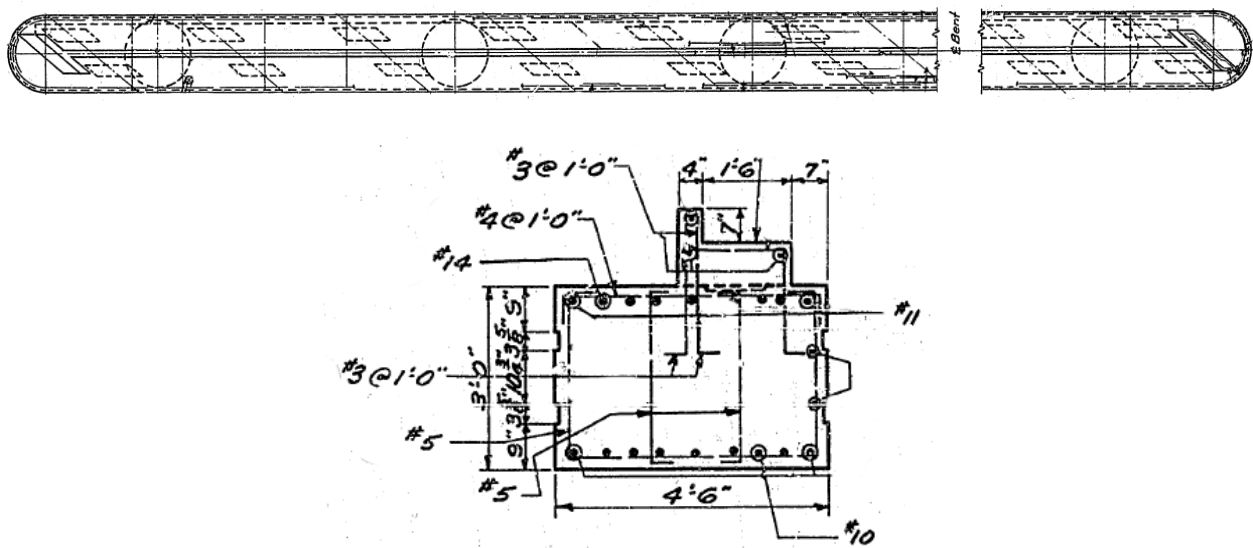


Figure 4.4. Plan (for typical six column bent) and section view of crossbeam

The columns are spaced at 18 ft centerline to centerline. Each column is hollow with an outer diameter of 48 in and a wall thickness of 5 in. Twelve evenly spaced No. 5 bars provide the longitudinal reinforcement within each column. The columns also include twelve No. 3 steel cables each post-tensioned initially to 61 kips. Transverse reinforcement is provided by No. 2 spiral hooping spaced at 6 in on center (Figure 4.5). The columns are extended approximately 27 ft into the ground to act as piles.

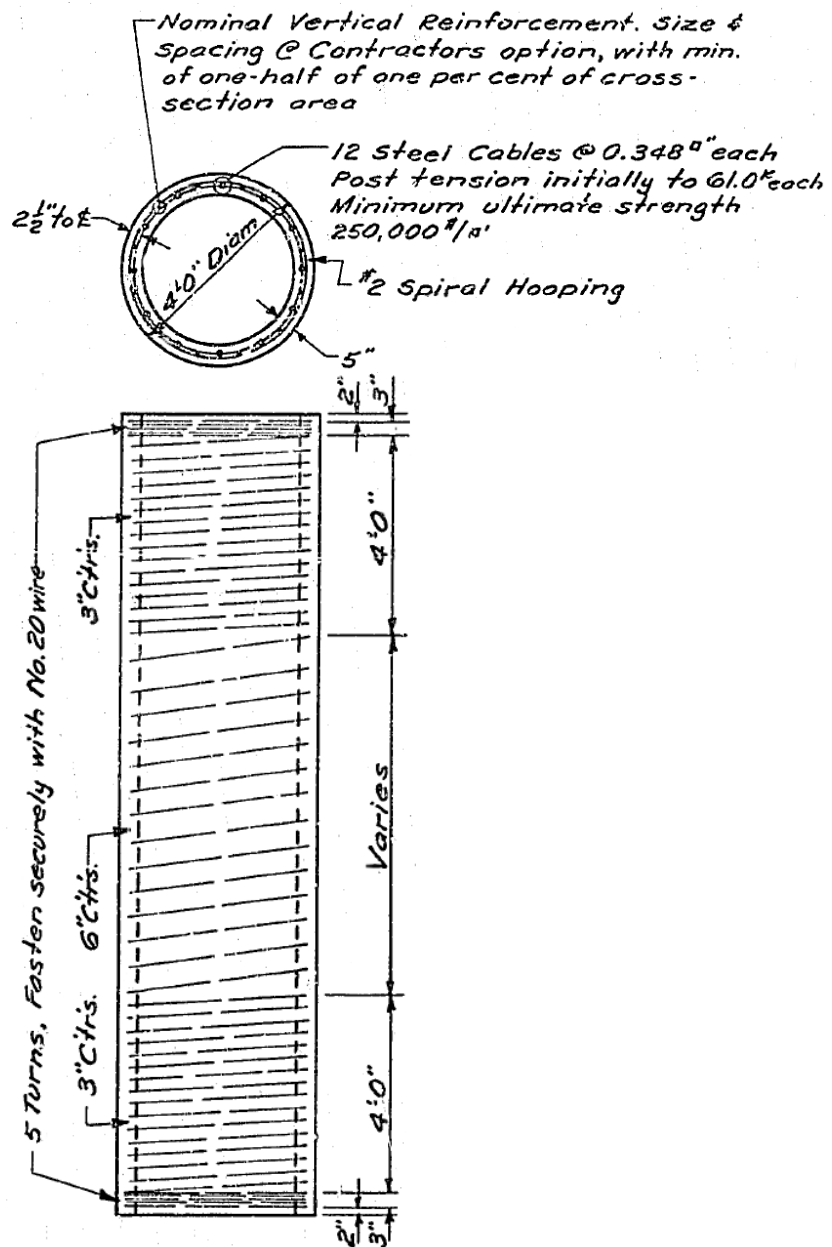


Figure 4.5. Typical pile (section and elevation view)

The columns (piles) and crossbeam were cast monolithically. Figure 4.6 shows the reinforcement details of the crossbeam-pile connection. The top 4 ft of each column is filled with class A concrete. This fill is further reinforced with sixteen No. 8 bars longitudinally, and No. 3

hoops spaced at 12 in transversely. In this section of the column, the hollow column is transversely reinforced with No. 2 spiral hooping spaced at 3 in over center.

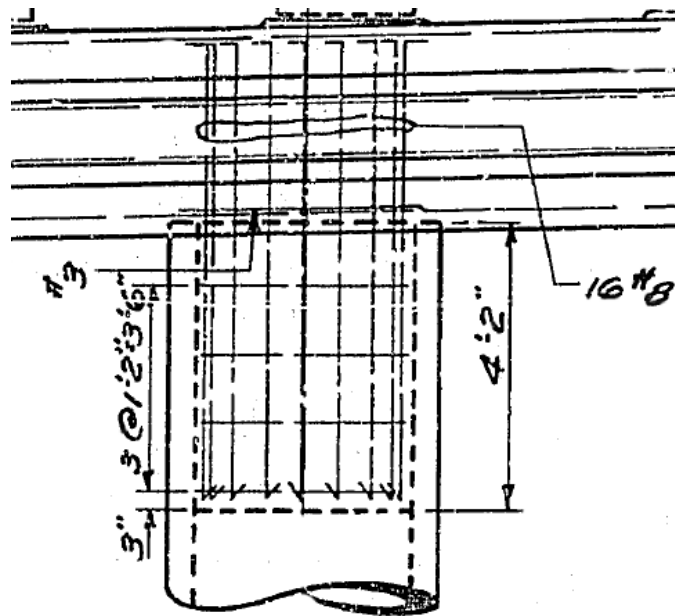


Figure 4.6. Crossbeam-pile connection

The I-girders rest upon laminated elastomeric bearing pads located on top of the crossbeam and abutment seats. They are restrained in the transverse direction by posts and girder stops. Figure 4.7 and 4.8 show the elastomeric bearing pad and the girder stops.

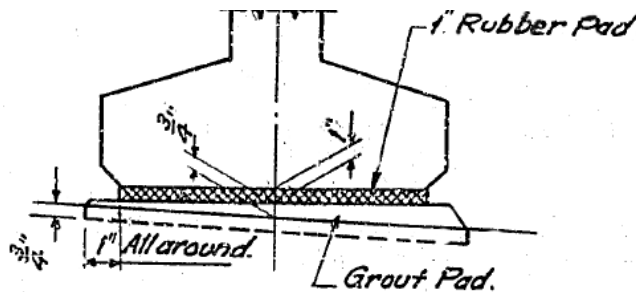


Figure 4.7. Bearing pad

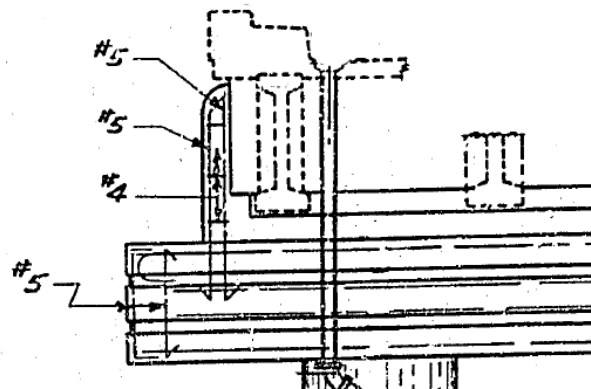


Figure 4.8. Girder restrainer

At each bent and at the abutments, the bridge deck is non-monolithically constructed. Rubber expansion joints are situated at each bent and at the abutments. They are 1 in wide and run the width of the roadway (Figure 4.9).

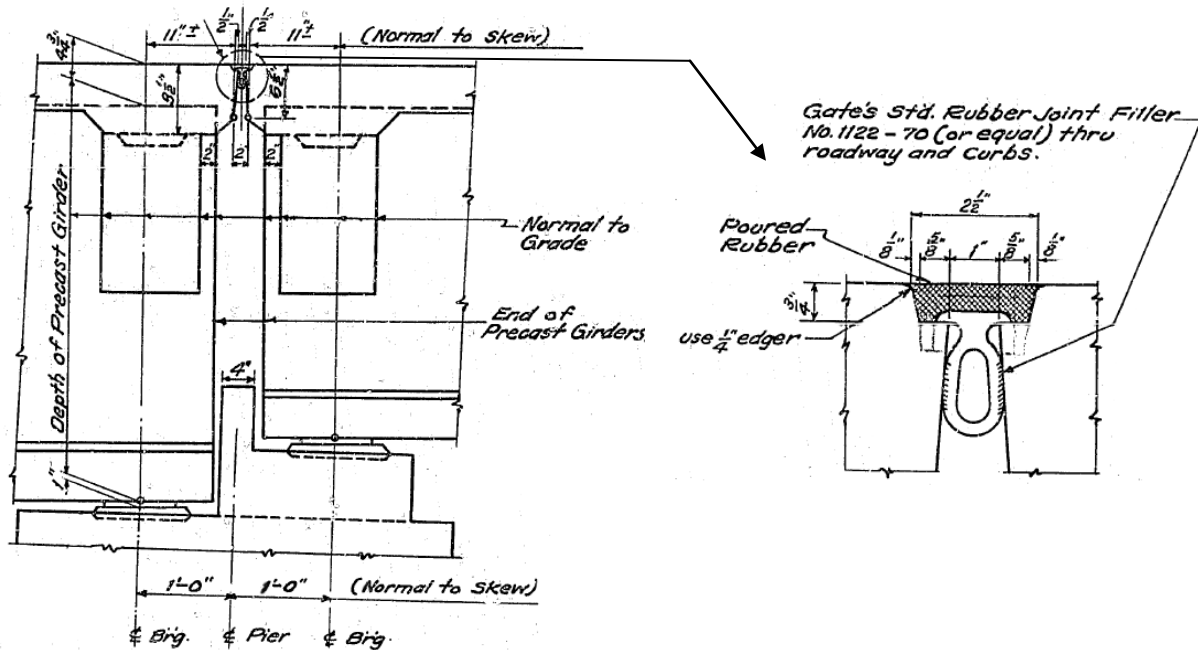


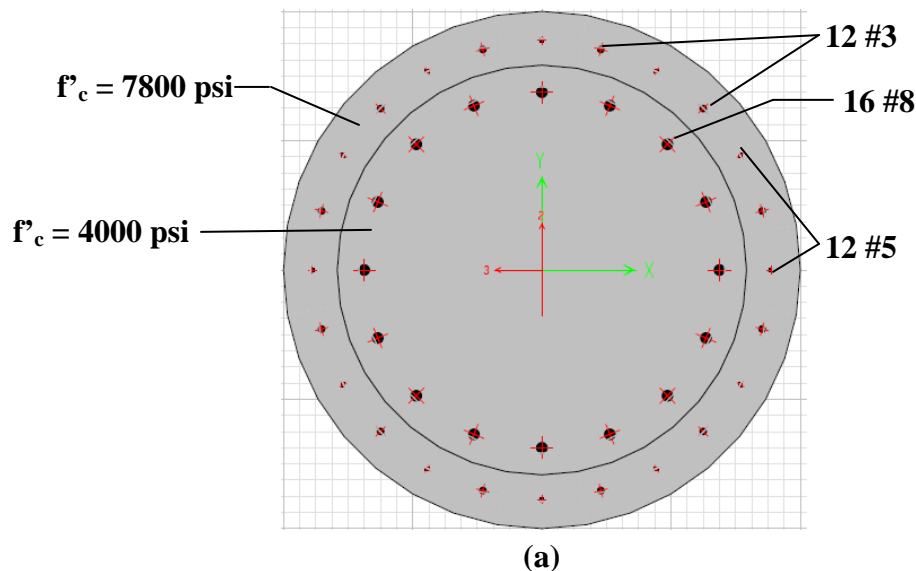
Figure 4.9. Expansion joint at intermediate piers

The abutments run across the width of the bridge, are 7 ft deep and 1 ft long for the top half and 3 ft long for the bottom half. Transverse and longitudinal reinforcements are placed throughout the cross-section as displayed in Figure 4.10. Sub-ground columns support the abutments and run about 33 ft deep below the abutment. The columns are tapered along the depth and are anchored down by a 21 ft x 15 ft x 5 ft and 15 ft x 9 ft x 2.75 ft reinforced concrete block for abutment A and B, respectively. Abutment A has four footings and abutment B has six footings.

4.2. STRUCTURAL MODEL

A three-dimensional finite-element model of the bridge was created using SAP2000 (2007) (see Figure 4.29). The deck and girders are combined together and modeled as one line of elastic beam elements, as this approach provides effective stiffness and mass distribution characteristics of the bridge. The bridge superstructure itself is expected to remain essentially elastic during earthquake ground motions. The beam element representing each span passes through the centroid of the superstructure. As mentioned in previous section, each span has unique geometrical properties which are described in Appendix A.

The cross-sections of the crossbeam and the column were accurately modeled by using the subprogram offered in SAP2000 (2007) called Section Designer. Section Designer lets the user draw the shape of the cross-section and also include the steel reinforcements. Figure 4.12 and Figure 4.13 show the sections for the column/pile and crossbeam used in the analysis. The shear reinforcements are not visible in the figures, but they are included in the computer model. Each of the columns and the crossbeam are represented by single three-dimensional frame elements which pass through the geometric center and mid-depth, respectively.



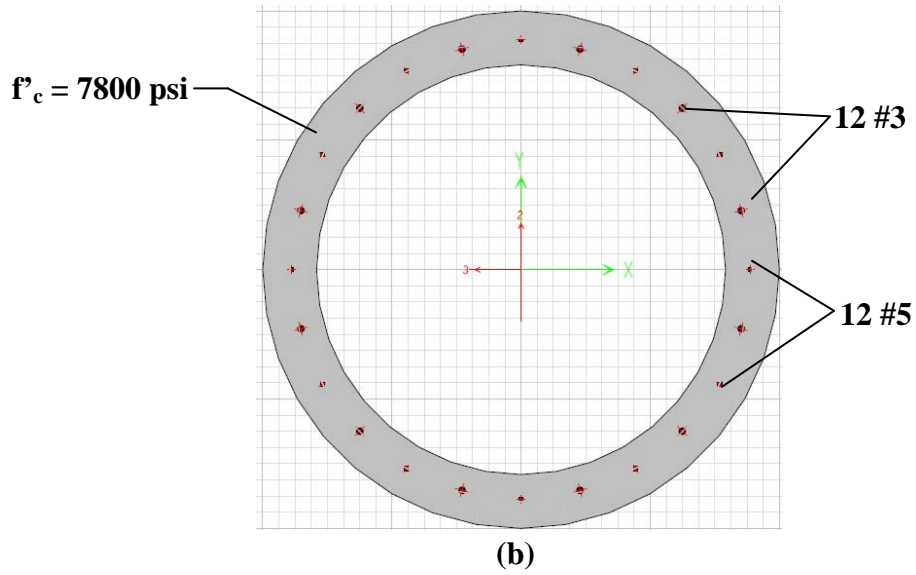


Figure 4.12. Column/pile cross-section model: (a) top 4 feet; and (b) rest of pile

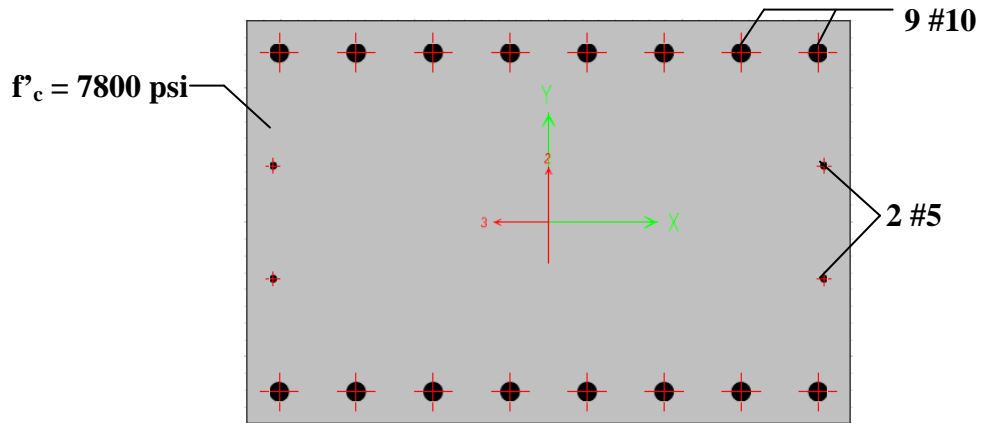


Figure 4.13. Crossbeam cross-section model

Every bent was modeled as a plane frame. Effective stiffness corresponding to a cracked cross section should be used for modeling RC columns. However, for prestressed concrete structures it is recommended to use un-cracked properties (Priestley, et al., 1996a) i.e.:

$$EI_e = 1.0EI_g \quad (4.1)$$

4.2.1. BOUNDARY AND CONNECTIVITY CONDITIONS

4.2.1.1. BEARINGS

The lateral shear capacity of elastomeric bearing pads is controlled by either the dynamic friction capacity between the pad and the bearing seat or the shear strain capacity of the pad. If friction force capacity governs, an elastomeric pad performs linearly due to shear deformations until the applied lateral force exceeds the friction force capacity. Once it is exceeded, the pad slides and the stiffness becomes nearly zero. If the shear strain capacity of the rubber governs, the pad performs linearly up to failure. The modeling of the elastomeric pad can be accomplished through the use of an elastic perfectly plastic material. The chore lies in determining the initial shear stiffness of the bearing and also the calculation of an appropriate coefficient of friction. The initial stiffness, k , can be calculated by Equation 4.2.

$$k = \frac{GA}{h} \quad (4.2)$$

Where G is the shear modulus, A is the bearing cross-sectional area, and h is the bearing height. Shear modulus values for elastomers in bridge bearings range between 160 psi and 240 psi, depending on their hardness. Since this value can vary over the bridge inventory, an average value of 200 psi is assumed as a typical value for this study. This may be a slightly higher value than would be typical for new rubber, but a large majority of these types of bearings are 20 - 30 years old and have likely hardened. The height of the pads is specified in the plans to be 1 inch. The area of the pad varies based on the girder size resting on the bearing. There are a total of four different bearing sizes used in this bridge (Appendix B.3).

Test results have demonstrated that the dynamic coefficient of friction between concrete and neoprene is approximately 0.40, and the maximum shear strain resisted by elastomeric pads

prior to failure is estimated at $\pm 150\%$ (Caltrans, 2008). For the given bridge pads, the friction capacity governs over shear strain capacity. Figure 4.14 shows the resulting force-displacement relationship calculated for the bearing pads. The pads are named A, B, C, and D, and they are further described in Appendix A. The bearings are only active in longitudinal translation of the deck. The other stiffnesses of the bearing pads were set relatively high to model the resistance of the girder stops in the transverse and rotational degrees of freedom of the bridge (Figure 4.7)

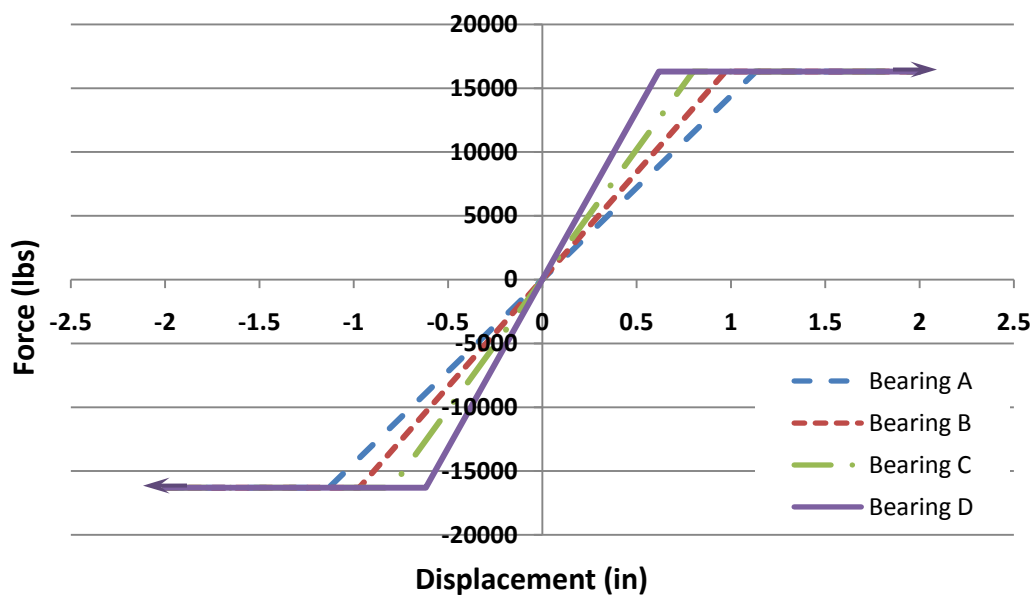


Figure 4.14. Model for elastomeric bearings

4.2.1.2. EXPANSION JOINTS

It is recognized that the pounding of decks can affect the way a bridge responds to seismic loading. A common way of representing pounding is by using a contact element including a linear spring with a gap between the girders. As illustrated in Figure 4.15, the contact element monitors the gap between adjacent girders of the bridge and is engaged once the associated gap is closed.

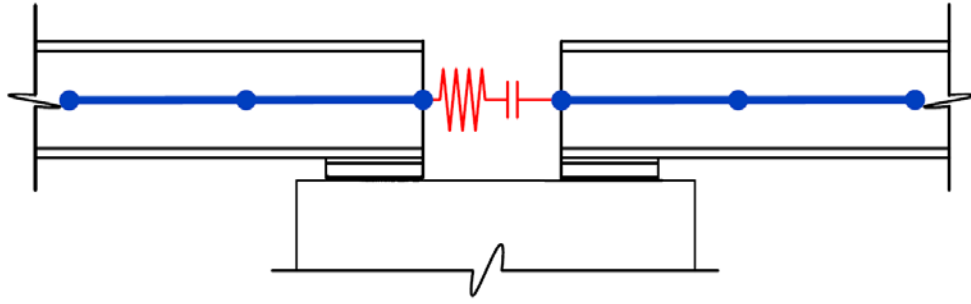


Figure 4.15. Pounding of bridge decks

Determining the characteristics of a contact element can be cumbersome. Muthukumar (2003) performed a study looking at the pounding in bridges and recommended a procedure for generating appropriate contact elements. Using a stereomechanical approach, the energy dissipated during impact can be derived and written as shown in equation 4.3.

$$\Delta E = \frac{k_h \delta_m^{n+1} (1-e^2)}{n+1} \quad (4.3)$$

Where ΔE is the energy dissipated, k_h is an impact stiffness parameter with a typical value of 25,000 k-in^{-3/2}, n is the Hertz coefficient typically taken as 3/2, e is the coefficient of restitution with a typical range of 0.6 - 0.8, and δ_m is the maximum penetration of the two decks. With the dissipated energy estimated, the parameters for the linear model are adjusted to yield the same energy dissipation. The first step is to limit the penetration to some maximum value δ_m . The effective stiffness, K_{eff} as seen in Figure 4.16 is then obtained as:

$$K_{eff} = k_h \sqrt{\delta_m} \quad (4.4)$$

In this study the maximum deformation or penetration δ_m is assumed to be 1 in., and thus the calculated K_{eff} comes out to be 1041 kip/in. The gap element of SAP2000 (2007) was utilized to account for the possibility of pounding when the longitudinal deformations close the gaps between spans as well as the gaps at the abutments. The gap element was set as a “compression-only” connection such that the element did not apply any resistance before the

closure of the gap. When the gap between the deck and abutment closed, pounding occurred. K_{eff} was assumed as the stiffness of the gap element at the contact location.

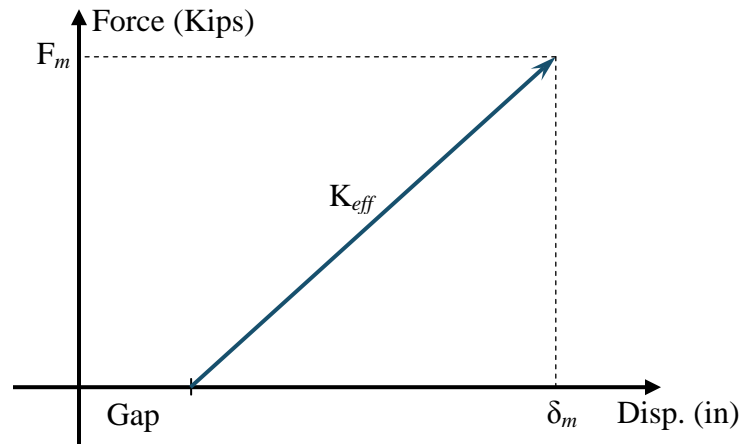


Figure 4.16. Characterization of contact element

4.2.1.3. ABUTMENTS

Bridge abutments primarily resist vertical loads but they also must take horizontal loads. Seismic loads can place great demands on bridge abutments. For instance, the longitudinal response of a bridge during seismic loading can increase the earth pressures on the abutment. Impact of the deck with the abutment can further increase these pressures.

The abutment in this study can be considered a spill-through type. The lateral resistance is to be provided by a combination of back wall and footing action. A typical spill-through-type abutment is shown in Figure 4.17, the only difference with Ravenna Bridge abutments being that the footings in this study are separated.

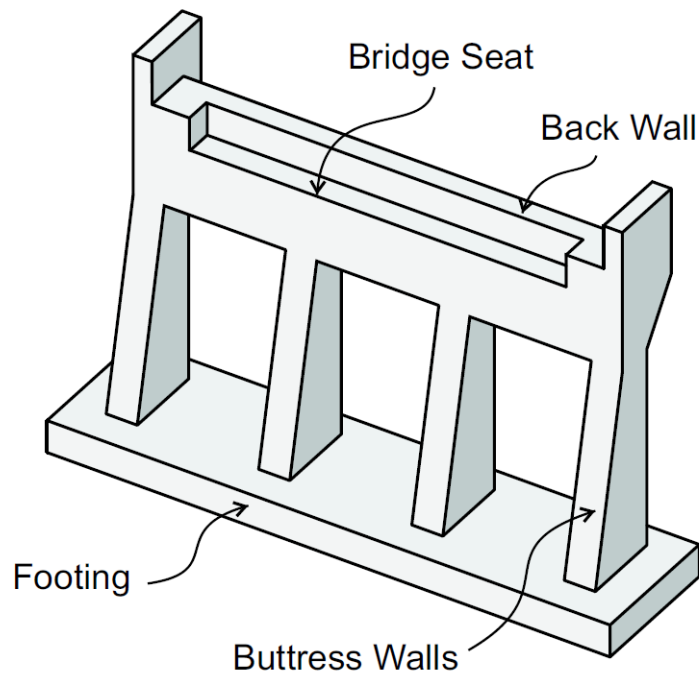


Figure 4.17. Spill-through abutment type

In the longitudinal direction, there are two types of resistance that are present. The first is a passive resistance which is developed as the abutment wall is pressed into the soil back-fill, as shown in Figure 4.18. Thus, passive resistance is provided by a combination of the soil and the footings. The other type is active resistance which occurs as the abutment is pulled away from the backfill. During this motion the footings provide the horizontal resistance. For this bridge, the wing walls are not very large, and therefore they do not contribute much to the transverse horizontal resistance of the abutment. Therefore, for all practical purposes, this study considers that transverse resistance is provided solely by the footings.

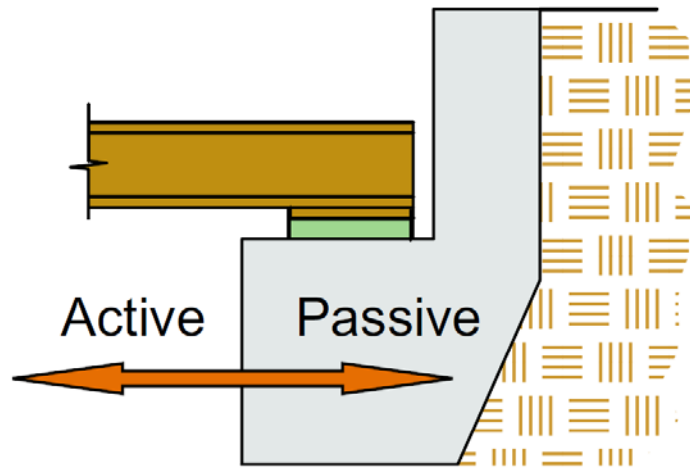


Figure 4.18. Definition of longitudinal abutment behavior

Based on a passive earth pressure test and force deflection results from large-scale abutment testing at UC Davis (Kutter, et al., 2003), the initial embankment fill stiffness is 20 kip/in/ft. The passive earth pressure reaches its maximum value when the soil reaches its ultimate strength of 5 ksf after sufficiently large movements of the walls, and it remains constant for further wall movements (Caltrans, 2008). Nonlinear plastic links were developed for the back wall soil interaction. Linear springs were calculated for the footings by following FEMA 356 (2000) (see Appendix A.7), based on the geometric characteristics of the abutment footing. The demand on the bridge footings did not exceed the design capacity, so yielding was not considered in the modeling of the abutment footings. The stiffness of the footings was activated for the movement of the abutments in all six global degrees of freedom. The abutments provide resistance only when the initial gap of 1 inch between the abutments and the superstructure is closed. Figure 4.19 shows the force-displacement relationship calculated for the back wall of the abutments (Appendix A.8). The strength of Abutment B is lower than Abutment A, because the calculated effective width of the abutment is 35% smaller.

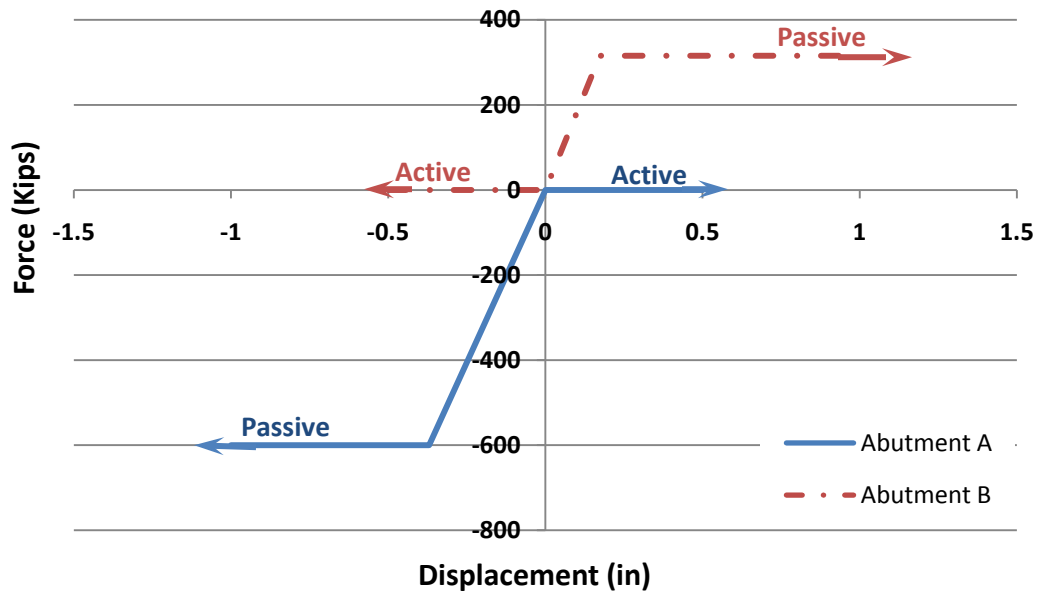


Figure 4.19. Model for abutment back wall

4.2.1.4. SOIL-PILE INTERACTION

Nonlinear springs along the pile shafts were used to model the effects of the surrounding soil on the pile stiffness and strength. The L-Pile (2002) program was used to compute p - y curves for the piles for the three different soils, namely dense sand, stiff clay, and loose sand. The water table was assumed at a depth of 15 ft from the ground surface

The concept of a p - y curve, described by Lymon (2006), can be defined graphically as shown in Figure 4.20. It was assumed that the pile was perfectly straight prior to driving and there was no bending of the pile during driving. The soil pressure acting against the pile prior to loading can be reasonably assumed to be uniform, Figure 4.21a. The resultant pressure for this condition is zero. If the pile is loaded laterally so that a pile deflection y_i occurs at the depth x_i , the soil stresses will become unbalanced as shown in Figure 4.21b. Therefore, a net soil reaction will be obtained by the integration of the soil pressures around the pile giving the unbalanced force per unit length of the pile. This process can be repeated in concept for a series of

deflections resulting in a series of forces per unit length of pile which may combine to form a p - y curve. In a similar manner, the sets of p - y curves along the pile as shown in Figure 4.20c can be obtained.

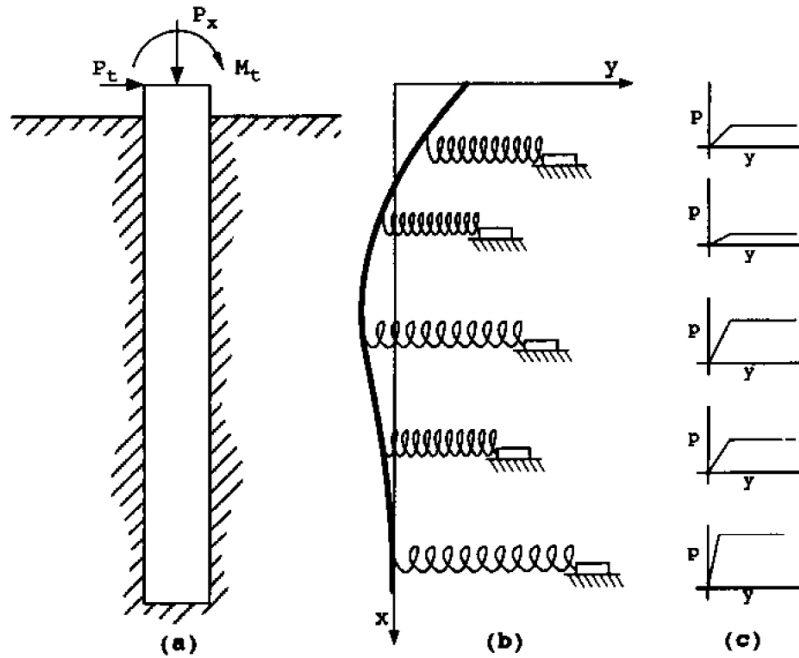


Figure 4.20. Schematic model of laterally loaded pile (Lymon, et al., 2006)

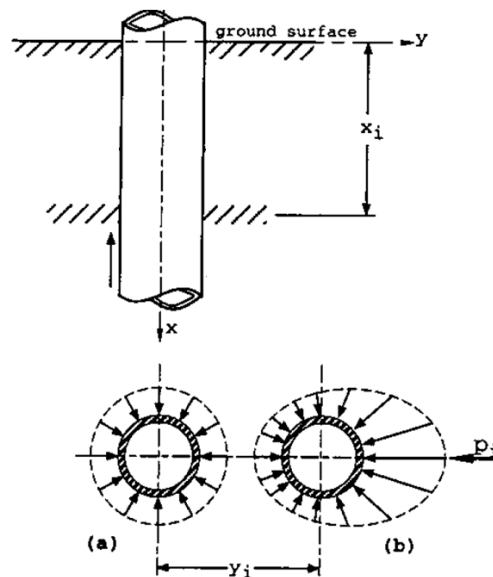


Figure 4.21. Definition of p and y as related to response of a pile to lateral loading (Lymon, et al., 2006)

Once the p - y curves at various depths of the pile have been obtained, a force-displacement relationship can be calculated by multiplying p with the tributary length of the pile between springs, similar to Figure 4.20b (Priestley, et al., 1996b). Thirteen nonlinear springs per pile were defined in L-pile, considering more springs per length close to a potential plastic hinge. Figure 4.22 shows a bilinearized lateral force-displacement relationship at different depths based on the data retrieved from L-Pile for loose sand. Results for other soil types are given in Appendix B.8

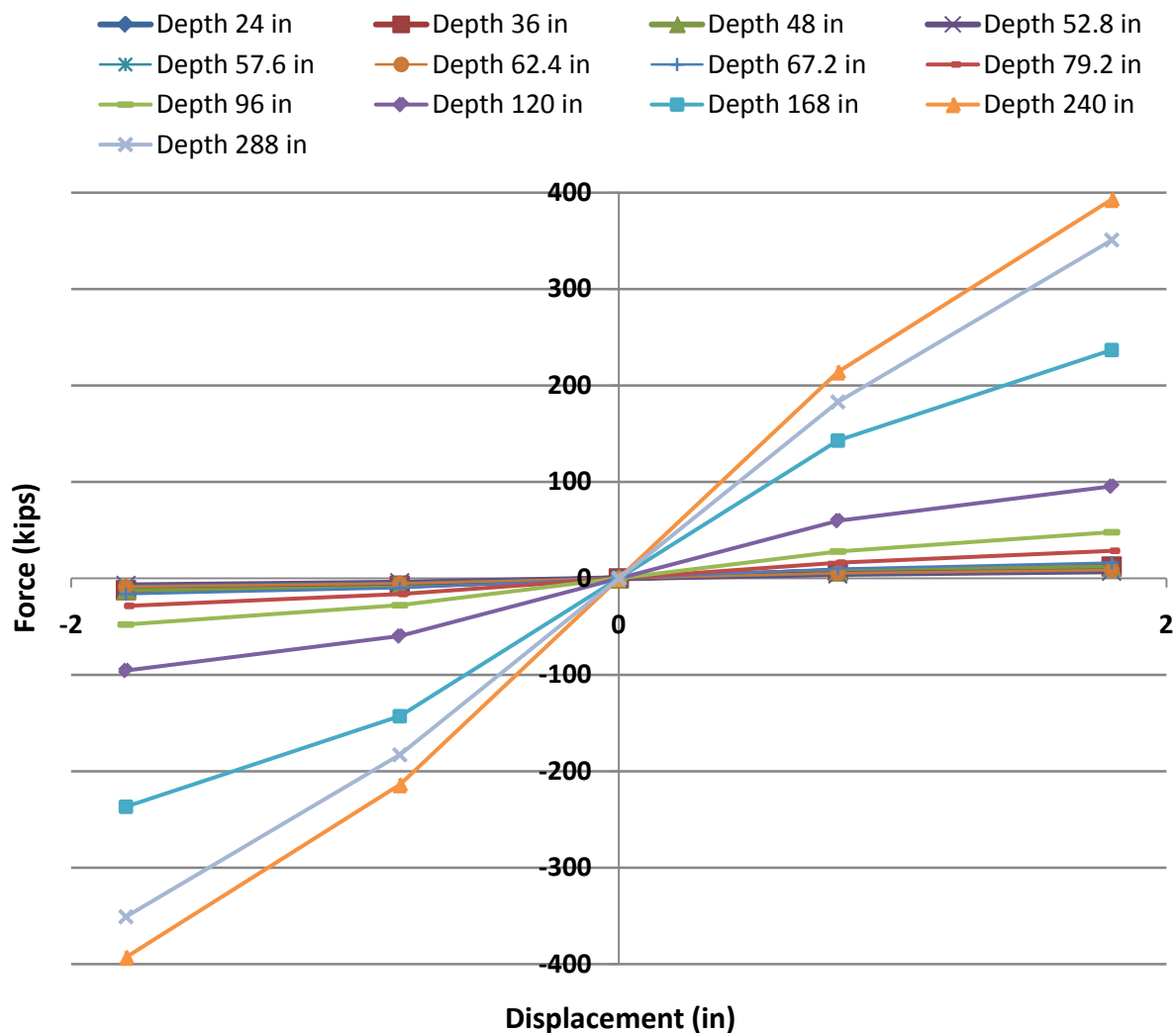


Figure 4.22. The relation between the lateral force and displacement used for characterization of the springs along the pile in the loose sand

The piles of all bents were assumed to extend 27 ft under the ground, so all bents had the same pile modeling. Figure 4.23 shows the SAP pile model with the attached nonlinear springs at various depths. The pin connection at the bottom of the pile restricts the pile from vertical and horizontal movement.

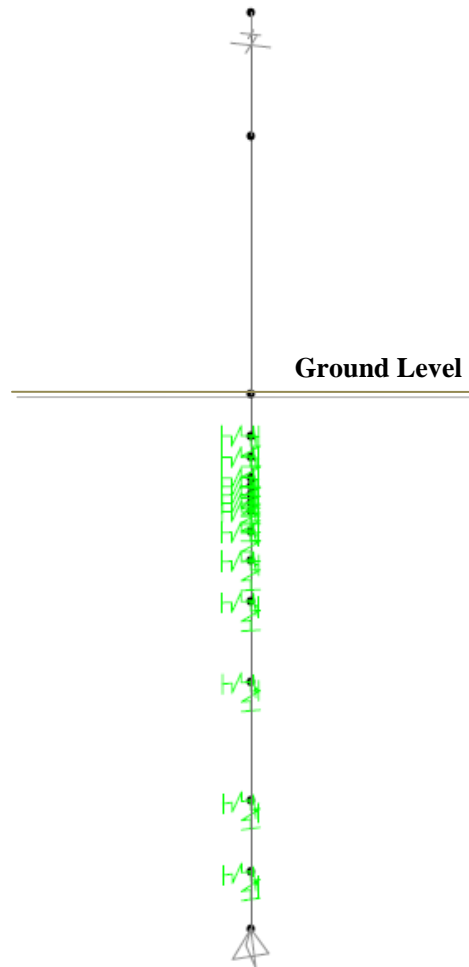


Figure 4.23. SAP model of column/pile

4.2.2. PLASTIC HINGE DEFINITION FOR PILES

For defining a plastic hinge in SAP 2000, different options exist. For the current research, a plastic hinge was defined using a plastic hinge length and a moment curvature relationship. The moment curvature relationship for the bridge columns was calculated using two different

methods: a 2-D numerical analysis using XTRACT (2002) and a 3-D finite element model for the piles using ABAQUS (Greenwood, 2008).

4.2.2.1. MOMENT CURVATURE RELATIONSHIP

For each column cross section, both the nominal and idealized moment-curvature diagrams for different axial loads is determined using XTRACT (2002) and is shown in Figure 4.24. In this figure, the dashed lines represent the actual moment-curvature curves and the solid lines represent the bilinearized moment-curvature curves.

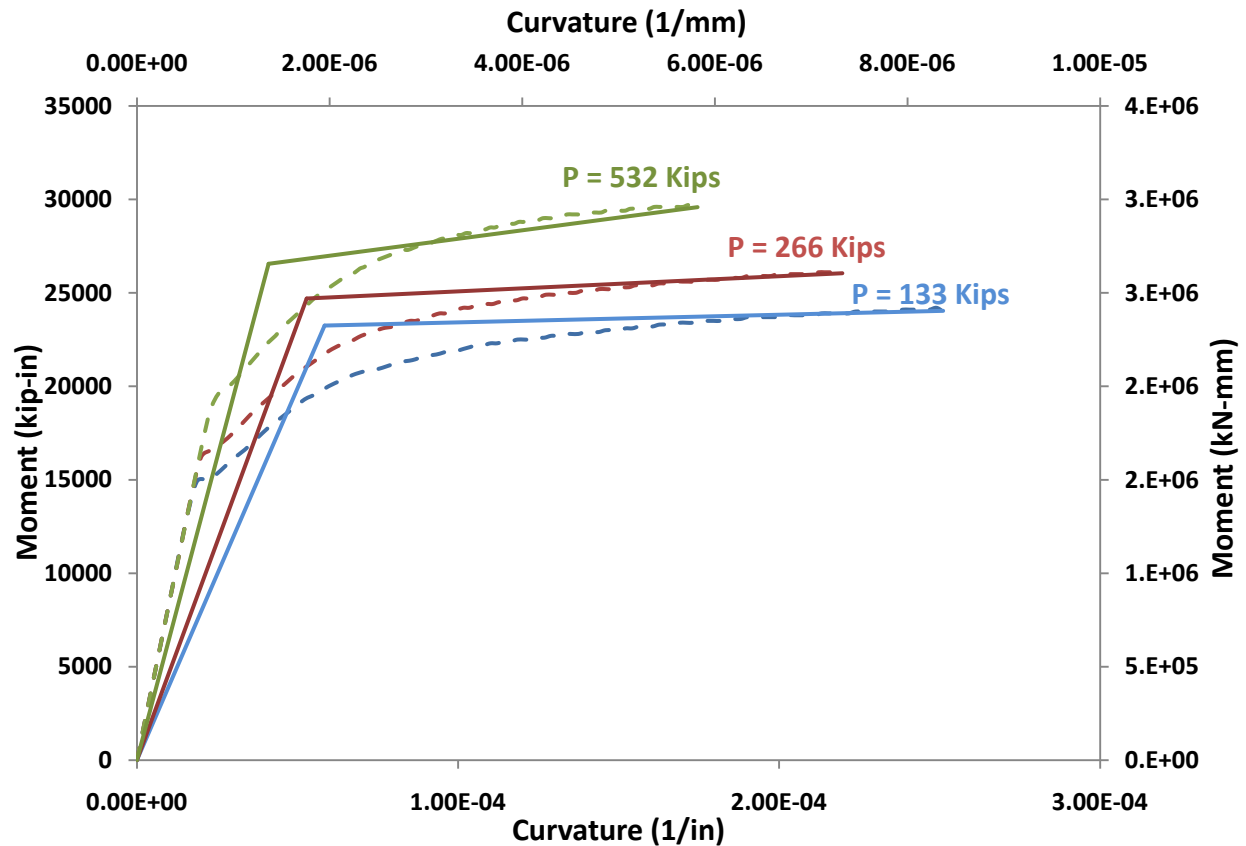


Figure 4.24 Moment-curvature curves of the columns/piles

Curvature properties are section dependent and can be determined by numerical integration methods. Input data of a cross-section include nonlinear material properties of

concrete and steel, and the detailed configuration of the section. The concrete maximum compression strain was taken as 0.004 due to the absence of any significant confinement. The yield strength of the rebar steel was taken as 40 ksi. For the Ravenna Bridge, all the columns have identical section dimensions and reinforcements. However, the moment-curvature relationship may not be the same because of different axial loads.

4.2.2.2. PLASTIC HINGE LENGTH

The curvature ductility demand in the plastic hinge region of a yielding pile-shaft can be estimated if the equivalent plastic hinge length of the pile is known. Ductility capacity of reinforced or prestressed concrete piles is frequently assessed without a soil medium and the pile loaded transversely in a statically determinate configuration (Sheppard, 1983; Park, et al., 1983; Banerjee, et al., 1987; Budek, 1997). A predetermined bending moment distribution, estimated from a soil-pile interaction analysis, is imposed on the pile to simulate the action of the soil on the pile. The actual interaction between the soil and pile, however, represents a highly indeterminate system with possible redistribution of bending moment upon yielding of the soil and pile. The predetermined bending moment, as commonly assumed for structural testing of piles, does not allow for such redistribution and may represent too severe of a condition for assessing the ductility capacity of the pile. Although analytical studies have shown that the equivalent plastic hinge length of concrete piles varies from one to two pile diameters depending on the soil stiffness and above-ground height (Priestley, et al., 1996a; Budek, et al., 2000), very few tests have been performed to verify such results.

The curvature ductility demand in the plastic hinge region of a pile-shaft can be estimated if the equivalent plastic hinge length of the pile is known. Although analytical studies have

shown that the equivalent plastic hinge length of concrete piles varies from one to two pile diameters depending on the soil stiffness and aboveground height (Priestley, et al., 1996a; Budek, et al., 2000), very few experimental tests have been performed to verify such results. In addition, these tests imposed a predetermined bending moment distribution, estimated from a soil-pile interaction analysis, on the pile to simulate the action of the soil on the pile (Sheppard, 1983; Park, et al., 1983; Banerjee, et al., 1987; Budek, 1997) The actual interaction between the soil and pile, however, represents a highly indeterminate system with possible redistribution of bending moment upon yielding of the soil and pile. The predetermined bending moment, as commonly assumed for structural testing of piles, does not allow for such redistribution and may represent a very conservative assessment for the ductility capacity of the pile.

In this research the plastic hinge length was calculated following Caltrans (2008) expression which read as follows:

$$L_p = 0.08(L_a + L_m) + D \quad (4.5)$$

Since the depth-to-maximum-moment L_m depends on the soil lateral strength, the equivalent plastic hinge length proposed by Caltrans varies with soil types and properties. Since the depth-to-maximum-moment, L_m , depends on the soil characteristics, the equivalent plastic hinge length proposed by Caltrans varies with soil types and properties. Recently, limited experimental tests on different types of sand soil (Chai, et al., 2002) have shown that the plastic hinge length depends solely on the above ground height and neither on the soil density nor lateral stiffness.

4.2.2.3. PLASTIC HINGE LOCATION

Under a horizontal earthquake ground motion, the lateral force associated with the inertia of the superstructure generates a bending moment distribution that varies with height but

diminishes after attaining a maximum bending moment below the ground level, as shown in Figure 4.25b. The depth-to-maximum-moment, L_m , depends on the soil characteristics and the flexural rigidity of the pile. LPILE (2002) was used to locate the plastic hinge for varying pile aboveground heights. The program computed deflections, shear forces, bending moments, and soil response with respect to depth in nonlinear soils. The soil behavior was modeled using p-y curves internally generated by the program. The depth-to-maximum-moment was calculated based on different soil types and above ground heights, and the results can be found in Appendix A.10. As the structure softens after yielding, moments are redistributed up the shaft, and the point of maximum moment (i.e., the subgrade hinge) migrates toward the surface. Thus, depth to plastic hinge may be taken as 0.7 times the depth to maximum moment found through an elastic analysis (Budek, et al., 2000).

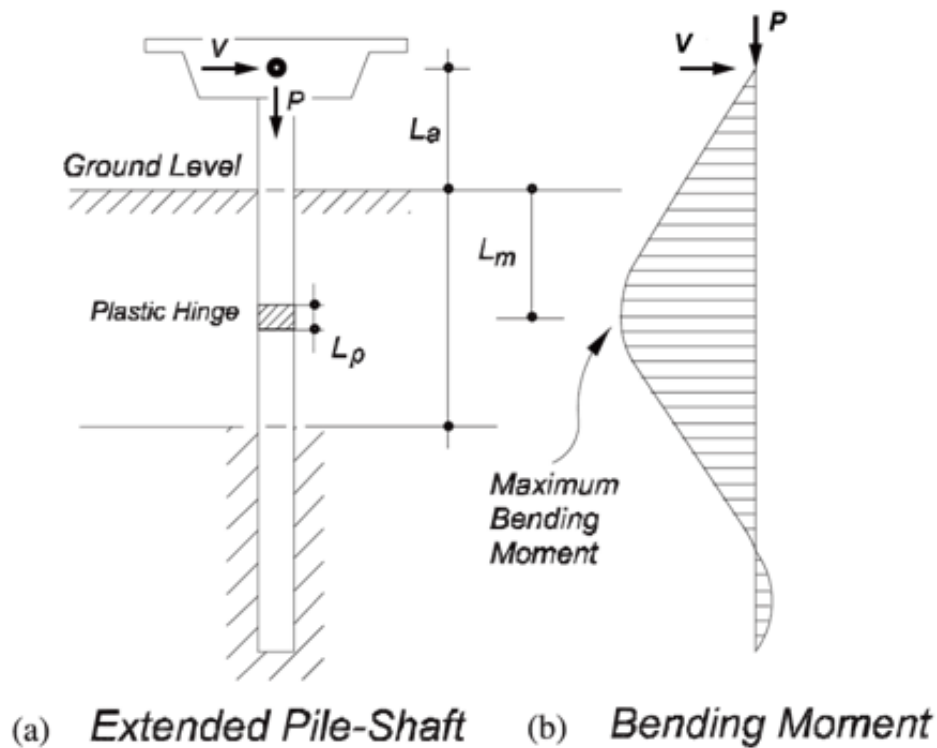


Figure 4.25. Transverse seismic response of extended pile-shafts (Chai, et al., 2002)

4.2.2.4. PLASTIC HINGE INPUT IN SAP2000

In this research, a lumped plasticity model is used with the assumption that plastic rotation occurs and concentrates at mid-height of a plastic hinge. A plastic rotation (θ_p) can be calculated using the plastic curvature and the equivalent plastic hinge length, L_p , as shown in Equation 4.8.

$$\theta_p = \Phi_p L_p = L_p (\Phi_u - \Phi_y) \quad (4.6)$$

The plastic rotation indicates the capacity of a section to sustain inelastic deformation and is used in SAP 2000 to define column plastic hinge properties. FEMA 356 (2000) provides a generalized force-deformation relation model shown in Figure 4.26 for the nonlinear static analysis procedure, which is the defaulted model in SAP2000 for the Axial Load-Moment hinge (PMM hinge in SAP2000).

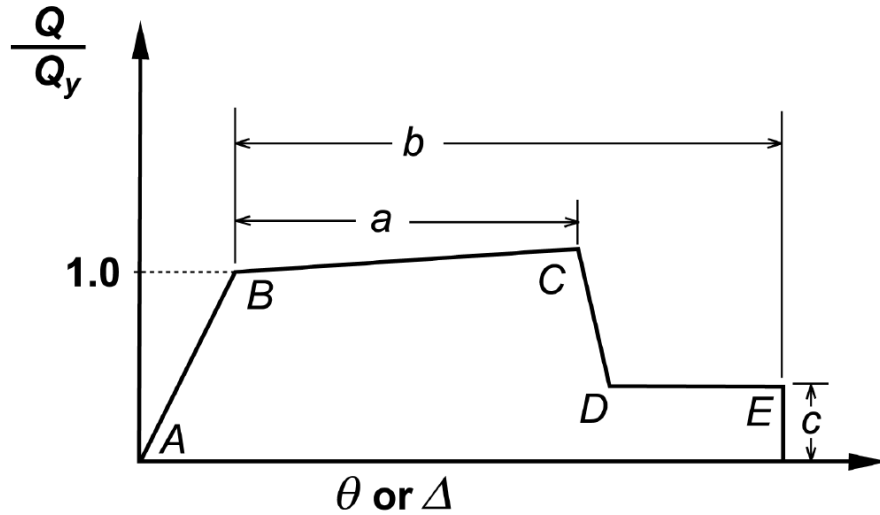


Figure 4.26. Generalized force-deformation relations for concrete elements

Three parameters, a , b and c are defined numerically in FEMA 356 (2000), and are permitted to be determined directly by analytical procedures. The moment and rotation are normalized by yield moment and yield rotation respectively (i.e. M/M_y and θ/θ_y). By default SAP

will calculate the yield forces and the yield rotation based on reinforcement and section provided. However, an absolute rotation value can overwrite the default value in defining a hinge property. The plastic rotation capacity angle, a , calculated with Equation 4.4 for a given column is at point C. The ultimate rotation angle, which is inputted as b in SAP, is taken as 1.5 times the plastic angle. It is indicated at point E, which defines a local failure at a plastic hinge.

The increase of moment strength at point C is taken as the over strength factor which is computed by using the bilinearized moment-curvature (M_u/M_y). The actual moment strength at point C is the product of the factor and the yielding moment. FEMA 356(2000) defines a 0.2 residual strength ratio before plastic hinge eventually fails. Figure 4.27 presents moment-rotation curves for one of the columns in Ravenna Bridge under three different axial loads.

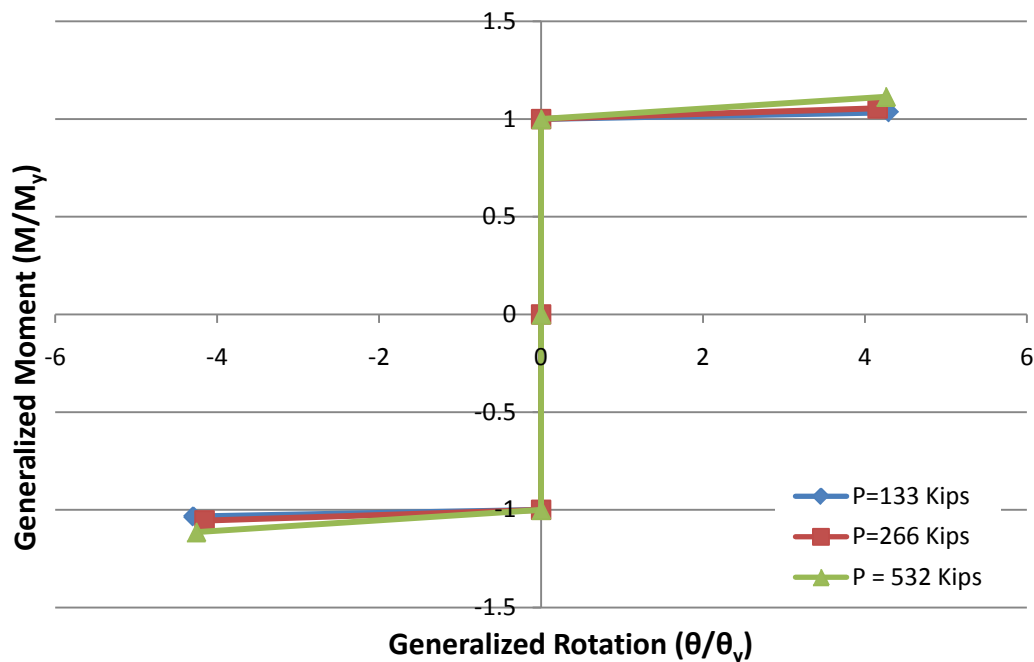


Figure 4.27. Moment-rotation relationship of the columns

During pushover analysis the level of the applied axial loads on the columns varies. In order to take that into considerations, SAP2000 requires an axial force- bending moment

interaction diagram and a moment rotation to define a PMM plastic hinge. This allows the program to estimate the yield moment strength for a column under any axial load. In other words, SAP2000 establishes yielding once a point is recorded on the outside of the axial load-moment interaction diagram. Beyond this point, the input moment-rotation curves are used as a pattern to estimate the nonlinear behavior of the hinge.

The interaction diagram was established using XTRACT (2002). Using XTRACT 2002 direct option for plotting the interaction diagram for a given cross section resulted in several problems because of the post-tension. In order to overcome this problem, the idealized moment-curvature curves for several axial loads were determined. The yield moment strength was recorded for each applied axial load. Using these data points the axial load-moment interaction diagram was established (Figure 4.28) and was fed into SAP2000.

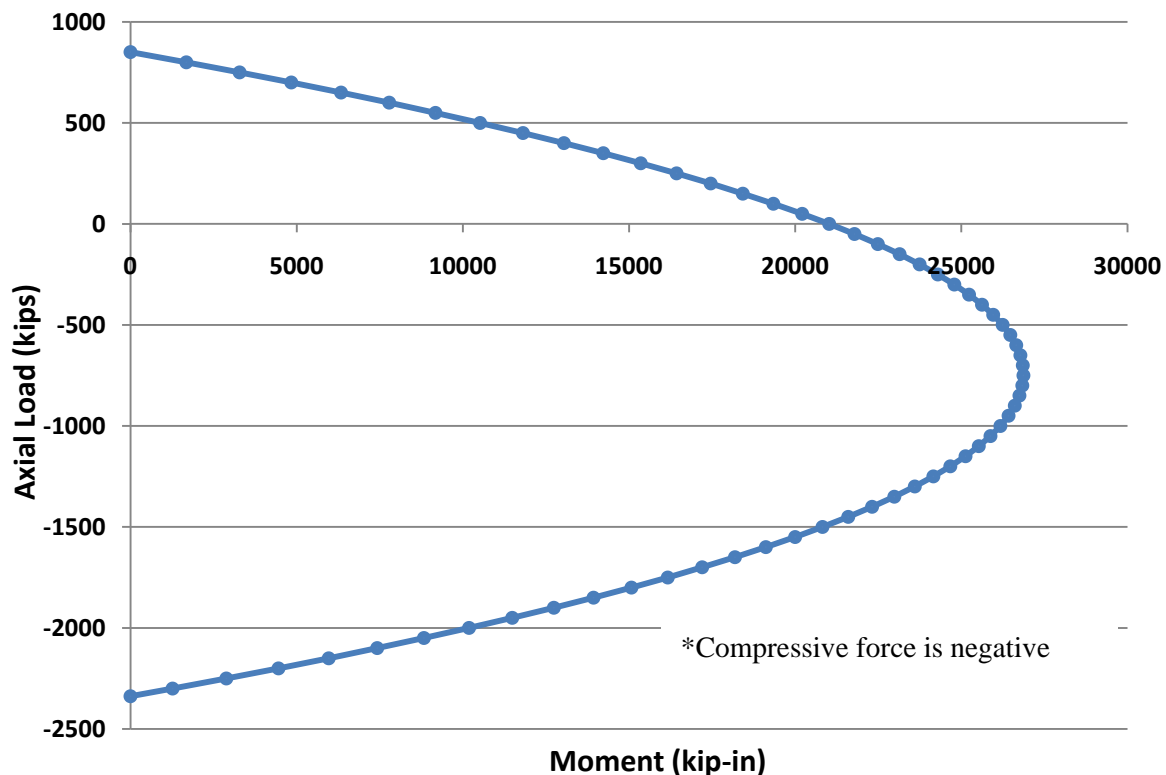


Figure 4.28. Axial load-moment interaction diagram of the columns

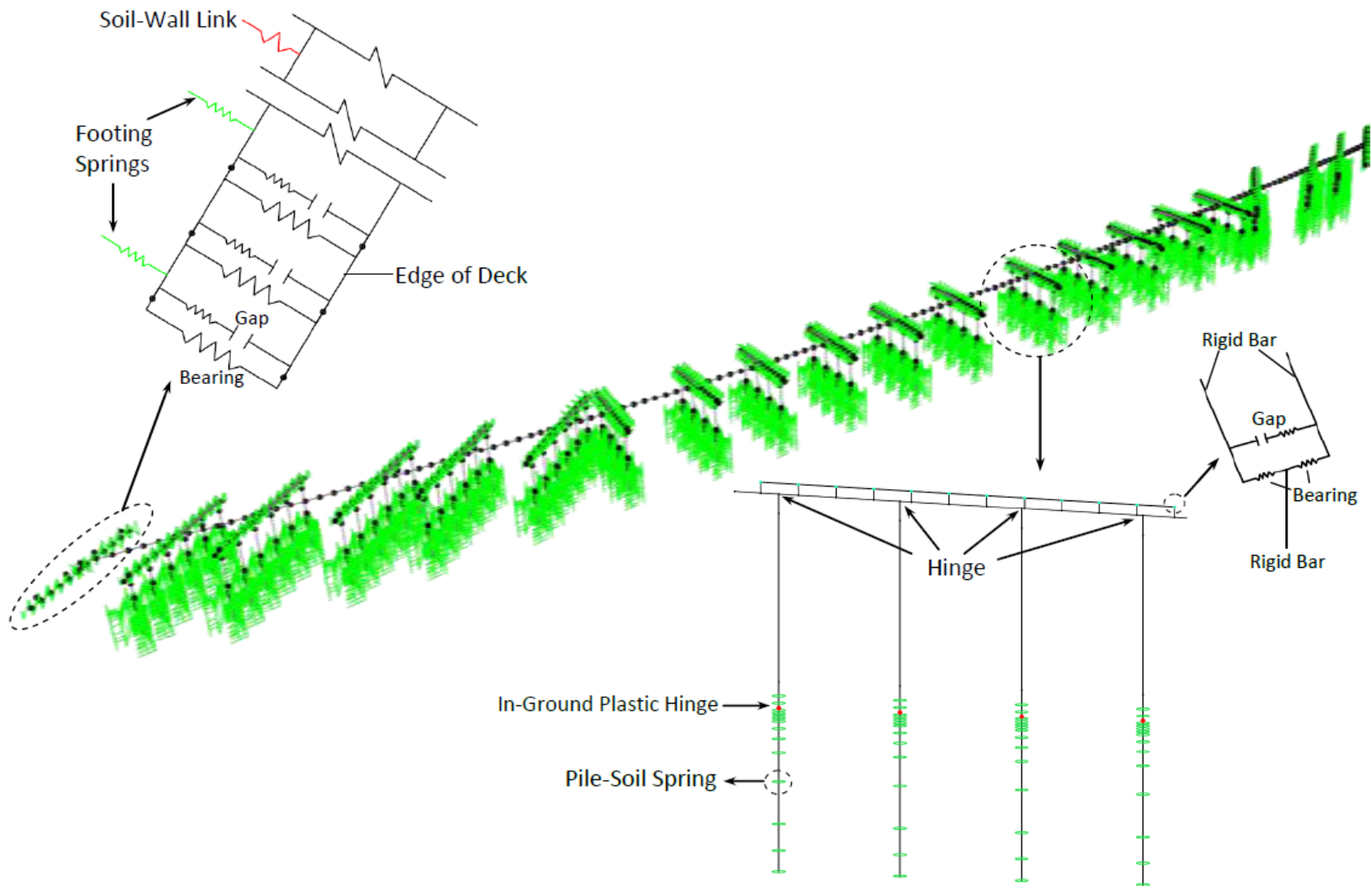


Figure 4.29. Final spine model of the Ravenna Bridge

4.3. PLASTIC HINGE LENGTH USING DETAILED FINITE ELEMENT OF THE PILE

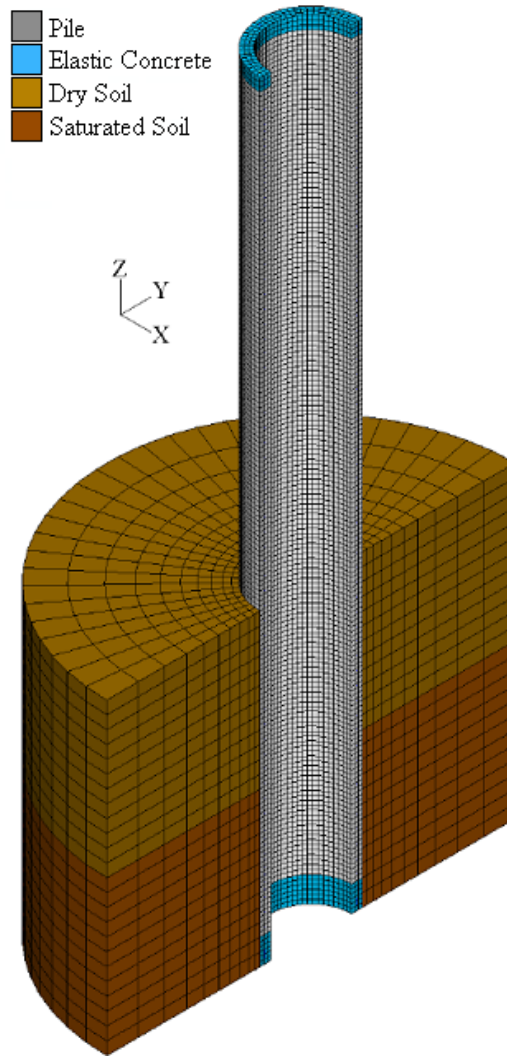


Figure 4.30. FE model of pile

In order to get a more in depth understanding of the performance of the piles a separate 3-D finite element modeling has been carried out (Greenwood, 2008, Figure 4.30). The above ground height of the pile was 18 ft while the subgrade length measured 12 ft. An axial load of 266 kip was applied as a uniformly distributed surface pressure on the free end of the pile.

The soil was specified as either Boston Blue Clay (i.e. stiff clay) or dense Ottawa Sand. The soil within the hollow core of the pile was neglected since it may have contracted over the

past decades. Hence, it would be unable to provide internal confining pressure. This was considered to be a conservative assumption with respect to the influence on failure mechanisms.

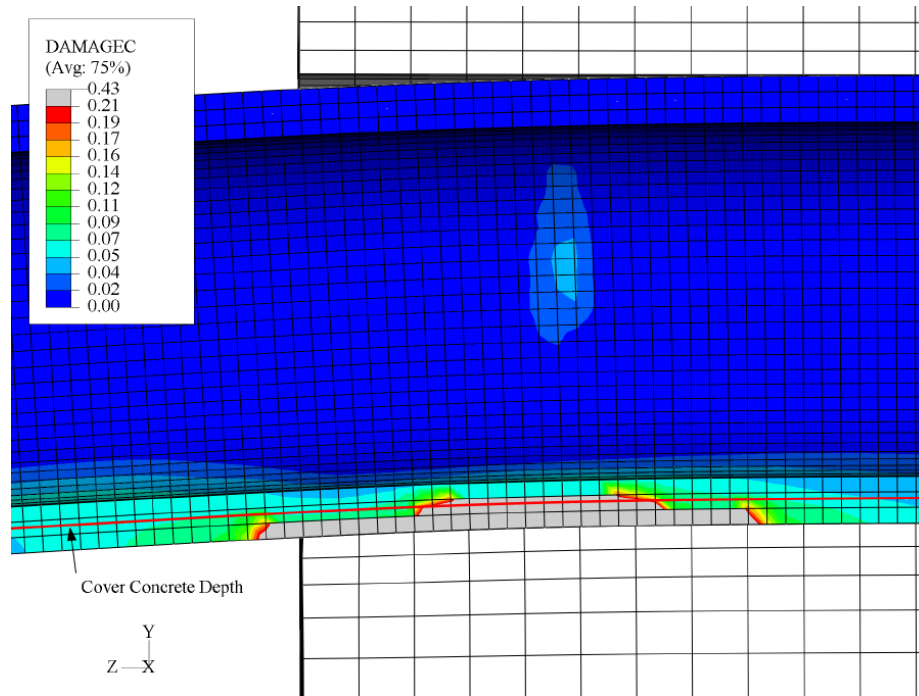


Figure 4.31. Failure of pile at plastic hinge location

The observed failure mechanism was spalling of the concrete cover at an average below ground depth of 24 in, as shown in Figure 4.31. For the pile embedded in clay, the plastic hinge formed at a depth of 28 in. and measured 2.88-D in length. Similarly, a plastic hinge measuring 3.0-D in length formed 20 in. below ground for the pile embedded in Ottawa Sand. It is evident that softer soils resulted in a greater depth to the center of the plastic hinge. In addition, it was found that the confining pressure supplied by the soil on the exterior surface of the pile does not provide an appreciable increase in pile capacity.

4.4. FE MODEL OF PILE TOP BOUNDARY CONDITION

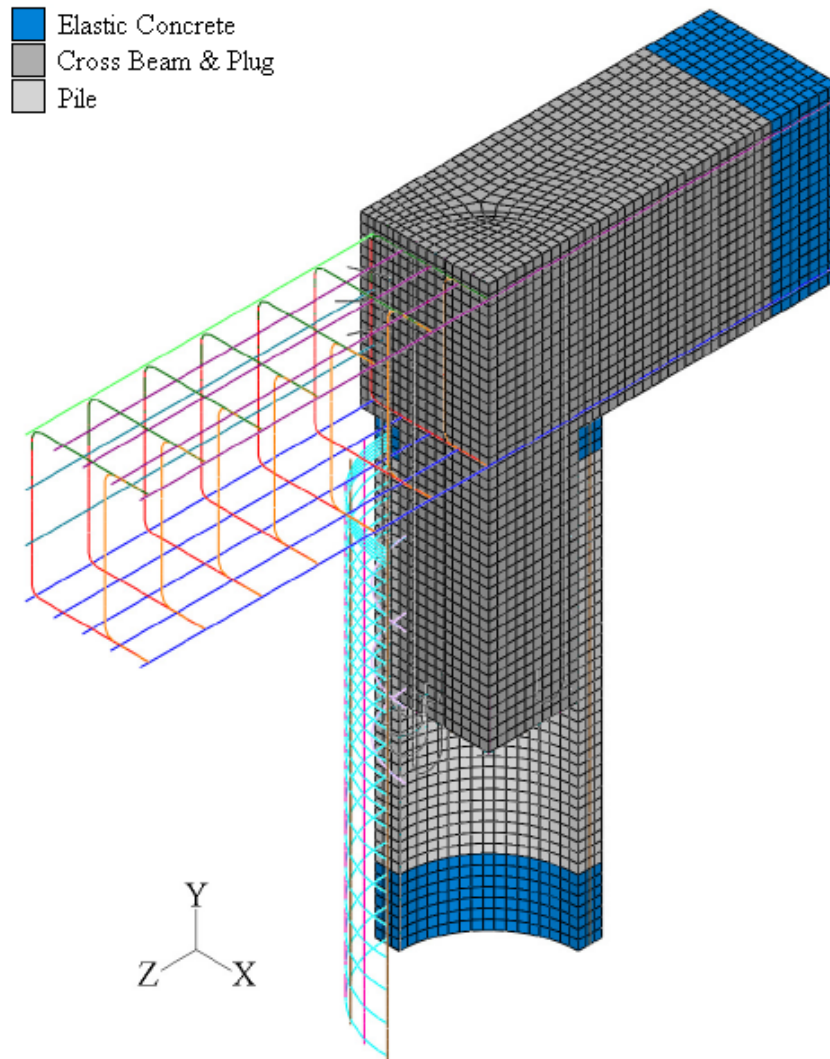


Figure 4.32. FE model of pile-crossbeam connection

One of the major factors that affect the performance of the bridge is the boundary condition at the top of the pile. Hence, the connection of the pile to the cross beam was analyzed using FE program (Greenwood 2008, Figure 4.34). The connection model was analyzed for axial loads of 266 kip and 133 kip.

The response of the in-situ connection is governed by the tensile capacity of the concrete (see Figure 4.35). Tensile cracking initiated at the reentrant corner where the plug is connected to

the cross beam. Nearly all of the reinforcing ties used to connect the plug to the cross beam yielded in tension, yet none of the ties failed. It was found that the rotation capacity of the connection was nearly independent of the magnitude of the applied axial load. A 50% reduction in axial load resulted in a 10% reduction in the ultimate moment response. A bilinearization of the moment-rotation responses obtained from the finite element model was used to represent the frame hinges in SAP2000 (Figure 4.36).

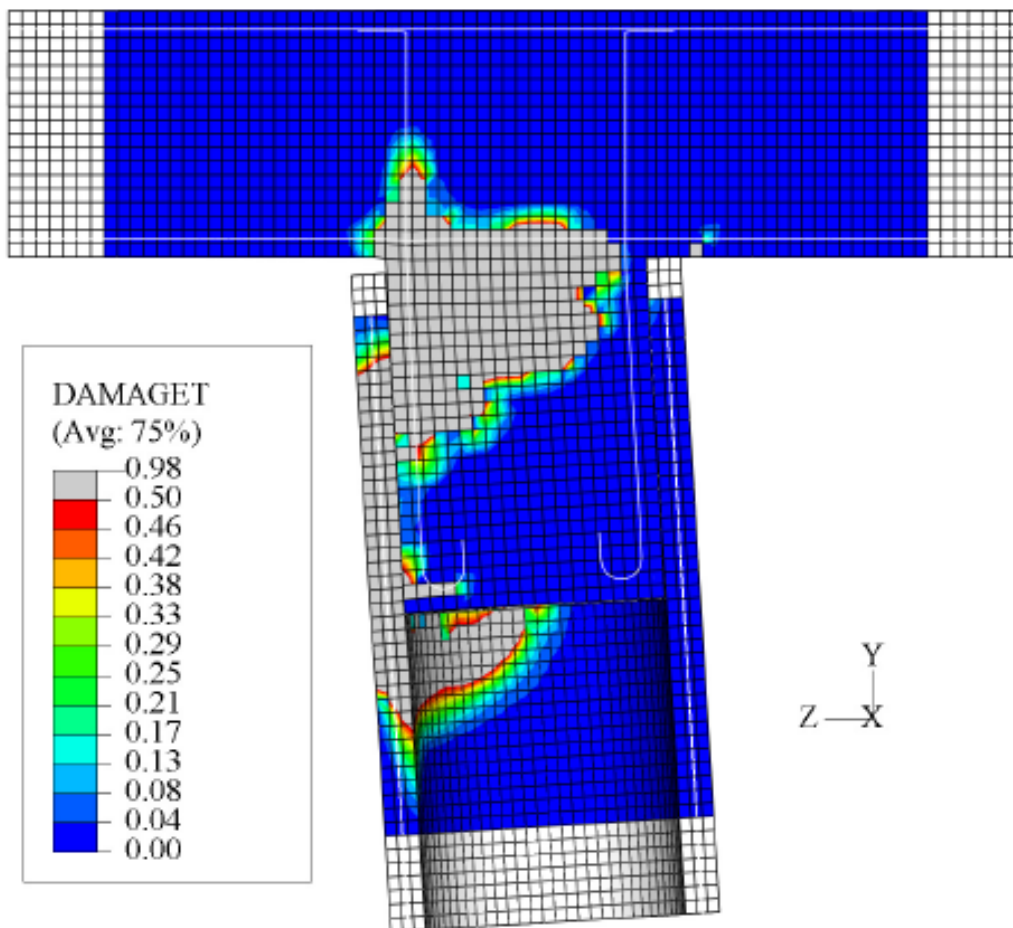


Figure 4.33. Failure of pile-crossbeam connection

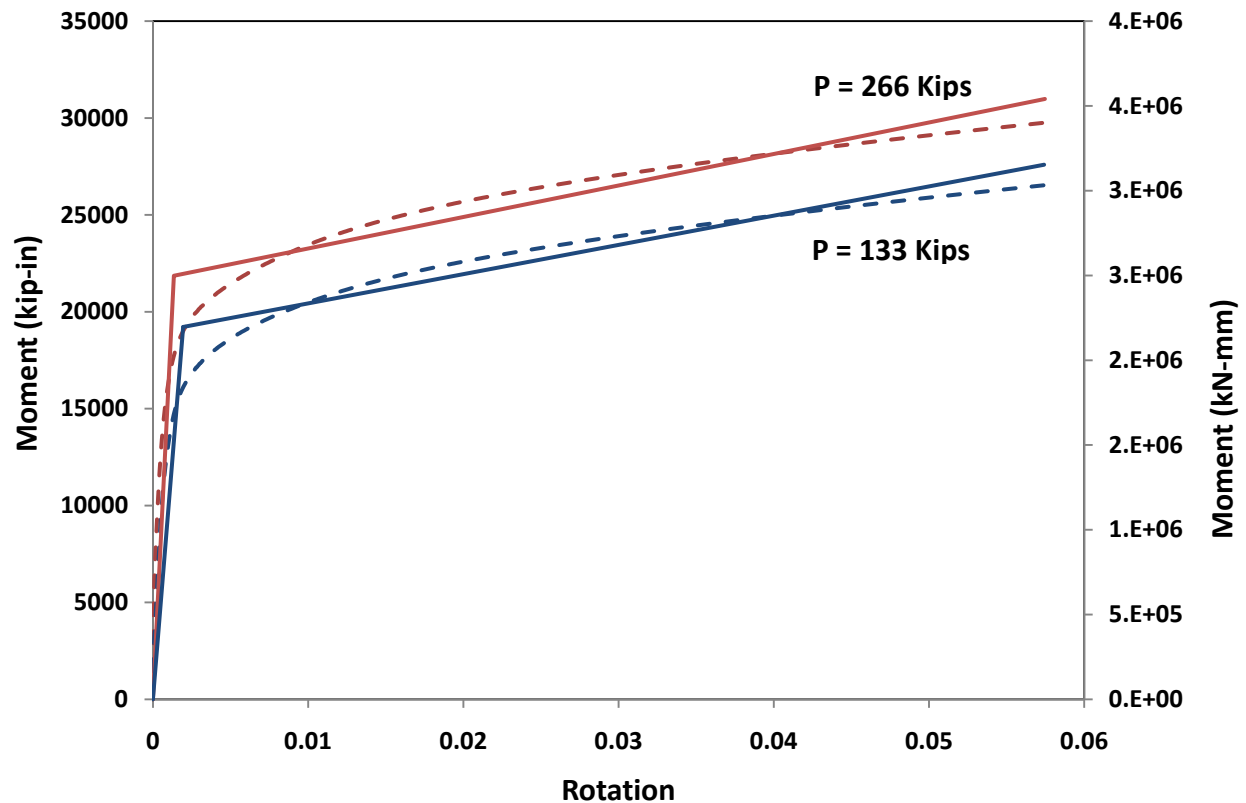


Figure 4.34. Moment-rotation relationship for pile-crossbeam connection

4.5. SEISMIC EXCITATIONS

For this research, three different ground motions including Moquegua (Peru earthquake 2001), and two from the Olympia (Washington earthquake 1949) were used. The Moquegua earthquake had a 2475-year return period, while the other two earthquakes had a 475 year and a 975-year return period. The Moquegua ground motion is a long-duration earthquake, while the other ground motions are short-duration events. Additionally, the Moquegua ground motion is a subduction-zone earthquake. The two Olympia, Washington ground motions were provided by WSDOT, which were specifically created by PanGEO Inc. using a probabilistic approach. Background on the provided design ground motions can be found at <http://pangeoinc.com>.

The N-S and E-W components correspond to the transverse and longitudinal axes of the bridges, respectively. Ground motions were modified to fit the target 5% damped acceleration

spectrum using the program RSPMATCH (Abrahamson, 1998). This program alters the frequency content of a ground motion by adding pulses of motion in the form of tapered cosine waves. The end result is a ground motion of the desired frequency content and PGA.

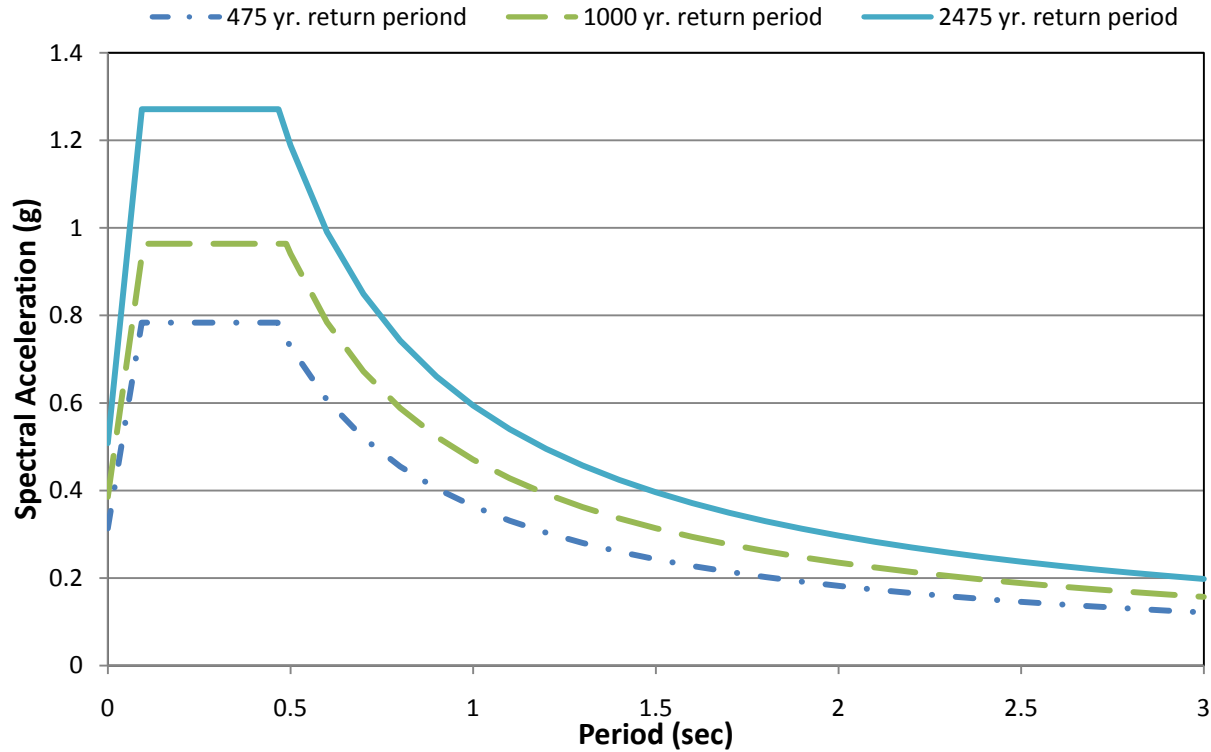


Figure 4.35. DRS corresponding to 475, 975, and 2475-year return period

Three elastic design response spectra (DRS), for soil class C, corresponding to 475, 975, and 2475-year return period, were developed for the Seattle area (USGS, 2002). These design response spectra are shown in Figure 4.37. Figure 4.38 shows the target acceleration spectrum, the acceleration spectra of the original Moquegua Earthquake, and the acceleration spectra of the modified Moquegua Earthquake after being modified in RSPMATCH (Abrahamson, 1998) to match the target acceleration spectrum. Figure 4.39 shows that the main characteristics of the ground motion were preserved after manipulation. Figure 4.40 through Figure 4.42 show the N-S and E-W time-history excitations. In the next chapters, a simple naming convention is used for the ground motions, with EQ1 standing for Olympia 475-year return period ground motion, EQ2

standing for Olympia 975-year return period ground motion, and EQ3 standing for Olympia 2475-year return period ground motion.

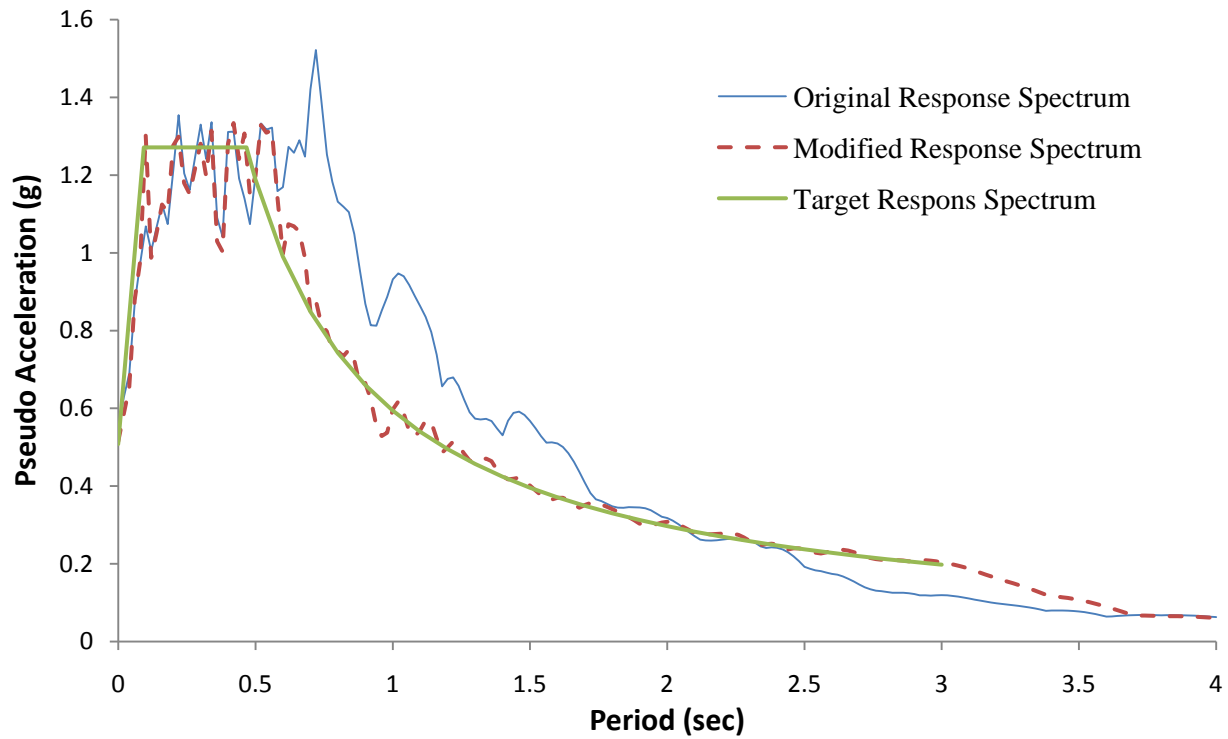


Figure 4.36. Moquegua, Peru Ground Motion (E-W) Spectral Acceleration

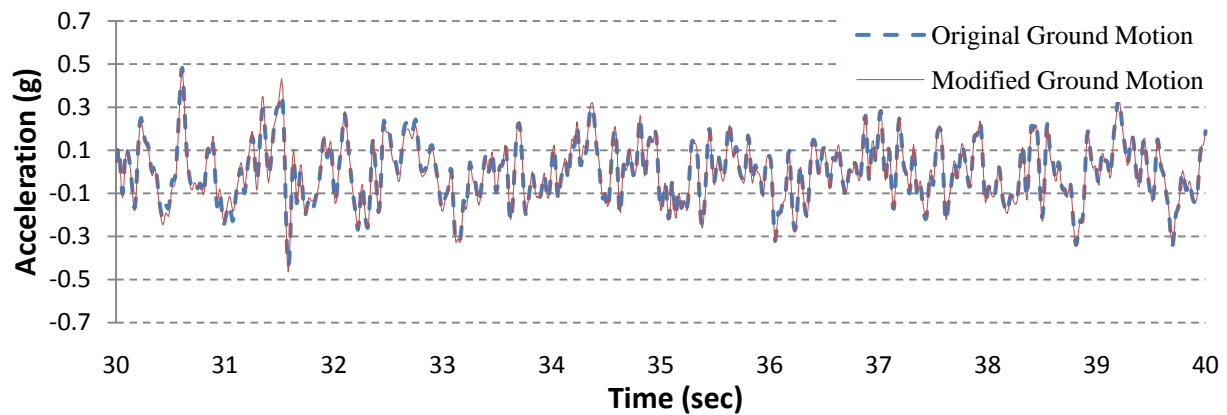


Figure 4.37. Modified and Original Moquegua, Peru Ground Motion (E-W) Time History

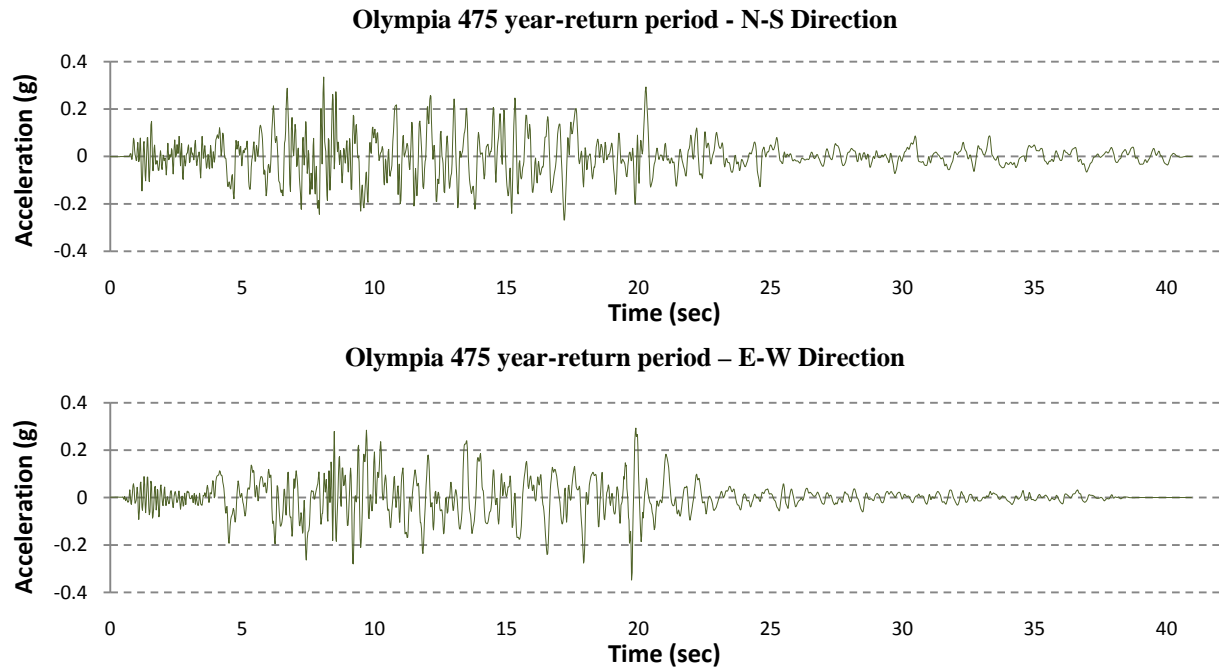


Figure 4.38. Time Histories for Olympia 475

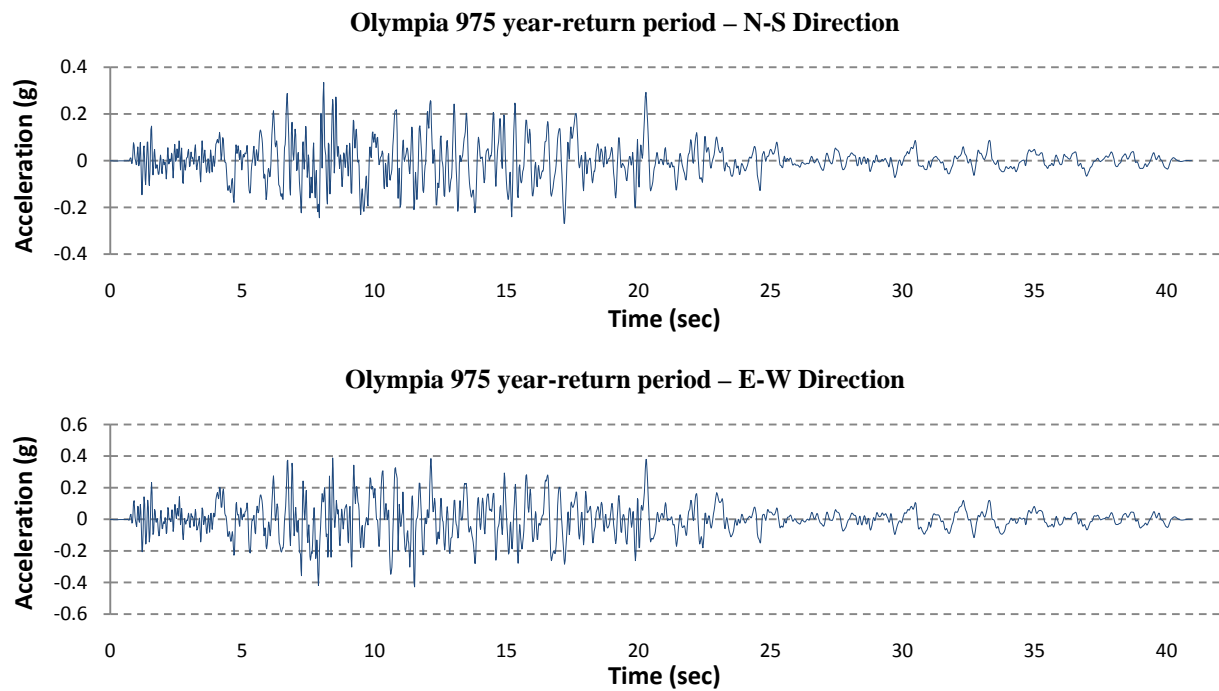


Figure 4.39. Time Histories for Olympia 975

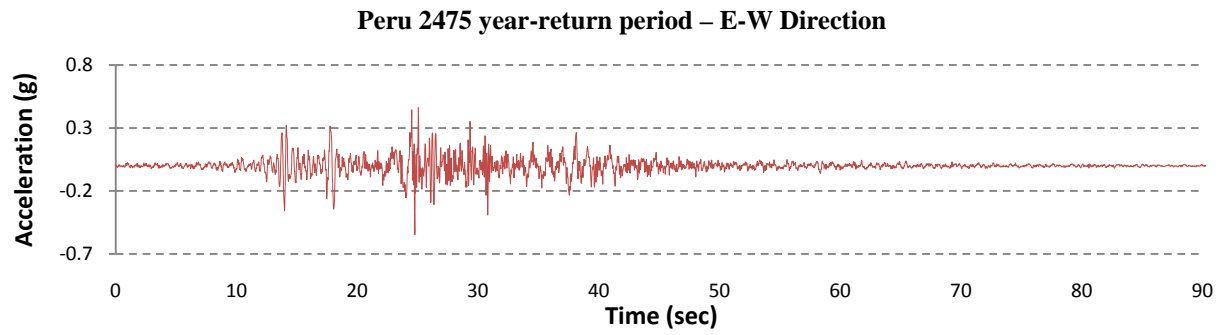
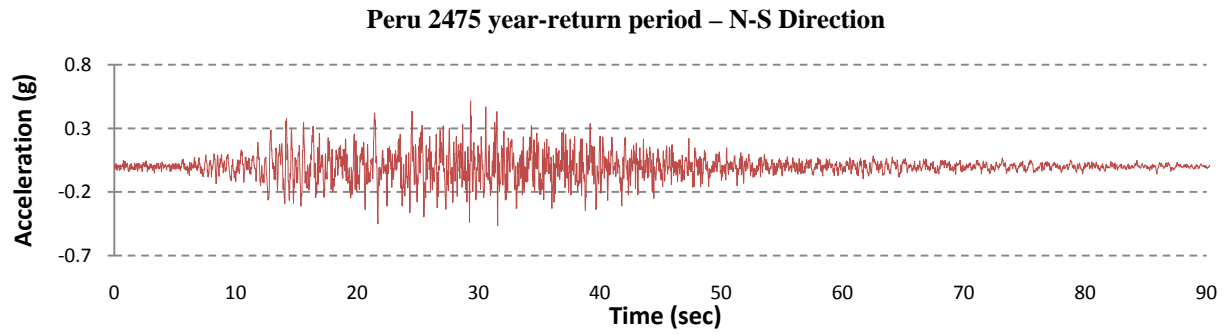


Figure 4.40. Time Histories for Peru 2475

CHAPTER 5: NONLINEAR DYNAMIC ANALYSIS RESULTS

In this section the results of the Nonlinear Dynamic Analysis (NLD) are presented. NLD is considered the most precise earthquake analysis, and thus will serve as benchmark for all the NLS described in Chapter 3. The three earthquakes described in Chapter 4 were used for the analysis, considering each fundamental direction separately. The simplified naming convention EQ1, EQ2, and EQ3 are adopted here, to represent the 475, 975, and 2475 year return period earthquake, respectively. In this chapter the crossbeam-pile connection is a pin.

5.1. LOOSE SAND

Figures 5.1 and 5.2 show the formation of plastic hinges under the given earthquakes for longitudinal and transverse directions, respectively. Expectedly, the severity of damage in the bridge is significantly increased going from EQ1 to EQ3 in both directions. Approximately 20% of the piles developed plastic hinges due to applying EQ1 in the longitudinal and transverse directions. These numbers are fairly small compared to the results when applying EQ3, for which approximately 50% of the piles developed plastic hinges in the longitudinal and transverse direction. EQ2 results indicate 35% and 19% plastic hinge development in the longitudinal and transverse directions, respectively.

From all six analyses, it is apparent that the center bents are going to be the most damaged in the event of an earthquake. The first piles in Bent10, from the east side, consistently suffered high displacement and forces for all analysis cases. The joint at the top of this pile was monitored to plot the displacement-time history results. The relative displacement between top joint and bottom of the pile in the global X and Y-directions were plotted versus time in Figures 4.3 and 4.4 for the longitudinal and transverse direction earthquakes, respectively. The maximum displacement is marked in the plots for each earthquake and direction.

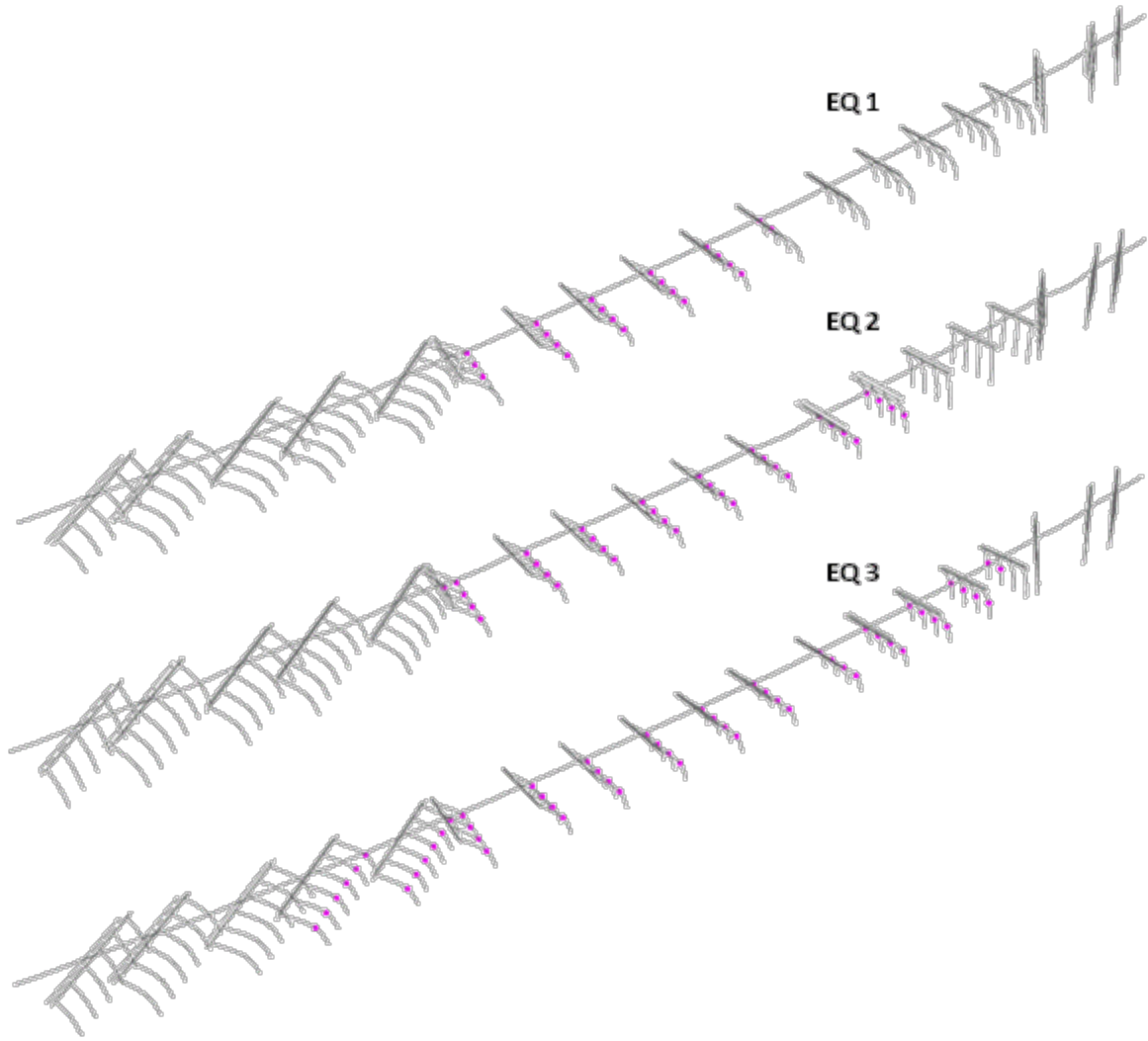


Figure 5.1. Hinge development for EQs in the longitudinal direction with loose sand

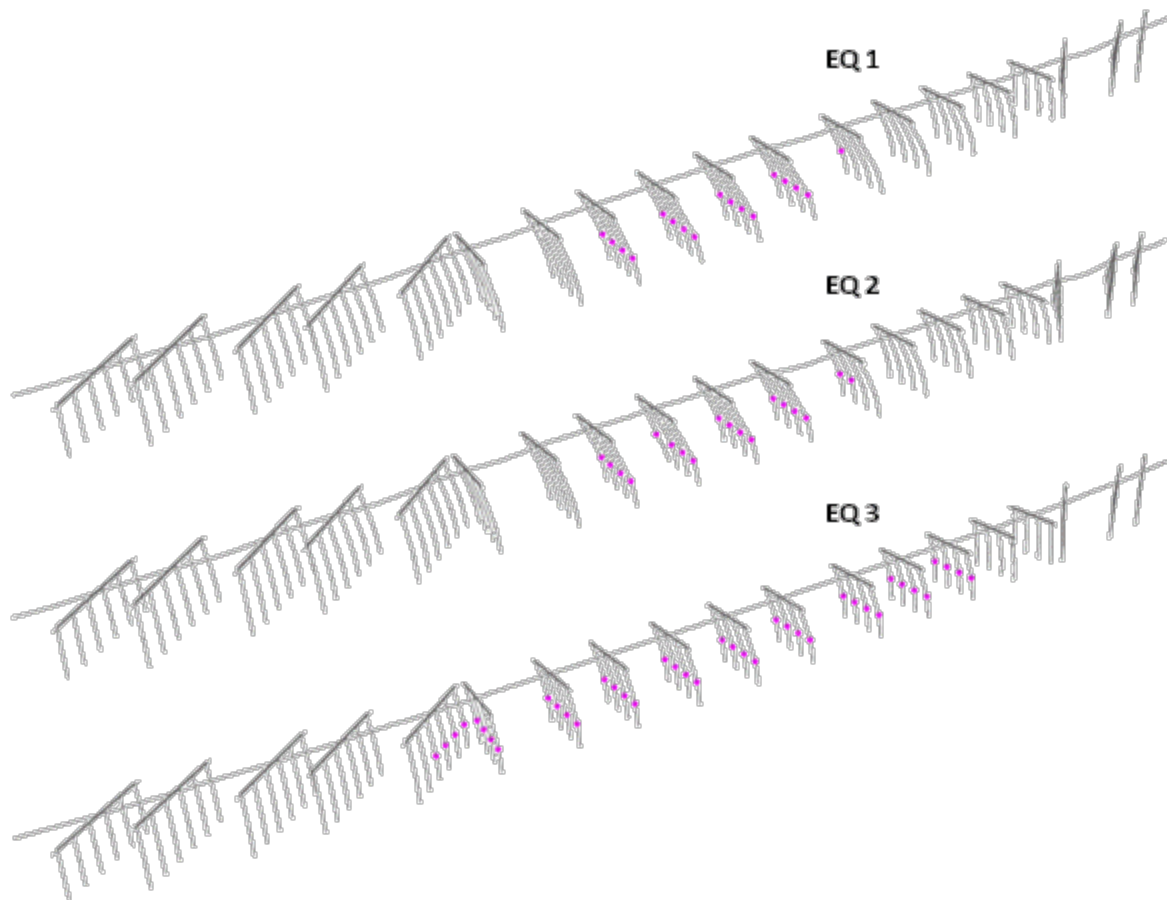


Figure 5.2. Hinge development for EQs in the transverse direction with loose sand

The longitudinal component of EQ3 causes failure in the bridge at 24.95 sec with a displacement of 8.176 in. The maximum displacement prior to failure is recorded at 23.21 sec, with a displacement of 9.472 in. A significant number of piles yielded at this point, but the bridge remained stable.

The analysis stopped at 6.37 sec for EQ2 in the transverse direction. The program failed to converge at this time step, which can be linked to an unstable state of the bridge. The transverse component of EQ3 causes failure in the bridge at 24.80 sec with a displacement of 11.269 in. This failure is further illustrated in Figure 5.5, showing the force-displacement hysteretic curves of the target pile. The failure is brittle since the pile behavior is fairly elastic until sudden inelastic deformation occurs followed by immediate failure.

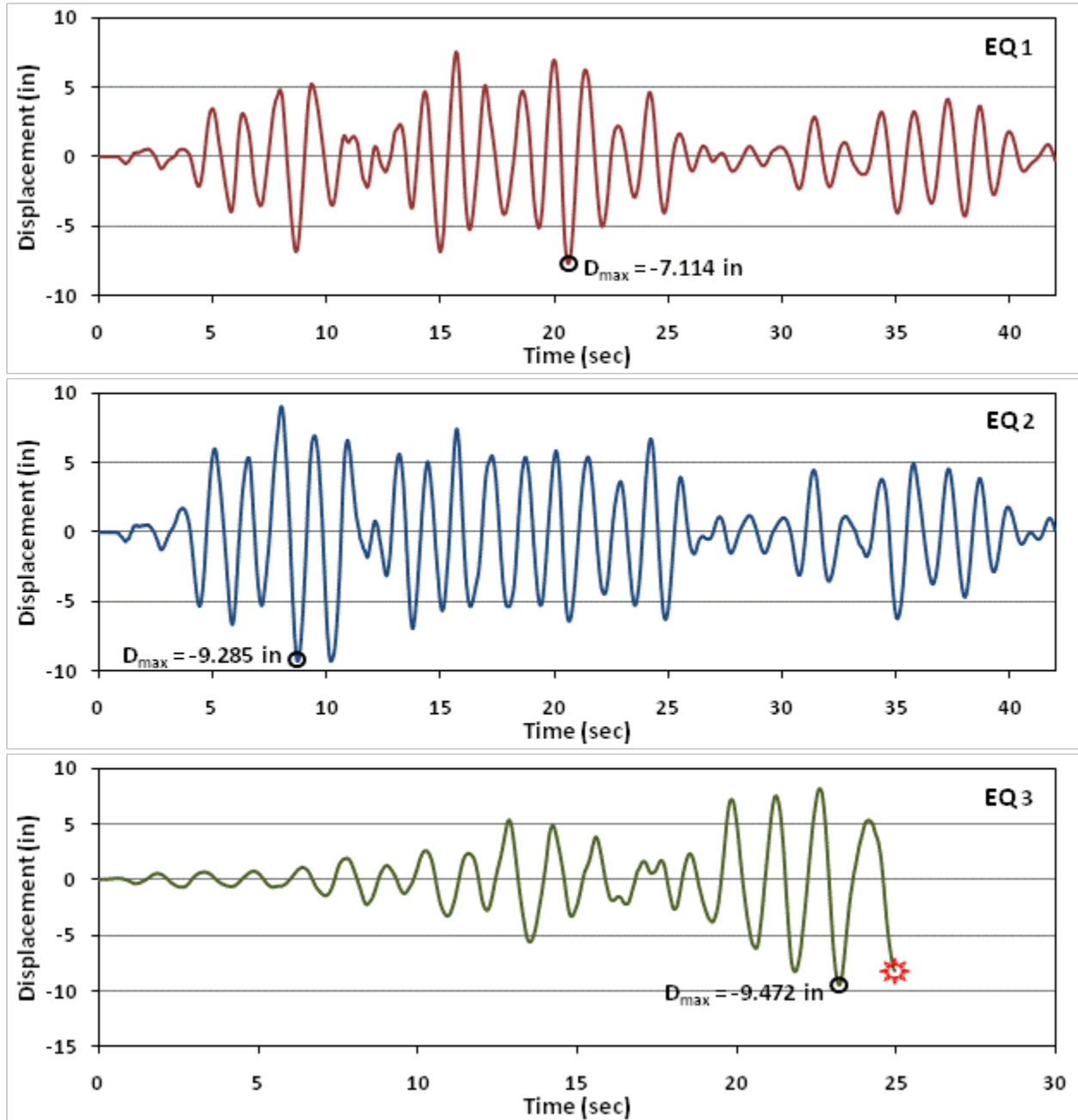


Figure 5.3 Target column displacement-time history for longitudinal EQs with loose sand

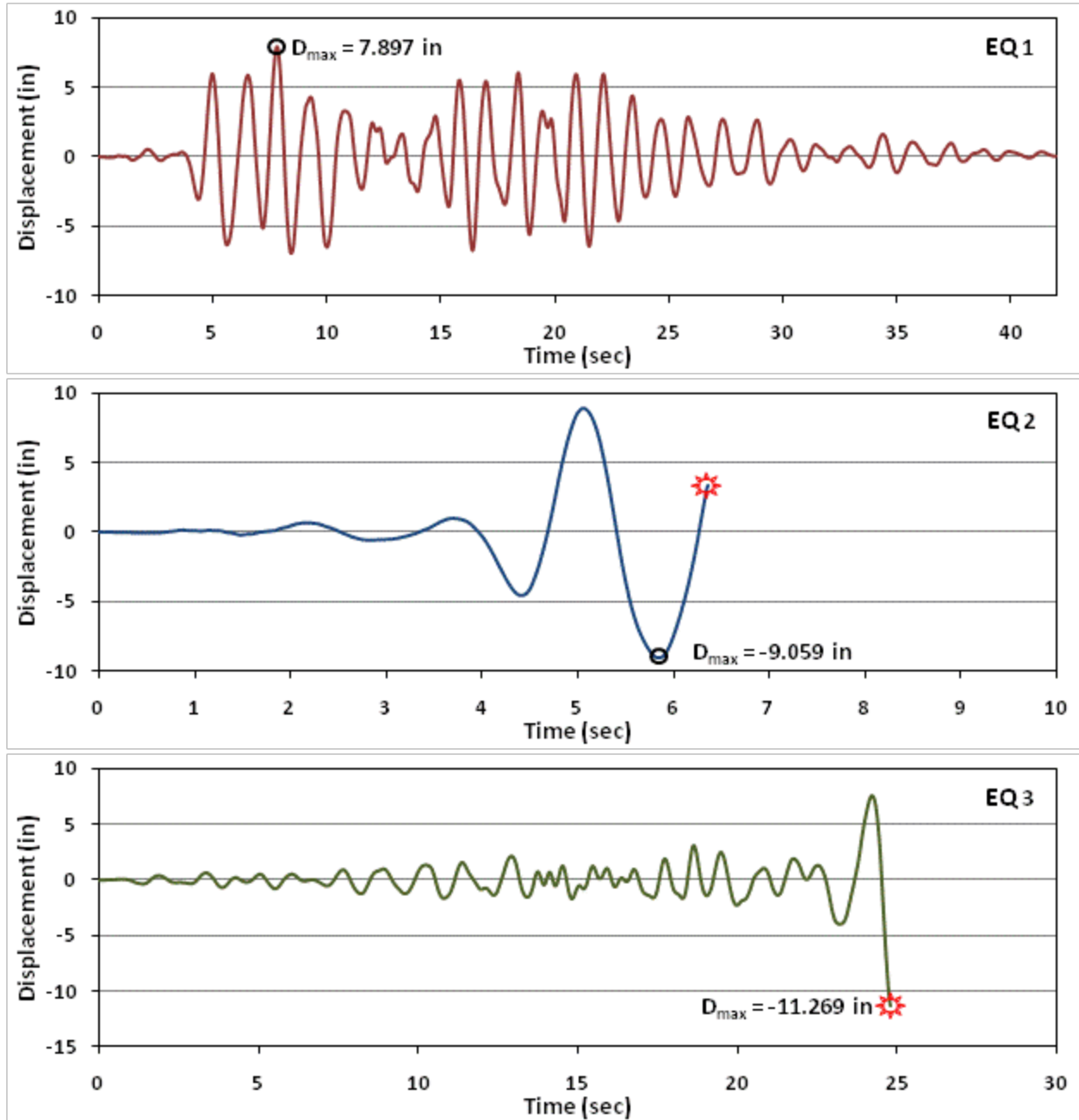


Figure 5.4 Target column displacement-time history for transverse EQs with loose sand

The shear capacity envelopes calculated using UCSD methodology (Appendix C) is presented as the dashed lines in Figure 5.5. As shown for EQ2 and EQ3, the pile failed in shear.

For all cases, the pile maximum shear value is close to or crosses the shear capacity envelope. Considering that the UCSD methodology was only proposed for reinforced concrete

columns and not prestressed hollow piles, it is not safe to rule out the possibility of brittle shear failure in the piles.

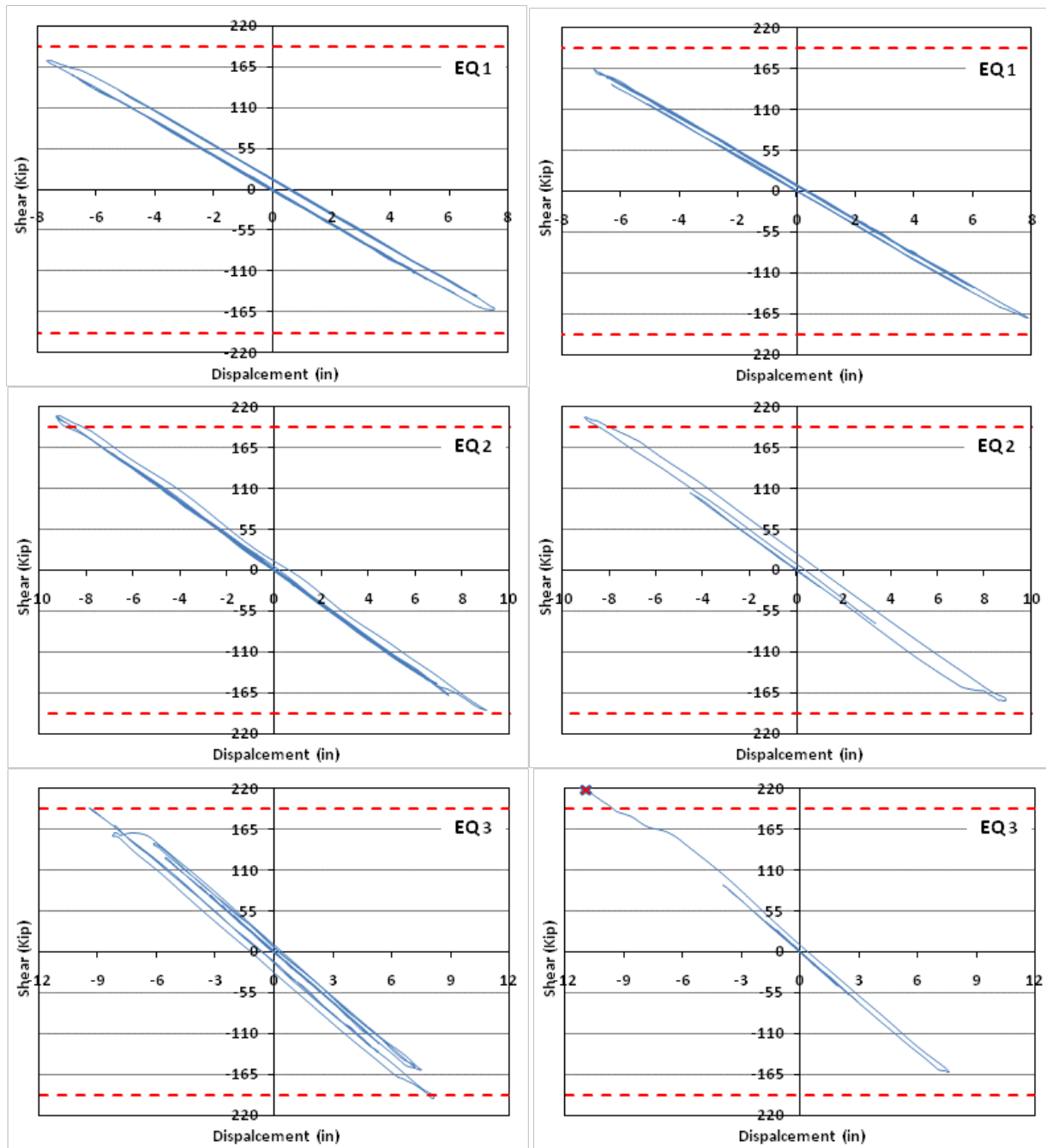


Figure 5.5 Force-Displacement hysteresis curves of the target column in the longitudinal (left) and transverse (right) direction with loose sand

5.2. DENSE SAND

Dense sand represented the most conservative scenario out of the soil types investigated during this research. Figure 5.6 and Figure 5.7 show the yielded piles in the bridge under the given earthquakes and directions. Circled in these figures are columns that suffered a rotational demand higher than their plastic rotational capacity. The three earthquakes have a more severe effect on the bridge in the transverse direction compared to the longitudinal direction. The bridge failed in the transverse direction for all earthquakes. In the longitudinal direction, the bridge failed under the effect of EQ3. However, the number of columns that yielded was higher in the longitudinal direction compared to the transverse direction.

25% and 39% of the piles developed plastic hinges under EQ1 in the longitudinal and transverse directions, respectively. Four columns failed as they were subjected to a rotational capacity exceeding their rotational capacity in the transverse direction under EQ1, and none did in the longitudinal direction. Under the effect of EQ2, 29% and 37% of the piles developed plastic hinges in the longitudinal and transverse direction, respectively. 13 piles failed in the transverse direction while none failed in the longitudinal direction. Under the effect of EQ3, 73% and 41% of columns developed plastic hinges in the longitudinal and transverse directions, respectively. One pile and 11 piles failed in the longitudinal and transverse directions, respectively.

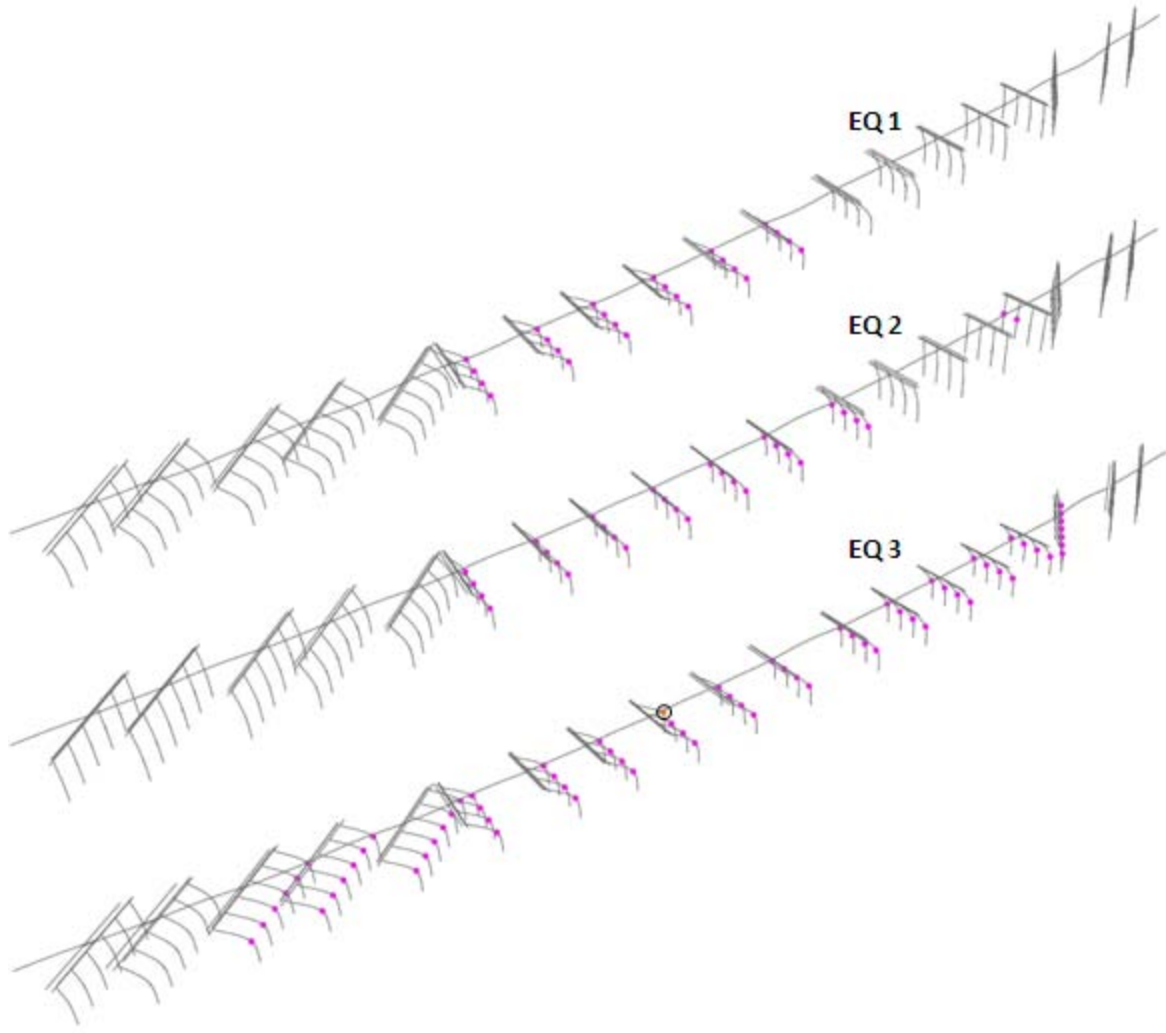


Figure 5.6. Hinge development for EQs in the longitudinal direction with dense sand

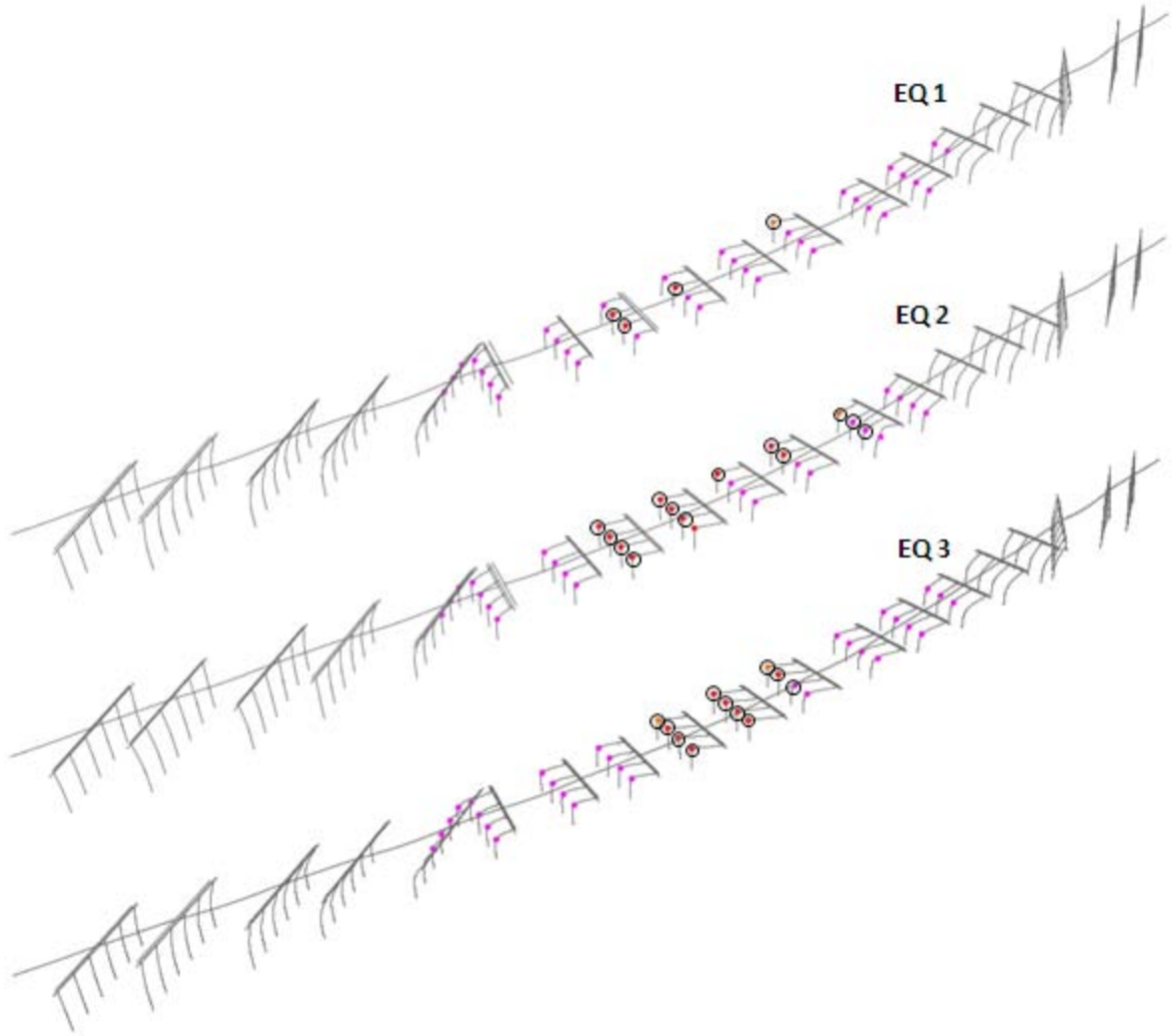


Figure 5.7. Hinge development for EQs in the transverse direction with dense sand

The first piles in Bent10, from the east side, consistently suffered high displacement and forces compared to the other piles for all analysis cases. The joint at the top of this pile was monitored to plot the displacement-time history results.

The displacement in the global X and Y-directions were plotted versus time in Figure 5.8 and Figure 5.9 for the longitudinal and transverse earthquake direction, respectively. The bridge failed at 24.11 sec for EQ3 in the longitudinal direction with a recorded displacement of 5.25 in. The bridge fails in the transverse direction at 17.11 sec for EQ1, at 16.24 sec for EQ2, and at 24.68 sec for EQ3 with a recorded displacement of 4.921 in., 7.048 in., and 6.320 in.,

respectively. The force-displacement hysteretic curves of the target pile are shown in Figure 5.10. The shear demand in dense sand is less than in loose sand. The failure observed from the hysteretic curves is also less brittle. Maximum shear values reach an average of 148 kips, considering both directions.

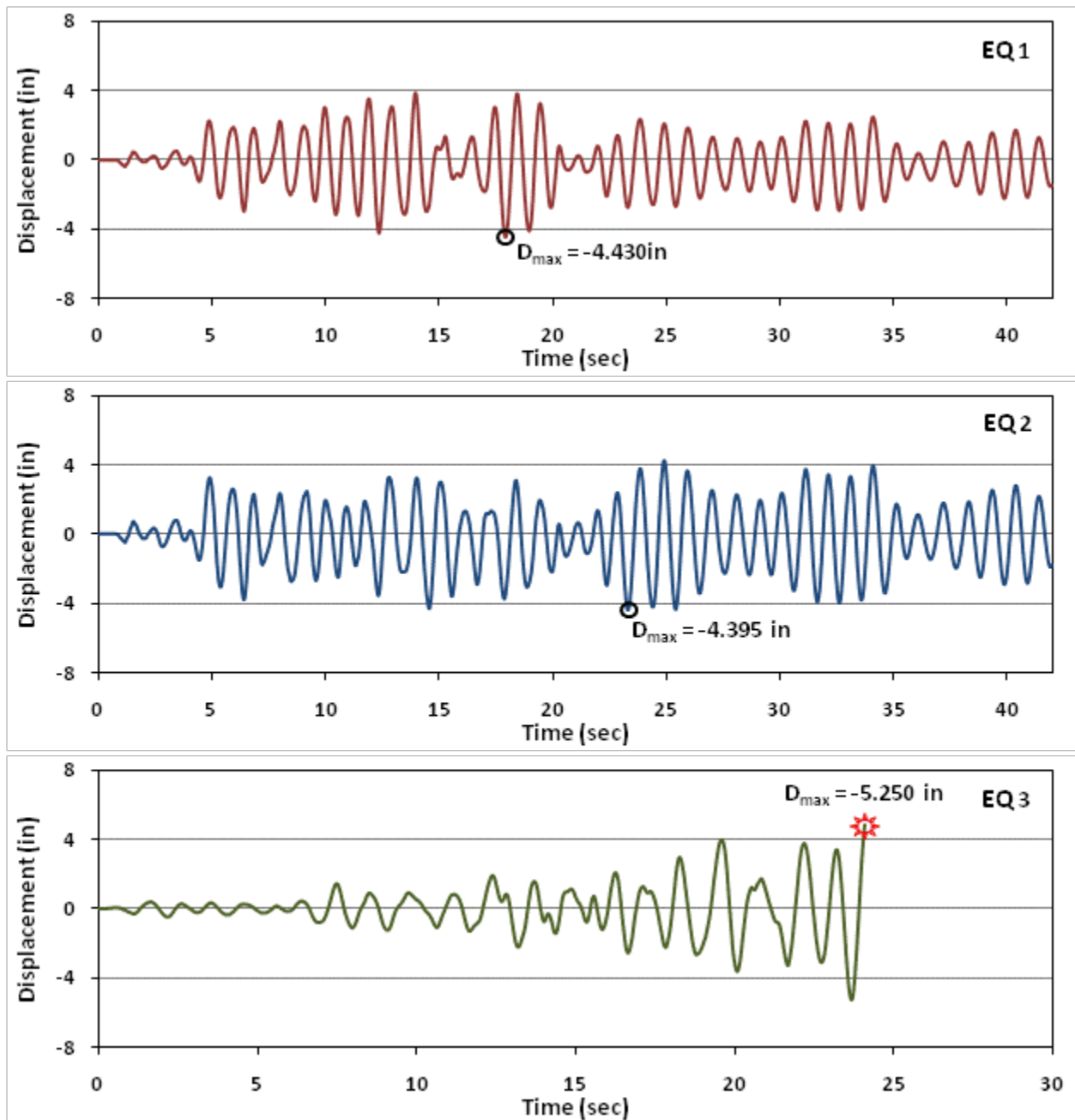


Figure 5.8. Target column displacement-time history for longitudinal EQs with dense sand

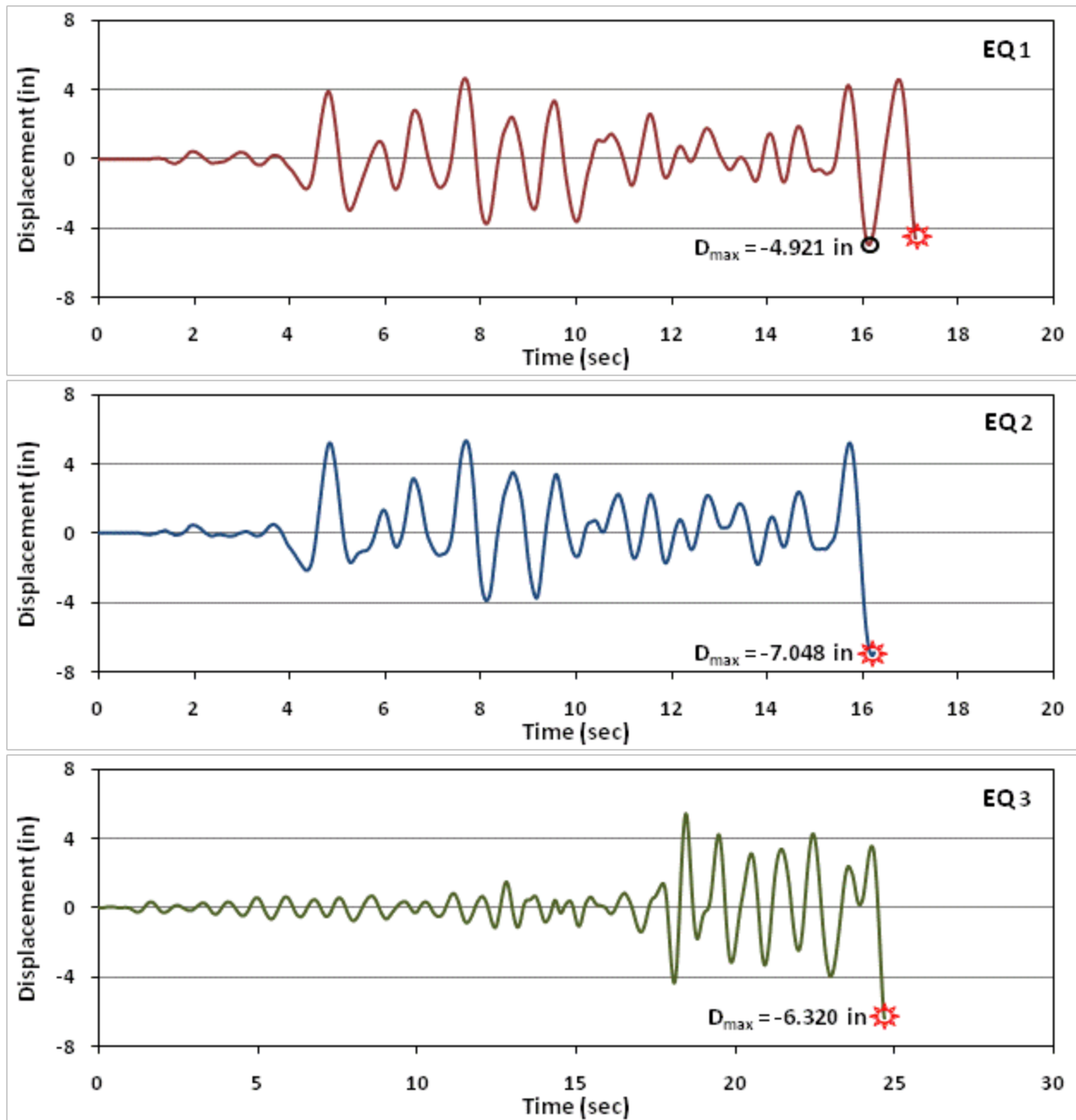


Figure 5.9. Target column displacement-time history for transverse EQs with dense sand

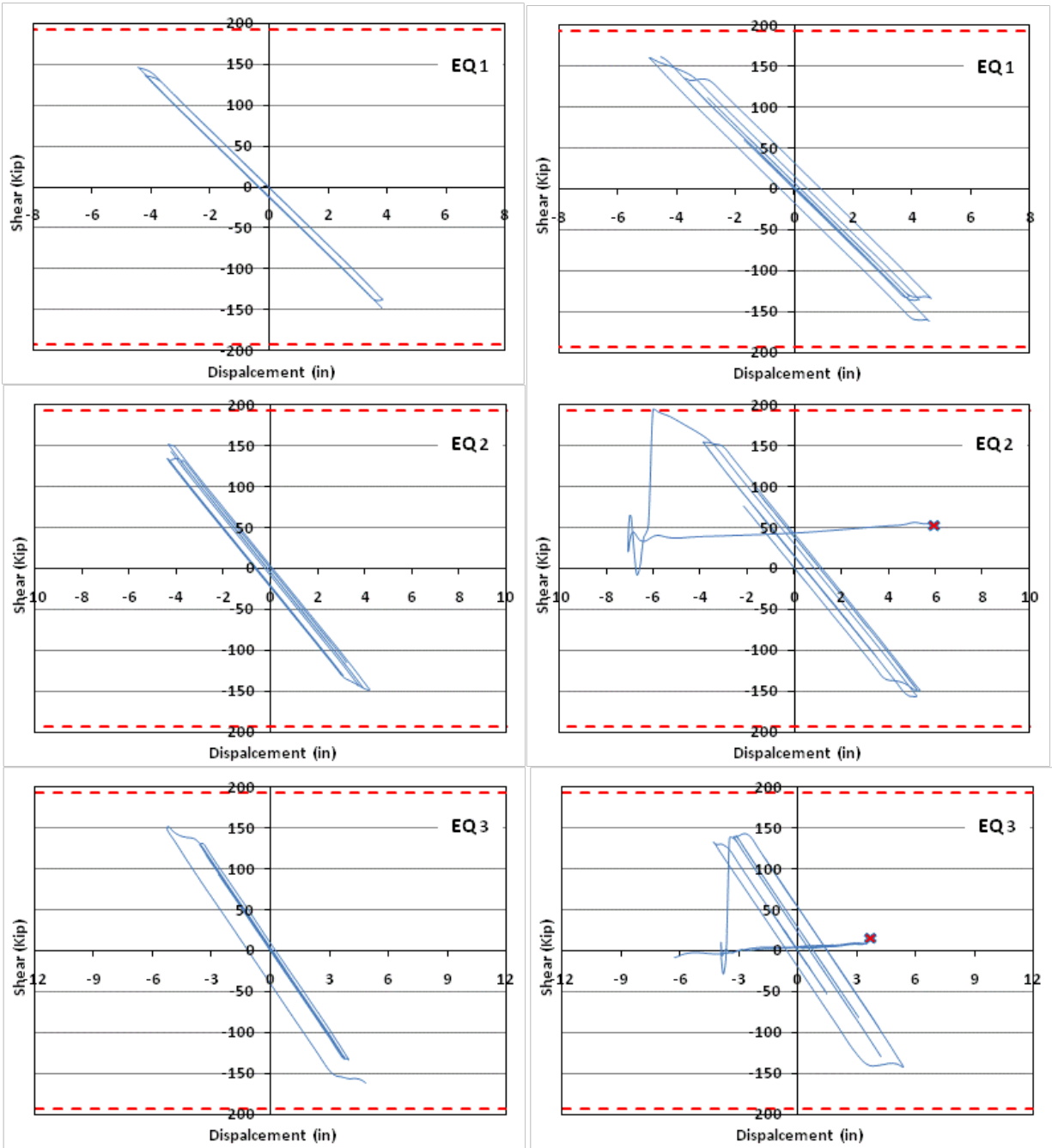


Figure 5.10. Force-Displacement hysteresis curves of the target column in the longitudinal (left) and transverse (right) direction with dense sand

5.3. STIFF CLAY

Figure 5.11 and Figure 5.12 are show which piles in the bridge exceeded their yielding capacity under the given earthquake and direction. The bridge behaved elastically for EQ1 and EQ2 in both directions. Under the effect of EQ3, 34% and 33% of the piles developed plastic hinges in the longitudinal and transverse directions, respectively. Three of the columns failed in the transverse direction for EQ3 (circled in Figure 5.12).

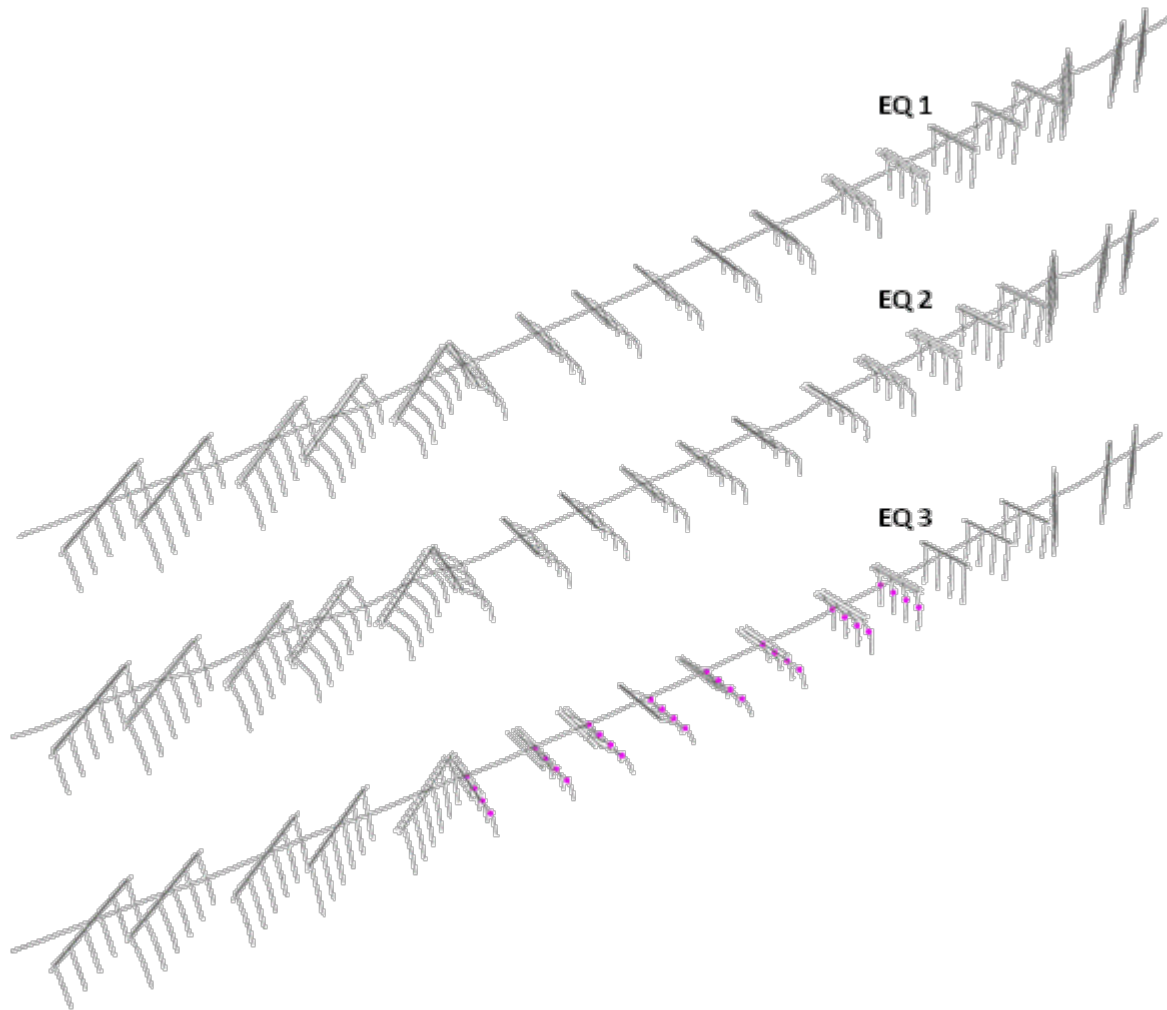


Figure 5.11. Hinge development for earthquakes in the longitudinal direction with stiff clay

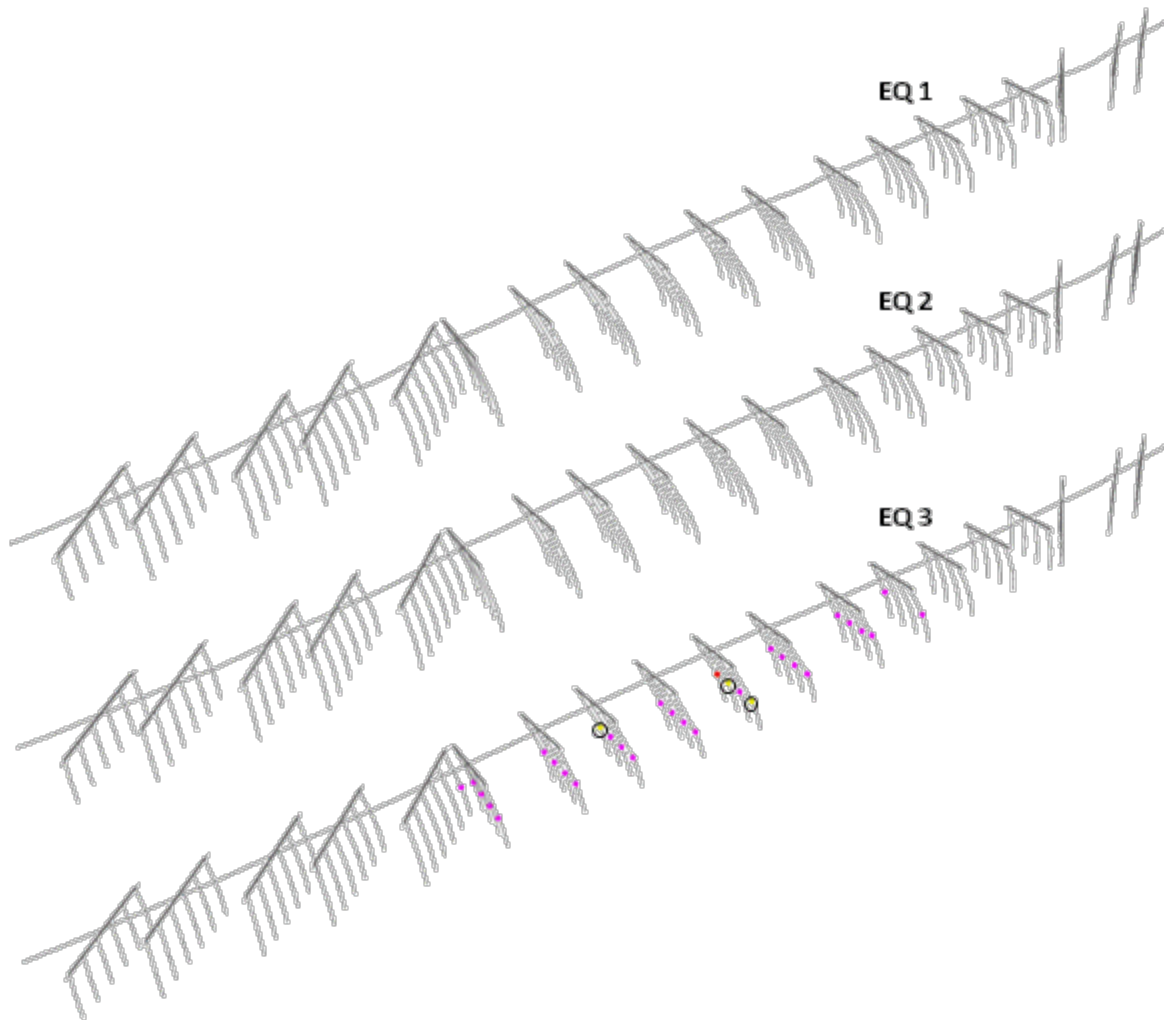


Figure 5.12. Hinge development for earthquakes in the transverse direction with stiff clay

Although none of the columns failed in the longitudinal direction for EQ3, the analysis failed to converge at 49.72 sec, as shown Figure 5.13. The maximum displacement recorded prior to that was 9.011 in. In the transverse direction the bridge failed at 37.90 sec and 11.079 in. displacement for EQ3, as shown in Figure 5.14. Maximum recorded displacements for EQ1 and EQ2 can be found in Figure 5.13 and Figure 5.14. The force-displacement hysteresis plots in Figure 5.15 show that there was a very low shear demand on the columns. It is safe to say that the columns will not have brittle shear failure if the bridge is founded on stiff clay. Based on the results of this section, stiff clay is the least conservative soil model for the bridge.

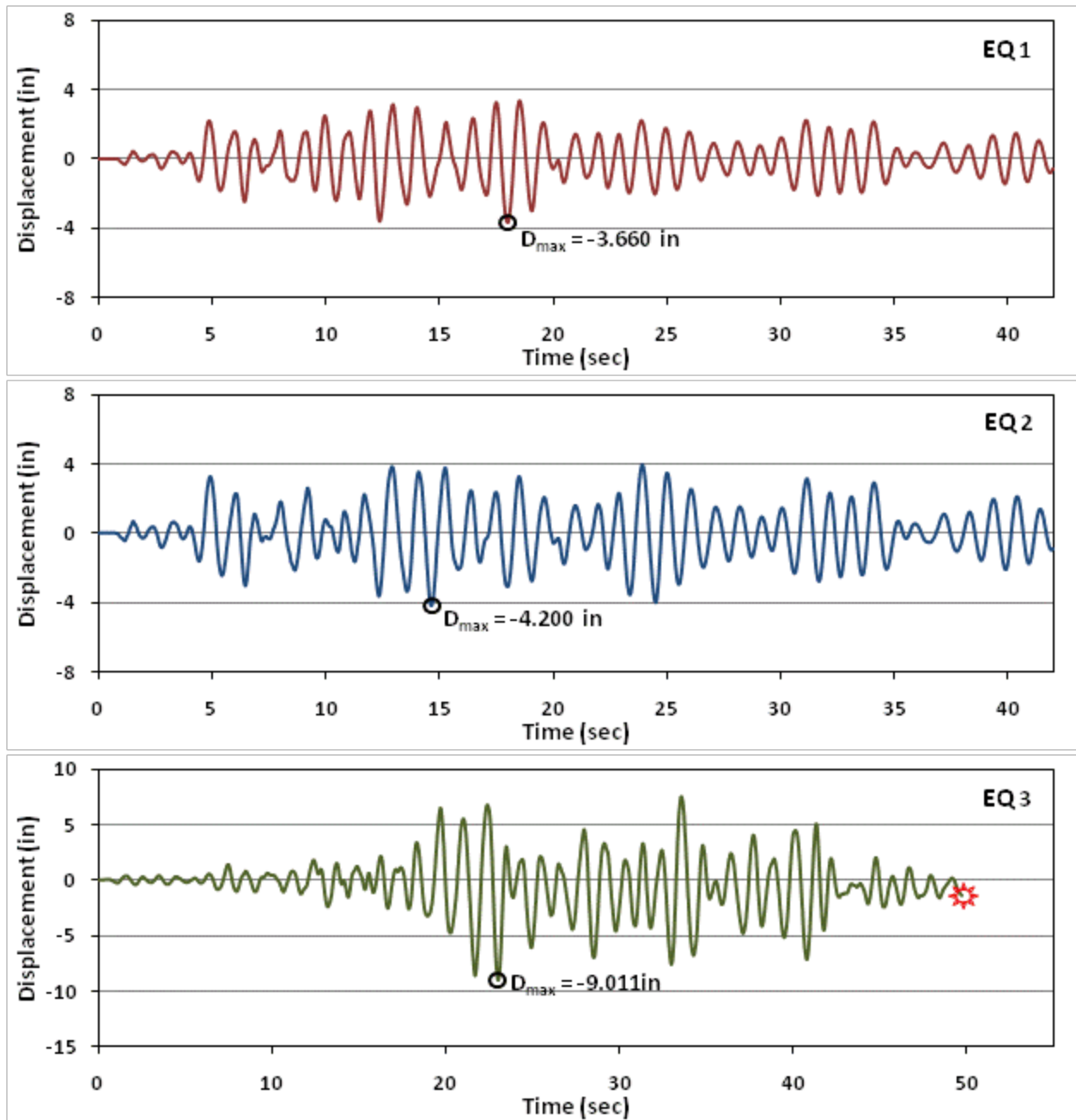


Figure 5.13. Target column displacement-time history for longitudinal EQs with stiff clay

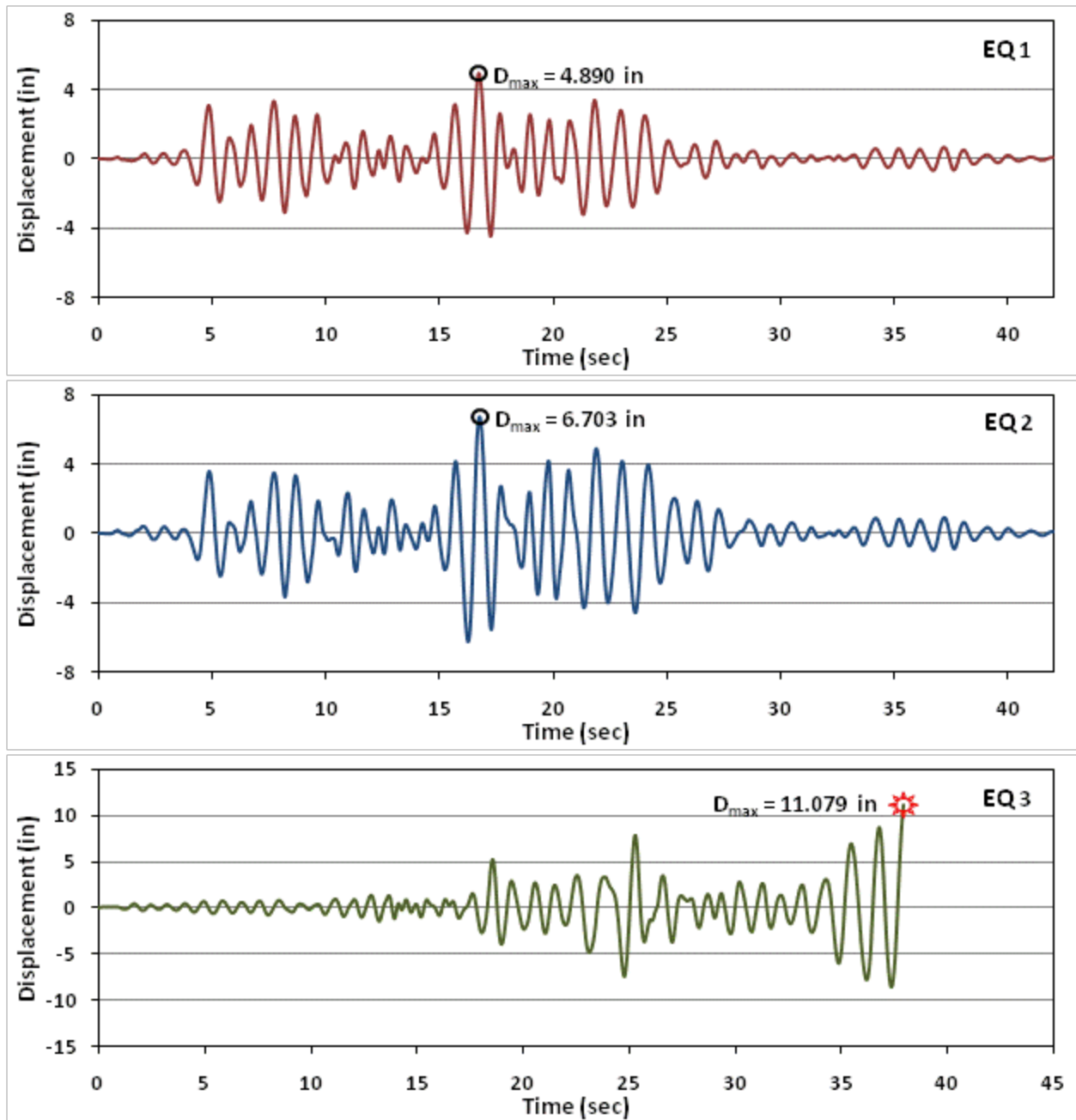


Figure 5.14. Target column displacement-time history for transverse EQs with stiff clay

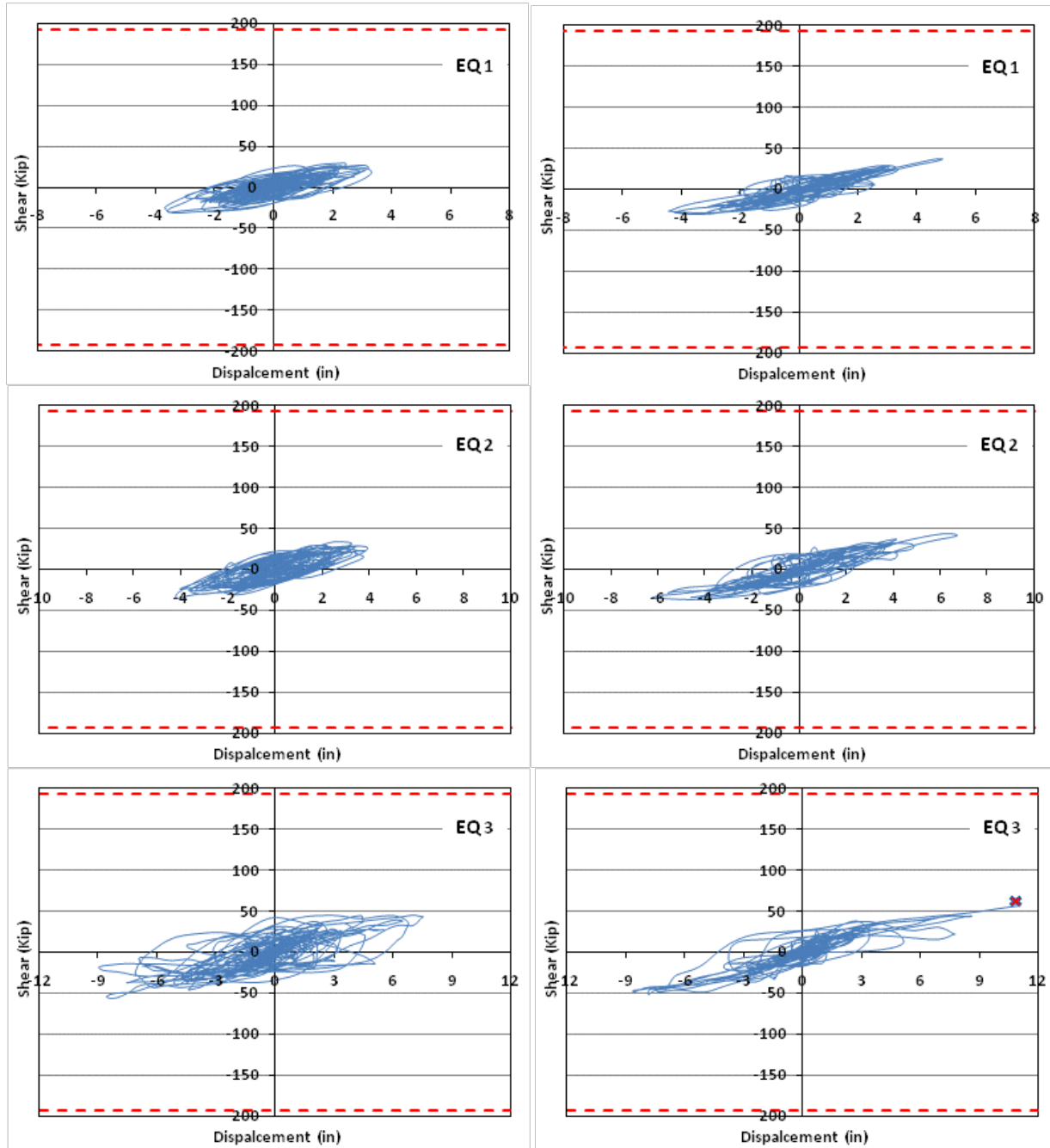


Figure 5.15. Force-Displacement hysteresis curves of the target column in the longitudinal (left) and transverse (right) direction with stiff clay

CHAPTER 6: NONLINEAR STATIC ANALYSIS RESULTS

A pushover analysis first requires a frequency analysis, as lateral accelerations are applied in proportion to the fundamental modal shape (standard eigenvalue analysis). For loose sand, and by neglecting second-order effects, the longest-periods in the longitudinal and transverse directions were 1.366, and 1.322 seconds, respectively. The mode for the longest period in the longitudinal direction has a Modal Participation Mass Ratio (MPMR) of 52.81% and 0% in the transverse direction. The mode for the longest period in the transverse direction has a MPMR of 54.87% of the system mass in the transverse direction and 0% in the longitudinal direction. Ninety-five modes of vibration are employed to reach over 90% mass participation in the two principal directions. Figure 6.1 shows the top four modes based on MPMR values in both principal directions.

Separate pushover analysis was performed in the longitudinal and transverse direction of the bridge. Since the bridge is not symmetric, analysis was carried out for both positive and negative transverse directions. The lateral acceleration thus obtained was applied to all model nodes in proportion to the respective longest-period modal shapes. Structure displacements were read with respect to the deck displacement at the location of the most critical pier (in terms of maximum plastic rotation). It is clear, that to identify the critical pier in each case (in order to construct the pushover curve with respect to its location), a preliminary pushover analysis of the structure is required.

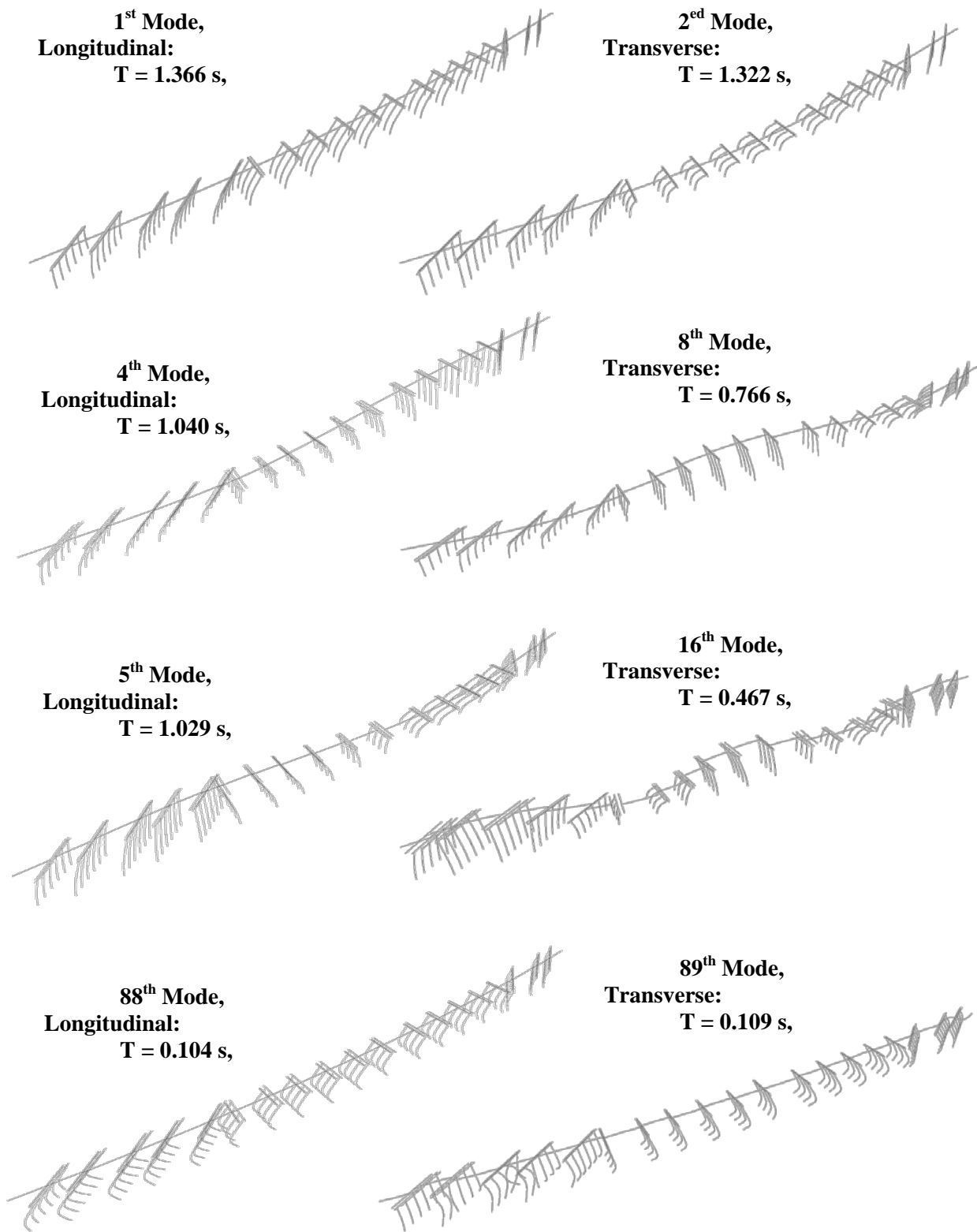


Figure 6.1 Four highest MPMRs in longitudinal and transverse direction of the bridge

The analysis of the lateral capacity of the bridge ended when the first plastic hinge reached its rotation capacity. This condition is shown in Figure 6.2 and Figure 6.3 for the transverse and longitudinal directions, respectively. In these figures plastic hinges are represented by dots, and the hinging sequence is numbered. The piers that reached their ultimate rotational capacity are circled. The piles of the center bents experienced the first yielding and ultimately failed for both longitudinal and transverse pushover analyses.

The capacity curves for the pushover analyses are shown in Figure 6.4. The dots describe the main phases of plastic hinging according to the hinge numeration of Figure 6.2 and Figure 6.3. The transverse capacity curves have very similar characteristics. The Ultimate Limit State (ULS) displacement and the first yielding displacement exhibited less than 2% difference between the two transverse directions capacity curves. Based on these results, it was decided to continue the analysis considering only one transverse direction.

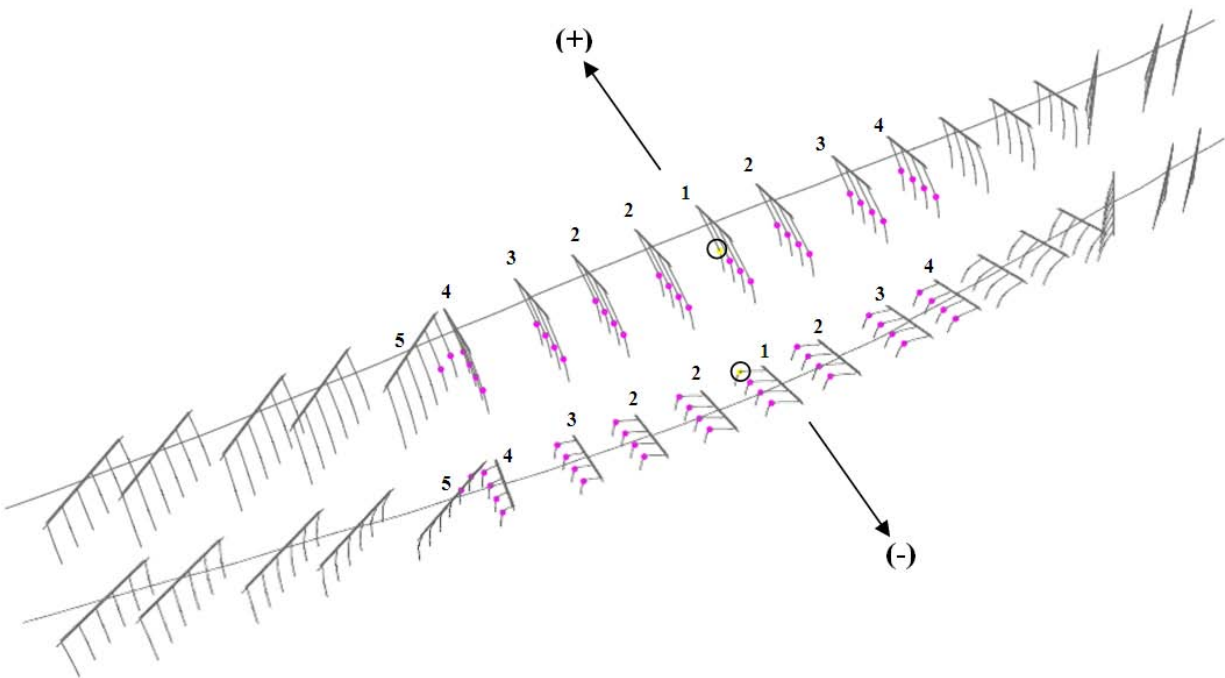


Figure 6.2 Hinging sequence up to transverse ultimate limit state condition

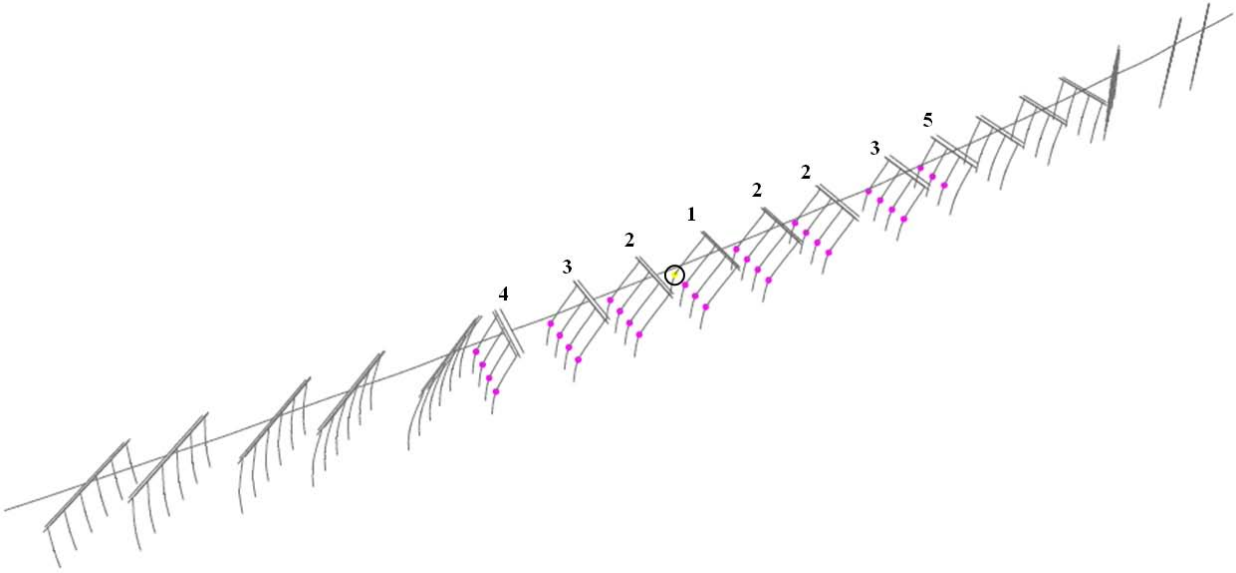


Figure 6.3 Hinging sequence up to longitudinal ultimate limit state condition

The initial stiffness in the transverse direction is 5.9% higher than the initial stiffness in the longitudinal direction as shown in Figure 6.4. The post yielding stiffness in both directions is about the same. 64% and 61% of the piles in the transverse and longitudinal directions, respectively, respond elastically until the bridge reached its ULS. The displacement capacity for both directions was approximately equal. However, the transverse direction reached this displacement at a strength 8.7% higher than the strength of the longitudinal direction.

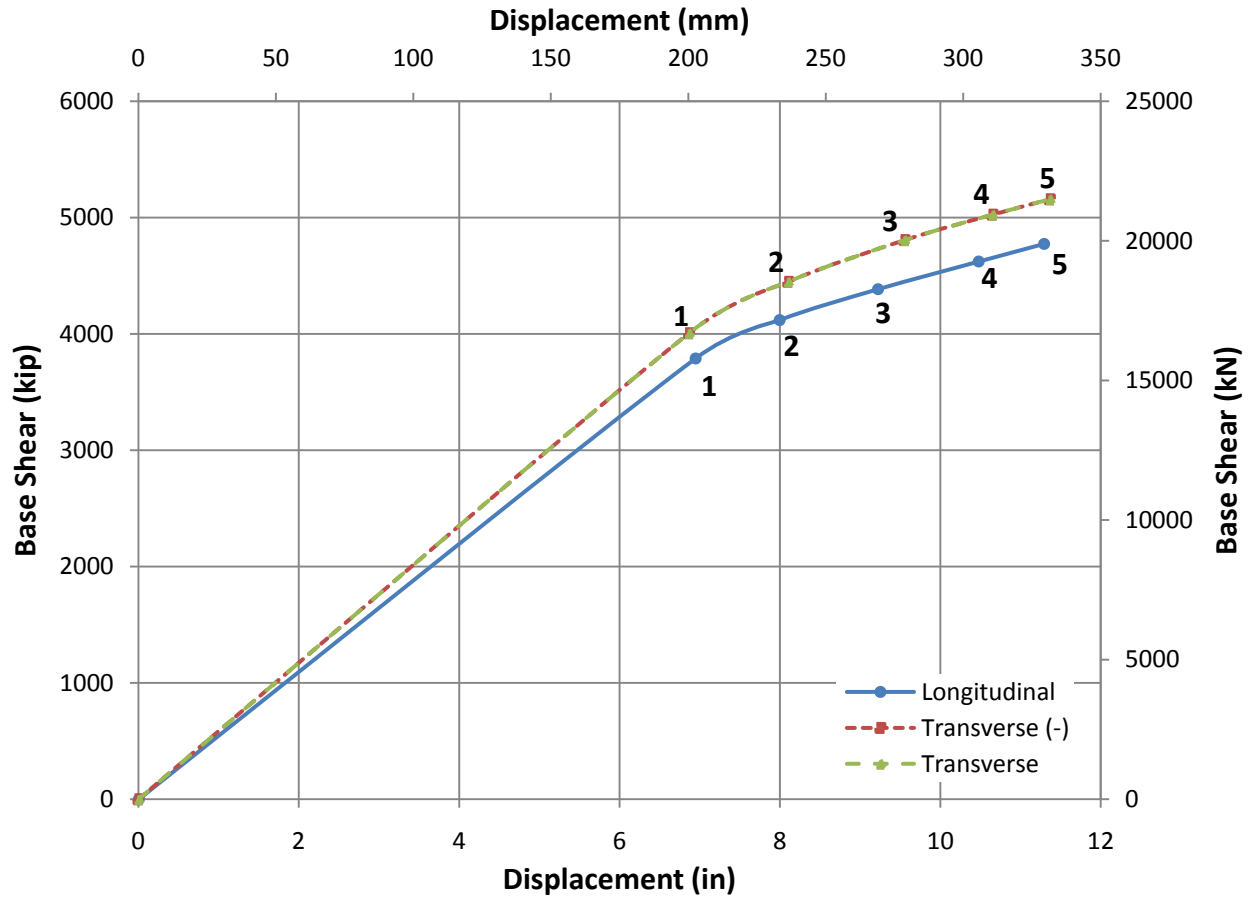


Figure 6.4 Capacity curves for longitudinal and transverse directions

ζ_{eff} and T_{eq} were calculated using Equations C.4 and C.9, respectively, for the longitudinal and transverse directions (Figure 6.5 and Figure 6.6). As shown in the figures, both ζ_{eff} and T_{eq} increased with increased bridge lateral displacement. At ULS (Figure 6.5), the transverse direction reached ζ_{eff} of 8.57% while the longitudinal direction reached only 7.43%. At ULS (Figure 6.6), the effective fundamental period increased by approximately 12.75% and 9.56% in the transverse and longitudinal directions, respectively. ζ_{eff} and T_{eq} increased in the transverse direction more than the longitudinal direction due to the larger reduction in the system stiffness resulting from structural deterioration and hinge formation.

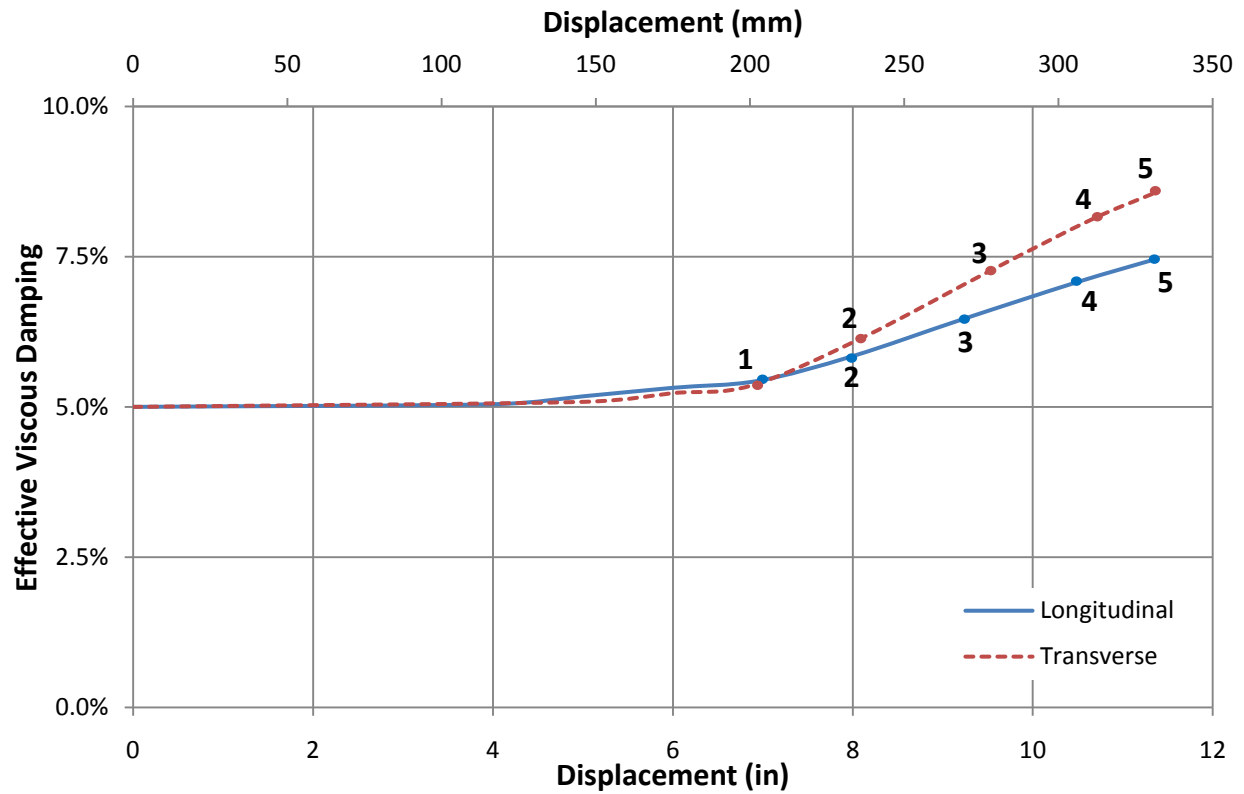


Figure 6.5 Yielding increase in effective viscous damping

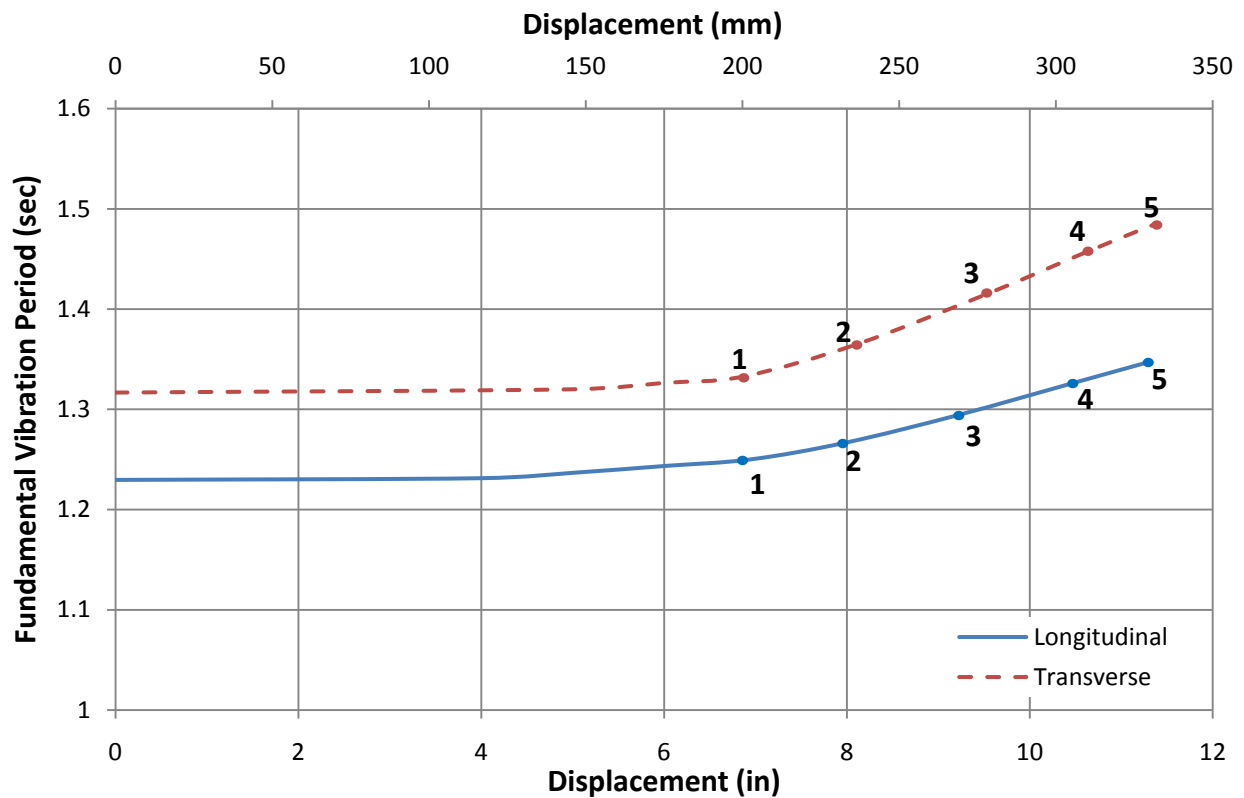


Figure 6.6 Influence of yielding on the natural period

6.1. SECOND-ORDER EFFECTS OF GEOMETRIC NONLINEARITY (P-DELTA)

When the load acting on a structure and the resulting deflections are small enough, the load-displacement relationship for the structure is linear. In this case, the equilibrium equations are formed according to the undeformed geometry of the structure and are independent of the applied load and the resulting deflection, and the results of analysis can be superposed.

If the load on the structure and/or the resulting deflections is large, then the load-deflection behavior may become nonlinear. In particular, when large stresses are present within a structure, equilibrium equations written for the original and the deformations are very small. This effect is called geometric nonlinearity, or the P-delta effect.

The manual for SAP2000 (2007) indicates that “an iterative analysis is required to determine the P-Delta axial forces in frame elements.” It explains that the axial force in each of the frame elements is estimated through a preliminary analysis of the structure. Next, considering these axial forces, equilibrium equations are re-solved, which may create different axial forces in the members “if the modified stiffness causes a force re-distribution.” Additional iterations are performed until the axial forces and deflections converge with a tolerance of 0.01.

The pushover analyses were repeated taking into considerations the P-delta effects. The results show that P-Delta effects were minimal for this bridge. The capacity curves including P-delta effect are shown in Figure 6.7 and Figure 6.8 for the longitudinal and transverse directions. As shown in the figure, the geometric nonlinearity resulted in a decrease in the initial stiffness by 10.5% and 11.2% in the longitudinal and transverse directions. These reductions resulted in slight increase in the fundamental periods of the undamaged structure, from 1.366 to 1.395 seconds (+2.1%) for longitudinal, and 1.322 to 1.350 seconds (+2.1%) for transverse. The

strength capacity decreased in both directions by approximately 6.5%. In the next sections, the P-delta effects were considered during the analysis.

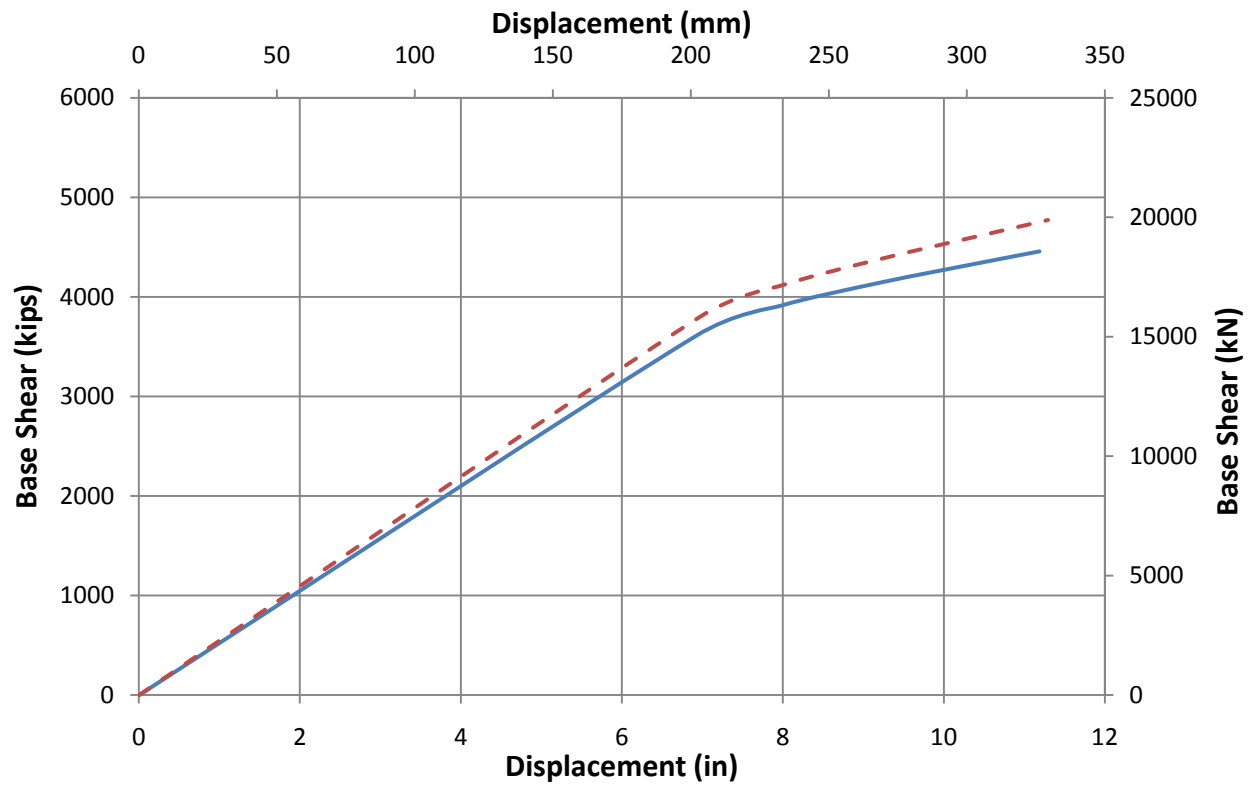


Figure 6.7 Longitudinal capacity curve with (continuous line) and without P-delta effects

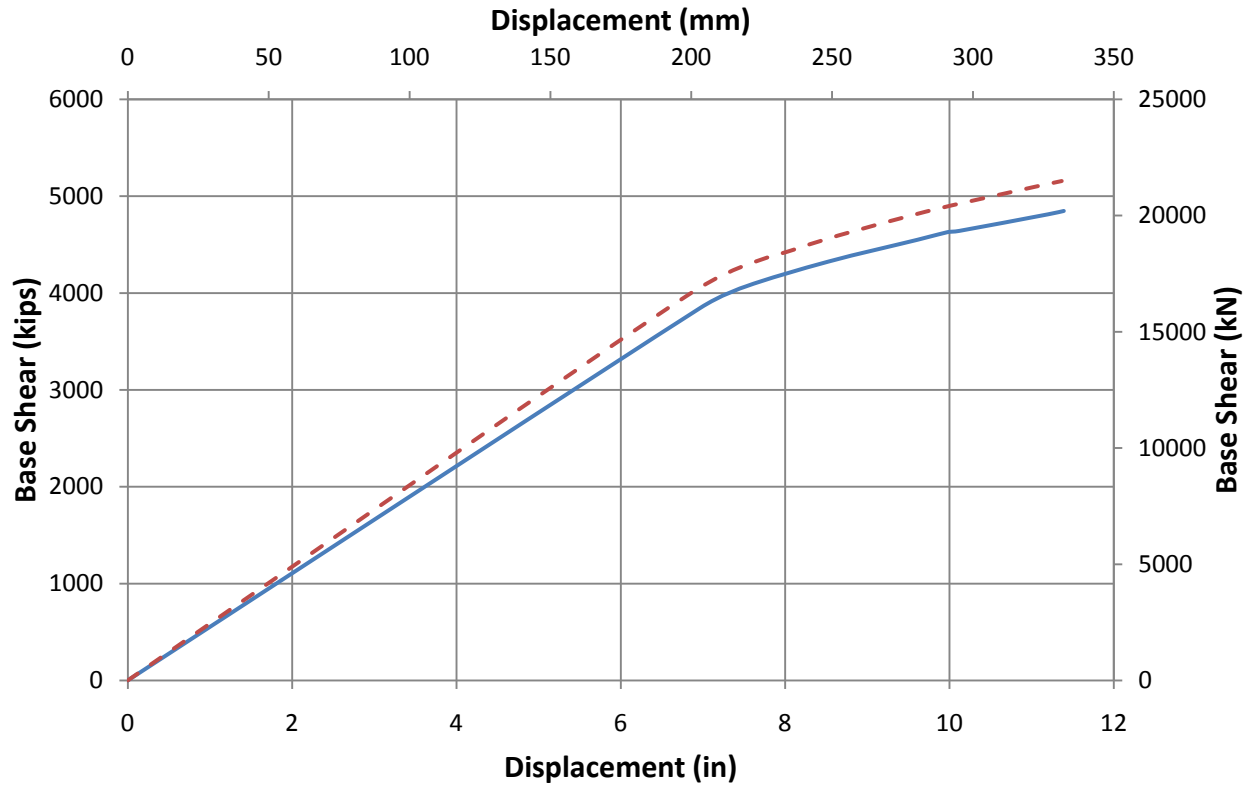


Figure 6.8 Transverse capacity curve with (continuous line) and without P-delta effects

6.2. TARGET DISPLACEMENT FROM NONLINEAR STATIC ANALYSIS

In this section the capacity of the bridge and earthquake demand are used together by the methodology for structural assessment explained in Chapter 3 to obtain the performance point and the corresponding straining actions. Before these methodologies can be applied, the pushover curves were converted to capacity diagrams using the procedure outlined in Section 4.1. The resulting capacity diagrams are presented in Figure 6.9 for both fundamental directions. The obtained performance points are in Acceleration-Displacement format (AD). To convert these points back they are multiplied with the conversion factor Γ .

All the results are tabulated in Table 4.4. Values shown in parentheses are percentage differences from NDA results and the given ductility values are calculated as the ratio of the displacement demand to first yield displacement.

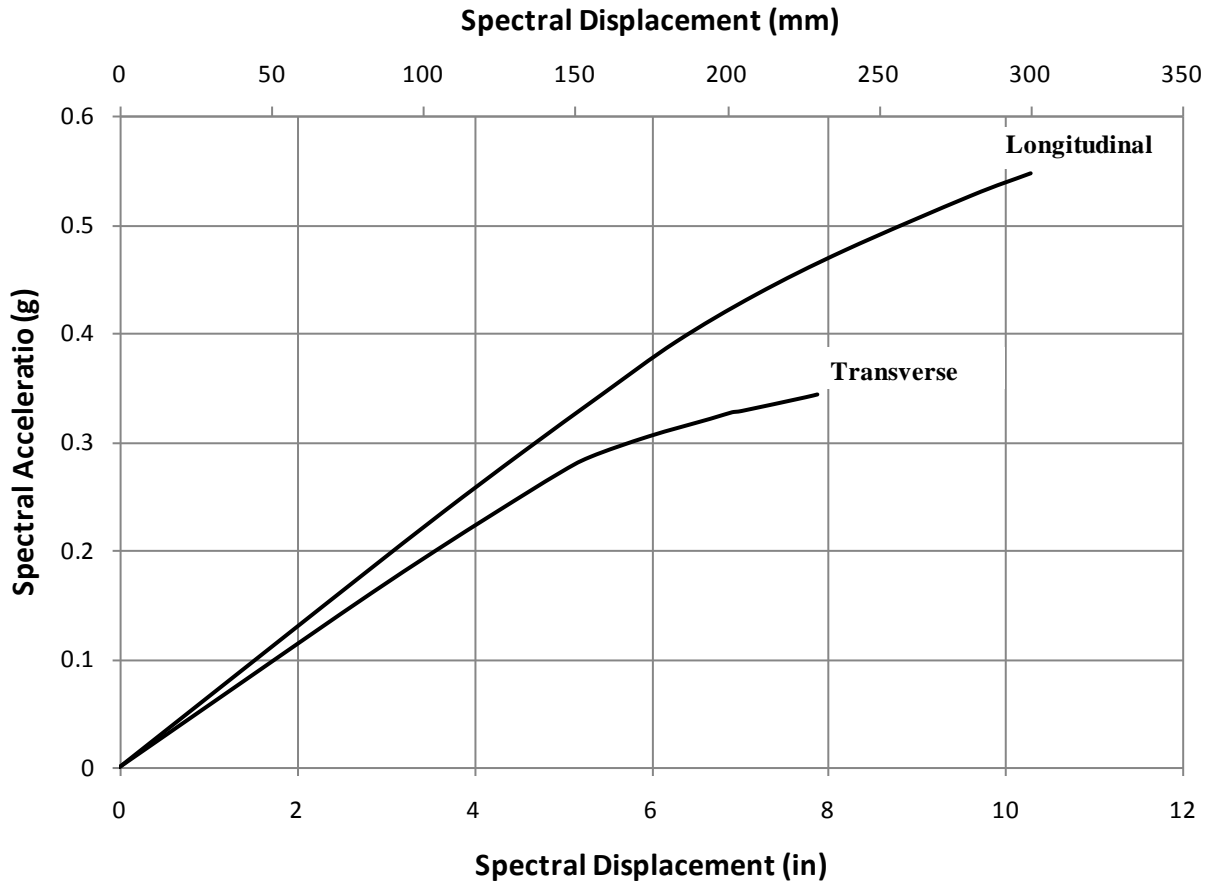


Figure 6.9 Capacity diagrams for both fundamental directions

6.2.1. CAPACITY SPECTRUM METHOD IN ATC-40

This bridge was classified as Type C according to ATC-40. However, since ATC-40 does not provide rigorous definitions for the structural behavior types, results for all three structural behavior types are presented to form a basis for further discussion. Results are shown in Figure 6.10 and Figure 6.11 for the longitudinal and transverse direction, respectively. The results are also tabulated in Table 4.4.

For EQ1 the response of the bridge is elastic. Within the elastic range, the pushover results for all structural types were approximately the same. For EQ3 where the bridge yielded, damping represented by the structural type played a more important rule. Moving from structure

type A to type C, there was an increase in the displacement by 6.1% and 16.7% in the longitudinal and transverse direction, respectively. As a general rule, the more inelastic deformation the structure is expected to undergo, the more important it becomes to pick an appropriate structure type for an ACT-40 CSM.

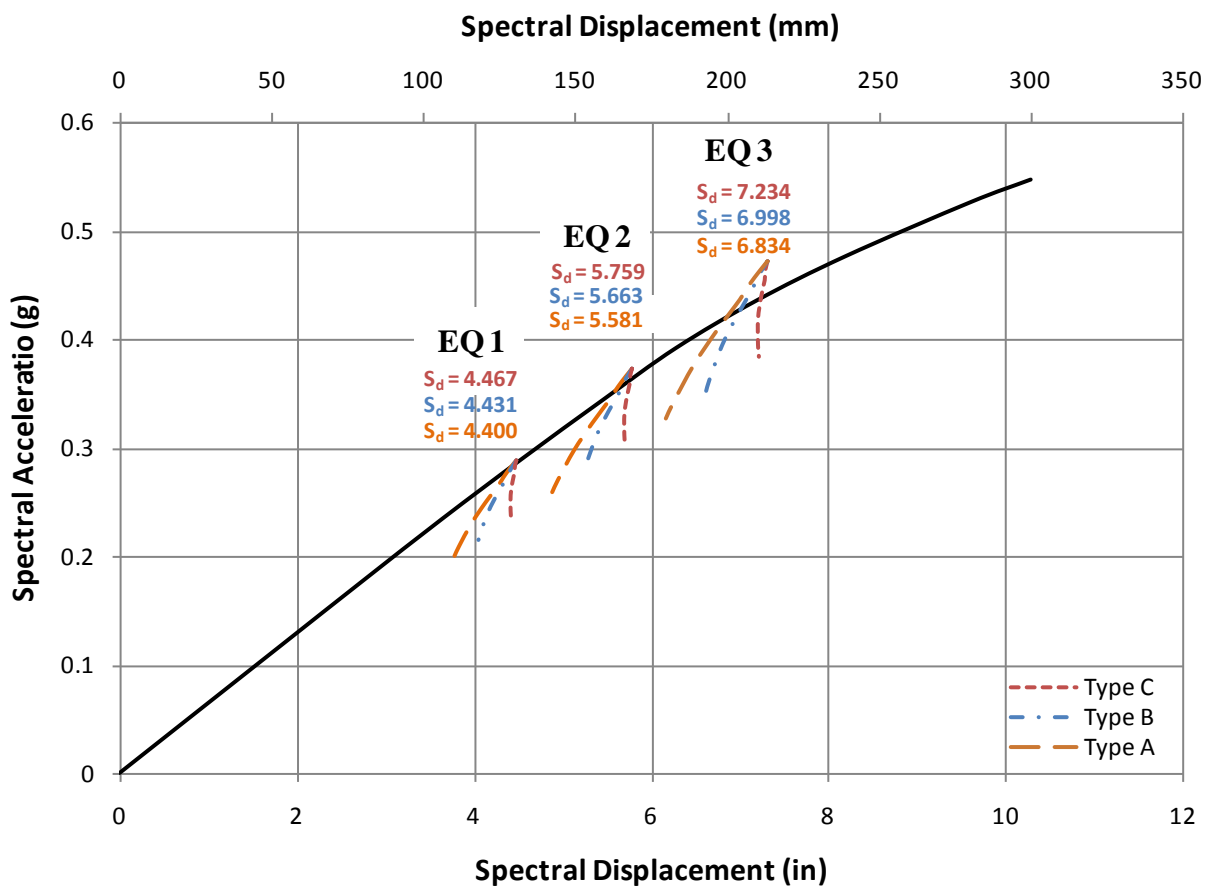


Figure 6.10 Results from CSM in ATC-40 in the longitudinal direction

Comparing NLD results to CSM in ATC-40 showed that CSM in ATC-40 overestimated the displacement demand in the transverse direction and underestimated the displacement demand in the longitudinal direction. For EQ1, difference in estimating the displacement demand was approximately $\pm 30\%$. This difference decreased with increasing the earthquake ground motion. For EQ3, CSM in ATC-40 underestimated the displacement demands by approximately 6 to 19%.

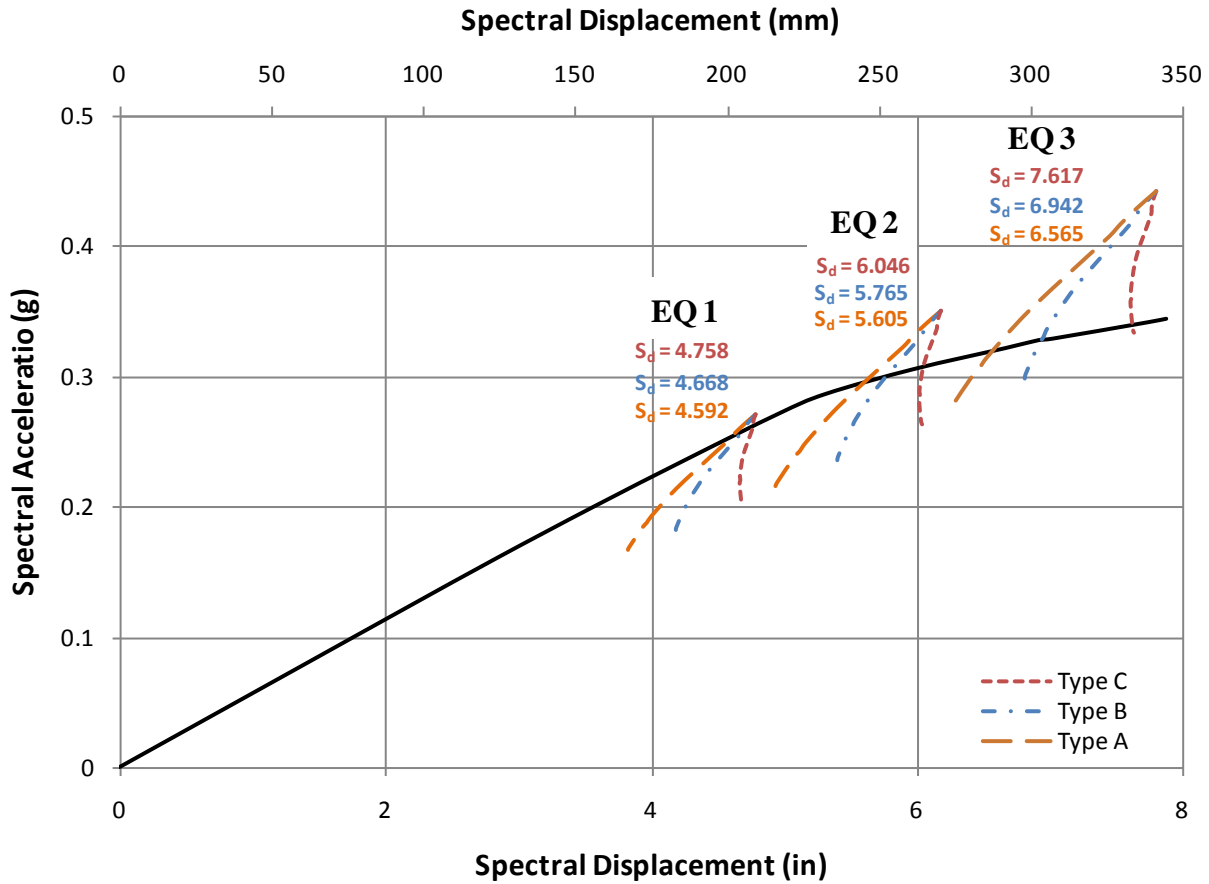


Figure 6.11 Results from CSM in ATC-40 in the transverse direction

6.2.2. IMPROVED CAPACITY SPECTRUM METHOD (FEMA 440)

The improvement suggested by FEMA 440 (2005) on the CSM, proved to be very effective since this method gave consistently the most accurate results compared to NLD. It underestimated the demand displacement for all cases, except for EQ1 in transverse direction (+36%), but the average difference with NDA is 13%. Based on this aspect, the improved CSM gives the best results.

One other positive aspect of the improved CSM is that the structure type is not a factor in the calculations of demand displacement. As proven in the previous section, the structure type has a significant effect on the demand predictions. The measures taken to bypass this factor

might be conservative for most structures, but for this bridge, the improvements suggested by FEMA440 increase the accuracy of demand prediction substantially.

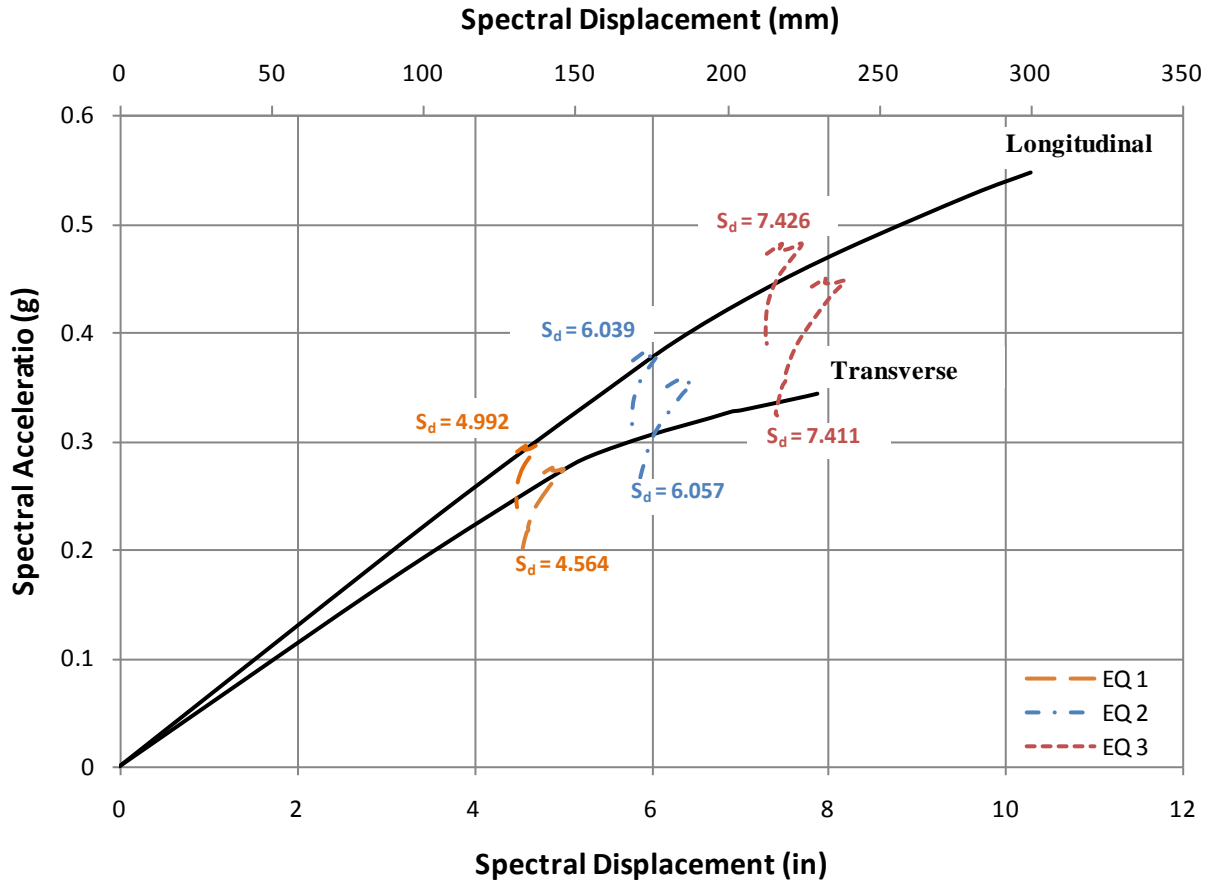


Figure 6.12 Improved CSM results for both fundamental directions

6.2.3. CAPACITY SPECTRUM METHOD WITH INELASTIC DESIGN SPECTRA

As pointed out earlier, when inelastic design spectra are used in CSM, updating the bilinear representation of the capacity diagram depending on the trial performance point is not justifiable due to the incompatibility of the capacity and demand diagrams. In this study, a single elasto-plastic (EP) representation for each of the capacity diagrams (Figure 6.13) was used without any updating during the analysis.

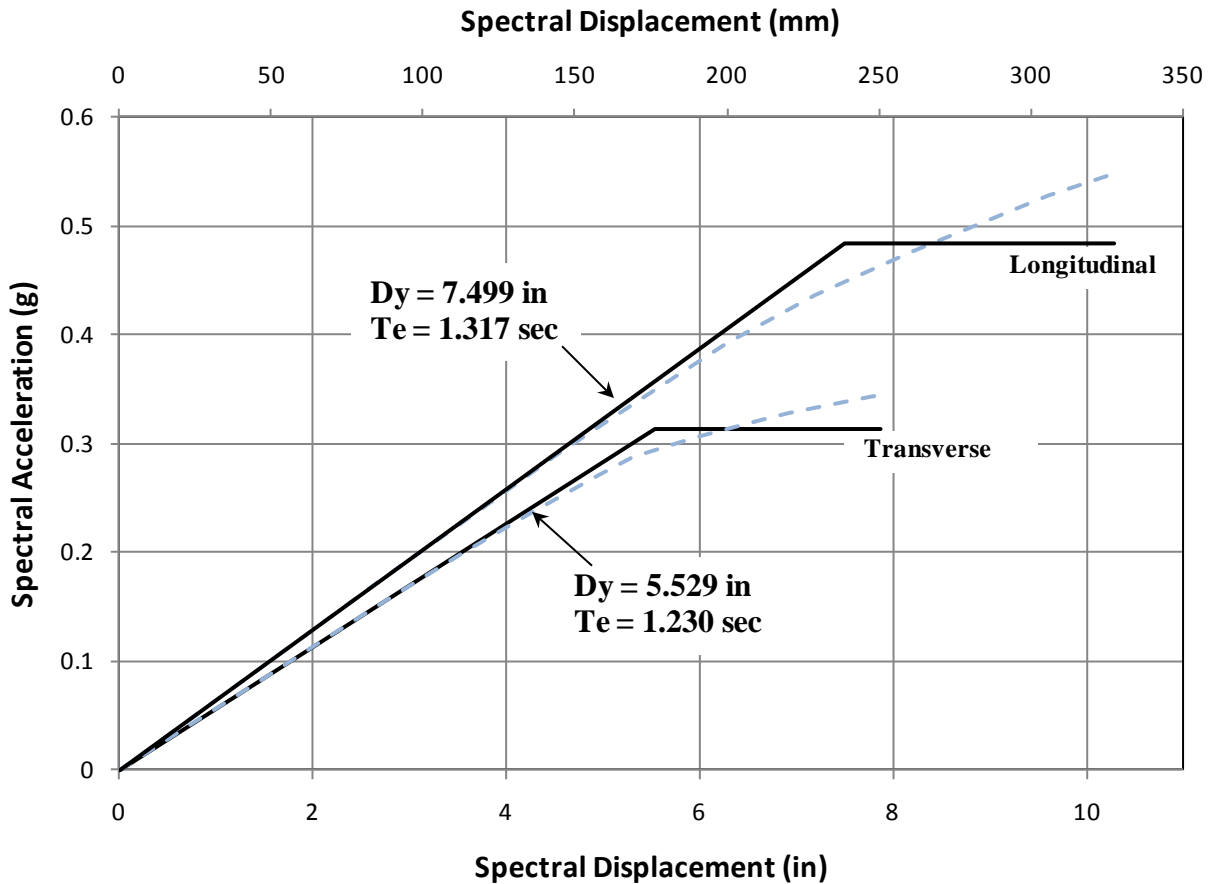


Figure 6.13 Elasto-plastic representations (solid lines) for capacity diagrams (dashed lines) in both fundamental directions

Results for the longitudinal and transverse direction are shown in Figure 6.14 and Figure 6.15, respectively. This version of CSM was less accurate in determining the displacement demand on the bridge compared to CSM in ATC-40. The difference between this version of the CSM and the NDA reached up to 35% in one case. This was mainly attributed to the lack of the possibility of updating the bilinear representation and using single elasto-plastic representations, confirming the importance of this feature of CSM. Using the elasto-plastic representation of the capacity curve added one more source for approximation. Out of the four cases used, the Miranda and Bertero (1994) method offered slightly better results than the other methods.

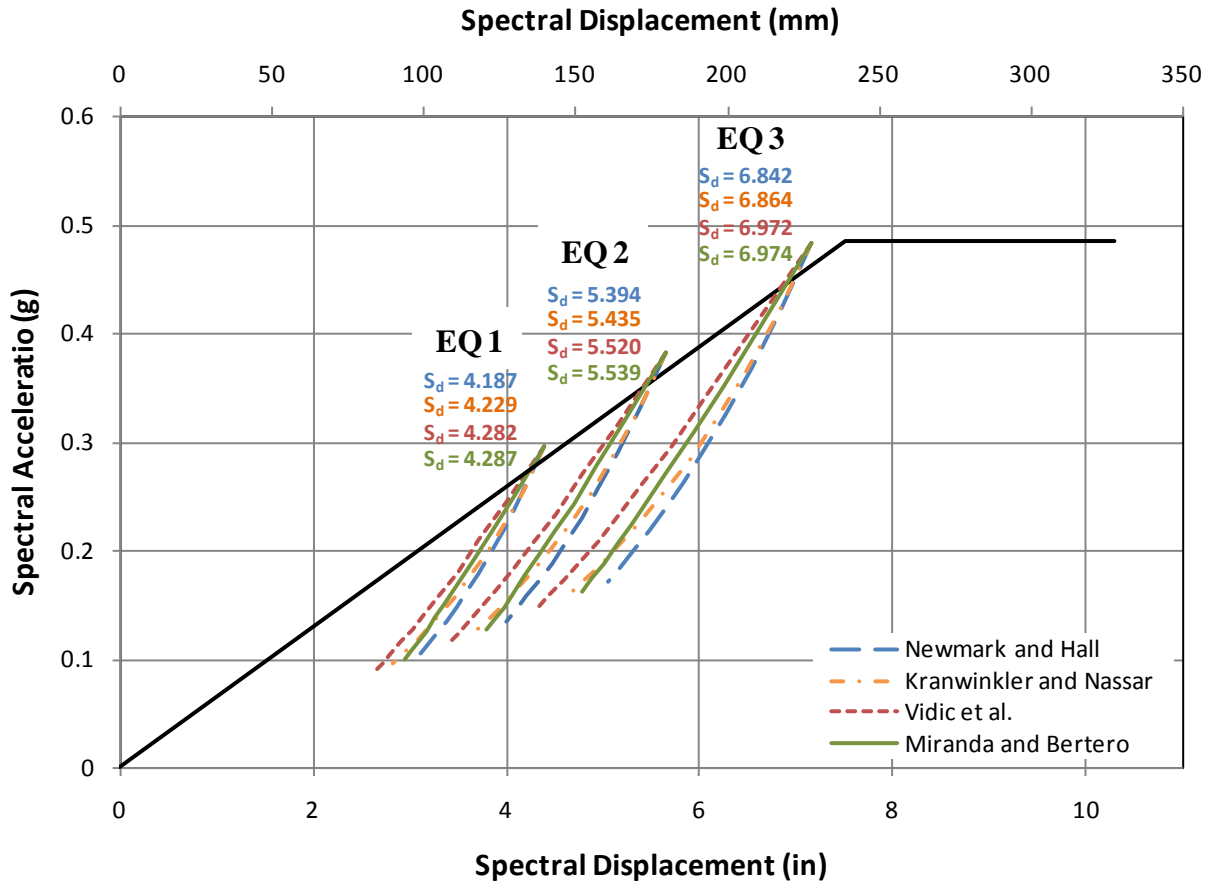


Figure 6.14 Results from CSM with inelastic design spectra for the longitudinal direction

In the light of the above discussions, this version of the CSM was found to be inappropriate for assessment of structures with force-deformation relationships that cannot be idealized using bilinear representation. Unfortunately, this is the case for most of the structures that one may come across in practice, including this bridge.

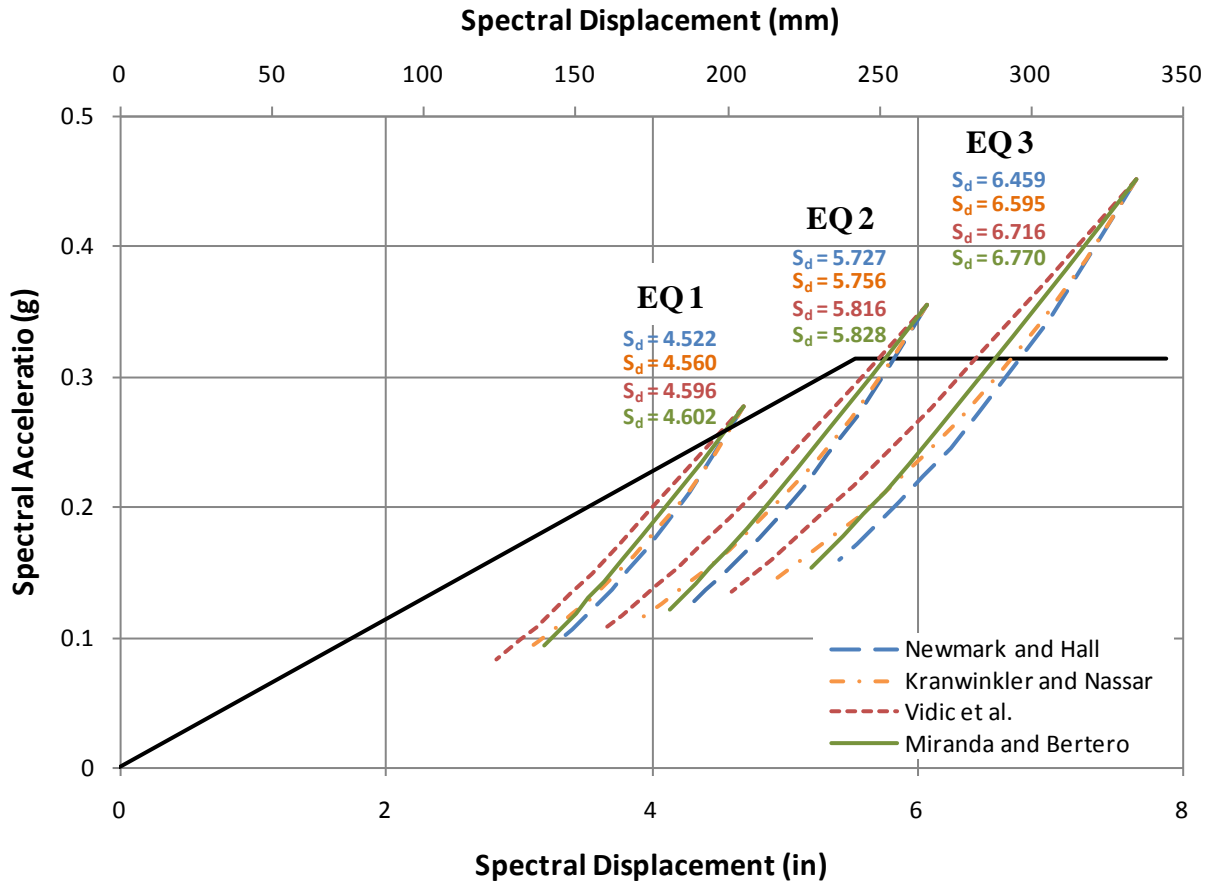


Figure 6.15 Results from CSM with inelastic design spectra for the transverse direction

6.2.4. CSM WITH EQUIVALENT ELASTIC SPECTRA FROM DAMPING MODELS

Results for the longitudinal and transverse direction are shown in Figure 6.16 and Figure 6.17, respectively. Out of all versions of CSM applied in this study, this method provides the least accurate results, severely underestimating the displacement demand imposed on the bridge except under EQ1 in the transverse direction. In the longitudinal direction, displacement demand was underestimated by up to 52% when compared to NLD. In the transverse direction, the predictions were much better with an underestimation of the displacement demand by 26%.

As the severity of ground motion increased, the level of nonlinearity associated with the structural response increased and more ductility was expected from the bridge. But, the ductility

damping relationships become constant as the ductility increases (Figure 3.11). Thus, this version of CSM utilizing equivalent linear systems suffers from the latter problem and yielded poor approximations for displacement response under severe ground motions such as the EQ3 record.

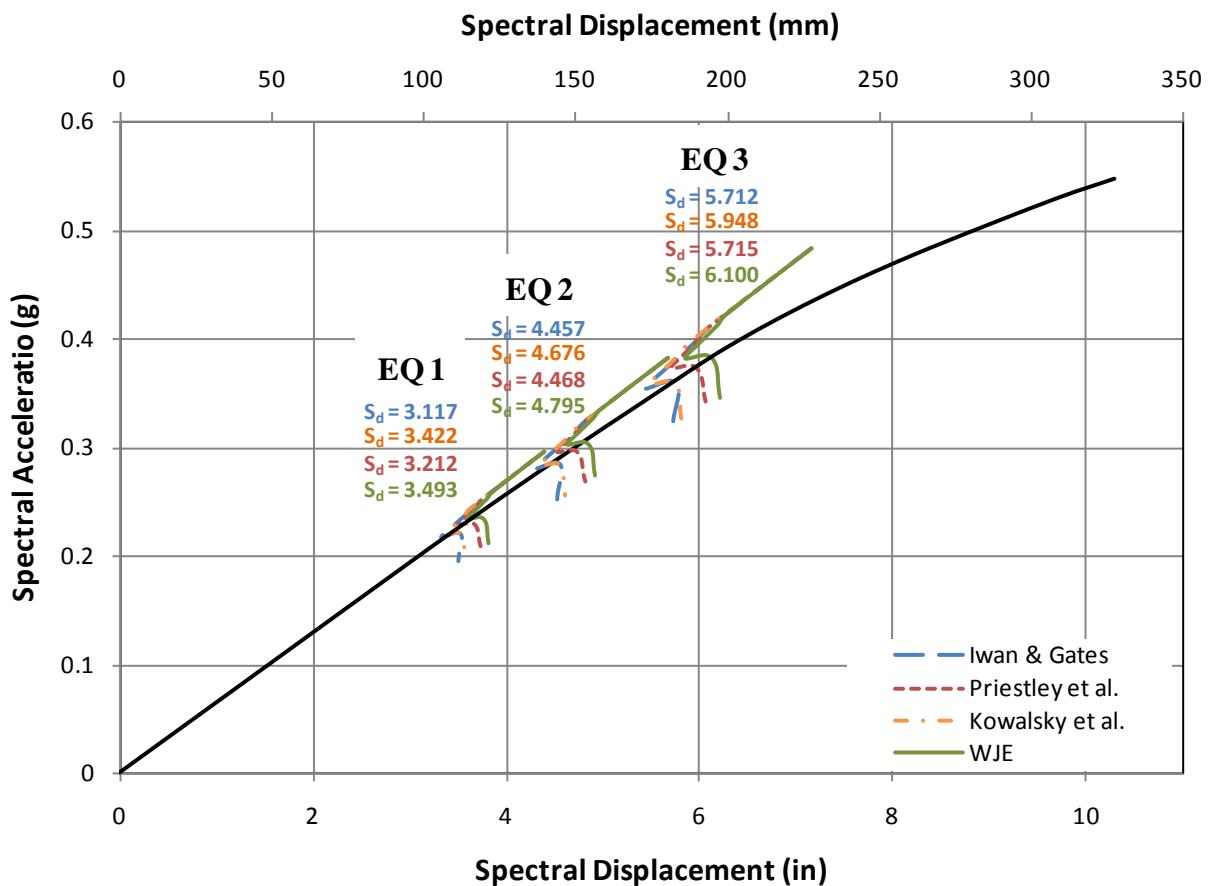


Figure 6.16 Graphical solution from CSM with equivalent elastic spectra from damping models for the longitudinal direction

If updating of the bilinear representation is abandoned for this version of CSM and a single EP force deformation relationship is used, as in the case of CSM with inelastic design spectra, slightly better results can be obtained. Although not reported here, this possibility was investigated and it was found that, like the results of CSM with inelastic design spectra, the method consistently and intolerably underestimated the displacement demand.

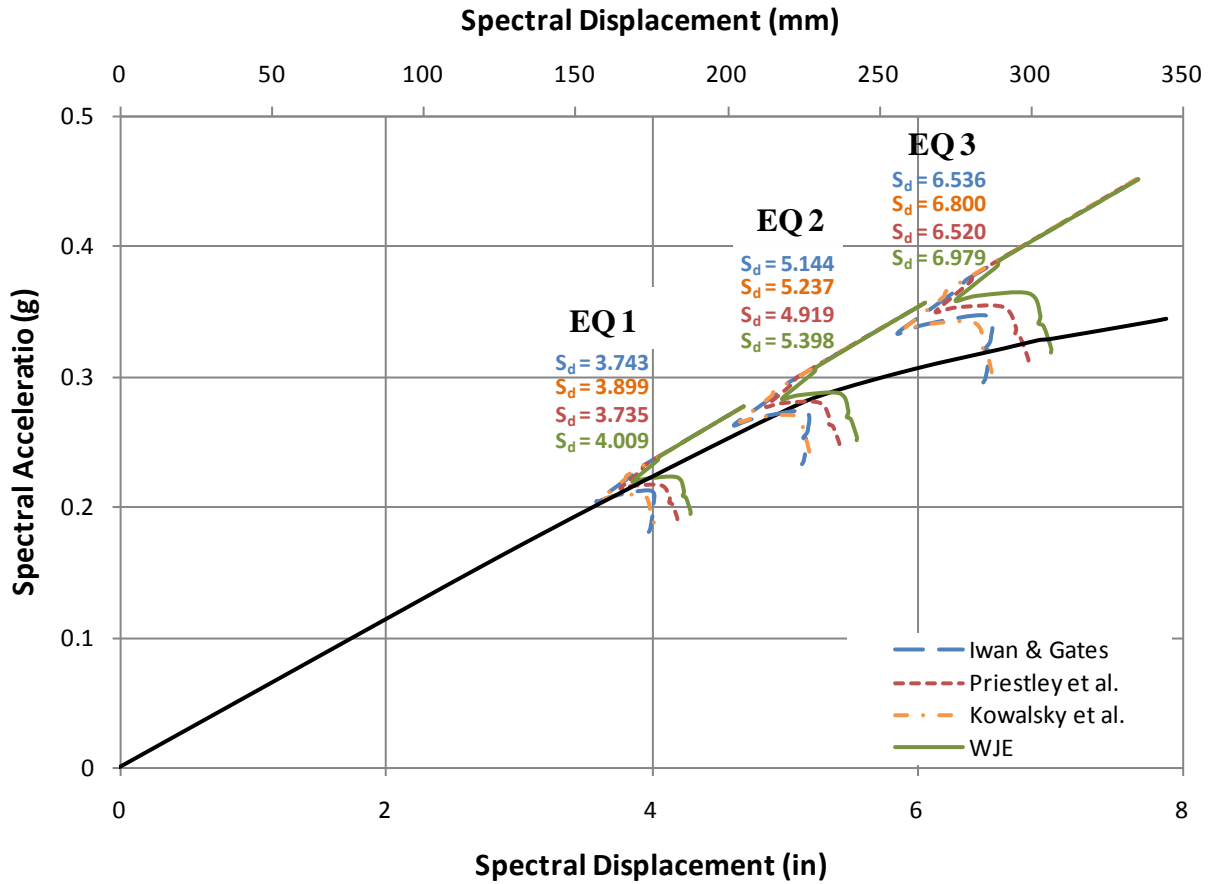


Figure 6.17 Graphical solution from CSM with equivalent elastic spectra from damping models for the transverse direction

6.2.5. ADVANCED CSM

Representation of the displacement-time history for the SDOF is shown in Figure 6.18 and Figure 6.19 for longitudinal and transverse directions, respectively. Like all the other cases, this method also underestimated the displacement demand. In the transverse direction, the displacement difference is as low as 7% for EQ1, but it increases to 32% for EQ3. This is evidence that the nonlinear behavior of the bridge under an earthquake cannot be captured using a SDOF. On the positive side, the SDOF time history analysis provides insight on how the bridge is going act during the earthquake. Time and approximate value for maximum displacement at failure can be retrieved easily with advanced CSM.

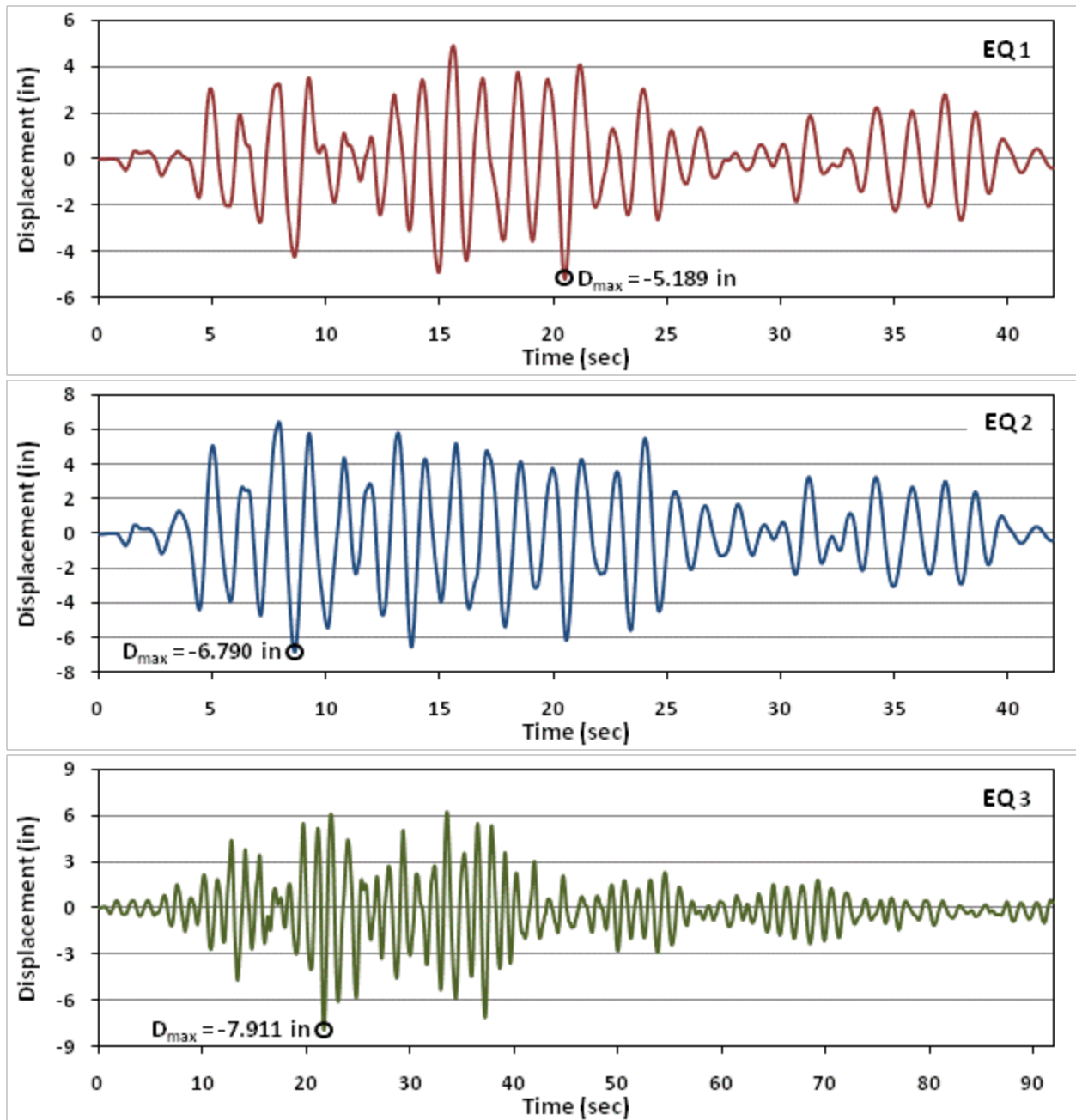


Figure 6.18 Results for advanced CSM using SDOF considering longitudinal direction

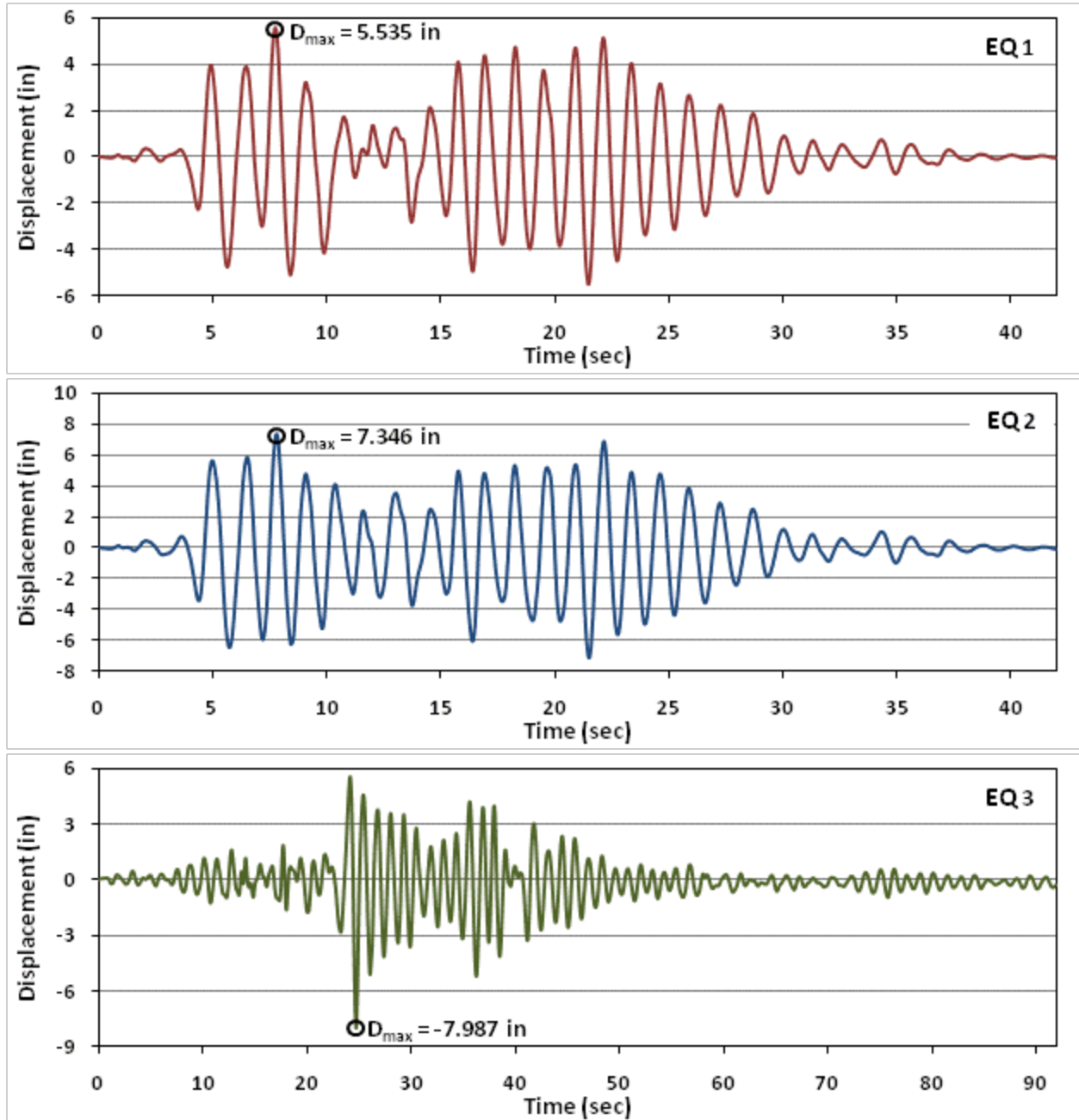


Figure 6.19 Results for advanced CSM using SDOF considering transverse direction

6.2.6. DISPLACEMENT COEFFICIENT METHOD (DCM)

Numerical results for this method can be found in Table 4.4. This method was one of the least accurate methods. It systematically underestimated the structural response by a factor ranging from 8 to 38% for all the cases considered in this research.

Table 6.1 Summary of results in nonlinear static analysis

Analysis Method	Results	Longitudinal						Transverse					
		EQ 1		EQ 2		EQ 3		EQ 1		EQ 2		EQ 3	
		Disp. (in)	μ	Disp. (in)	μ	Disp. (in)	μ	Disp. (in)	μ	Disp. (in)	μ	Disp. (in)	μ
<i>Nonlinear Dynamic Analysis</i>	Time History Analysis (MDOF)	7.115	1.03	7.91	1.14	9.913	1.43	5.189	0.75	9.553	1.38	11.763	1.70
<i>ATC-40 Approach</i>	Type A	4.840 (-32.0)	0.70	6.159 (-22.1)	0.89	7.581 (-23.5)	1.09	6.467 (24.6)	0.93	7.973 (-16.5)	1.14	9.458 (-19.6)	1.36
	Type B	4.875 (-31.5)	0.70	6.244 (-21.0)	0.90	7.772 (-21.6)	1.12	6.574 (26.7)	0.94	8.222 (-13.9)	1.18	10.029 (-14.7)	1.44
	Type C	4.914 (-30.9)	0.71	6.351 (-19.7)	0.92	8.046 (-18.8)	1.16	6.702 (29.2)	0.96	8.660 (-9.3)	1.24	11.041 (-6.1)	1.59
<i>CSM with Inelastic Design Spectra</i>	Newmark and Hall	4.606 (-35.3)	0.56	5.957 (-24.7)	0.72	7.589 (-23.4)	0.91	6.368 (22.7)	0.82	8.532 (-10.7)	1.04	9.304 (-20.9)	1.17
	Kranwinkler and Nassar	4.652 (-34.6)	0.56	6.001 (-24.1)	0.72	7.615 (-23.2)	0.92	6.422 (23.8)	0.82	8.585 (-10.1)	1.04	9.507 (-19.2)	1.19
	Vidic et al.	4.710 (-33.8)	0.57	6.093 (-22.9)	0.74	7.740 (-21.9)	0.93	6.473 (24.7)	0.83	8.695 (-9.0)	1.05	9.688 (-17.6)	1.21
	Miranda and Bertero	4.716 (-33.7)	0.57	6.114 (-22.7)	0.74	7.743 (-21.9)	0.93	6.481 (24.9)	0.83	8.717 (-8.7)	1.05	9.769 (-17.0)	1.22
<i>CSM with Equivalent Elastic Spectra from Damping Models</i>	Iwan & Gates	3.426 (-51.9)	0.49	4.939 (-37.5)	0.71	6.288 (-36.6)	0.91	5.267 (1.5)	0.76	7.483 (-21.7)	1.07	9.418 (-19.9)	1.35
	Priestley et al.	3.762 (-47.1)	0.54	5.178 (-34.5)	0.75	6.559 (-33.8)	0.95	5.486 (5.7)	0.79	7.648 (-19.9)	1.10	9.813 (-16.6)	1.41
	Kowalsky et al.	3.530 (-50.4)	0.51	4.952 (-37.4)	0.72	6.292 (-36.5)	0.91	5.255 (1.3)	0.75	7.091 (-25.8)	1.02	9.395 (-20.1)	1.35
	WJE	3.841 (-46.0)	0.55	5.308 (-32.9)	0.77	6.734 (-32.1)	0.97	5.643 (8.7)	0.81	7.935 (-16.9)	1.14	10.083 (-14.3)	1.45
<i>Coefficient Method</i>	FEMA 356	4.484 (-37.0)	0.65	5.884 (-25.6)	0.85	7.432 (-25.0)	1.07	4.788 (-7.7)	0.69	6.279 (-34.3)	0.90	7.930 (-32.6)	1.14
<i>FEMA 440 Approach</i>	Improved CSM	5.022 (-29.4)	0.73	6.683 (-15.5)	0.97	8.241 (-16.9)	1.19	7.036 (35.6)	1.01	8.649 (-9.5)	1.24	10.756 (-8.6)	1.54
	Improved CM	4.511 (-36.6)	0.65	5.919 (-25.1)	0.85	7.477 (-24.6)	1.08	4.833 (-6.9)	0.69	6.338 (-33.7)	0.91	8.004 (-32.0)	1.15
<i>Advanced CSM</i>	Time History Analysis (SDOF)	5.189 (-27.1)	0.75	6.790 (-14.1)	0.98	7.911 (-20.2)	1.14	5.535 (6.7)	0.80	7.346 (-23.1)	1.06	7.987 (-32.1)	1.15

* EQ1 = 475 yr. return period EQ; EQ2 = 1000 yr. return period EQ; EQ3 = 2475 yr. return period EQ.

* Ductility (μ) values are obtained by dividing target displacement by first-yield displacement

6.2.7. CONCLUSIONS ON THE METHODOLOGY FOR STRUCTURAL ASSESSMENT

The limitations to the proposed method are due to inherent assumptions of CSM; one is the deficiency in representing MDOF structures as SDOF systems. This might introduce a significant amount of error in cases where torsional effects due to asymmetry of mass and stiffness in plan and elevation are present and where the structure responds as a combination of the first and the higher modes.

Another drawback of the CSM is that it relies on the pushover curves, which might not include all features of a building, such as soft stories and higher mode effects as pointed out above. In addition, pushover curves might be significantly different in push and pull directions and they might be in two orthogonal directions. Therefore, the more regular the structure is, the more accurate the results are. This is not the case in this study, where the analyzed structure is a long span curved bridge.

Updating of bilinear representations along the capacity diagram is adopted in order to increase the accuracy. In addition, for the determination of the performance point, a procedure analogous to Procedure B in ATC-40 is utilized to guarantee convergence. It is found that the original CSM in ATC-40 yields significantly different results for different structural behavior types; a wrong classification might result in misleading and nonconservative demand estimates that are too inaccurate to be used for design or retrofit purposes. Updating of bilinear representation could not be used in the version of CSM with inelastic design spectra due to the incompatibility of the capacity and demand diagrams. This entailed a significant inaccuracy in the results and a substantial underestimation of the displacement demands. Moreover, the significance of updating bilinear representations for capacity diagrams that are not suitable for characterization with single elasto-plastic or for bilinear force-deformation relationships is

demonstrated. CSM with equivalent elastic spectra from damping models predicted displacement demand very poorly. The advanced CSM also provided poor results, most likely due to inherent assumptions of CSM. This method can be further verified using analytical and experimental results of structures from different construction types such as RC, steel, etc. Furthermore, the kinematic hardening behavior assumption with the bilinear force-deformation relationship can be relaxed, and more complicated models – such as a trilinear model with stiffness and strength degradation – can be employed to obtain the peak responses. Still, the proposed advanced method can be used as an accurate and reliable method for the inelastic assessment of *simple* structures.

Overall, the improved CSM in FEMA440 gave the most accurate nonlinear static analysis results. The analysis is very time saving and simple, which opens up the possibility for further evaluation of the bridge. Beyond the scope of this section, this method will be used for assessment of displacement demand when using nonlinear static analysis.

6.3. DIFFERENT SOILS

The I-5 Ravenna Bridge is founded on layers of sandy gravel and sandy clay with varying thickness. The dynamic soil-structure interaction (SSI) was initially modeled based on the assumption that a loose sand soil condition would best capture the actual soil condition. Because of the influence of the inherent uncertainties in boundary conditions on the expected displacements of the structure, the pile and abutment springs were also modeled based on other two soil types: dense sand and stiff clay. Sub-grade plastic hinge locations were modified using L-Pile (2002) for each soil type. The capacity curve for the different soil types is shown in Figure 6.20 and Figure 6.21 for longitudinal and transverse directions, respectively.

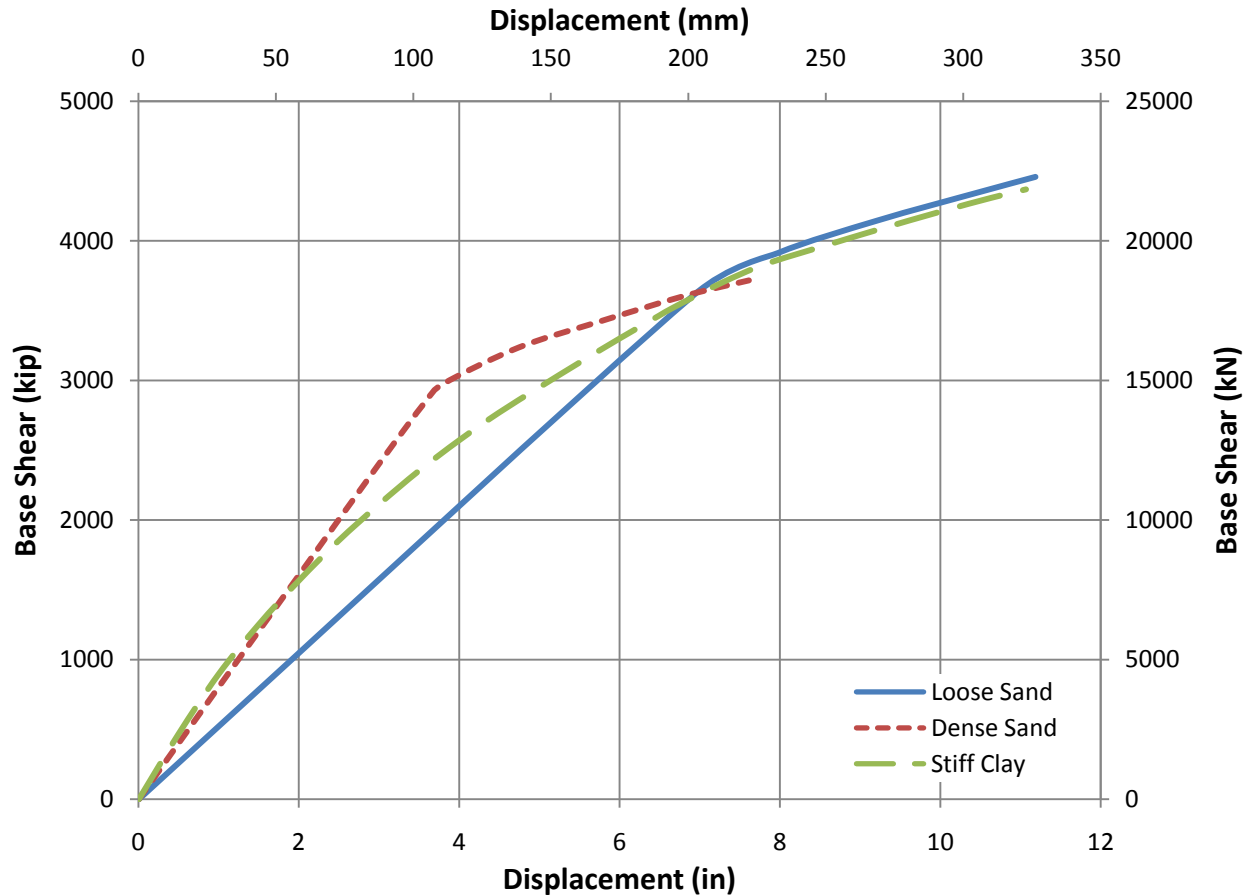


Figure 6.20. Effects of soil type on the pushover curve in longitudinal direction

For both directions, the post yield stiffness of the structure is very similar for all three soil conditions. This may be interpreted as the pile's performance was independent of the confining soil after hinge formation had taken place. Changing the soil type from loose sand to stiff clay or dense sand increased the initial stiffness in the longitudinal direction by 50 and 52%, respectively. In addition, the longitudinal ULS displacement reduced from 11.19 in. for loose sand condition to 11.07 and 7.61 in. for stiff clay and dense sand conditions, respectively. In the transverse direction, changing the soil type from loose sand to stiff clay or dense sand increased the initial stiffness by 58 and 120%, respectively. Also, the transverse ULS displacement reduced from 11.39 in. for the loose sand condition to 11.19 and 7.39 in. for stiff clay and the dense sand condition, respectively. Also, Table 1 presents effects of the soil type on the performance point

corresponding to the three different spectra. As shown in the table going from loose sand to dense sand decreased the displacements by an average of 53% in the longitudinal direction and 37% in the transverse direction. The decrease was more pronounced for EQ3. As a conclusion, different mechanical properties of pile and abutment springs resulted in significant variations in the expected inelastic displacements.

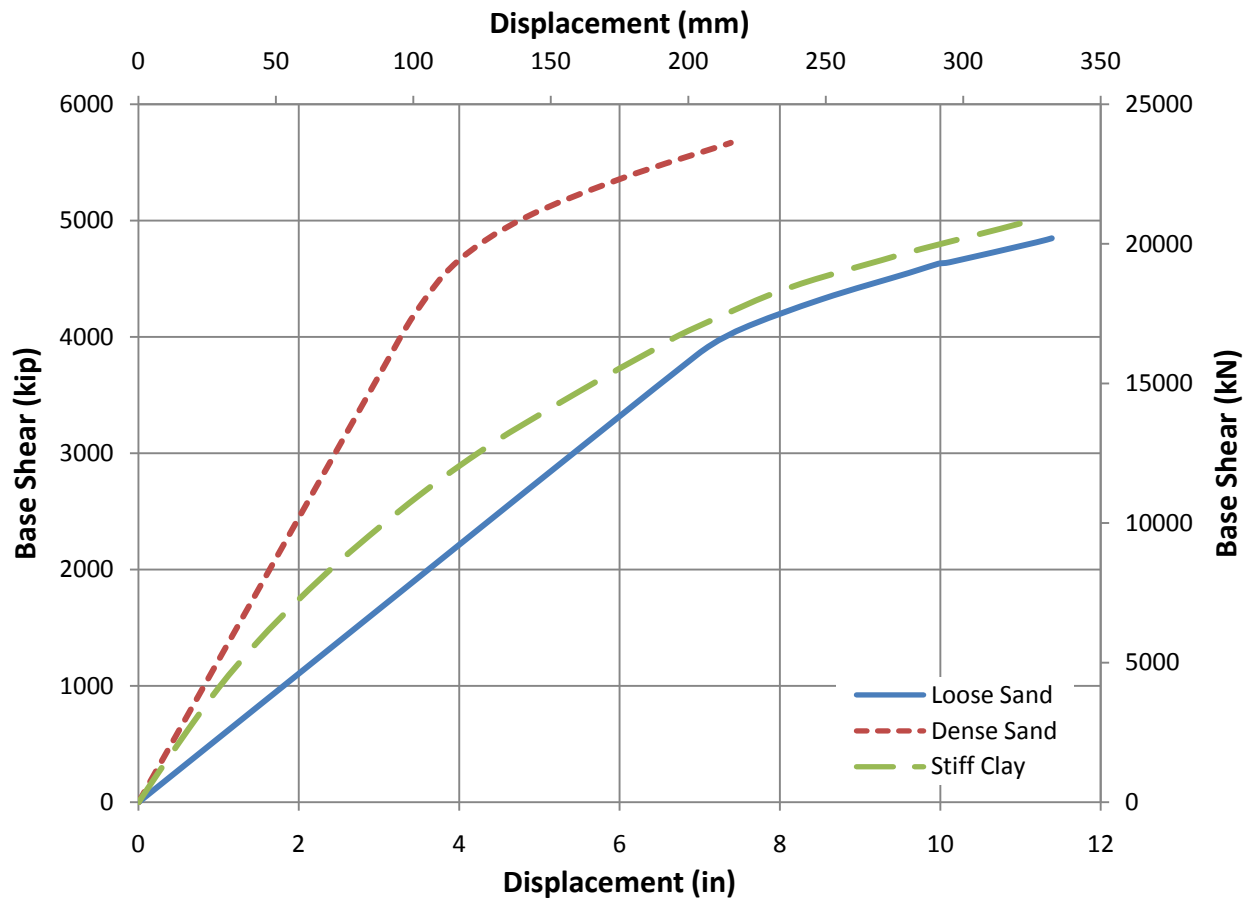


Figure 6.21. Effects of soil type on the pushover curve in transverse direction

Figure 6.22 and Figure 6.23 show the columns that develop a plastic hinge in the stiff clay model for the longitudinal and transverse directions, respectively. Figure 6.24 and Figure 6.25 show the columns that develop a plastic hinge in the dense sand model for the longitudinal and transverse directions, respectively. It is clear that dense sand causes more columns to yield than stiff clay due to higher stiffness.

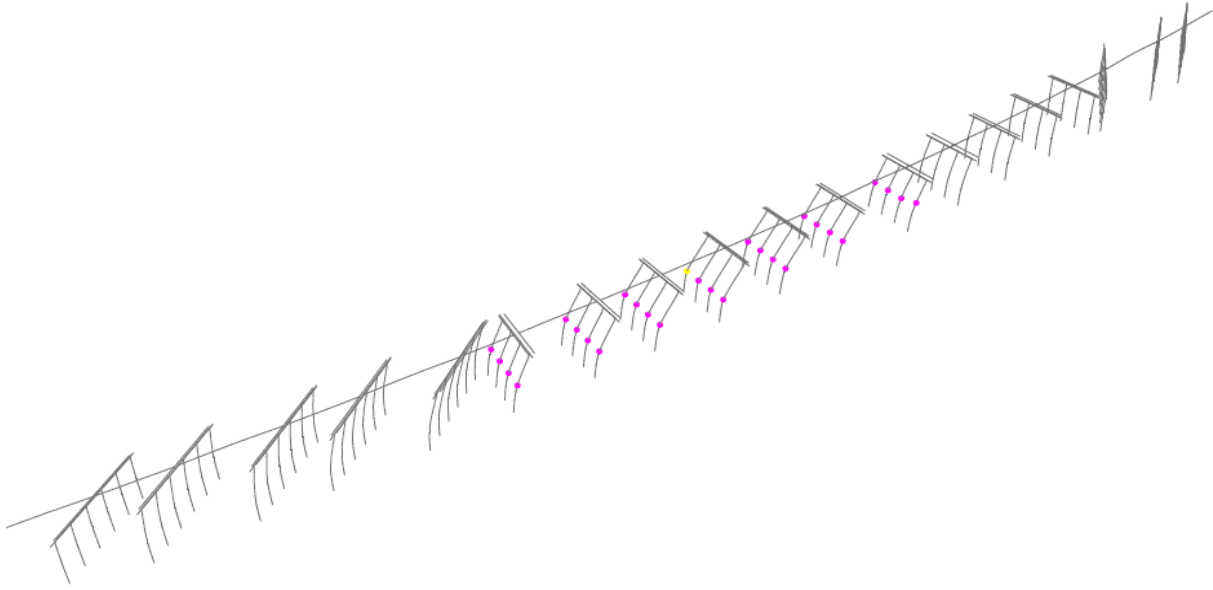


Figure 6.22. Pushover hinge development in longitudinal direction with stiff clay

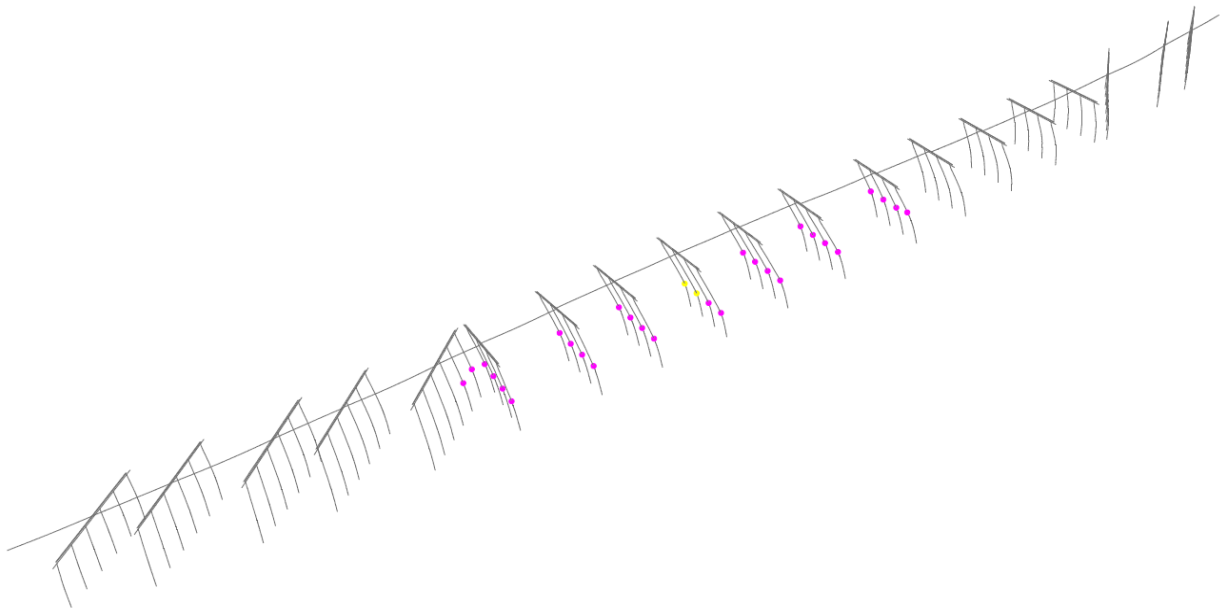


Figure 6.23. Pushover hinge development in transverse direction with stiff clay

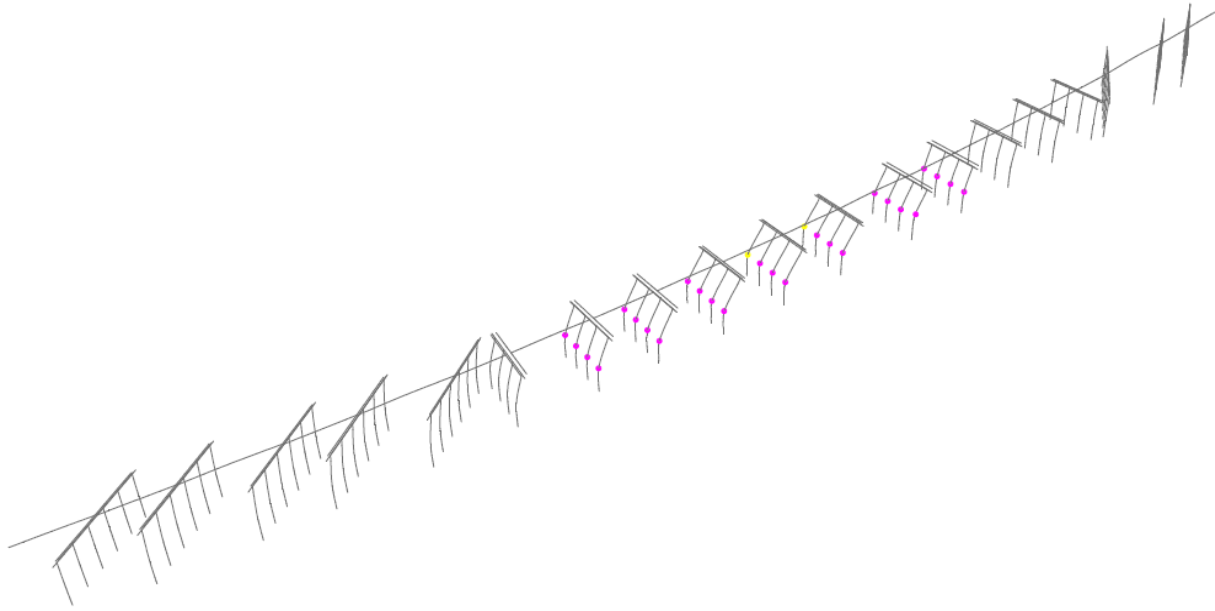


Figure 6.24. Pushover hinge development in longitudinal direction with dense sand

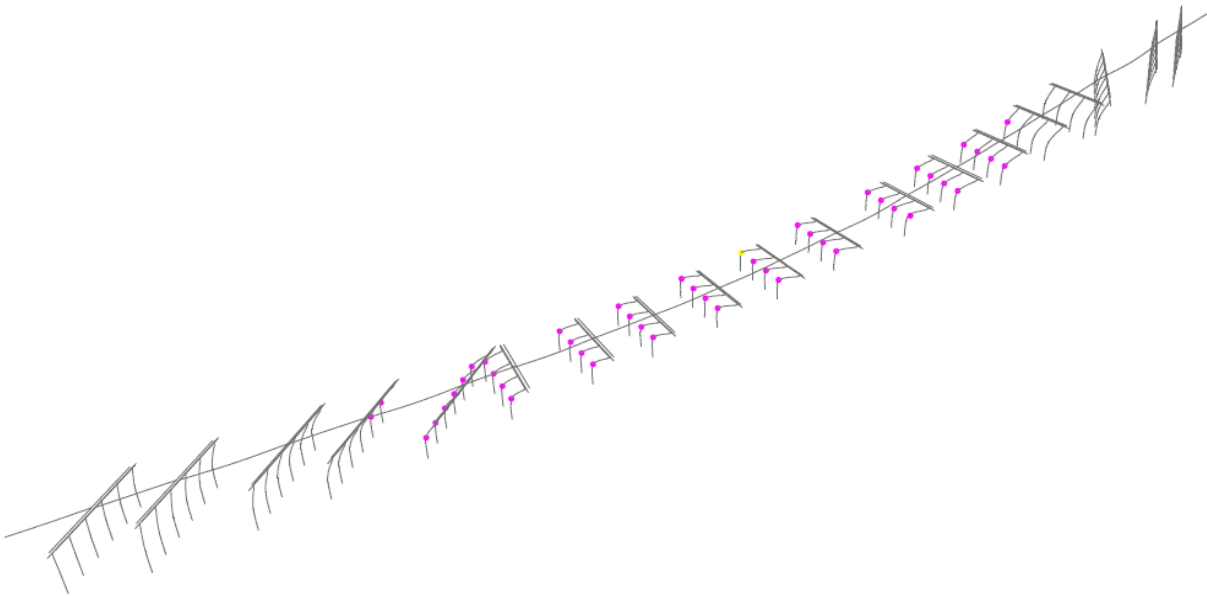


Figure 6.25. Pushover hinge development in transverse direction with dense sand

Having the pushover curve for all the soils, the performance point was calculated based on the improved capacity spectrum method in FEMA 440 (2005) for the three earthquakes. These results are summarized in Table 6.2. Also given is the percent difference compared to NDL results for each performance point.

Table 6.2. Displacement summary and assessment of NLS with different soil models

	Modal Analysis		System Capacity			Performance Points			Demand Ductility		
	Period (sec)	MPMR (%)	1 st Yield (in)	ULS (in)	Ductility	EQ1 (in) (%)	EQ2 (in) (%)	EQ3 (in) (%)	EQ1	EQ2	EQ3
<i>Longitudinal</i>											
Loose Sand	1.37	52.18	6.92	11.19	1.62	5.02 (-41.7)	6.68 (-39.0)	8.24 (-)	0.73	0.97	1.19
Dense Sand	1.04	39.92	3.58	7.61	2.13	2.52 (-75.8)	3.08 (-42.7)	3.77 (-)	0.36	0.45	0.54
Stiff Clay	1.02	44.63	6.65	11.07	1.66	3.33 (-9.9)	4.46 (+5.8)	5.86 (-)	0.48	0.64	0.85
<i>Transverse</i>											
Loose Sand	1.32	54.87	6.96	11.39	1.64	7.04 (-85.1)	8.65 (-)	10.76 (-)	1.02	1.25	1.55
Dense Sand	0.94	56.22	3.45	7.39	2.14	4.35 (-)	5.5 (-)	6.84 (-)	0.63	0.79	0.99
Stiff Clay	0.97	48.2	6.75	11.19	1.66	5.34 (+45.0)	7.13 (+42.7)	9.42 (-)	0.77	1.03	1.36

* MPMR is the Modal Participation Mass Ratio

*1st Yield is considered the displacement at which the first column starts yielding

*With perf. point are given in brackets percentage difference with NLD results; (-) represents failure in NLD

CHAPTER 7: EFFECTS OF PILE-CROSSBEAM CONNECTION

As explained earlier, a 2-D model has been used to get a moment curvature relationship that was fed to SAP 2000 for plastic hinge definition. A more in-depth analysis was carried out on the pile using 3-D finite element models (Greenwood 2008). The detailed 3-D FE models resulted in a plastic hinge length for the pile and the moment rotation relationship at the top of the pile (i.e. at the crossbeam, see section 4.3). These results were implemented into SAP 2000 and pushover analysis was carried out. Figure 7.1 shows the capacity curves considering the loose sand model in the transverse direction. The results of three different models are presented in the figure: (1) pinned pile-crossbeam connection and plastic hinge length based on Caltrans (2008), (2) spring at the pile top and plastic hinge length based on Caltrans (2008), and finally (3) spring at the pile top and plastic hinge length from detailed 3-D FE.

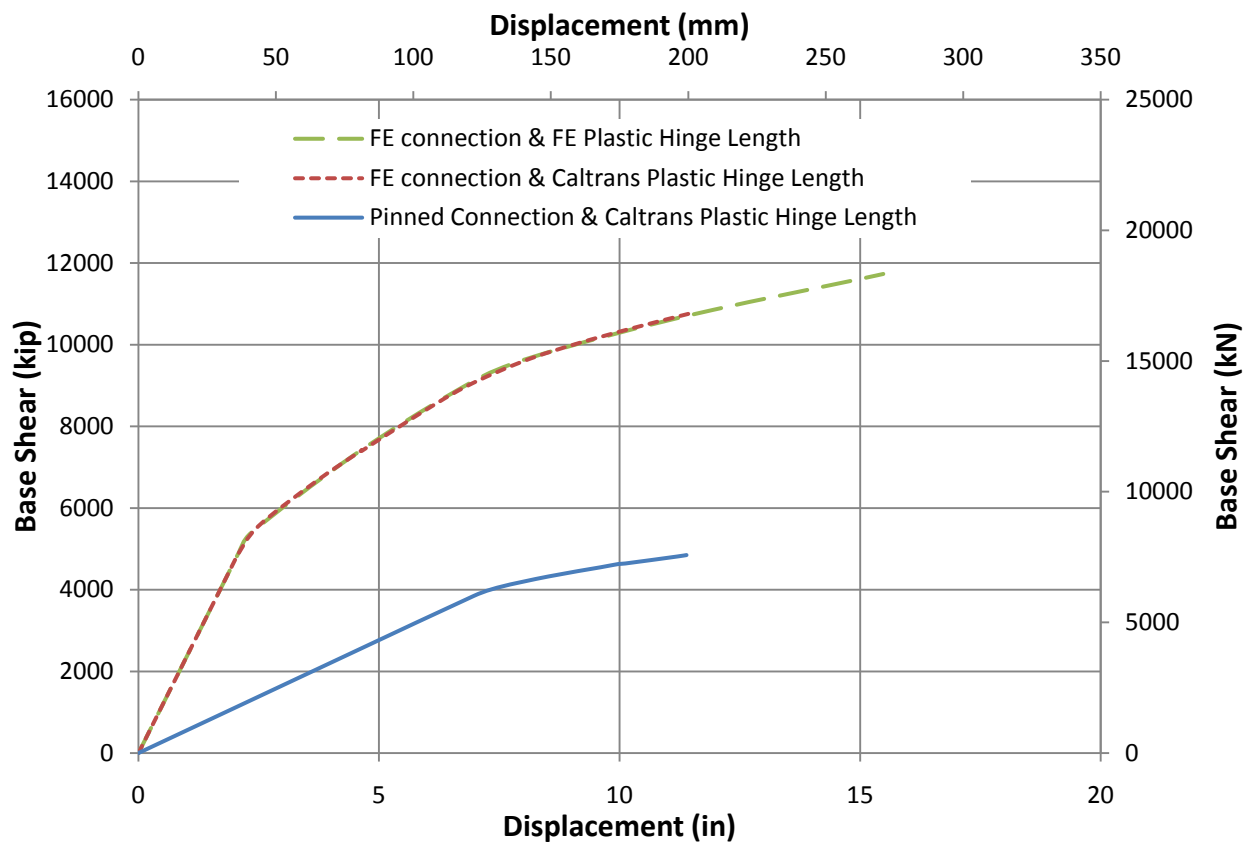


Figure 7.1. Capacity curve comparison between different models

Adding stiffness of the FE pile-crossbeam connection to the initial model increases the initial stiffness of the structure by 375% with an increase of 9% in the displacement capacity. Changing the pile hinge definition based on the detailed 3-D FE plastic hinge length resulted in an increase in the displacement capacity by 35%, reaching approximately 15.5 in. As there were several uncertainties in determining the plastic hinge length from the detailed 3-D FE, it was decided to keep using the plastic hinge length for the piles as defined in Caltrans (2008). However, the stiffness at the pile-crossbeam connection was implemented in the model for the three different soil types.

7.1. NLS ANALYSIS

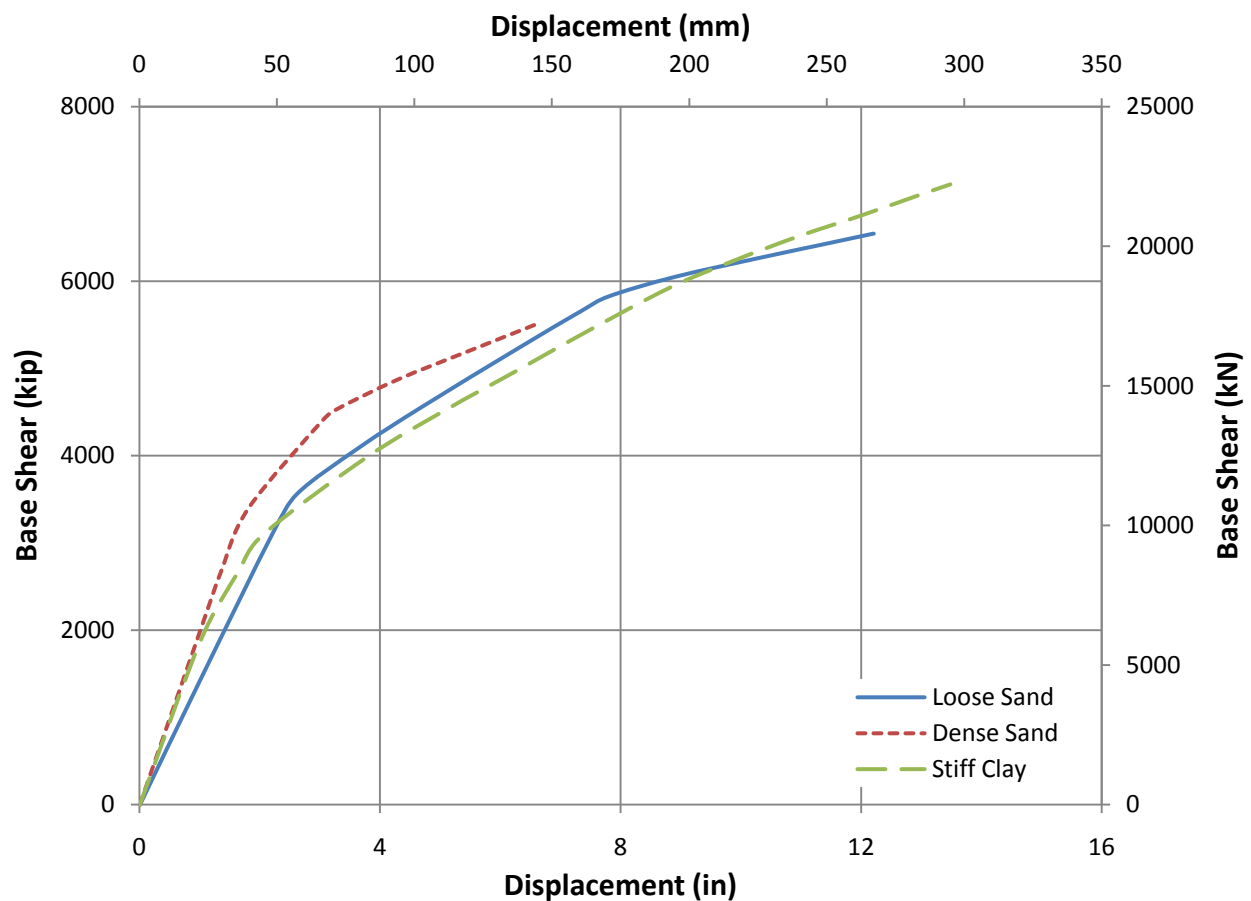


Figure 7.2. Capacity curves for different soil models in the longitudinal direction

The capacity curves for the different soil models are shown in Figure 7.2 and Figure 7.3 for the longitudinal and transverse directions, respectively. Including the pile-crossbeam connection stiffness increased the strength and displacement capacity of the bridge for all soil types. Post-yielding stiffness is very similar for the three soils, and the initial stiffness of the bridge increases with a change from loose sand to stiff clay to dense sand. Dense sand offers the most conservative results by having the lowest displacement capacity and strength. Figure 7.4 and Figure 7.5 show the piles that yielded under EQ3 with the dense sand model in the longitudinal and transverse directions, respectively. 25% of the connections yielded in the longitudinal direction, and 64% yielded in the transverse direction. The performance points for all the earthquakes and soil models are summarized in Table 7.1. The performance points have been significantly reduced with the inclusion of stiffness at pile-crossbeam connections in the model.

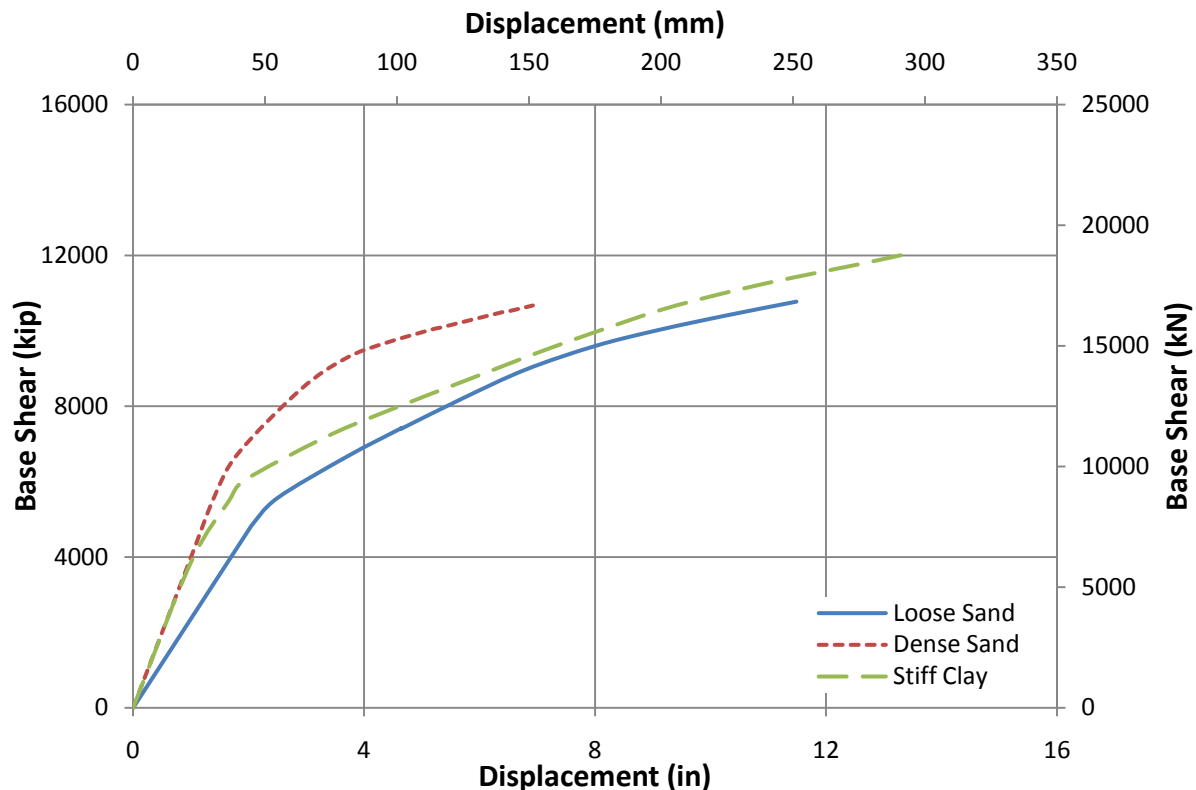


Figure 7.3. Capacity curves for different soil models in the transverse direction

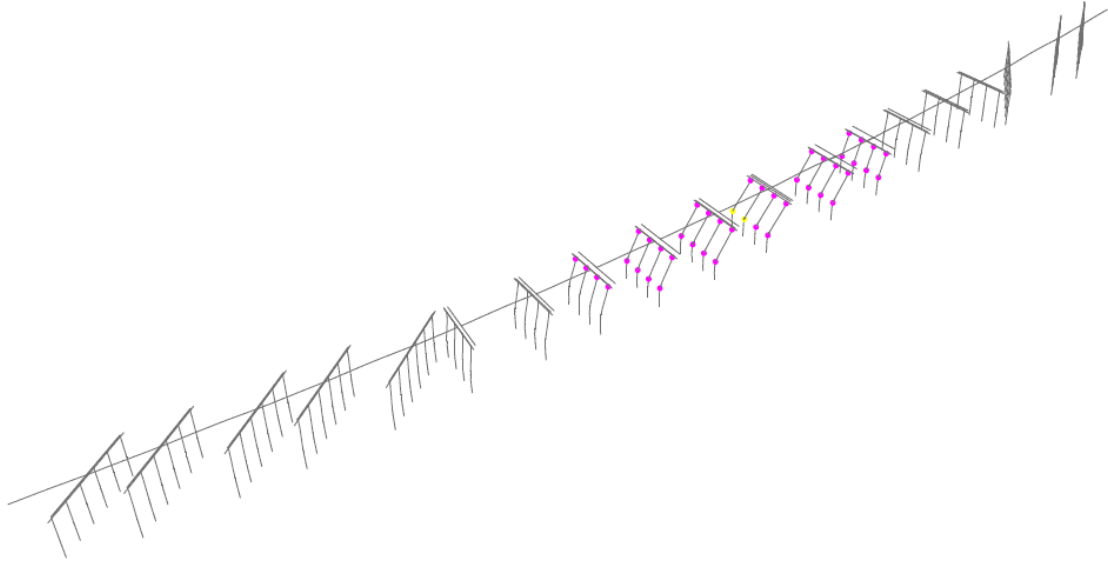


Figure 7.4. Hinge development for EQ3 in the longitudinal direction of dense sand model

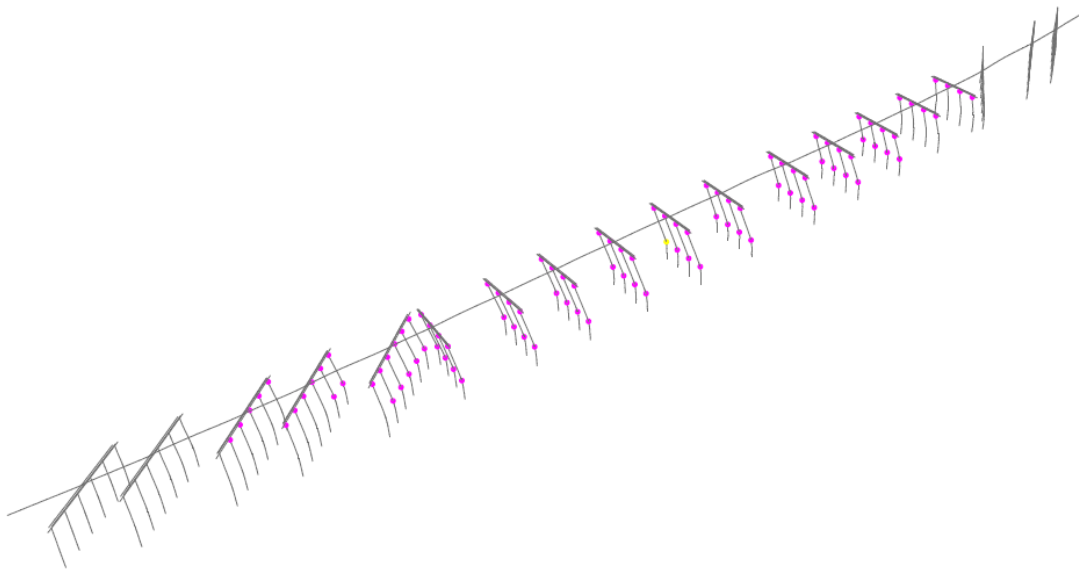


Figure 7.5. Hinge development for EQ3 in the transverse direction of dense sand model

Table 7.1. Displacement summary and assessment of NLS with different soil models

	Modal Analysis		System Capacity			Performance Points			Demand Ductility		
	Period (sec)	MPMR (%)	1 st Yield (in)	ULS (in)	Ductility	EQ1 (in)	EQ2 (in)	EQ3 (in)	EQ1	EQ2	EQ3
<i>Longitudinal</i>											
Loose Sand	0.86	44.31	7.81	12.21	1.56	2.4	2.73	3.76	0.31	0.35	0.48
Dense Sand	0.67	32.6	3.05	6.58	2.16	1.41	1.79	2.36	0.46	0.59	0.77
Stiff Clay	0.69	33.76	8.79	13.48	1.53	1.53	2.17	2.99	0.20	0.28	0.38
<i>Transverse</i>											
Loose Sand	0.76	68.81	6.8	11.49	1.69	3.36	4.51	5.96	0.43	0.58	0.76
Dense Sand	0.57	63.7	2.91	6.92	2.38	2.3	3.02	3.92	0.79	1.04	1.35
Stiff Clay	0.55	66.28	8.11	13.42	1.65	2.52	3.4	4.84	0.32	0.44	0.62

* MPMR is the Modal Participation Mass Ratio

*1st Yield is considered the displacement at which the first column starts yielding

7.2. NDL ANALYSIS

For NDL analysis, it was recognized that the strength increase in bridge capacity would significantly improve the dynamic performance of the bridge. In order to illustrate that, the dense sand model was subjected to EQ3 ground motion in both fundamental directions, independently. Hinges developed in the longitudinal and transverse directions as shown in Figure 7.6. The bridge failed in the longitudinal direction at 24.57 sec. Prior to this failure, the maximum displacement at the target column was 4.093 in., as seen in Figure 7.8. The maximum displacement experienced in the transverse direction was 3.897 in. The force-displacement hysteresis curves of the target pile are shown in Figure 7.7. Also, indicated is the shear strength of the column using UCSD methodology.

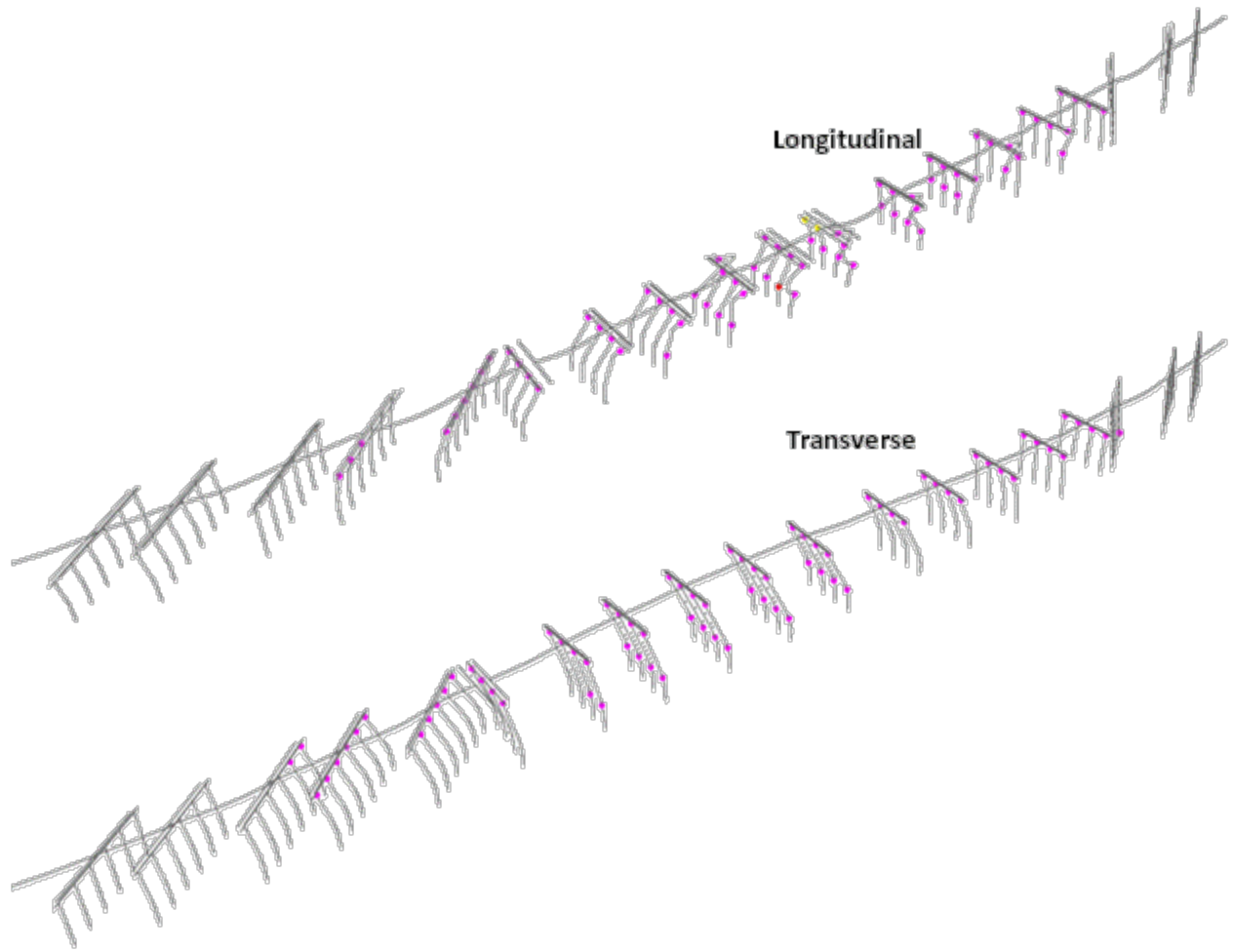


Figure 7.6. Hinge development of dense sand model with FE pile-crossbeam connections under EQ3 ground motion and given direction.

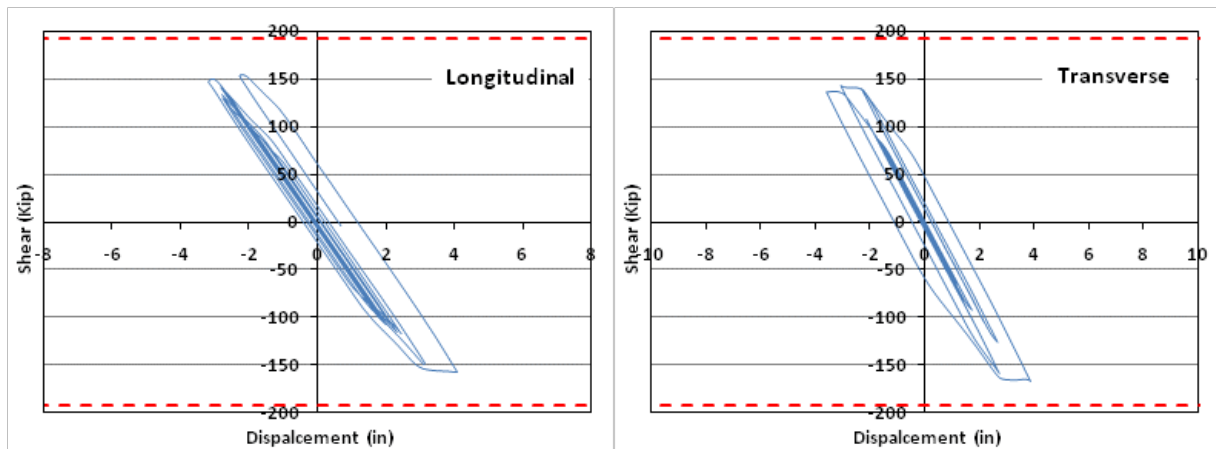


Figure 7.7. Force-Displacement hysteresis curves of the target column in dense sand model with FE pile-crossbeam connections for EQ3 and given directions.

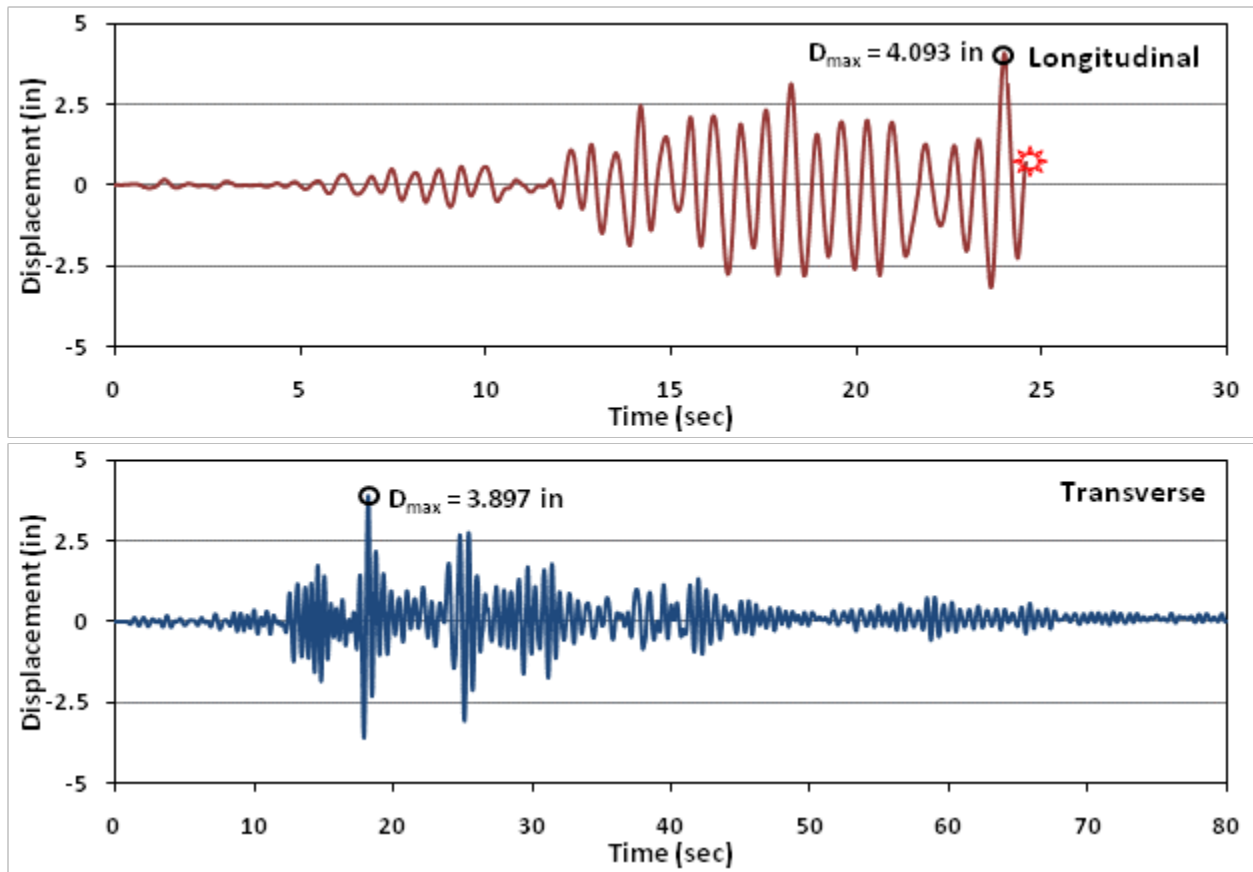


Figure 7.8. Target column displacement-time history in dense sand model with FE pile-crossbeam connections for EQ3 and given directions.

CHAPTER 8: CONCLUSIONS

The Ravenna Bridge was selected by Washington State Department of Transportation (WSDOT) to be evaluated for seismic loading. The Ravenna Bridge is founded on precast/prestressed hollow core concrete piles, which have been noted to behave very poorly under seismic loading (Budek, et al., 1997a, 1997b). Two types of analysis were performed: Nonlinear Static (NLS) and Nonlinear Dynamic (NLD). A three-dimensional “spine” model of the bridge was created using SAP2000 (2007), including modeling of the bridge bearings, expansions joints, and soil-structure interaction. The nonlinear response of the bridge was investigated by using three ground motions with different return periods. The effects of soil-structure-interaction (SSI) were investigated as well. The list below summarizes the conclusions drawn from this research:

- Dense sand offers the most conservative soil model out of the three soil models considered. Piles are much more vulnerable to failure, as shown in the NDL analysis, where even a low level earthquake, EQ1, induced overall bridge failure. Stiff clay is the least conservative soil model, because the bridge behaved elastically for both EQ1 and EQ2 in NDL analysis. Failure was still induced to the bridge for EQ3.
- Overall performance of the piles is nonductile, and failures are very brittle. The shear force-displacement hysteresis curves reinforce this observation, where elastic behavior of piles is followed by an immediate and abrupt failure in all failure cases. Ductility values are on average less than 1.5 considering overall bridge performance.
- Bents 6-16 are the primary bents that experience inelastic deformation under earthquake loads. This observation is validated by both NLS and NLD analysis. In particular, columns in Bent 10 (Figure 4.2) experienced failure first in all NLS analysis cases.

- The FE pile-crossbeam connection model helped improve the performance of the bridge significantly. NLS analysis resulted in no failure for all earthquake levels. Also, the performance displacement for the maximum level earthquake, EQ3, was on average less than 62% of the ULS. Overall, the NDL analysis showed that a large portion of the connections experience yielding, but the failure of the bridge is still governed by the piles.
- Since the Ravenna Bridge is a considerably large bridge, the NLS analysis proved to be very inferior to NLD analysis, due to the higher mode effects. NLS offers a great insight on the ultimate capacity of the bridge, but it cannot be relied on in practice to predict performance under earthquake loads. It is highly recommended for future studies, that a research be conducted in the area of “Multi-Modal Pushover Analysis”, where the higher mode effects are accounted for in the NLS.
- Bridge is safe for a 475-year-return-period earthquake, but the larger earthquakes will probably cause failure.

Based on the research conducted, the Ravenna Bridge is prone to failure under large earthquake loads. Considering that the failures are going to be brittle, it is strongly encouraged by the results of this research to move ahead with the retrofitting program for this bridge as soon as possible.

REFERENCE

- Abebaw, M. (2008). "Seismic Retrofit of Rectangular Bridge Columns Using CFRP Wrapping".
Washington State University. Pullman, Washington.
- Abrahamson, N. A. (1998). "Empirical Ground-Motion Relations for Subduction-Zone Earthquakes and Their Application to Cascadia and Other Regions". *Seismological Society of America*. 93 (4), 1703-1729.
- ATC-40 (1996). "Seismic Evaluation and Retrofit of Concrete Buildings". *Applied Technology Council*. Redwood City, California.
- Atkinson, G. M., & Boore, D. M. "Empirical Ground-Motion Relations for Subduction-Zone Earthquakes and Their Application to Cascadia and Other Regions". 93 (4), 1703-1729.
- Banerjee, S., Stanton, J. F., & Hawkins, N. M. (1987). "Seismic performance of precast prestressed concrete piles". 2 (113), 381-396.
- Bertero, V. V. (1995). Tri-service manual methods. *Vision 2000, Sacramento, Structural Engineers Association of California* .
- Bonvalot, E. (2006). "Dynamic Response of Bridges to Near-Fault, Forward Directivity Ground Motions". Pullman, Washington: Washington State University.
- Borzi, B., & Elnashai, A. S. (2000). "Refined Force Reduction Factors for Seismic Design". *Engineering Structures* , 22 (10), 1244-1260.
- Buckle, I., Friedland, I., Mander, J., Martin, G., Nutt, R., & Power, M. (2006). "Seismic Retrofitting Manual for Highway Structures: Part1 - Bridges". Buffalo, New York: Multidisciplinary Center for Earthquake Engineering Research.
- Budek, A. M. (1997). "The inelastic behavior of reinforced concrete piles and pile shafts". San Diego: Univ. of California.

- Budek, A. M., Benzoni, G., & Priestley, M. J. (1997a). "Analytical Studies on the Inelastic Seismic Response of Solid and Hollow Precast Prestressed Piles". Division of Structural Engineering. La Jolla, California: University of California, San Diego.
- Budek, A. M., Benzoni, G., & Priestley, M. J. (1997b). "Experimental Investigation of Ductility of In-Ground Hinges in Solid and Hollow Prestressed Piles". Division of Structural Engineering. La Jolla, California: University of California, San Diego.
- Budek, A. M., Priestley, M. J., & Benzoni, G. (2000). "Inelastic seismic response of bridge drilled-shaft RC pile/columns". *Journal of Structural Engineering*. 4 (126), 510-517.
- Caltrans (2008). *Seismic Design Criteria 1.4*. California Department of Transportation.
- Chai, Y. H., & Hutchinson, T. C. (2002). "Flexural strength and ductility of extended pile-shafts. II: Experimental study". *Journal of Structural Engineering*. 128 (5), 595-602.
- Chang, F. K., & Krinitzsky, E. L. (1997). "Duration, spectral content, and predominant period of strong motion earthquake records from western United States". U.S.A.C.E. Waterways Experiment Station, Vicksburg, Mississippi: Miscellaneous Paper 5-73-1.
- Chopra, A. K., & Goel, R. K. (1999). "Capacity-Demand-Diagram Methods for Estimating Seismic Deformation of Inelastic Structures: SDF Systems". *Pacific Earthquake Engineering Research Center*. University of California, Berkeley.
- Chopra, A. K., & Goel, R. K. (2000). "Evaluation of NSP to Estimate Seismic Deformation: SDF Systems". *Journal of Structural Engineering, ASCE*, 126 (4), 482-490.
- Cofer, W. F., McLean, D. I., & Zhang, Y. (1997). "Analytical Evaluation of Retrofit Strategies for Multi-Column Bridges". *Washington State Transportation Center*. Pullman, Washington.

- Cofer, W. F., Zhang, Y., & McLean, D. I. (2002). "A Comparison of Current Computer Analysis Methods for Seismic Performance of Reinforced Concrete Members". *Finite Elements in Analysis and Design*. 38 (9), 835-861.
- Fajfar, P. (2000). "A Nonlinear Analysis Method for Performance-Based Seismic Design". *Engineering of Structures*. 16 (3), pp. 573-592.
- Fajfar, P. (1999). "Capacity Spectrum Method Based on Inelastic Demand Spectra". *Earthquake Engineering & Structural Dynamics*. 28 (9), 979-993.
- FEMA 273 (1997). "NEHRP Guidelines for the Seismic Rehabilitation of Buildings". *Federal Emergency Management Agency*. Washington, District of Columbia.
- FEMA 356 (2000). "Prestandard and Commentary for the Seismic Rehabilitation of Buildings". *Federal Emergency Management Agency*. Washington, District of Columbia.
- FEMA 440 (2005). "Improvement of Nonlinear Static Seismic Analysis Procedures". *Federal Emergency Management Agency*. Washington, District of Columbia.
- Freeman, S. A. (1978). "Prediction of Response of Concrete Buildings to Severe Earthquake Motion". *American Concrete Institute Publication SP-55*, 589-605.
- Freeman, S. A., Nicoletti, J. P., et al. (1975). Evaluations of Existing Buildings for Seismic Risk - A Case Study of Puget Sound Naval Shipyard, Bremerton, Washington. *1st U. S. National Conference on Earthquake Engineering, Berkeley*. EERI.
- Gillie, J. L. (2005). "Nonlinear Response Spectra of Forward-Directivity Ground Motions". *Washington State University*. Pullman, Washington.
- Greenwood, S. M. (2008). "Analytical Performance Evaluation of Hollow Prestressed Piles and Pile-Cap Connections in the I-5 Ravenna Bridge". *Washington State University*. Pullman, Washington.

- Gregor, N. J., Silva, W. J., Wrong, I. G., & Youngs, R. R. (2002). "Ground-Motion Attenuation Relationships for Cascadia Subduction Zone Megathrust Earthquakes Based on a Stochastic Finite-Fault Model". *Seismic Society of America*. 92 (5), 1923-1932.
- Hanks, T. C., & McGuire, R. K. (1981). "The character of high-frequency strong ground motion". *Seismic Society of America*. 71 (6), 2017-2095.
- Itani, R. Y., & Lian, X. (2003). "Effects of Retrofitting Applications on Reinforced Concrete Bridges". *Washington State Department of Transportation*. Pullman, Washington.
- Iwan, W. D., & Gates, N. C. (1979). "Estimating Earthquake Response of Simple Hysteretic Structures". *Journal of the Engineering Mechanics Division, ASCE*. 105 (EM3), 391-405.
- Kim, H., Min, K. -W., et al. (2005). "Evaluation of Capacity Spectrum Method for Estimating the Peak Inelastic Responses". *Journal of Earthquake Engineering*, 9 (5), 695-718.
- Kowalsky, M., & Priestley, M. J. (1994b). "Displacement-Based Design, a Methodology for Seismic Design Applied to SDOF Reinforced Concrete Structures". *University of California*. San Diego, La Jolla, California.
- Krawinkler, H., & Nassar, A. A. (1992). "Nonlinear Seismic Analysis and Design of Reinforced Concrete Buildings". *Elsevier Applied Science*. New York, 23-40.
- Kutter, B. L., Martin, G., Hutchinson, T., Harden, C., Gajan, S., & Phalen, J. (2003). "Study of Modeling of Nonlinear Cyclic Load-Deformation Behavior of Shallow Foundations". *PEER workshop*. Berkeley, California.
- Lin, Y. -Y., & Chang, K. -C. (2003). "An Improved Capacity Spectrum Method for ATC-40". *Earthquake Engineering & Structural Dynamics*. 32 (13), 2013-2025.

- Lin, Y. -Y., Chang, K. -C., & et al. (2004a). "Comparison of Displacement Coefficient Method and Capacity Spectrum Method with Experimental Results of RC Columns". *Earthquake Engineering & Structural Dynamics*. 33 (1), 35-48.
- Lin, Y. -Y., Chuang, T. -F., & et al. (2004b). "A Mathematical Basis for the Convergence of the Capacity Spectrum Method". *Earthquake Engineering & Structural Dynamics* , 33 (9), 1059-1066.
- L-Pile Plus 4 (2002). ENSOFT, INC.'s.
- Lymon, C. R., & Shin-Tower, W. (2006). "Verification of computer program LPILE as a valid tool for design of a single pile under lateral loading".
- Mahaney, A. J., Paret, F. T., & et al. (1993). "Capacity Spectrum Method for Evaluating Structural Response During the Loma Prieta Earthquake". *National Earthquake Conference*. Memphis.
- McDaniel, C. C. (2006). "Seismic Assessment and Retrofit of Existing Multi-Column Bent Bridges". *Washington State Transportation Center*. Pullman, Washington.
- Miranda, E., & Bertero, V. (1994). "Evaluation of Strength Reduction Factors for Earthquake-Resistant Design". *Earthquake Engineering & Structural Dynamics*. 10 (2), 357-379.
- Muthukumar, S. (2003). "A Contact Element Approach with Hysteresis Damping for the Analysis and Design of Pounding in Bridge". *Georgia Institute of Technology*.
- Newmark, N. M., & Hall, W. J. (1982). "Earthquake Spectra and Design". *Earthquake Engineering Research Institute, EERI*. Berkeley, California.
- PanGEO, I. (2005). Retrieved from <<http://pangeoinc.com>>.
- Park, R., & Falconer, T. J. (1983). "Ductility of prestressed concrete piles subjected to simulated seismic loading". *PCI Journal*. 28 (5), 113-144.

- PNSN (2008). "Deep Quakes in Washington and Oregon". *University of Washington*. Retrieved from Pacific Northwest Seismograph Network:
<http://www.pnsn.org/INFO_GENERAL/platecontours.html>.
- Priestley, M. J., Kowalsky, M. J., & et al. (1996a). "Preliminary Development of Direct Displacement-Based Design for Multi-Degree of Freedom Systems". *Engineering Structures*. 23 (11), 1453-1460.
- Priestley, M. J., Seible, F., & Calvi, G. M. (1996b). "Seismic Design and Retrofit of Bridges". *Wiley-Interscience*.
- Rahnama, M., & Krawinkler, H. (1993). "Effects of Soft Soil and Hysteresis Model on Seismic Demands". *The John A. Blume Earthquake Engineering Center, Stanford University*. Stanford, California
- Reinhorn, A. M. (1997). "Inelastic Analysis Techniques in Seismic Evaluations." in Seismic Design Methodologies for the Next Generation of Codes (Krawinkler and Fajfar), from Workshop, Bled Solvenia, June 24-27, 1997 (Balkema Publishers), 277-287.
- Rossetto, T., & Elnashai, A. (2005). "A New Analytical Procedure for the Derivation of Displacement-Based Vulnerability Curves for Populations of RC Structures". *Engineering Structures*. 27 (3), 397-409.
- SAP2000 11.0.0 Structural Analysis Program (2007). *Computer and Structures, Inc.* Berkeley, California.
- Sheppard, D. A. (1983). "Seismic design of prestressed concrete piling". *PCI Journal*. 28 (2), 20-49.

- Symans, M. D., Shattarat, N. K., McLean, D. I., & Cofer, W. F. (2003). "Evaluation of Displacement-Based Methods and Computer Software for Seismic Analysis of Highway Bridges". *Washington State Department of Transportation*. Pullman, Washington.
- Takeda, T., Sozen, M. A., & et al. (1970). "Reinforced Concrete Response to Simulated Earthquakes". *Journal of the Structural Division*. 96 (12), 2557-2573.
- USGS (2002). "Seismic hazard maps for the conterminous U.S. for 2002". Retrieved July 2008, 20, from 12. U.S. Geological Survey. <<http://earthquake.usgs.gov>>
- Vidic, T. P., Fajfar, P., & et al. (1994). "Consistent Inelastic Design Spectra: Strength and Displacement". *Earthquake Engineering and Structural Dynamics*. 23 (5), 507-521.
- WJE (1996). "Seismic Dynamic Analysis for Building. Final Manuscript Prepared for U". Emeryville, California: S. Army Engineering Division by Wiss, Janney, Elnster Associates, Inc. Emeryville, California.
- XTRACT v.2.6.2 Educational, Cross Section Analysis Program (2002). *Imbsen and Associates, Inc.* Sacramento, California.
- Xue, Q. (2001). "Assessing the Accuracy of the Damping Models Used in Displacement-Based Seismic Demand Evaluation and Design of Inelastic Structures". *Soil Dynamics and Earthquake Engineering*. 3 (2), 37-45.
- Zhang, Y., Cofer, W. F., & McLean, D. I. (1999). "Analytical Evaluation of Retrofit Strategies for Multi-Column Bridges". *Journal of Bridge Engineering*. 4 (2), 143-150.

APPENDIX

APPENDIX A

A.1. DEMAND DIAGRAM ACCORDING TO NEWMARK AND HALL (1982)

A tri-partite plot is utilized for the construction of elastic design spectrum according to Newmark and Hall (1982). A 50th percentile or an 84.1th percentile spectrum can be obtained using this procedure. Explanations below refer to Figure A.1; Chopra's description (2000) provides the basis for what follows.

- i. The three dashed lines corresponding to peak values of ground acceleration, \ddot{u}_{go} , velocity, \dot{u}_{go} , and displacement, u_{go} , are plotted for design ground motion.
- ii. According to damping factor, amplification factors are determined using the equations given in Table A.1.
- iii. \ddot{u}_{go} is multiplied with the amplification factor α_A to obtain the straight line b-c presenting the constant value of pseudo-acceleration, S_a .
- iv. \dot{u}_{go} is multiplied with the amplification factor α_V to obtain the straight line c-d representing a constant value of pseudo-velocity, S_v .
- v. u_{go} is multiplied with the amplification factor α_D to obtain the straight line e-d representing a constant value of deformation, S_d .
- vi. For periods shorter than 1/33 sec, T_a , velocity is equal to the line represented by \ddot{u}_{go} and for periods longer than 33 sec, T_f , velocity is equal to the line represented by u_{go} .
- vii. Straight lines are plotted for transitions from T_a to T_b and T_e to T_f .
- viii. Once the pseudo-velocity spectrum is obtained, pseudo-acceleration and deformation spectrum can be obtained using the relations given in Equation A.1, where ω_n is the natural frequency of the SDOF system and related to elastic period by Equation A.2.

$$\frac{S_a}{\omega_n} = S_v = \omega_n S_d \quad (\text{A.1})$$

$$\omega_n = \frac{2\pi}{T_e} \quad (\text{A.2})$$

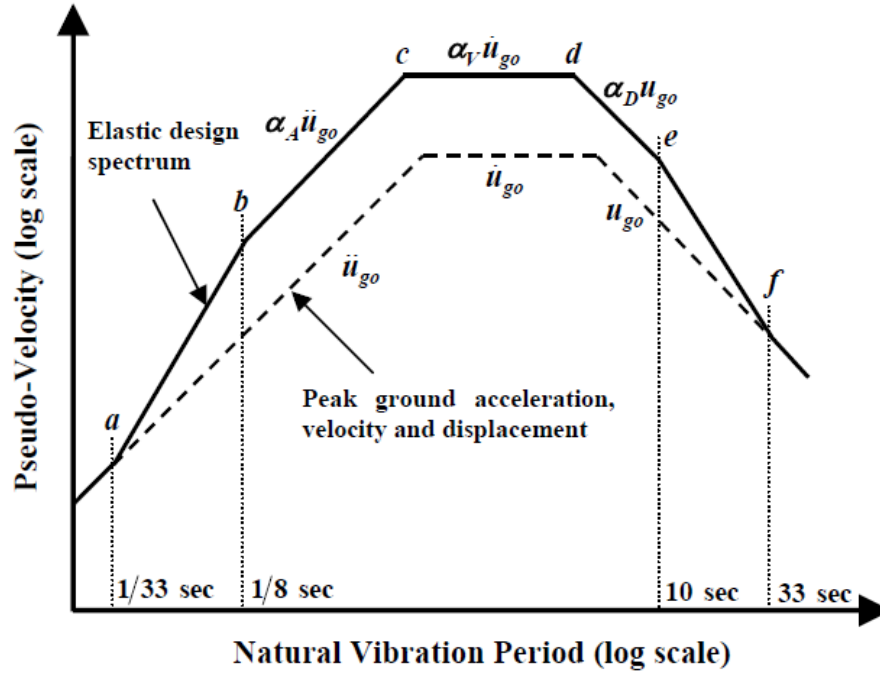


Figure A.1. Newmark and Hall (1982) elastic spectrum, reproduced from Chopra (2000)

Table A.1. Amplification factors: elastic design spectra, Newmark and Hall (1982)

	Median (50 th percentile)	One Sigma (84.1 th percentile)
α_A	$3.21 - 0.68 \ln \zeta$	$4.38 - 1.04 \ln \zeta$
α_V	$2.31 - 0.41 \ln \zeta$	$3.38 - 0.67 \ln \zeta$
α_D	$1.82 - 0.27 \ln \zeta$	$2.73 - 0.45 \ln \zeta$

A.2. DAMPING MODIFICATION FACTOR, κ , IN ACT-40(1996)

ATC-40 introduces the damping modification factor, κ , in order to account for the effect of imperfect hysteresis loops. This term is calculated using the appropriate equation from Table A.2. Structural behavior types definitions are given in Table A.3.

A maximum value of 45 percent is set for the value of allowable equivalent damping, ζ_{eq} . When multiplied with the appropriate damping modification factor from Table A.2, and added to 5 percent elastic damping, 40, 30, and 20% of maximum allowable damping is obtained for Type A, B, and C structures, respectively.

Table A.2. Equations used for calculation the damping modification factor, κ (ATC-40, 1996)

Structural Behavior Type	ζ_{eq} (percent)	κ
Type A	≤ 16.25	1.0
	> 16.25	$1.13 - 0.51 \frac{(\mu - 1)(1 - \alpha)}{\mu(1 + \alpha\mu - \alpha)}$
Type B	≤ 25	0.67
	> 25	$0.845 - 0.446 \frac{(\mu - 1)(1 - \alpha)}{\mu(1 + \alpha\mu - \alpha)}$
Type C	Any Value	0.33

Table A.3. Structural behavior types (ATC-40, 1996)

Shaking Duration	Essentially New Building ¹	Average Existing Building ²	Poor Existing Building ³
Short	Type A	Type B	Type C
Long	Type B	Type C	Type C

¹ Buildings whose primary elements make up an essentially new lateral system and little strength or stiffness is contributed by non-complying elements.

² Buildings whose primary elements are combinations of existing and new elements, or better than average existing systems

³ Buildings whose primary elements make up non-complying lateral force resistance systems with poor or unreliable behavior.

A.3. MODIFICATION FACTORS IN CM (FEMA356, 2000)

C_0 is the modification factor to relate the spectral displacement and the likely building roof displacement. The modal participation (or transformation) factor given by Equation 3.10 can be used for this purpose, or alternatively Table A.4 provided in FEMA 356(2002) can be used.

Table A.4. Values for the modification factor C_0

Number of Stories	Modification Factor*
1	1.0
2	1.2
3	1.3
5	1.4
10+	1.5

* Linear interpolation shall be used to calculate the intermediate values

C_1 is the modification factor to relate the expected maximum inelastic displacements to displacements calculated for linear elastic response. C_1 can be calculated using the Equation A.3. C_1 cannot exceed 1.5 for $T_{eff} < 0.1$, and cannot be taken as less than 1.0 in any case.

$$C_1 = \begin{cases} 1.0 & T_e \leq T_0 \\ \left[\frac{1 + (R - 1) T_0 / T_{eff}}{R} \right] & T_e > T_0 \end{cases} \quad (A.3)$$

Where, T_0 is the characteristic period of the spectrum, defined as the period associated with the transition from the constant acceleration segment of the spectrum to the constant velocity segment, equivalent to T_c in section A.1. R is the ratio of inelastic strength demand to the calculated yield strength coefficient and is given by the Equation A.4.

$$R = \frac{S_a}{V_y/W} \frac{1}{C_0} \quad (A.4)$$

Where, S_a is the response spectrum acceleration at the effective fundamental period of the building and W is the total dead and anticipated live load of the building.

C_2 is the modification factor to represent the effect of hysteresis shape on the maximum displacement response. It takes into account the increase in displacement demand if hysteresis loops exhibit considerable pinching. Values of C_2 for different framing systems and performance levels are listed in Table A.5.

Table A.5. Values for the modification factor C_2

Structural Performance Level	$T_{eff} = 0.1$		$T_{eff} \geq T_0$	
	Framing Type 1*	Framing Type 2**	Framing Type 1*	Framing Type 2**
Immediate Occupancy	1.0	1.0	1.0	1.0
Life Safety	1.3	1.0	1.1	1.0
Collapse Prevention	1.5	1.0	1.2	1.0

* Structures in which more than 30% of the shear at any level is resisted by components or elements whose strength and stiffness may deteriorate during the design earthquake. Such elements include: ordinary moment-resisting frames, concentrically-braced-frames, frames with partially restrained connections, tension-only braced frames, unreinforced masonry walls, shear-critical walls and piers, or any combination of the above.

** All frames not assigned to Framing Type 1.

C_3 is the modification factor to represent increased displacements due to second-order effects. While moderate strain hardening does not have a significant influence on the displacement demand, strain softening can considerably increase this coefficient. Therefore for buildings with positive post-yield stiffness, C_3 shall be set equal to 1.0. For buildings with negative post-yield stiffness, C_3 shall be calculated using the Equation A.5.

$$C_3 = 1 + \frac{|\alpha|(R - 1)^{3/2}}{T_{eff}} \quad (A.5)$$

A.3.1. IMPROVED MODIFICATION FACTORS (FEMA440, 2005)

The FEMA-440(FEMA440, 2005) document proposes several improvements to the FEMA-356 Coefficient Method (FEMA356, 2000) for estimating the target displacement. The first improvement is a modified formula for C_1 given by:

$$C_1 = 1 + \frac{R - 1}{\alpha T_e^2} \quad (\text{A.6})$$

in which α is equal to 130, 90, and 60 for site classes B, C, and D, respectively. Furthermore, FEMA-440 recommends abandoning the upper limit on C_1 imposed in FEMA-356. The second improvement is to the coefficient C_2 which given by:

$$C_2 = 1 + \frac{1}{800} \left(\frac{R - 1}{T} \right)^2 \quad (\text{A.7})$$

Finally, FEMA-440 recommends deleting the coefficient C_3 and imposes a limitation on strength to avoid dynamic instability. This limitation on strength is specified by imposing a maximum limit on R given by:

$$R_{max} = \frac{\Delta_d}{\Delta_y} + \frac{\alpha_2^{-t}}{4} \quad (\text{A.8})$$

Where

$$t = 1 + 0.15 \ln(T) \quad (\text{A.9})$$

In which Δ_d is the deformation corresponding to peak strength, Δ_y is the yield deformation, and α_2 is the slope (a negative value) of the strength-degradation segment of the force-deformation curve.

APPENDIX B

B.1. SUPERSTRUCTURE GEOMETRY

Table B.1 describes the I-girder dimension used in the superstructure of the bridge. Figure B.1 and B.2 depict the shape of the girders. Table B.2 (with Figure B.3) summarizes the built up of each span based on girder combination.

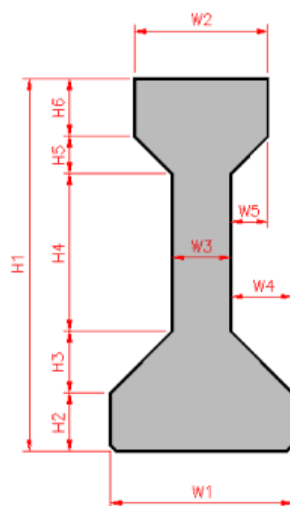


Figure B.1. WSDOT girder

Table B.1. Girder dimension (in inches)

Series	H1	H2	H3	H4	H5	H6	W1	W2	W3	W4	W5
10	44	0	0	0	0	0	14	14	14	0	0
20	24	4	2	12	2	4	14	14	5	4.5	4.5
30	24	3.5	1.5	14	1.5	3.5	14	14	5	4.5	4.5
40	32	4	2	21	1.5	3.5	16	14	5	5.5	4.5
50	34	5	2	22	1.5	3.5	19	14	5	7	4.5
60	42	5	2	22	1.5	3.5	19	14	5	7	4.5
70	44	6	3	29	2	4	24	16	5	9.5	5.5
80	50	6	3	34	2	5	24	19	5	9.5	7
90	53	6	3	37	2	5	24	24	5	9.5	9.5
100	58	6	3	42	2	5	24	24	5	9.5	9.5
109	64	6	3	48	2	5	24	24	5	9.5	9.5

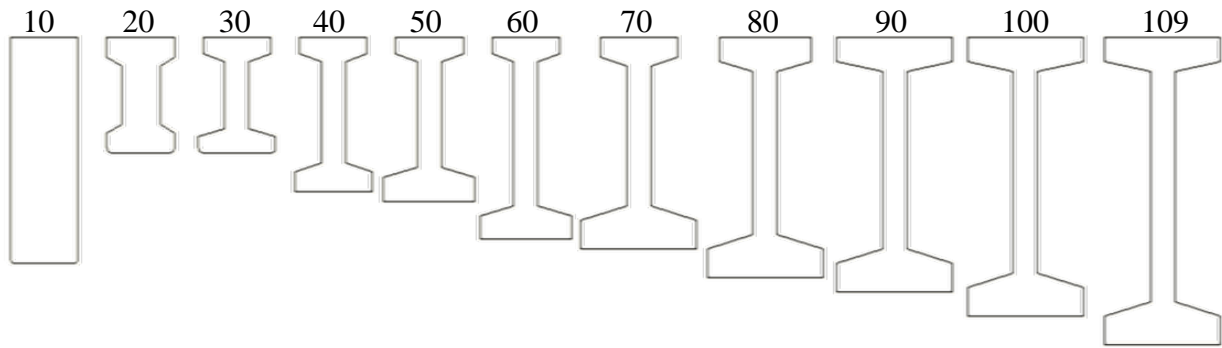


Figure A.2. Model of all girders used in the Ravenna Bridge (with series numbers)

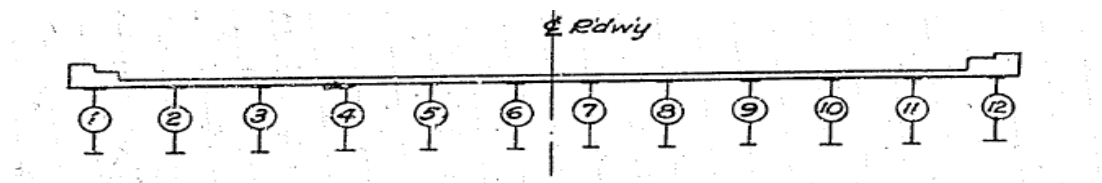


Figure B.3. Girder numbering along the width of spans

Table B.2. Assigned girder to individual spans

Span	#1 ¹	#2	#3	#4	#5	#6	#7	#8	#9	#10	#11	#12
1	60 ²	60	60	60	60	60	60	60	60	60	60	60
2	60	60	60	60	60	60	60	60	60	60	60	60
3	80	80	80	80	80	80	80	80	80	80	80	80
4	60	60	60	60	60	60	60	60	60	60	60	60
5	80	80	80	80	80	80	80	80	80	80	80	80
6	20	20	20	30	40	40	50	60	60	70	80	80
7	80	80	80	80	80	80	80	80	80	80	80	80
8	60	60	60	60	60	60	60	60	60	60	60	60
9	70	70	70	70	70	70	70	70	70	70	70	70
10	70	70	70	70	70	70	70	70	70	70	70	70
11	70	70	70	70	70	70	70	70	70	70	70	70
12	90	90	90	90	90	90	90	90	90	90	90	90
13	70	70	70	70	70	70	70	70	70	70	70	70
14	70	70	70	70	70	70	70	70	70	70	70	70
15	70	70	70	70	70	70	70	70	70	70	70	70
16	70	70	70	70	70	70	70	70	70	70	70	70
17	100	100	90	80	70	60	50	40	40	30	20	10
18	100	100	100	100	100	100	100	100	100	100	100	100
19	50	50	50	50	50	50	50	50	50	50	50	50
20	50	50	50	50	50	50	50	50	50	50	50	50

¹Location of girder with respect to Figure A.3.

²Number of girder series (reference to Figure A.2 and Table A.1)

Finally, the geometrical properties for each span are summarized in Table B.3. These properties are used to define the spine model used to define the superstructure of the bridge.

Table B.3. Span properties

Span	Length (ft)	Area (in ²)	Weight (kip/ft)	I _x (in ⁴)	I _y (in ⁴)	I _z (in ⁴)
1	57.10	11456.00	11.93	40859953	748600157	789460110
2	55.50	11456.00	11.93	40859953	748600157	789460110
3	77.92	13187.00	13.74	54483576	841937032	896420608
4	57.16	11456.00	11.93	40859953	748600157	789460110
5	80.02	13187.00	13.74	54483576	841937032	896420608
6	43.50	11607.98	12.09	53018271	808687487	861705758
7	73.49	13187.00	13.74	54483576	841937032	896420608
8	59.60	11456.00	11.93	40859953	748600157	789460110
9	67.50	12478.97	13.00	44472079	803779287	848251366
10	67.50	12478.97	13.00	44472079	803779287	848251366
11	67.50	12478.97	13.00	44472079	803779287	848251366
12	90.00	13719.45	14.29	60836239	870714957	931551196
13	67.50	12478.97	13.00	44472079	803779287	848251366
14	67.50	12478.97	13.00	44472079	803779287	848251366
15	67.50	12478.97	13.00	44472079	803779287	848251366
16	63.58	12478.97	13.00	44472079	803779287	848251366
17	55.25	12216.70	12.73	66800668	837024320	903824989
18	99.27	14026.96	14.61	69502803	887247290	956750093
19	52.75	10975.97	11.43	31378844	722729266	754108111
20	54.75	10975.97	11.43	31378844	722729266	754108111

B.2. ABOVE-GROUND HEIGHT OF PILES

The span length of each cross beam is summarized in Table B.4. Also, the above ground height is estimated for columns located on the outer left, center and outer right of each bent. The estimation is done by subtracting the elevation value of these points by the approximate height of the superstructure and cross beam. The elevation values are provided in the plan.

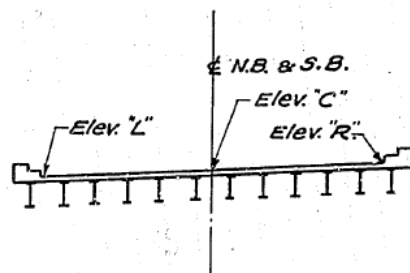


Figure B.4. Orientation of piers

Table B.4. Cross-beam length and above ground height of columns

Bent	Length (ft)	Col. L (ft)	Col C (ft)	Col. R (ft)
1	99.41	16.29	17.39	16.84
2	100.33	26.54	27.85	27.20
3	101.83	26.95	28.31	27.63
4	103.00	26.20	27.57	26.89
5	104.67	26.10	27.48	26.79
6	67.00	24.98	26.18	25.58
7	67.00	25.40	26.60	26.00
8	67.00	25.14	26.34	25.74
9	67.00	24.97	26.17	25.57
10	67.00	24.81	26.01	25.41
11	67.00	22.92	24.12	23.52
12	67.00	22.42	24.62	23.52
13	67.00	22.25	23.45	22.85
14	67.00	21.08	22.28	21.68
15	67.00	19.91	21.11	20.51
16	67.00	18.71	19.91	19.31
17	127.75	17.37	18.80	18.09
18	129.34	18.12	19.56	18.84
19	131.08	16.97	18.43	17.70

B.3. BEARINGS

Table B.5 provides the dimensions for different bearings used in the bridge. It also contains calculated initial stiffness and yielding point for each bearing type.

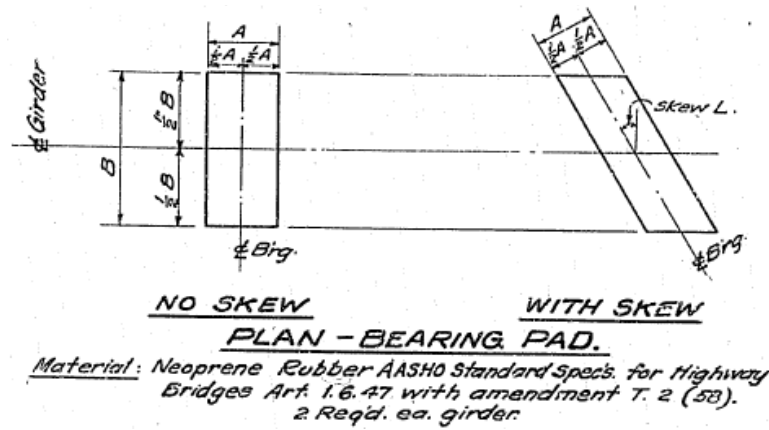


Figure B.5. Bearing dimensions

Table B.5. Bearing properties and calculated model

Series	A (in)	B (in)	h (in)	Area (in ²)	G ² (psi)	Ke (lb/in)	U _y ¹ (in)
10-30	6	12	1	72	200	14400	1.13236
40	6	14	1	84	200	16800	0.9706
50	6	17	1	102	200	20400	0.79931
60	6	17	1	102	200	20400	0.79931
70	6	22	1	132	200	26400	0.61765
80	6	22	1	132	200	26400	0.61765
90	6	22	1	132	200	26400	0.61765
100	6	22	1	132	200	26400	0.61765

¹U_y = calculated yield displacement (U_y = Ke/F_y)

²G = shear strength

From previous calculations the total weight of the superstructure is 19567 kips. Considering that there are 21 bents (the abutment bents carry only half of the tributary span weight) an average normal force per bent of 978 kips is calculated. There are twelve girders in each span and 24 girders are located at every bent. This means that there are 24 bearing caps per bent. Following this criteria the normal force acting on every bearing cap is approximately, $N=978/24=40.8$ kips. The yielding force is then,

$$F_y = N\mu = 40.8 (0.40) = 16.306 \text{ kips} = 16306 \text{ lbs} \quad (\text{B.1})$$

B.4. MATERIALS

Figure B.6 to B.9 provide stress-strain curves for the materials used in the model.

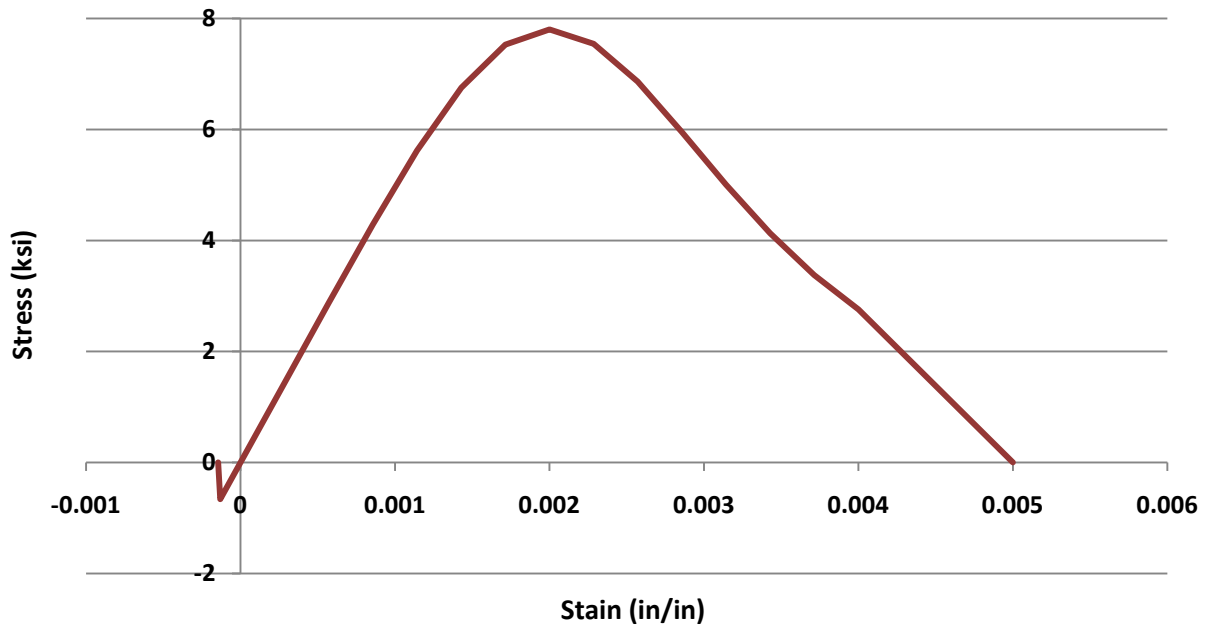


Figure B.6. Stress-strain curve for 7800 psi concrete

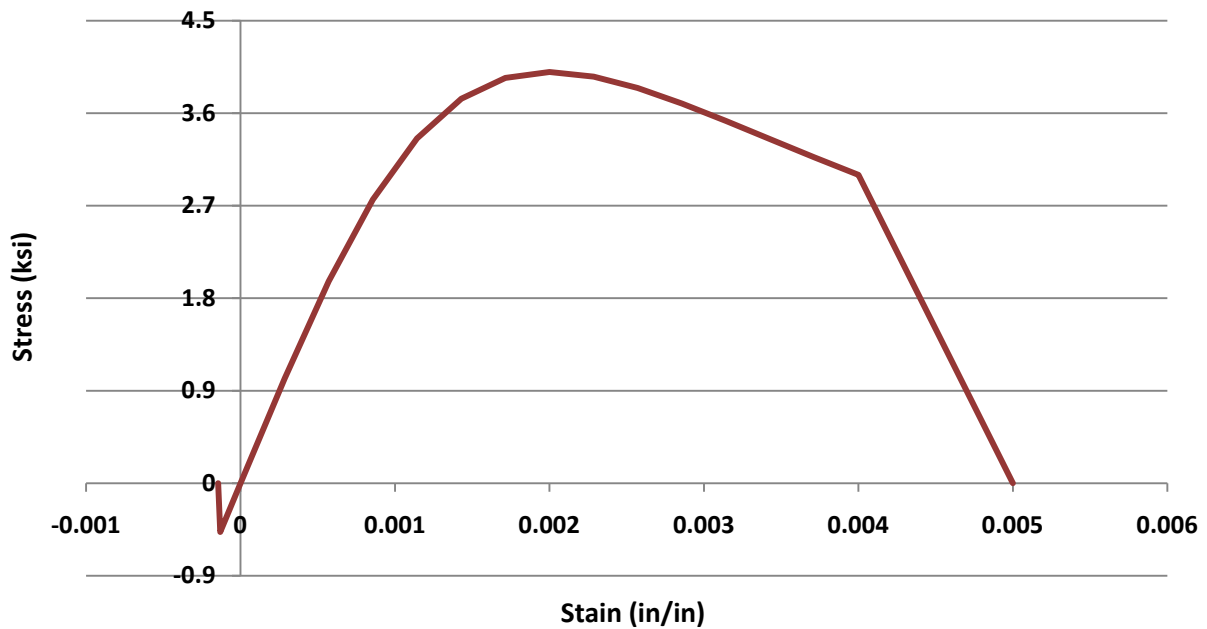


Figure B.7. Stress-strain curve for 4000 psi concrete (Class A)

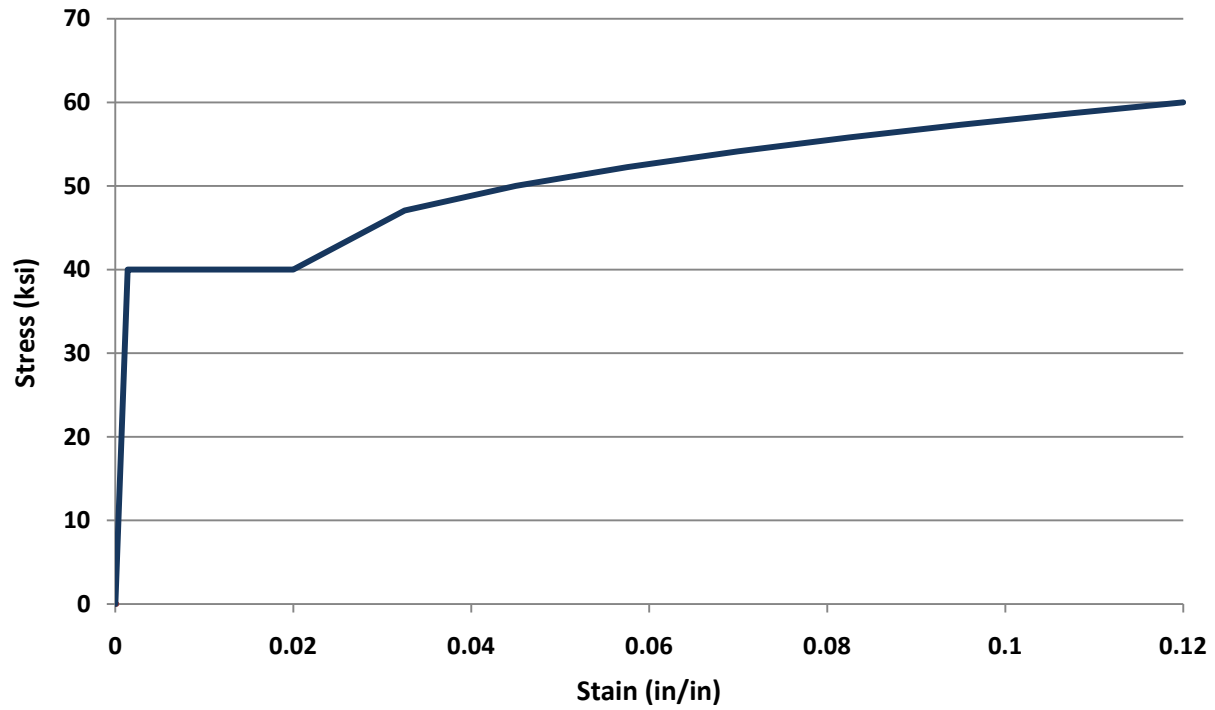


Figure B.8. Compressive stress-strain curve for grade 40 steel

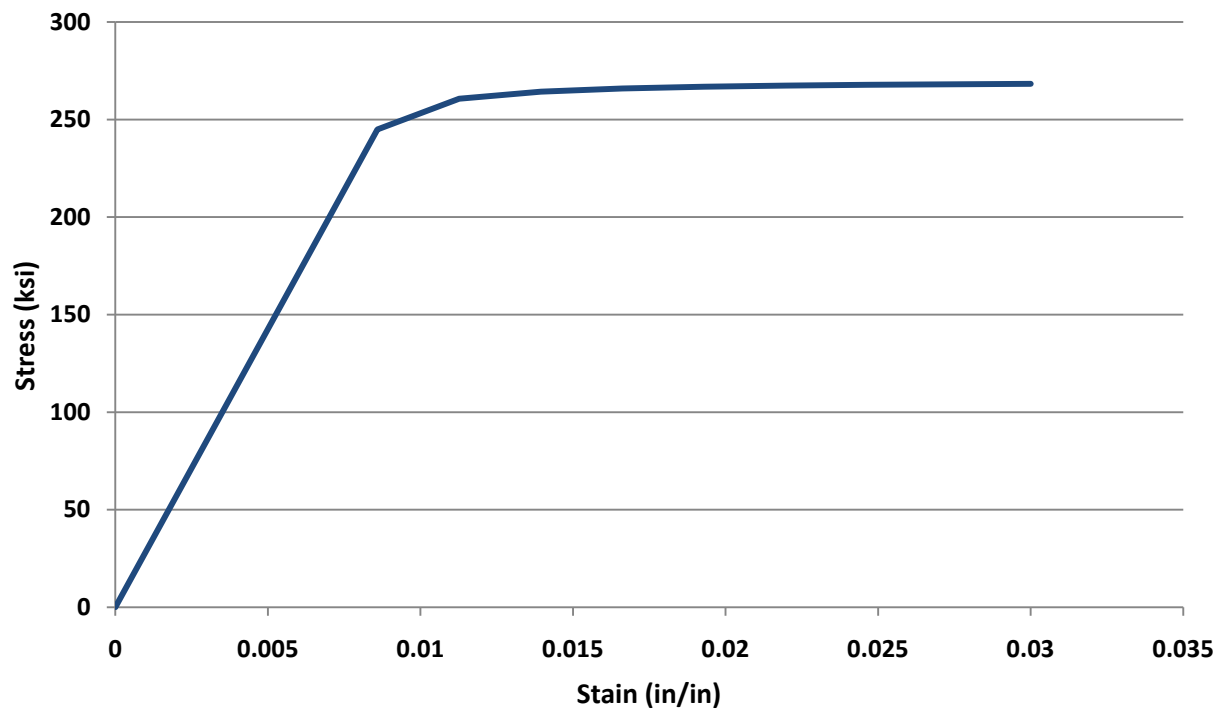


Figure B.9. Compressive stress-strain curve for grade 270 steel (Prestress)

B.5. EXPANSION JOINTS

The effective stiffness of the gap elements is given in Table B.6. Equation 4.3 is used to calculate this value.

Table B.6. Gap element calculations

$k_h =$	2083.33 kip-in ^{-3/2} /5.5ft
$n =$	1.5
$e =$	0.8
$\delta_m =$	1 in
$a =$	0.1
$k_{eff} =$	2083.33 kip-in ⁻¹ /5.5ft

B.6. FOUNDATION STIFFNESS – FEMA 356 (2000)

The footing spring stiffnesses were computed following FEMA 356 recommendations as described in Figure B.10. The computed spring stiffnesses are shown in Table B.7, Table B.8, Table B.9 for loose sand, dense sand, and stiff clay, respectively.

Table B.7. Footing spring stiffness for loose sand (kip/in)

Loose Sand					
Abutment A					
Kx	Ky	Kz	Kxx	Kyy	Kzz
919.12	946.19	789.32	6592648.48	11165814.57	9910168.84
Abutment B					
Kx	Ky	Kz	Kxx	Kyy	Kzz
688.35	719.25	570.76	2173286.36	4068387.07	3494882.83

Table B.8. Footing spring stiffness for dense sand (kip/in)

Dense Sand					
Abutment A					
Kx	Ky	Kz	Kxx	Kyy	Kzz
3678.38	3786.74	3158.93	26384243.28	44686375.92	39661193.31
Abutment B					
Kx	Ky	Kz	Kxx	Kyy	Kzz
2754.81	2878.51	2284.24	8697645.00	16281971.43	13986767.10

Table B.9. Footing spring stiffness for stiff clay (kip/in)

Stiff Clay					
Abutment A					
Kx	Ky	Kz	Kxx	Kyy	Kzz
790.58	813.87	574.49	4798280.54	8126735.56	9376702.19
Abutment B					
Kx	Ky	Kz	Kxx	Kyy	Kzz
592.08	618.67	415.41	1581767.58	2961065.28	3306752.49

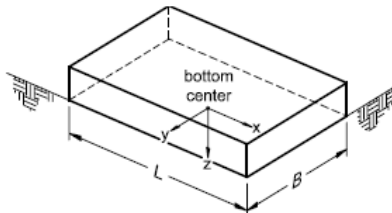
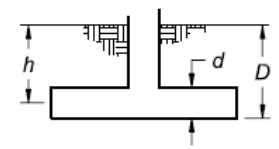
Degree of Freedom	Stiffness of Foundation at Surface	Note
Translation along x-axis	$K_{x, sur} = \frac{GB}{2-v} \left[3.4 \left(\frac{L}{B} \right)^{0.65} + 1.2 \right]$	 <p>Orient axes such that $L \geq B$</p>
Translation along y-axis	$K_{y, sur} = \frac{GB}{2-v} \left[3.4 \left(\frac{L}{B} \right)^{0.65} + 0.4 \frac{L}{B} + 0.8 \right]$	
Translation along z-axis	$K_{z, sur} = \frac{GB}{1-v} \left[1.55 \left(\frac{L}{B} \right)^{0.75} + 0.8 \right]$	
Rocking about x-axis	$K_{xx, sur} = \frac{GB^3}{1-v} \left[0.4 \left(\frac{L}{B} \right) + 0.1 \right]$	
Rocking about y-axis	$K_{yy, sur} = \frac{GB^3}{1-v} \left[0.47 \left(\frac{L}{B} \right)^{2.4} + 0.034 \right]$	
Torsion about z-axis	$K_{zz, sur} = GB^3 \left[0.53 \left(\frac{L}{B} \right)^{2.45} + 0.51 \right]$	
Degree of Freedom	Correction Factor for Embedment	Note
Translation along x-axis	$\beta_x = \left(1 + 0.21 \sqrt{\frac{D}{B}} \right) \cdot \left[1 + 1.6 \left(\frac{hd(B+L)}{BL^2} \right)^{0.47} \right]$	 <p>d = height of effective sidewall contact (may be less than total foundation height) h = depth to centroid of effective sidewall contact</p> <p>For each degree of freedom, calculate $K_{emb} = \beta K_{sur}$</p>
Translation along y-axis	$\beta_y = \beta_x$	
Translation along z-axis	$\beta_z = \left[1 + \frac{1}{21} \frac{D}{B} \left(2 + 2.6 \frac{B}{L} \right) \right] \cdot \left[1 + 0.32 \left(\frac{d(B+L)}{BL} \right)^{2/3} \right]$	
Rocking about x-axis	$\beta_{xx} = 1 + 2.5 \frac{d}{B} \left[1 + \frac{2d}{B} \left(\frac{d}{D} \right)^{-0.2} \sqrt{\frac{B}{L}} \right]$	
Rocking about y-axis	$\beta_{yy} = 1 + 1.4 \left(\frac{d}{L} \right)^{0.6} \left[1.5 + 3.7 \left(\frac{d}{L} \right)^{1.9} \left(\frac{d}{D} \right)^{-0.6} \right]$	
Torsion about z-axis	$\beta_{zz} = 1 + 2.6 \left(1 + \frac{B}{L} \right) \left(\frac{d}{B} \right)^{0.9}$	

Figure B.10. Elastic solutions for rigid footing spring constraints (FEMA356, 2000)

B.7. LONGITUDINAL BACK WALL RESPONSE – CALTRANS (2008)

Caltrans (Caltrans, 2008) states that the linear elastic demand model shall include effective abutment stiffness, K_{eff} that accounts for expansion gaps, and incorporates a realistic value for the embankment fill response. The abutment embankment fill stiffness is nonlinear and is dependent upon the material properties of the abutment backfill. Based on passive earth pressure tests and the force deflection results from large-scale abutment testing at UC Davis, the initial embankment fill stiffness is $K_i \approx 20$ kip-in/ft (11.5 kN-mm/m). The initial stiffness shall be adjusted proportional to the back wall/diaphragm height, as documented in the following equation:

$$K_{abut} = \begin{cases} K_i \times w \times \left(\frac{h}{5.5}\right) & \text{U.S.units} \\ K_i \times w \times \left(\frac{h}{1.7}\right) & \text{S.I.units} \end{cases} \quad (B.2)$$

Where, w is the width of the back wall or the diaphragm for seat and diaphragm abutments, respectively.

The passive pressure resisting the movement at the abutment increases linearly with the displacement, as shown in Figure B.11. The maximum passive pressure of 5 ksf (239 kPa), presented in the following equations is based on the ultimate static force developed in the full scale abutment testing conducted at UC Davis (Kutter, et al., 2003).

$$P_{bw \text{ or } P_{dia}} = \begin{cases} A_e \times 5 \text{ ksf} \times \left(\frac{h_{bw \text{ or } h_{dia}}}{5.5}\right) & (\text{ft, kip}) \\ A_e \times 239 \text{ kPa} \times \left(\frac{h_{bw \text{ or } h_{dia}}}{1.7}\right) & (\text{m, kN}) \end{cases} \quad (B.3)$$

The effective abutment area for calculating the ultimate longitudinal force capacity of an abutment is presented in equation B.4.

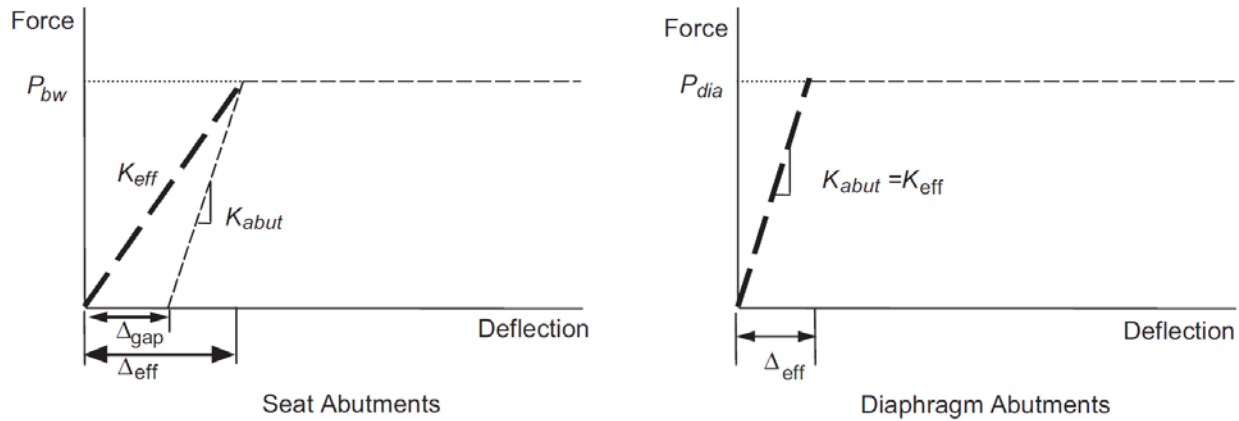


Figure B.11. Effective abutment stiffness

$$A_e = \begin{cases} h_{bw} \times w_{bw} & \text{Seat Abutments} \\ h_{dia} \times w_{dia} & \text{Diaphragm Abutments} \end{cases} \quad (B.4)$$

$h_{dia} = h_{dia}^*$ = Effective height if the diaphragm is not designed for full soil pressure (see Figure B.12)

$h_{dia} = h_{dia}^{**}$ = Effective height if the diaphragm is designed for full soil pressure (see Figure B.13)

For seat abutments the back wall is typically designed to break off in order to protect the foundation from inelastic action. The area considered effective for mobilizing the backfill longitudinally is equal to the area of the back wall. See Figure B.12.

For diaphragm abutments the entire diaphragm is typically designed to engage the backfill immediately when the bridge is displaced longitudinally. Therefore, the effective abutment area is equal to the entire area of the diaphragm. If the diaphragm has not been designed to resist the passive earth pressure exerted by the abutment backfill, the effective abutment area is limited to the portion of the diaphragm above the soffit of the girders. See Figure B.12.

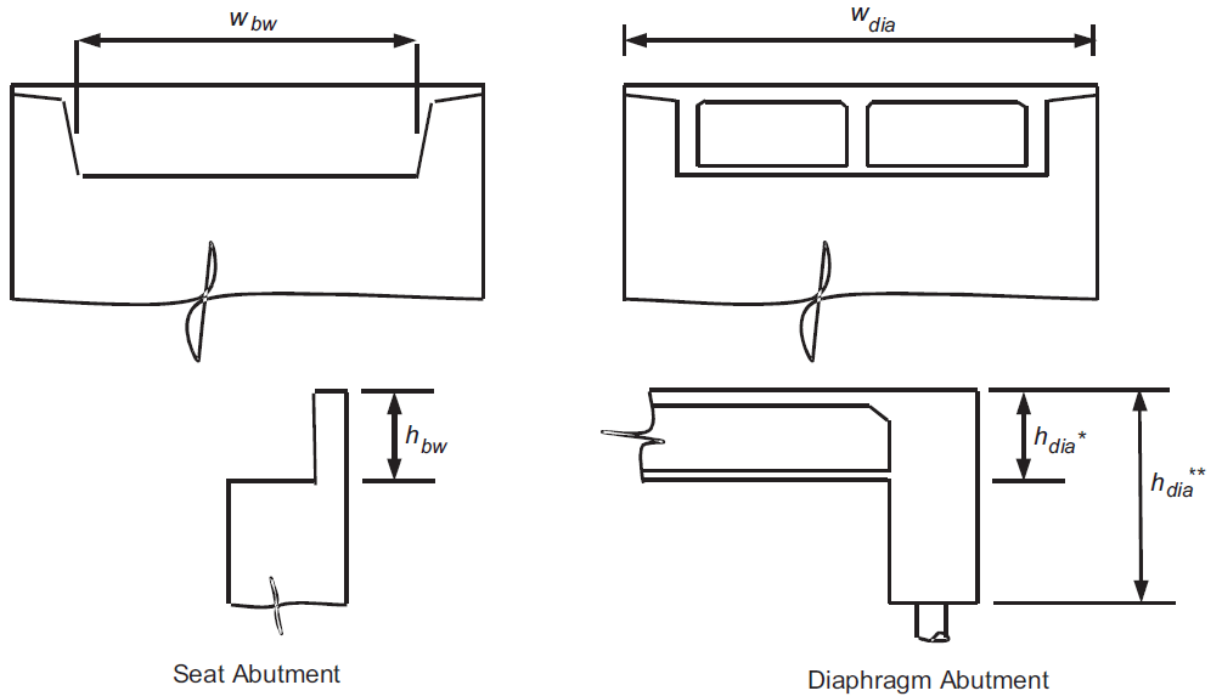


Figure B.12. Effective abutment area

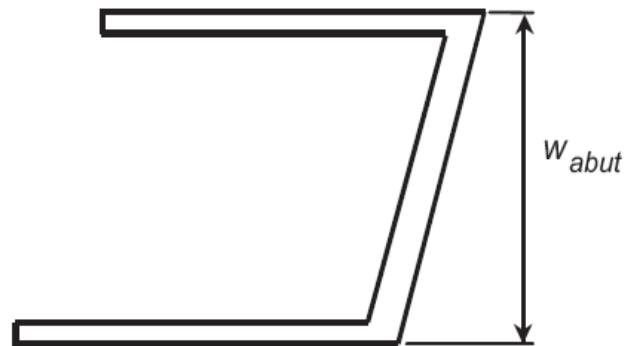


Figure B.13. Effective abutment width for skewed bridges

B.8. SOIL-PILE INTERACTION

Table B.10 through B.12 summarize the data of p - y curves for different soils. Figure B.14 and Figure B.15 show the force-displacement relationships of springs calculated (based on p - y curves) for dense sand and stiff clay respectively. Figure 4.21 shows the force-displacement relationships for loose sand.

Table B.10. Results of p-y curves for dense sand

P-Y values for dense sand													
Soil Depth (inches) ==>	24	36	48	52.8	57.6	62.4	67.2	79.2	96	120	168	240	288
Deflection, y (inches)	Lateral Soil Resistance, p (pounds/inch)												
0.00	0	0	0	0	0	0	0	0	0	0	0	0	0
0.07	352	530	708	779	850	921	992	660	798	993	1391	1992	2393
0.13	662	1005	1349	1487	1624	1760	1896	1301	1567	1928	2712	3921	4727
0.20	905	1391	1880	2075	2270	2462	2653	1904	2280	2758	3907	5729	6948
0.27	1079	1679	2288	2530	2771	3009	3243	2457	2920	3458	4940	7376	9013
0.33	1196	1882	2583	2862	3138	3411	3678	2951	3477	4024	5799	8834	10890
0.40	1271	2020	2788	3094	3397	3694	3985	3383	3949	4466	6491	10096	12565
0.47	1317	2109	2926	3252	3574	3889	4196	3753	4340	4801	7034	11165	14033
0.53	1346	2167	3018	3357	3692	4019	4337	4064	4658	5050	7451	12054	15298
0.60	1363	2203	3077	3426	3770	4106	4431	4323	4912	5232	7768	12784	16376
0.67	1374	2226	3116	3471	3821	4162	4493	4535	5114	5364	8004	13376	17283
0.73	1380	2241	3141	3500	3854	4199	4533	4707	5271	5458	8179	13850	18039
0.80	1384	2250	3156	3518	3875	4223	4559	4846	5394	5526	8308	14228	18664
1.80	1389	2264	3184	3552	3914	4267	4607	5360	5789	5688	8651	15563	21250

Table B.11. Results of p-y curves for loose sand

P-Y values for loose sand													
Soil Depth (inches) ==>	24	36	48	52.8	57.6	62.4	67.2	79.2	96	120	168	240	288
Deflection, y (inches)	Lateral Soil Resistance, p (pounds/inch)												
0.00	0	0	0	0	0	0	0	0	0	0	0	0	0
0.07	40	60	80	88	96	104	112	101	124	156	220	316	380
0.13	80	120	159	175	191	207	223	203	247	311	439	631	759
0.20	119	179	238	262	286	310	333	303	370	464	655	944	1136
0.27	158	237	316	347	379	410	442	402	491	615	869	1255	1512
0.33	195	293	392	431	470	509	548	501	610	762	1079	1562	1884
0.40	232	349	466	512	559	606	652	597	727	906	1284	1866	2253
0.47	267	402	538	592	645	699	753	692	841	1045	1484	2165	2618
0.53	301	454	607	668	729	790	850	784	953	1180	1678	2458	2977
0.60	334	504	674	742	809	877	944	874	1061	1309	1865	2746	3331
0.67	365	551	738	812	886	960	1033	962	1166	1432	2045	3027	3680
0.73	394	596	799	880	960	1040	1119	1046	1267	1549	2217	3301	4021
0.80	422	639	857	944	1030	1115	1200	1128	1364	1660	2382	3567	4356
1.80	660	1023	1387	1530	1671	1808	1942	1985	2348	2653	3947	6549	8354

Table B.12. Results of p-y curves for stiff clay

P-Y values for stiff clay													
Soil Depth,(inches) ==>	24	36	48	52.8	57.6	62.4	67.2	79.2	96	120	168	240	288
Deflection, y (inches)	Lateral Soil Resistance, p (pounds/inch)												
0.00	0	0	0	0	0	0	0	0	0	0	0	0	0
0.07	184	193	203	207	210	214	218	227	240	259	296	353	390
0.13	275	289	303	309	315	320	326	339	359	387	443	527	583
0.20	327	344	361	367	374	381	387	403	427	460	527	627	694
0.27	490	514	539	549	559	569	579	603	638	688	788	938	1037
0.33	582	612	641	653	665	677	689	718	759	818	937	1115	1234
0.40	871	915	959	977	995	1012	1030	1073	1135	1224	1401	1667	1845
0.47	1035	1088	1141	1162	1183	1204	1225	1276	1350	1455	1666	1983	2194
0.53	1302	1368	1434	1461	1487	1514	1541	1604	1697	1830	2095	2493	2759
0.60	1548	1627	1706	1737	1769	1801	1832	1908	2018	2176	2492	2965	3281
0.67	1713	1801	1888	1923	1958	1993	2028	2112	2234	2408	2758	3281	3631
0.73	1841	1935	2029	2066	2104	2141	2179	2269	2400	2588	2963	3526	3901
0.80	2315	2433	2551	2598	2645	2692	2740	2853	3018	3254	3726	4434	4906
1.80	2753	2893	3033	3090	3146	3202	3258	3393	3589	3870	4431	5273	5834

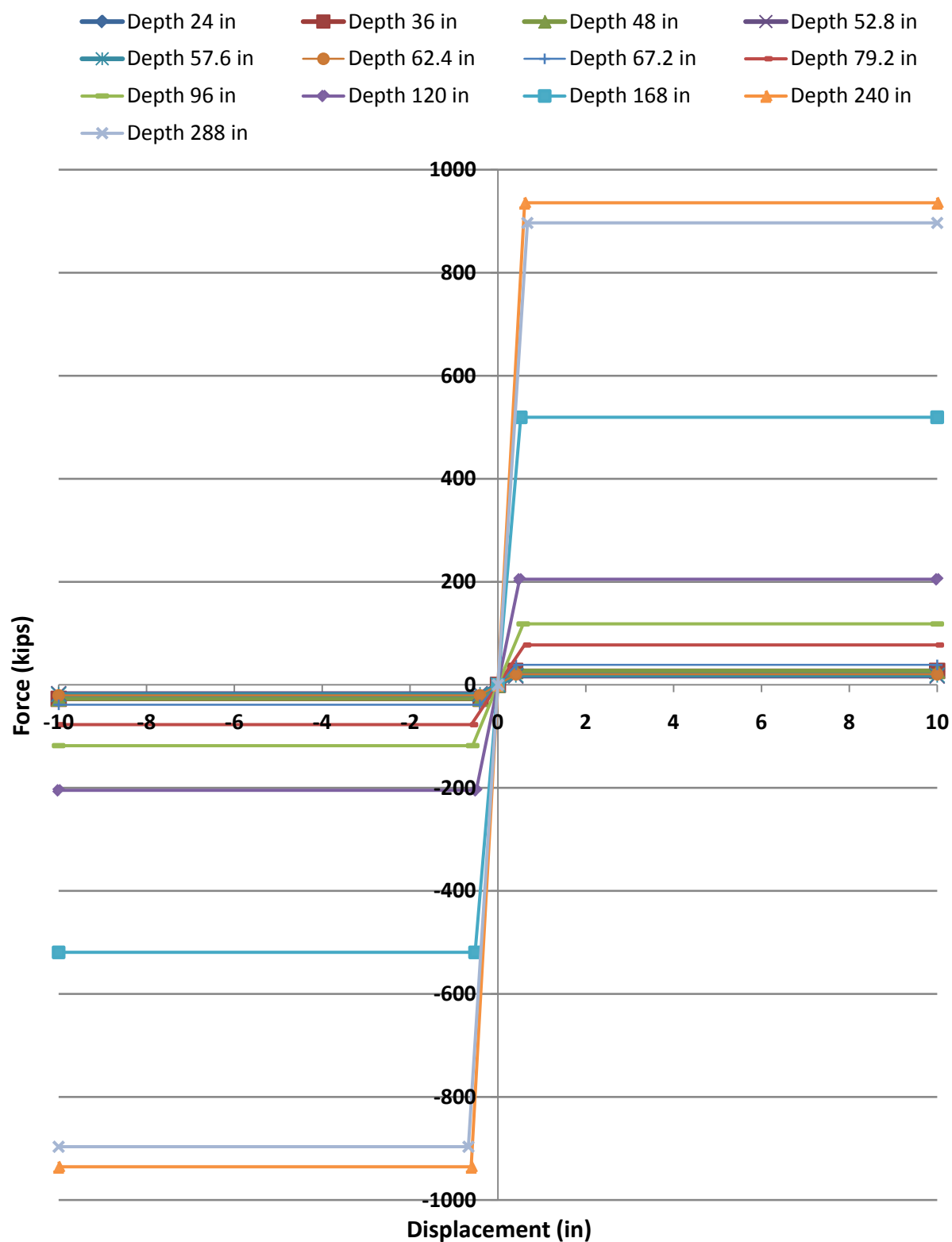


Figure B.14. The relation between the lateral force and displacement used for characterization of the springs along the pile in the dense sand

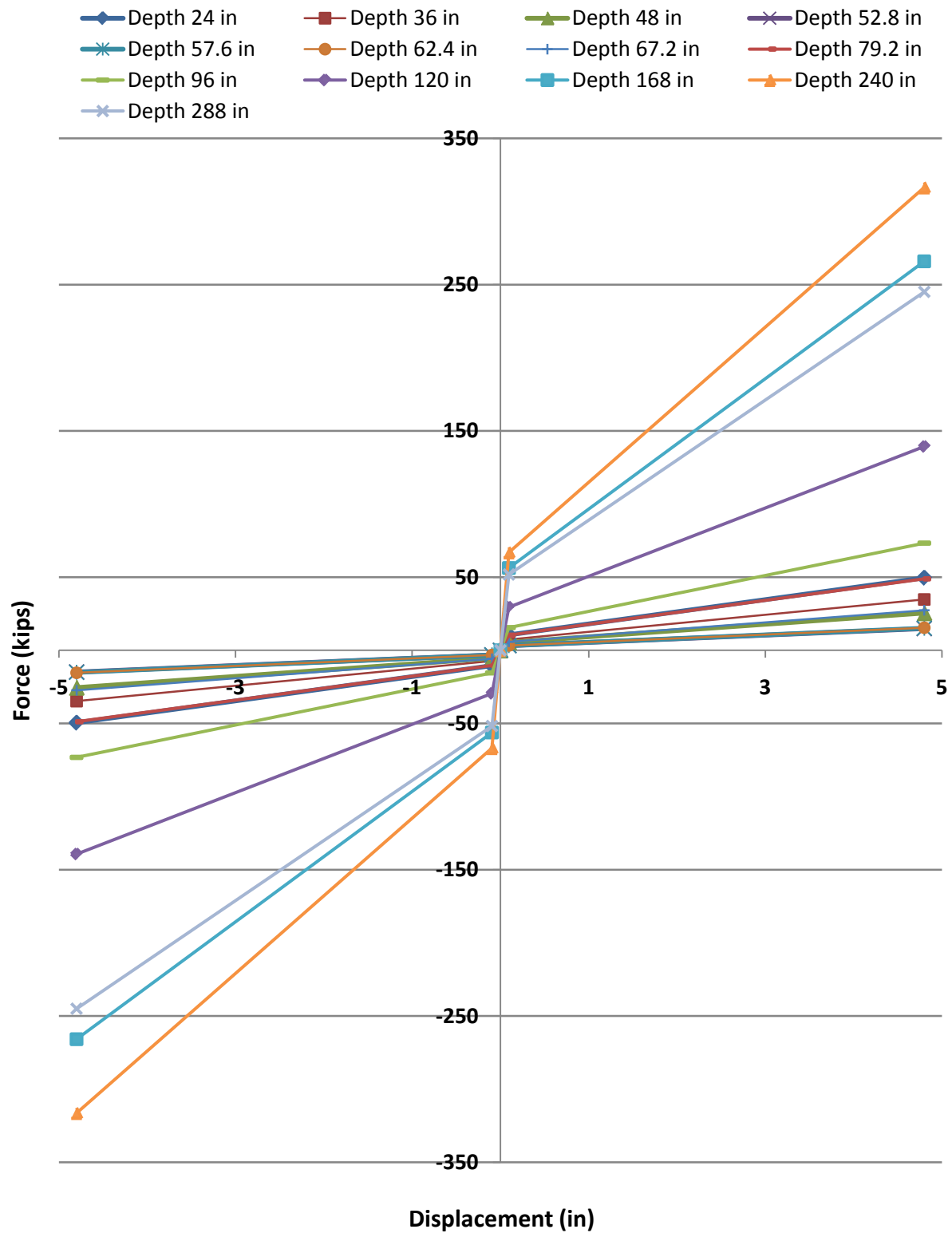


Figure B.15. The relation between the lateral force and displacement used for characterization of the springs along the pile in the stiff clay

B.9. SOIL PROPERTIES

Table B.13. Soil parameters

	Dense Sand	Loose Sand	Stiff Clay
E (psi)	5800	1450	1233
v	0.5	0.5	0.35
G (ksi)	1933	483	457
γ_{dry} (pcf)	126	110	133
γ' (pcf)	63.5	48.4	71
Phi	41	31	0
c (k/ft²)	0	0	2.94
k_{dry} (pci)	225	25	1000
k_{sat} (pci)	125	20	1032
E50(Dr)%	77.38	26	0.5

Where,

E - Modulus of elasticity,

N - Poisson ratio,

G - Shear modulus,

γ - Unit weight of soil,

Phi - Friction angle of soil,

c - Cohesion of soil,

k - Modulus of subgrade. This parameter is required for lateral analysis only,

E50 - Strain at 50% deflection in P-Y curve.

B.10. PLASTIC HINGES

Table B.14 provides the data for the bilinearized moment-curvature curves. The below ground depth of the plastic hinges varies with the above ground height of a pile. The hinge location for all three soil type can be found in Table B.15, where each bent is considered separately.

Table B.14. Bilinearized moment-curvature data

Axial Load	Φ_y	Φ_u	M_y	M_u	α^1	μ_Φ^2
(kip)	(1/in)	(1/in)	(kip-in)	(kip-in)		
133	5.84E-05	2.51E-04	23250	24040	1.034	4.30
266	5.29E-05	2.20E-04	24700	26050	1.055	4.16
532	4.10E-05	1.75E-04	26560	29590	1.114	4.26

¹ α = Over strength ratio (M_u/M_y)

² μ_Φ = Curvature ductility (Φ_u/Φ_y)

Table B.15. Average below ground depth of plastic hinges for bents

Below Ground Depth (in)			
Bent	Dense Sand	Loose Sand	Stiff Clay
2	40.58	59.32	8.35
3	35.69	49.07	7.91
4	35.49	48.61	7.89
5	35.85	49.34	7.92
6	35.90	49.43	7.92
7	36.43	50.70	7.98
8	36.23	50.29	7.96
9	36.36	50.55	7.97
10	36.44	50.72	7.98
11	36.52	50.88	7.98
12	37.42	52.72	8.06
13	37.66	52.24	8.04
14	37.74	53.38	8.09
15	38.30	54.53	8.14
16	38.86	55.68	8.19
17	39.43	56.85	8.24
18	40.06	57.93	8.29
19	39.71	57.19	8.25
20	40.26	58.30	8.30

APPENDIX C

C.1. SHEAR CAPACITY DEGRADATION MODEL

The nominal shear strength, estimated based on UCSD models, is contributed from three components corresponding to concrete, transverse reinforcement and axial load contributions.

The nominal shear strength is given by:

$$V_n = V_c + V_s + V_p \quad (C.1)$$

a) The concrete contribution, V_c

The V_c component considers the aggregate interlock in the concrete. It is given by

$$V_c = \alpha \beta \gamma \sqrt{f'_c} \zeta A_g \quad (C.2)$$

In Equation (C.2), α is a factor that accounts for the aspect ratio and is given by

$$\alpha = 1 \leq 3 - \frac{M}{VD} \leq 1.5 \quad (C.3)$$

Where M is the applied moment, V is the applied shear, and D is the external diameter of the column. β is a factor that accounts for the longitudinal reinforcement ratio and refers to the cracks width. By considering the position of the neutral axis as shown in Figure C.1, it is given by:

$$\beta = 0.5 + 20 \frac{A_{st}}{\frac{\pi D^2}{4}} \leq 1 \quad (C.4a)$$

or

$$\beta = 0.5 + 20 \frac{A_{st}}{A_g} \leq 1 \quad (C.4b)$$

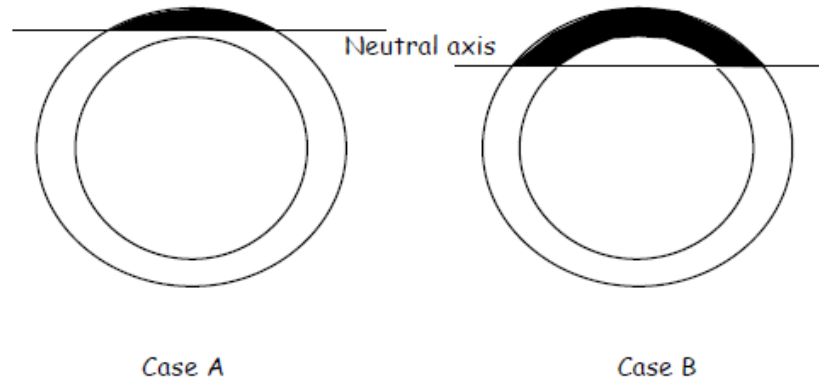


Figure C.1. Neutral Axis Positions for Hollow Circular Columns

If the neutral axis is entirely within the wall thickness (Case A) then equation (C.4a) must be used. The Equation (C.4b) is appropriate if the neutral axis is deeper than the wall thickness (Case B). In Equations (C.4), A_{st} is the total area of longitudinal reinforcement, and A_g is the gross area. Figure 2.2 shows the variation of a parameter γ , which decreases with the increasing curvature ductility. ξ is a coefficient introduced in order to express the section shear area as a percentage of the gross area. It can be estimated on the basis of the elastic beam theory. For a hollow section with $r_1/r_2 > 0.6$ (r_1 outer radius and r_2 inner radius) it can be said that $\xi = 0.533$.

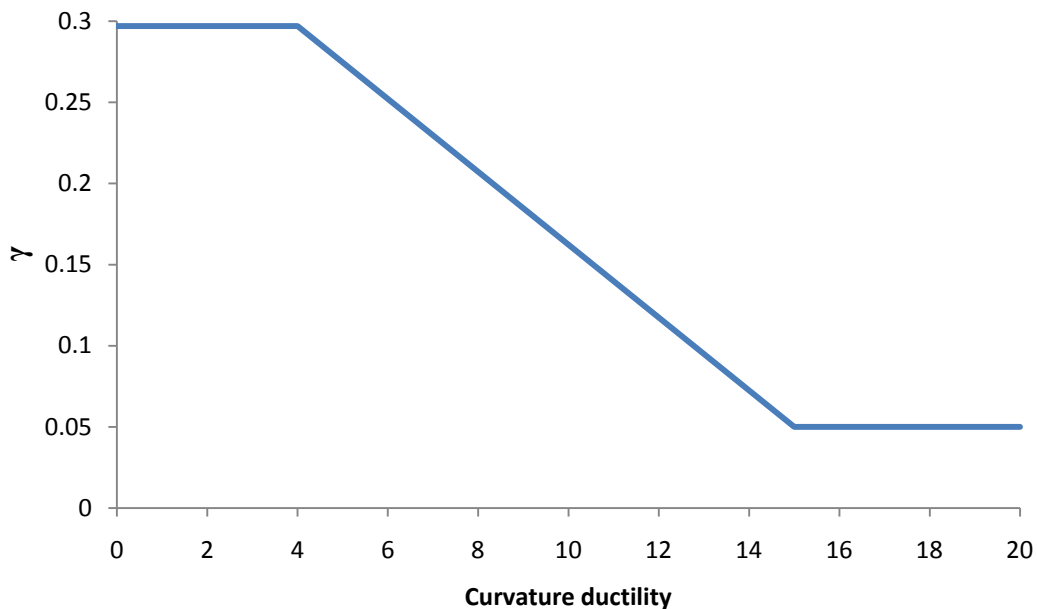


Figure C.2. Reduction of Concrete Shear Component (γ) with Curvature Ductility

b) Transverse reinforcement contribution, V_s

The V_s component is contributed from the strength of the transverse reinforcement. In this case, the transverse reinforcement is provided by a continuous spiral. The V_s component is dependent on the number of spiral layers crossed by a shear crack.

$$F_v = 2A_h f_{yh} \cos \alpha \quad (C.14)$$

The angle α increases from 0 to $\pi/2$ as the distance x between the crack and the column axis perpendicular to the applied shear force increases from 0 to R' , R' is the radius of the spiral, f_{yh} is the nominal strength of the spiral steel and A_h is the area of the spiral.

The average capacity of the spirals is thus given by:

$$F_{va} = \frac{\pi}{2} A_h f_{yh} \quad (C.15)$$

If θ is the angle of the shear crack with respect to a vertical axis, the number of spiral layers crossed by the crack is given by:

$$n = \frac{(D-c-cover)}{s} \cot \theta \quad (C.16)$$

Where D is the external diameter of the column, c is the neutral axis depth at ultimate and s is the spacing between the spiral layers, as shown in Figure 2.3. Therefore V_s is given by:

$$V_s = \frac{\pi}{2} A_h f_{yh} \frac{(D-c-cover)}{s} \cot \theta \quad (C.17)$$

In the UCSD Model, θ is equal to 30° .

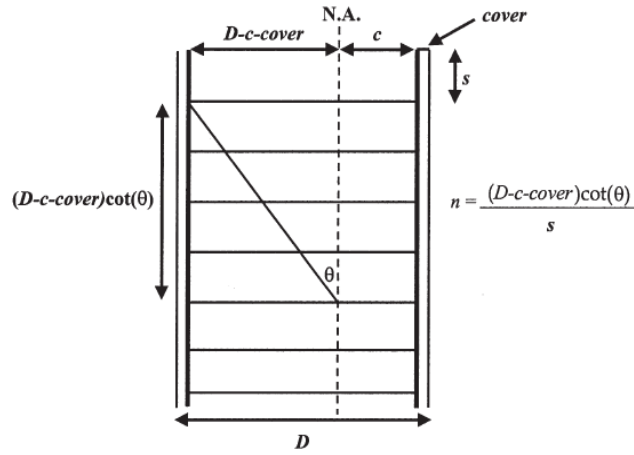


Figure C.3. Effects of concrete compression zone on truss mechanism

c) Axial load contribution, V_p

In the UCSD Model, the shear strength enhancement resulting from axial compression is considered as an independent component of shear strength, resulting from a diagonal compression strut, as shown on Figure 2.5, given by:

$$V_p = P \tan \alpha = P \frac{(D - c_{yield})}{2H} \quad \text{for } P > 0 \quad (\text{C.18a})$$

$$V_p = 0 \quad \text{for } P < 0 \quad (\text{C.18b})$$

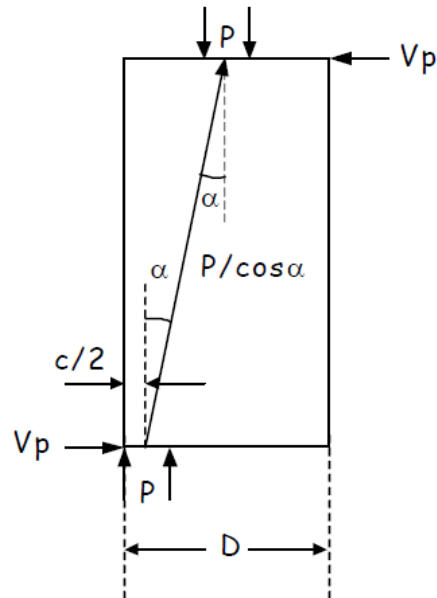


Figure C.4. Axial load component of shear

It is shown from Figure C.4 that P is the axial load and α is the angle between the column axis and the strut from the point of load application to the center of the flexural compression zone at the column plastic hinge critical section. c_{yield} is the neutral axis depth at the ideal flexural capacity, given by the moment–curvature analysis and corresponding to a concrete longitudinal strain in compression $\epsilon_c=0.004$ or a steel strain $\epsilon_s=0.015$, whichever occurs first, and H the height of the column.

It has to be noticed that three components model has provided very good results in predictions of solid columns behavior. But it might not provide such good results for hollow columns as we do not know exactly how to adapt the V_p component to this geometric particularity. Nevertheless, we will assume a full V_p contribution. Note that the preceding equations correspond to assessment as the aim of this study is to predict the behavior of the column. To transform those equations into design equations, γ and V_p have to be multiplied by a reduction coefficient of 85/100 and the angle θ has to be taken equal to 35° , which leads to a conservative margin.

C.2. NLD ANALYSIS RESULTS

The maximum forces and plastic-rotation values for the piles in the center bents are given in Tables C.1 to C.6 for all soil models in the longitudinal and transverse direction. It was deemed sufficient to consider the first column from the east of each bent, since the columns experience approximately the same force and displacement within a bent. The maximum force and rotation values give an insight on how many of the piles fail or experience yielding. SAP2000 (2007) only records plastic rotation values, so in the tables a rotation value of 0 represents a pre-yielding state. Since it is not expected to get each earthquake component

separately, the results in both fundamental directions were combined using the Square-Root-of-Sum-of-Square (SRSS) method. These results are given in Tables 4.6 to 4.9 for all soil models.

Table C.1. NLD results for loose sand model in the longitudinal direction

	Bent #	P (Kip)	V_x (Kip)	V_y (Kip)	M_x (Kip-in)	M_y (Kip-in)	R_x (Radians)	R_y (Radians)
Earthquake 1	6	257.27	139.95	5.40	829.62	20544.01	0.000000	0.000000
	7	291.65	149.17	5.14	803.17	23103.83	0.000000	0.000000
	8	257.57	164.23	4.53	715.31	25424.50	0.000071	0.002828
	9	290.95	165.88	5.46	855.82	25503.63	0.000085	0.003087
	10	269.28	162.70	4.63	726.35	25176.28	0.000072	0.002476
	11	330.82	162.21	4.71	730.68	25141.34	0.000072	0.002485
	12	328.75	155.79	7.45	1173.74	24345.34	0.000117	0.002051
	13	267.88	155.79	6.69	1061.74	24345.34	0.000106	0.001757
	14	277.12	155.79	8.84	1386.29	24345.34	0.000000	0.000000
	15	277.25	155.79	8.78	1365.93	24345.34	0.000000	0.000000
	16	274.51	155.79	7.40	1151.17	24345.34	0.000000	0.000000
Earthquake 2	6	260.33	141.84	7.93	1250.83	22446.04	0.000000	0.000000
	7	292.11	162.12	6.81	1092.46	25307.96	0.000109	0.002927
	8	258.18	165.05	7.36	1154.10	25640.28	0.000114	0.006405
	9	292.28	167.93	6.25	973.59	25698.67	0.000096	0.006151
	10	271.24	167.45	5.74	907.72	25678.85	0.000090	0.005279
	11	333.66	169.15	7.46	1191.23	25702.74	0.000119	0.006365
	12	331.48	167.42	9.11	1428.94	25582.61	0.000142	0.003617
	13	270.48	164.44	10.09	1579.46	25425.10	0.000156	0.002247
	14	279.29	164.44	9.66	1511.48	25425.10	0.000000	0.000000
	15	278.72	164.44	12.03	1847.71	25425.10	0.000000	0.000000
	16	276.94	164.44	13.56	2089.10	25425.10	0.000000	0.000000
Earthquake 3	6	262.58	167.49	6.77	1069.99	26474.60	-0.000226	-0.001561
	7	297.16	177.07	5.03	795.46	27472.47	-0.000073	-0.001606
	8	266.24	183.59	6.84	1088.13	28471.19	-0.000065	-0.000977
	9	300.03	199.46	9.28	1475.12	30992.93	-0.000253	-0.004548
	10	277.88	197.78	6.48	1033.51	30925.26	0.000160	-0.003633
	11	337.21	192.39	11.70	1832.66	29731.88	0.000781	-0.005189
	12	334.96	195.69	7.55	1572.88	30297.47	0.000222	-0.003925
	13	278.10	190.63	8.89	1397.76	29314.62	-0.000320	-0.001193
	14	285.53	180.65	9.92	1559.11	27959.02	-0.000507	0.002549
	15	285.07	180.65	10.24	1616.76	26250.66	-0.000313	0.001837
	16	235.84	160.82	12.64	1977.93	24400.92	0.000041	0.000209

Table C.2. NLD results for loose sand model in the transverse direction

	Bent	P	V_x	V_y	M_x	M_y	R_x	R_y
	#	(Kip)	(Kip)	(Kip)	(Kip-in)	(Kip-in)	(Radians)	(Radians)
Earthquake 1	6	265.82	10.61	129.36	20420.21	1685.67	0.000000	0.000000
	7	304.37	6.85	147.49	23160.24	1093.39	0.000000	0.000000
	8	275.05	4.91	157.06	24524.82	774.40	0.000938	-0.000187
	9	308.80	7.95	168.11	26288.33	1259.90	0.000893	-0.000034
	10	286.67	9.53	170.61	26647.17	1511.29	0.000997	0.000090
	11	345.78	10.36	166.09	25680.97	1628.37	0.002410	0.000471
	12	344.42	10.20	162.71	25060.64	1613.87	0.000139	0.000028
	13	278.10	10.70	161.70	24209.72	1210.69	0.000000	0.000000
	14	265.53	11.04	139.63	23416.46	1036.92	0.000000	0.000000
	15	253.07	11.37	97.56	18195.23	2195.53	0.000000	0.000000
	16	241.52	13.77	76.90	12030.64	2157.91	0.000000	0.000000
Earthquake 2	6	264.14	9.32	156.61	24333.67	1493.34	-0.001309	0.000260
	7	305.53	6.37	160.82	24840.74	995.59	-0.003339	0.000664
	8	316.77	3.06	359.66	54825.94	919.89	-0.004079	0.000821
	9	308.80	7.95	168.11	26288.33	1259.90	0.012237	-0.000403
	10	286.72	5.35	206.55	31901.82	1098.44	0.003036	0.000439
	11	346.00	7.65	183.63	28356.41	1206.09	0.004245	0.000808
	12	344.61	8.59	165.88	25542.35	1355.48	0.001138	0.000226
	13	352.13	7.28	188.79	29117.50	1216.39	0.000908	0.000278
	14	352.57	7.37	185.95	28679.40	1223.03	0.000000	0.000000
	15	313.01	9.47	133.10	18241.30	1529.67	0.000000	0.000000
	16	242.34	14.63	92.17	14402.91	2294.97	0.000000	0.000000
Earthquake 3	6	267.21	8.05	157.44	24482.55	1269.55	-0.005744	0.001143
	7	304.85	5.49	181.20	28902.79	1607.95	-0.005007	0.000806
	8	274.70	4.16	213.04	33287.71	1103.20	-0.002857	0.000189
	9	309.25	8.44	227.31	35593.48	1329.42	-0.002620	0.000059
	10	287.87	6.48	221.18	34724.36	2302.85	-0.004285	0.000261
	11	347.41	7.12	213.44	33185.23	2438.91	-0.005960	0.000327
	12	345.21	5.49	202.14	31344.83	1280.30	-0.004956	-0.000745
	13	278.10	190.63	204.14	30185.23	1210.69	-0.002549	-0.000507
	14	285.53	184.41	9.92	25187.23	1036.92	-0.001837	-0.000313
	15	285.07	180.65	10.24	24195.23	2195.53	-0.000209	0.000041
	16	243.99	19.79	118.77	18346.30	3105.39	0.000000	0.000000

Table C.3. NLD results for dense sand model in the longitudinal direction

	Bent #	P (Kip)	V_x (Kip)	V_y (Kip)	M_x (Kip-in)	M_y (Kip-in)	R_x (Radians)	R_y (Radians)
Earthquake 1	6	230.43	142.90	12.43	2124.88	24430.13	-0.000225	-0.001133
	7	260.10	154.00	9.80	1675.22	26317.03	-0.000234	-0.001790
	8	233.62	164.27	9.22	1566.95	28037.38	-0.000145	-0.001765
	9	263.00	167.47	13.15	2247.27	28535.51	-0.000149	-0.001313
	10	243.62	158.57	12.32	2105.81	27041.10	-0.000223	-0.001049
	11	296.07	149.33	12.05	2057.43	25459.05	0.000000	-0.001141
	12	293.96	140.66	11.46	1955.91	23982.37	0.000000	0.000000
	13	243.96	123.84	7.97	1361.87	21122.05	0.000000	0.000000
	14	250.23	119.20	8.20	1400.52	20349.86	0.000000	0.000000
	15	249.05	114.39	12.74	2175.62	19529.15	0.000000	0.000000
	16	207.17	112.83	14.87	2542.81	19276.55	0.000000	0.000000
Earthquake 2	6	230.66	145.38	10.93	1869.33	24837.64	0.000132	0.000794
	7	260.10	161.11	8.95	1529.51	27525.33	0.000342	-0.001451
	8	233.25	170.96	12.04	2057.40	29196.88	0.000402	-0.001989
	9	262.90	169.25	13.19	2253.02	28877.63	0.000474	-0.001843
	10	243.77	162.25	12.88	2199.87	27685.26	0.000442	-0.002004
	11	296.14	159.33	10.34	1764.72	27177.58	0.000406	-0.002688
	12	294.42	159.02	11.07	1890.13	27109.66	0.000164	-0.001844
	13	244.08	143.38	10.07	1720.07	24476.38	0.000000	0.000000
	14	250.26	130.26	8.21	1401.62	22206.31	0.000000	0.000000
	15	249.20	141.34	10.78	1841.66	24089.11	0.000000	0.000000
	16	206.98	140.64	13.14	2245.93	24007.69	-0.000048	-0.000242
Earthquake 3	6	230.94	162.01	10.46	1788.58	27725.09	0.000354	0.001709
	7	260.83	175.45	11.61	1983.45	29935.13	0.000367	-0.002823
	8	234.40	203.72	15.04	2333.69	34874.60	-0.000188	-0.005485
	9	263.58	177.75	15.90	2369.63	30356.16	-0.000399	-0.005266
	10	244.44	170.94	11.00	1879.93	29178.55	-0.000315	-0.003478
	11	296.86	162.14	14.50	2474.96	27647.65	-0.000370	-0.001982
	12	294.93	185.89	12.99	2216.58	31690.37	-0.000565	-0.003333
	13	245.00	170.32	12.91	2205.74	29037.81	-0.000635	-0.002635
	14	250.83	167.65	11.08	1892.30	28631.16	0.000117	-0.002857
	15	250.38	162.52	12.80	2187.46	27801.63	-0.000294	-0.001552
	16	208.12	151.18	15.70	2685.43	25832.72	-0.000196	0.000857

Table C.4. NLD results for dense sand model in the transverse direction

	Bent #	P (Kip)	V_x (Kip)	V_y (Kip)	M_x (Kip-in)	M_y (Kip-in)	R_x (Radians)	R_y (Radians)
Earthquake 1	6	234.35	25.51	143.00	24402.44	4361.72	0.001940	-0.000386
	7	268.10	31.23	148.24	25316.21	5337.48	0.002273	-0.001103
	8	243.58	31.79	161.63	27657.02	5434.09	0.001986	-0.001406
	9	274.34	22.61	166.82	28498.25	3862.38	-0.002474	0.000289
	10	256.27	26.02	173.11	29517.61	4445.71	0.002789	0.000508
	11	309.17	29.00	188.04	26437.21	3729.95	-0.003121	-0.000515
	12	305.16	25.43	159.68	27210.89	4340.15	0.001425	0.000284
	13	264.29	27.56	150.32	25631.95	4708.71	0.000887	0.000046
	14	259.61	19.95	143.78	24544.42	3406.50	0.000546	0.000109
	15	256.42	26.50	133.72	22819.95	4524.68	0.000000	0.000000
	16	216.60	29.02	113.09	19317.14	4958.57	0.000000	0.000000
Earthquake 2	6	236.70	32.00	157.52	26903.77	5472.78	-0.003486	0.000705
	7	273.01	43.80	169.14	28855.81	7486.73	-0.006083	-0.000890
	8	243.39	25.82	163.35	27836.77	4413.66	-0.012104	-0.001596
	9	272.63	35.16	212.35	36332.05	6010.82	-0.011219	-0.000787
	10	256.59	27.42	196.98	33594.14	4685.77	-0.009515	0.000300
	11	307.69	21.63	196.48	27316.27	3692.80	-0.007582	0.000639
	12	305.20	31.86	289.99	25658.61	5190.95	-0.009504	-0.001526
	13	256.11	30.82	158.31	26965.19	5266.31	0.002653	-0.000294
	14	260.72	23.52	144.80	24723.73	4015.72	0.002077	0.000413
	15	257.23	31.63	138.85	23671.77	5400.11	0.000000	0.000000
	16	216.67	32.65	112.39	19166.92	5579.34	0.000000	0.000000
Earthquake 3	6	233.96	47.71	140.68	24101.49	8157.19	-0.003357	0.000668
	7	268.75	37.52	152.44	25997.53	6411.95	-0.004249	0.000720
	8	239.62	35.44	160.49	27401.79	6057.63	0.002183	0.000529
	9	271.59	35.30	182.18	31036.91	6034.69	-0.008268	0.000546
	10	252.53	40.62	151.34	25853.83	6939.72	-0.006153	0.001433
	11	305.41	28.59	164.84	28146.17	4880.86	-0.006557	0.000718
	12	305.26	43.49	157.21	26807.41	7423.74	-0.004823	-0.000678
	13	252.27	41.23	144.16	24710.52	7043.46	-0.003315	-0.000659
	14	257.27	25.12	142.78	24381.42	4289.08	-0.000730	-0.000145
	15	253.96	39.37	134.53	22942.04	6722.05	0.000000	0.000000
	16	213.30	35.68	121.18	20692.09	6097.15	0.000000	0.000000

Table C.5. NLD results for stiff clay model in the longitudinal direction

	Bent #	P (Kip)	V_x (Kip)	V_y (Kip)	M_x (Kip-in)	M_y (Kip-in)	R_x (Radians)	R_y (Radians)
Earthquake 1	6	240.73	90.90	4.09	765.29	14930.28	0.000000	0.000000
	7	272.42	99.89	3.93	735.55	16083.86	0.000000	0.000000
	8	244.33	114.11	5.07	949.30	17417.23	0.000000	0.000000
	9	275.06	121.05	5.74	1073.15	17972.86	0.000000	0.000000
	10	254.82	115.78	5.27	986.50	17347.91	0.000000	0.000000
	11	309.09	112.56	5.67	1056.00	16838.08	0.000000	0.000000
	12	307.08	99.16	4.85	903.12	15461.72	0.000000	0.000000
	13	255.32	85.33	3.44	641.14	13829.34	0.000000	0.000000
	14	262.04	85.47	3.47	645.16	13732.40	0.000000	0.000000
	15	260.78	87.26	5.48	1016.13	13614.12	0.000000	0.000000
	16	216.41	88.55	7.13	1319.81	13621.06	0.000000	0.000000
Earthquake 2	6	240.94	111.98	6.16	1151.32	17411.22	0.000000	0.000000
	7	272.47	119.61	4.27	798.87	17746.98	0.000000	0.000000
	8	244.35	133.27	4.90	916.00	19235.79	0.000000	0.000000
	9	275.13	134.45	5.56	1039.31	19425.18	0.000000	0.000000
	10	254.86	132.10	5.44	1017.45	19143.44	0.000000	0.000000
	11	309.24	140.61	5.39	1004.17	19749.30	0.000000	0.000000
	12	307.09	133.49	6.05	1125.48	18907.03	0.000000	0.000000
	13	255.35	104.77	3.74	696.30	16204.68	0.000000	0.000000
	14	262.11	102.28	4.04	749.61	15559.46	0.000000	0.000000
	15	260.81	98.47	5.64	1044.58	15030.45	0.000000	0.000000
	16	216.23	95.66	7.23	1337.68	14663.76	0.000000	0.000000
Earthquake 3	6	241.64	174.16	11.59	2163.95	25433.17	0.000298	-0.001934
	7	273.26	177.59	5.99	1117.98	26364.20	0.000109	-0.001996
	8	245.03	182.23	7.95	1486.53	26781.79	0.000084	-0.002953
	9	275.96	183.09	12.49	2304.00	27031.13	0.000384	-0.004344
	10	255.71	184.24	11.09	2074.73	27125.62	0.000082	-0.002982
	11	310.94	189.94	9.97	1859.21	28350.12	0.000069	-0.003858
	12	308.40	190.40	8.83	1641.87	28172.56	0.000115	-0.003183
	13	256.76	181.97	5.78	1074.96	26586.77	0.000053	-0.001008
	14	263.24	173.21	6.49	1205.21	24999.84	0.000000	0.000000
	15	262.63	161.36	9.87	1827.59	22774.89	0.000000	0.000000
	16	219.41	149.70	13.60	2516.15	20721.04	0.000000	0.000000

Table C.6. NLD results for stiff clay model in the transverse direction

	Bent #	P (Kip)	V_x (Kip)	V_y (Kip)	M_x (Kip-in)	M_y (Kip-in)	R_x (Radians)	R_y (Radians)
Earthquake 1	6	244.14	8.94	122.80	18063.11	1672.33	0.000000	0.000000
	7	278.88	8.66	137.48	19559.05	1620.67	0.000000	0.000000
	8	251.10	6.64	142.31	20223.81	1243.98	0.000000	0.000000
	9	282.26	8.69	144.41	20531.41	1625.76	0.000000	0.000000
	10	262.86	9.34	143.25	20381.18	1747.30	0.000000	0.000000
	11	316.85	8.72	140.84	19832.23	1624.42	0.000000	0.000000
	12	315.70	9.22	133.81	18888.98	1717.11	0.000000	0.000000
	13	263.21	9.92	117.45	17224.24	1848.75	0.000000	0.000000
	14	269.28	10.17	100.70	15419.02	1890.66	0.000000	0.000000
	15	266.58	10.73	87.03	13501.80	1990.39	0.000000	0.000000
	16	222.84	11.26	79.23	12427.48	2084.03	0.000000	0.000000
Earthquake 2	6	246.02	10.26	144.28	20473.97	1920.16	0.000000	0.000000
	7	280.11	10.33	156.46	22455.79	1935.19	0.000000	0.000000
	8	251.59	10.89	163.46	23669.30	2040.86	0.000000	0.000000
	9	283.14	10.49	166.88	24241.72	1961.28	0.000000	0.000000
	10	264.12	11.35	165.60	24069.77	2123.87	0.000000	0.000000
	11	318.20	12.63	162.13	23210.87	2354.12	0.000000	0.000000
	12	317.62	13.25	152.70	21495.70	2467.26	0.000000	0.000000
	13	264.76	15.79	139.53	19636.22	2942.53	0.000000	0.000000
	14	270.58	14.69	123.48	17569.34	2732.21	0.000000	0.000000
	15	267.53	14.30	98.32	15031.71	2653.51	0.000000	0.000000
	16	223.80	13.90	90.25	13800.16	2572.09	0.000000	0.000000
Earthquake 3	6	247.28	18.05	173.85	25272.36	3377.31	0.001205	-0.000240
	7	281.83	13.98	180.18	26358.06	2617.04	0.004110	-0.000818
	8	254.15	13.21	190.37	28459.91	2471.21	0.007246	0.000515
	9	287.08	18.05	216.61	32906.49	3351.80	-0.001990	-0.000363
	10	266.24	15.72	200.15	29712.59	2941.13	0.013447	0.000454
	11	319.97	14.20	208.70	31619.97	2640.69	0.004267	0.000427
	12	318.22	16.43	185.85	27014.65	3059.87	0.003680	0.000732
	13	266.10	19.54	178.72	25879.74	3640.88	0.000181	0.000036
	14	272.91	21.82	160.96	22822.14	4054.09	0.000000	0.000000
	15	270.49	23.73	140.37	19755.76	4393.98	0.000000	0.000000
	16	228.37	25.57	129.11	18108.27	4717.37	0.000000	0.000000

Table C.7. SRSS combined NDL results for the loose sand model

	Bent #	P (Kip)	V_x (Kip)	V_y (Kip)	M_x (Kip-in)	M_y (Kip-in)	R_x (Radians)	R_y (Radians)
Earthquake 1	6	274.73	140.35	129.47	20437.06	20613.05	0.000000	0.000000
	7	312.15	149.33	147.58	23174.16	23129.69	0.000000	0.000000
	8	278.37	164.30	157.13	24535.25	25436.29	0.000941	0.002834
	9	315.54	166.07	168.19	26302.26	25534.73	0.000897	0.003087
	10	286.93	162.98	170.67	26657.07	25221.60	0.001000	0.002478
	11	368.79	162.54	166.15	25691.36	25194.01	0.002411	0.002529
	12	366.43	156.12	162.88	25088.11	24398.77	0.000182	0.002051
	13	278.24	156.16	161.84	24232.99	24375.42	0.000106	0.001757
	14	277.13	156.18	139.91	23457.45	24367.41	0.000000	0.000000
	15	283.14	156.20	97.96	18246.43	24444.14	0.000000	0.000000
	16	291.92	156.40	77.26	12085.59	24440.79	0.000000	0.000000
Earthquake 2	6	271.97	142.14	156.81	24365.79	22495.66	0.001309	0.000260
	7	313.38	162.25	160.96	24864.75	25327.54	0.003341	0.003001
	8	317.37	165.08	359.74	54838.08	25656.78	0.004081	0.006457
	9	316.23	168.12	168.22	26306.35	25729.54	0.012237	0.006164
	10	287.37	167.54	206.63	31914.73	25702.34	0.003037	0.005297
	11	370.78	169.32	183.78	28381.42	25731.03	0.004247	0.006416
	12	368.31	167.64	166.13	25582.29	25618.49	0.001147	0.003624
	13	352.24	164.60	189.06	29160.31	25454.18	0.000922	0.002264
	14	353.58	164.60	186.20	28719.20	25454.50	0.000000	0.000000
	15	314.70	164.71	133.65	18334.64	25471.08	0.000000	0.000000
	16	292.07	165.09	93.16	14553.63	25528.47	0.000000	0.000000
Earthquake 3	6	269.63	167.68	157.58	24505.92	26505.03	0.005748	0.001935
	7	315.80	177.16	181.27	28913.74	27519.48	0.005008	0.001797
	8	274.71	183.64	213.15	33305.49	28492.55	0.002858	0.000995
	9	321.03	199.64	227.50	35624.03	31021.43	0.002632	0.004548
	10	290.89	197.88	221.27	34739.74	31010.88	0.004288	0.003642
	11	374.16	192.52	213.76	33235.79	29831.75	0.006011	0.005199
	12	371.02	195.77	202.28	31384.27	30324.51	0.004961	0.003995
	13	283.11	269.60	204.34	30217.57	29339.61	0.002569	0.001296
	14	293.62	258.15	14.03	25235.44	27978.25	0.001906	0.002568
	15	292.96	255.48	14.48	24249.18	26342.31	0.000376	0.001837
	16	303.34	162.03	119.44	18452.62	24597.73	0.000041	0.000209

Table C.8. SRSS combined NDL results for the dense sand model

	Bent #	P (Kip)	V_x (Kip)	V_y (Kip)	M_x (Kip-in)	M_y (Kip-in)	R_x (Radians)	R_y (Radians)
Earthquake 1	6	313.61	145.16	143.54	24494.78	24816.44	0.001953	0.001197
	7	272.26	157.14	148.56	25371.58	26852.83	0.002285	0.002103
	8	305.38	167.31	161.89	27701.37	28559.13	0.001991	0.002257
	9	274.87	168.99	167.34	28586.72	28795.72	0.002478	0.001344
	10	290.40	160.69	173.55	29592.63	27404.12	0.002798	0.001166
	11	318.61	152.12	188.43	26517.15	25730.84	0.003121	0.001252
	12	314.12	142.94	160.09	27281.10	24371.93	0.001425	0.000284
	13	288.11	126.87	150.53	25668.11	21640.54	0.000887	0.000046
	14	283.01	120.86	144.02	24584.35	20633.00	0.000546	0.000109
	15	285.48	117.42	134.33	22923.43	20046.45	0.000000	0.000000
	16	342.82	116.50	114.06	19483.78	19904.09	0.000000	0.000000
Earthquake 2	6	311.91	148.86	157.90	26968.63	25433.44	0.003488	0.001062
	7	275.16	166.96	169.38	28896.32	28525.34	0.006093	0.001702
	8	305.79	172.90	163.79	27912.70	29528.60	0.012111	0.002550
	9	273.32	172.86	212.76	36401.84	29496.56	0.011229	0.002004
	10	290.14	164.55	197.40	33666.09	28078.99	0.009525	0.002026
	11	317.44	160.79	196.75	27373.21	27427.31	0.007593	0.002763
	12	314.41	162.18	290.20	25728.13	27602.16	0.009505	0.002394
	13	290.05	146.66	158.62	27019.99	25036.51	0.002653	0.000294
	14	282.60	132.37	145.03	24763.43	22566.48	0.002077	0.000413
	15	284.96	144.84	139.27	23743.30	24686.96	0.000000	0.000000
	16	342.93	144.38	113.15	19298.06	24647.48	0.000048	0.000242
Earthquake 3	6	313.49	168.89	141.07	24167.76	28900.18	0.003376	0.001835
	7	271.86	179.42	152.88	26073.08	30614.13	0.004265	0.002913
	8	307.17	206.77	161.19	27500.98	35396.79	0.002191	0.005510
	9	272.09	181.22	182.87	31127.24	30950.18	0.008278	0.005294
	10	291.42	175.70	151.74	25922.09	29992.46	0.006161	0.003762
	11	316.05	164.64	165.47	28254.77	28075.17	0.006567	0.002108
	12	314.77	190.91	157.75	26898.90	32548.29	0.004856	0.003401
	13	291.09	175.23	144.74	24808.77	29879.84	0.003375	0.002716
	14	283.50	169.52	143.21	24454.75	28950.64	0.000739	0.002861
	15	285.72	167.22	135.13	23046.09	28602.74	0.000294	0.001552
	16	344.28	155.33	122.19	20865.62	26542.51	0.000196	0.000857

Table C.9. SRSS combined NDL results for the stiff clay model

	Bent #	P (Kip)	V_x (Kip)	V_y (Kip)	M_x (Kip-in)	M_y (Kip-in)	R_x (Radians)	R_y (Radians)
Earthquake 1	6	299.41	91.33	122.87	18079.31	15023.65	0.000000	0.000000
	7	280.39	100.26	137.54	19572.87	16165.31	0.000000	0.000000
	8	292.30	114.30	142.40	20246.08	17461.60	0.000000	0.000000
	9	284.61	121.36	144.52	20559.43	18046.24	0.000000	0.000000
	10	277.61	116.16	143.34	20405.04	17435.68	0.000000	0.000000
	11	332.65	112.90	140.95	19860.32	16916.25	0.000000	0.000000
	12	330.48	99.59	133.90	18910.56	15556.77	0.000000	0.000000
	13	277.04	85.91	117.50	17236.16	13952.37	0.000000	0.000000
	14	271.14	86.07	100.76	15432.51	13861.94	0.000000	0.000000
	15	271.25	87.91	87.20	13539.98	13758.84	0.000000	0.000000
	16	331.74	89.26	79.55	12497.36	13779.57	0.000000	0.000000
Earthquake 2	6	298.05	112.45	144.41	20506.32	17516.78	0.000000	0.000000
	7	281.52	120.06	156.51	22469.99	17852.18	0.000000	0.000000
	8	292.01	133.71	163.53	23687.02	19343.75	0.000000	0.000000
	9	285.42	134.86	166.97	24263.98	19523.93	0.000000	0.000000
	10	277.30	132.59	165.69	24091.27	19260.90	0.000000	0.000000
	11	333.78	141.17	162.22	23232.58	19889.11	0.000000	0.000000
	12	331.98	134.14	152.81	21525.14	19067.33	0.000000	0.000000
	13	276.72	105.95	139.58	19648.57	16469.67	0.000000	0.000000
	14	272.01	103.33	123.54	17585.32	15797.53	0.000000	0.000000
	15	271.41	99.50	98.48	15067.96	15262.88	0.000000	0.000000
	16	331.26	96.66	90.54	13864.84	14887.63	0.000000	0.000000
Earthquake 3	6	296.72	175.09	174.23	25364.84	25656.42	0.001241	0.001949
	7	283.41	178.14	180.28	26381.76	26493.77	0.004111	0.002157
	8	290.09	182.71	190.53	28498.70	26895.56	0.007246	0.002998
	9	289.31	183.98	216.97	32987.05	27238.15	0.002027	0.004359
	10	276.29	184.91	200.46	29784.93	27284.61	0.013447	0.003016
	11	336.23	190.47	208.94	31674.58	28472.84	0.004268	0.003882
	12	333.26	191.11	186.06	27064.49	28338.24	0.003682	0.003266
	13	275.24	183.02	178.82	25902.05	26834.91	0.000189	0.001009
	14	273.44	174.58	161.09	22853.94	25326.42	0.000000	0.000000
	15	271.62	163.09	140.72	19840.11	23194.89	0.000000	0.000000
	16	325.89	151.87	129.83	18282.25	21251.23	0.000000	0.000000